Impact of Injector Deposits and Spark Plug Gap on Engine Performance and Emissions

By

Tawfik Badawy

A thesis submitted to

The University of Birmingham

For the degree of

DOCTOR OF PHILOSOPHY

School of Mechanical Engineering

The University of Birmingham

April 2018

UNIVERSITYOF
BIRMINGHAM

University of Birmingham Research Archive

e-theses repository

Abstract

This research has focused on obtaining a comprehensive understanding of gasoline direct injector coking effects on fuel injection, engine performance and emissions. The impact of spark plug electrode gap on flame kernel development, engine performance, and emissions was also investigated.

In this study, the deposit build-up inside the injector nozzles and on the injector tips reduced the plume cone angle, while it increased the plume penetration length, plume separation angles, mean droplet velocity and size for the coked injector. The coked injectors showed a higher degree of inhomogeneity and poorer repeatability in mixture preparation. The combustion analysis demonstrated that the coked injectors showed lower load and lower combustion stability, compared with the clean injector under the same operating conditions. Significantly higher unburned hydrocarbon emissions and particulate number concentration were also observed for the coked injectors. The location and topography of the deposits demonstrated that they extensively formed in the external holes of the injector, and reduced in size and quantity through the internal holes.

The increase of the spark plug gap resulted in an increase for the flame kernel growth area. The maximum in-cylinder pressure, turbulent flame speed, heat release rate and the mass fraction burned increased with the spark plug gap. The engine output increased slightly and the combustion process became more stable due to the reduction in cyclic variations as the spark plug gap increased. With the maximum spark plug gap, the engine produced minimum hydrocarbon emissions and particulate number concentration. The NOx emissions were increased as the spark plug gap became wider, due to the higher temperature accompanied with the increase in flame speed and in-cylinder pressure.

Acknowledgements

Dedication

I wish to dedicate this thesis

To my father,

To my mother,

To my brothers,

To my sisters,

And friends

Contents

List of Figures

List of Tables

List of Abbreviations

a	Diameter of the Injected Fuel Flow
AIT	After Ignition Timing
ATDC	After Top Dead Centre
BTDC	Before Top Dead Centre
Ca	Calcium
CAD	Crank Angle Degree
CCD	Charge-Coupled Device
CFD	Computational Fluid Dynamics
CLD	Chemiluminescence Detector
CNF	Cumulative Number Fraction
CO	Carbon Monoxide
CO_2	Carbon Dioxide
COP	Coil-on-Plug
COV	Coefficient of Variation
Cr	Chromium
Cu	Copper
CVF	Cumulative Volume Fraction
DCA	Deposit Control Additives
DISI	Direct Injection Spark Ignition
DMS	Differential Mobility Spectrometer
DPFs	Diesel Particulate Filters
E	Laser Fluence
ECU	Electronic Control Unit
EDS	Energy Dispersive X-Ray Spectroscopy
EGR	Exhaust Gas Recirculation
EH	External Hole
EMOP	Exhaust Maximum Opening Position
ETBE	Ethyl Tertiary Butyl Ether
ETCS	Engine Timing Control System
EVC	Exhaust Valve Closed
EVO	Exhaust Valve Open

Fe	Iron
FID	Flame Ionisation Detector
FPS	Frames Per Second
FSI	Fuel Stratified Injection
FWHM	Full Width at Half Maximum
GDI	Gasoline Direct Injection
HRR	Heat Release Rate
ICE	Internal Combustion Engine
IH	Internal Hole
IMEP	Indicated Mean Effective Pressure
IMOP	Intake Maximum Opening Position
IVC	Intake Valve Closed
IVO	Intake Valve Open
L	The Length of the Flame Boundary
LDM	Long Distance Microscopy
MFB	Mass Fraction Burned
NDIR	Non-Dispersive Infra-Red
NOx	Nitrogen Oxides
OS	Outer Surface
P	Total Pressure
PAHs	Polycyclic Aromatic Hydrocarbons
PDPA	Phase Doppler Particle Analyser
PFI	Port Fuel Injection
PID	Proportional-Integral-Derivative
PLIF	Planar Laser Induced Fluorescence
PM	Particulate Matter
PN	Particulate Number
Q_{ion}	Ionization Energy
$Q_{rot, vib}$	Rotational and Vibrational Energy
Q_{elec}	Electronic Energy Transfer
R&D	Research and Development
RFSI	Radio Frequency Sustained Plasma Ignition System
ROI	Region of Interest

S	Sulfur
SEM	Scanning Electron Microscope
S_f	Number of Photons Incident Per Pixel
SI	Spark Ignition
SLID	Spatial Light Intensity Distribution
SMD	Sauter Mean Diameter
SOC	Start of Combustion
SOI	Start of Injection
ST	Seat
T	Temperature
T90	90% Distillation Temperature
TWCs	Three-Way Catalysts
UBHC	Unburned Hydrocarbons
ULG	Unleaded Gasoline
UV	Ultraviolet
Ve	Excited Volume
We	Weber Number
X_{tr}	Tracer Mole Fraction
Zn	Zinc
ρ_L	Fuel Density
β_o	Fluctuation Wave Vibration Amplitude
ΔS	The Augmentation of the Flame Area
Δt	Time Interval between the Two Images
η_c	Transmission Efficiency of Optics and Filters
θ	Plumes Relative Angle
λ	Relative Air/Fuel Ratio
σ	Absorption Cross Section
σ_t	Fuel Surface Tension
υ	Spatial Frequency of the Incident Laser Radiation
ϕ	Fluorescence Quantum Yield
Ωc	Collection Solid Angle of the Optics

List of Publication

1- **Assessment of gasoline direct injector fouling effects on fuel injection, engine performance and emissions**, **Tawfik Badawy**, Mohammadreza Anbari Attar, Hongming, and Akbar Ghafourian, **Applied Energy**, 220, 2018, 351-374.

2- **Investigation of injector coking effects on spray characteristic and engine performance in gasoline direct injection engines**, **Tawfik Badawy**, Mohammadreza Anbari Attar, Peter Hutchins, Hongming Xu, Jens Krueger Venus, and Roger Cracknell, **Applied Energy**, 220, 2018, 375-394.

3- **Impact of spark plug gap on flame kernel propagation and engine performance**, **Tawfik Badawy**, Bao Xiuchao, and Hongming Xu, **Applied Energy**, 191, 2017, 311-327.

4- **Investigation of deposit effect on multi-hole injector spray characteristics and air/fuel mixing process**, Bo Wang, **Tawfik Badawy**, Yizhou Jiang, Hongming Xu, and Akbar Ghafourian, **Fuel**, 191, 2017, 10-24.

5- **Numerical analysis of deposit effect on nozzle flow and spray characteristics of GDI injectors**, Bo Wang, Yizhou Jiang, Peter Hutchins, **Tawfik Badawy**, and Hongming Xu, **Applied Energy,** 191, 2017, 350-362.

6- **Experimental characterization of closely coupled split isooctane sprays under flash boiling conditions**, Ziman Wang, **Tawfik Badawy**, Bo Wang, Yizhou Jiang, and Hongming Xu, **Applied Energy**, 183, 2017, 189-219.

7- **The influence of flash boiling conditions on spray characteristics with closely coupled split injection strategy**, Ziman Wang, Changzhao Jiang, Hongming Xu, **Tawfik Badawy**, Bo Wang, and Yizhou Jiang, **Applied Energy**, 187, 2017, 523-533.

8- **Laminar burning characteristics of ethyl propionate, ethyl butyrate, ethyl acetate, gasoline and ethanol fuels**, Tawfik Badawy, Jake Williamson, and Hongming Xu, Fuel, 183, 2016, 627-640.

9- **Microscopic characterization of isooctane spray in the near field under flash boiling condition**, Ziman Wang, Bo Wang, Changzhao Jiang, Hongming Xu, and Tawfik Badawy, Applied Energy, 180, 2016, 598-606.

10- **Study of near nozzle spray characteristics of ethanol under different saturation ratios**, Bo Wang, Tawfik Badawy, Yanfei Li, Hongming Xu, Yizhou Jiang, and Xinyu Zhang, SAE Technical Paper, 2016, No. 2016-01-2189.

11- **Optical investigation of influence of injector nozzle deposit on particulate matter emissions drift**, Mohammadreza Anbari Attar, Tawfik Badawy, and Hongming Xu, internal Combustion Engines, IMechE, 2015, London.

Chapter 1

INTRODUCTION

The aim of this chapter is to present an overview of the PhD research investigation conducted by the author, which mainly focuses on the impacts of injector fouling on spray characteristics and engine performance. The study of injector fouling due to the formation of solid deposits over the inner nozzles and the outer surface of the injector is of particular concern with nearly all injector designs for GDI application. Therefore, a more detailed study of the side effects of the injector deposits is driven by the demand for higher engine performance and reduced engine emissions. Furthermore, a comprehensive examination is carried out to study the effect of spark plug gap on flame kernel development, engine performance, and emissions.

1.1 Research Background

Over the past few decades, a number of studies have been conducted to achieve substantial improvements in the fuel economy of automotive engines. Automotive designers are seeking to develop engines with higher power, lower specific fuel consumption and lower carbon dioxide (CO_2) emissions, which can meet with future stringent emission requirements [1]. Therefore, the maximum new fleet average CO_2 emissions in 2015 and 2020 are 130 g/km and 95g/km respectively, from the recently proposed EU regulations [2, 3]. In order to achieve these needs, China, the U.S and Europe are rapidly moving towards the development of GDI engines instead of conventional PFI engines due to their benefits in those aspects [4]. By combining such engines with innovative downsizing concepts and turbocharging, this would result in 10-30% reductions in fuel consumption and CO_2 emissions depending on the degree

of downsizing and the combustion process [5, 6]. The analysis of a 40% downsizing of a DI gasoline engine, along with turbocharging, yields a 21% reduction in fuel consumption [7].

The development of the primary production automotive from the PFI engine towards the GDI engine is associated with some theoretical advantages which are summarized as follows: 1) an improved fuel economy up to approximately 25%, resulting from lower heat losses, lower pumping losses and higher volumetric efficiency; 2) improved transient response; 3) extended EGR tolerance limit; 4) the equivalence ratio can be precisely controlled. However, this transformation is also associated with the following areas of concern: 1) the rate of fuel injector deposits formation becomes relatively higher; 2) the UBHC emissions during light-load becomes relatively higher, 3) for a wide range of operating conditions the controlling process of stratified charge combustion becomes more complicated; 4) stratified charge and part load operations generate higher local NO_x production; 5) the rate of particulate matter emissions produced becomes higher; 6) the combination of lower fuel lubricity and higher pressure causes wear to the fuel system's components; 7) the maximum utilization of the advantages of the three-way catalyst becomes restricted; 8) the rate of cylinder bore wear is increased.

All injector designs for GDI application concern the phenomenon of deposit formation as a significant source of injector fouling, affecting the GDI engine performance; and therefore in any development program for GDI engines this phenomenon must be accorded resources and sufficient time. The risk of deposit build-up through the fuel injector holes occurs due to the exposure to a severe combustion environment and higher gas temperatures [8]. Fuel injector deposits experience a high rate of formation when fuel with various properties such as high viscosity, low volatility and reactivity of the unsaturated hydrocarbon chains (olefins,

aromatics) is employed [4, 9-16]. The controlling of such deposits is considered as one of the main challenges for advanced gasoline direct injection engines (GDI).

Recently, several studies have been conducted to investigate the injector deposits' phenomena [17-20]. However, their impacts on the mass flow rate reduction, spray characteristics, GDI engine performance and emissions have been much less thoroughly investigated, especially the deposits' influence regarding the mixture stratification process, diffusion phenomenon and PM emissions. Therefore, further investigation of the deposit formation, structure, physical and chemical analysis will be helpful, alongside their impacts on GDI engine performance and emissions.

The spark plug gap is another key factor which has a direct effect on the combustion process and consequently, the performance of a GDI engine. The incompatibility between the spark plug gap and the air/fuel mixture around the electrode results in misfire, backfire and knocking in GDI engines [21]. The evolution of the flame kernel is mainly linked to the effect of spark plug gap and consequently will affect the subsequent behavior of that flame; thereby influencing the engine's performance [22, 23]. Furthermore, the increase of gap spacing and gap projections is beneficial in improving the brake specific fuel consumption of the engine and the ability to ignite lean fuel/air ratios [24]. Recently, several studies have been conducted to investigate the spark plug gap effect phenomenon [21, 25]. However, the impact on the flame kernel propagation, combustion characteristics, GDI engine performance and emissions has been much less thoroughly investigated, especially the spark plug gap influence regarding the COV of IMEP, NOx, UBHC and PM emissions. Therefore, further investigation of several spark plug gaps impacts on GDI engine performance and emission will be helpful.

1.2 Objective and Approaches

The primary goal of this investigation was to study the effects of gasoline direct injector coking on fuel injection, mixture stratification, engine performance and emissions. Macroscopic spray characteristics of the coked injectors were investigated using high-speed imaging and Planar Laser Induced Fluorescence (PLIF) of the spray footprint. The fuel droplet size and velocity were characterised with a two-dimensional Phase Doppler Particle Analyser (PDPA). The impact of injector coking was further investigated by PLIF measurements of the in-cylinder charge stratification and repeatability in mixture preparation. Likewise, the effect of the electrode spark plug gap on flame kernel development, engine performance, and emissions were investigated. Planar Laser Induced Fluorescence (PLIF) was employed to investigate the combustion zone and the flame front development on the horizontal swirl plane after spark ignition for different spark plug gaps. The Cambustion DMS 500 was employed for the PM emissions of a GDI engine; whilst the gaseous emissions of hydrocarbons (HC) were analysed via an Horiba MEXA-7100DEGR gas analyser.

The main areas covered throughout this PhD study are summarized as follows:

- Effects of the injector tip deposits on spray dynamics and atomization

- Effects of the injector tip deposits on charge stratification and repeatability in mixture preparation

- Effects of the injector tip deposits on engine performance and emissions

- Effects of the injector tip deposits on mass flow rate reduction at different injection pressures

- Effects of the injector tip deposits on diffusion flame formation

- The physical characteristics and the elemental composition of the deposits

- Flame kernel propagation for different spark plug gaps

- Flame tomography imaging of the flame propagation using the PLIF technique for different spark plug gaps

- The effect of spark plug gap on engine combustion and emissions

1.3 Contributions to Knowledge

- This thesis highlights the significant negative impact of fouled injectors on PM emissions

- The PLIF technique was employed to investigate the effect of injector coking on in-cylinder charge stratification at the ignition timing and repeatability in mixture preparation

- X-ray 3D microtomography to provide visual scanning of the tip deposit, which provide supporting information for engine designing and CFD modelling of the injector deposits

- This is one of the few investigations focusing on the impact of the spark plug gap on PM emissions.

1.4 Thesis Outline

This thesis is composed of seven chapters. A brief outline of each chapter is presented below.

Chapter 2–Literature Review

This chapter covers a brief literature review of topics related to this thesis. Firstly, a detailed description of characteristics, mixture formation and operating modes of GDI engines is introduced. Secondly, spray characteristics of the GDI injector, injector fouling issue, the solution to reduce deposit formation and spark plug configuration are presented. Thirdly, an overview of the emission legislations and regulated engine-out emissions is presented. Finally, the principle of laser induced fluorescence (LIF), fuel distribution measurement using PLIF and a selection of fluorescence dopants, are reviewed.

Chapter 3-Experimental Setup and Techniques

This chapter gives detailed description of the single-cylinder optical engine test cell and instrumentation set-up, as well as detailed information of the data acquisition and recording systems. Furthermore, detailed descriptions of a fuel injection system, a phase Doppler particle analyzer (PDPA) system, a planar laser induced fluorescence (PLIF) system, the Schlieren optical method and a high-speed camera are introduced. Emission gas analysers are also briefly presented.

Chapter 4-Investigation of Injector Coking Effects on Spray, Mixture Stratification and Emissions

This chapter provides a comprehensive understanding of gasoline direct injector coking effects on fuel injection, engine performance and emissions. Deposit build-up in the coked injectors and fouling cycle repeatability is first examined by measurements of the fuel flow rate. Macroscopic spray characteristics of the clean and the coked injectors were investigated using high-speed imaging and planar laser induced fluorescence (PLIF) of the spray footprint. The

fuel droplets size and velocities were characterised with a two-dimensional Phase Doppler Particle Analyser (PDPA). Combustion analysis, using in-cylinder pressure data and the mass fraction burned (MFB) was used, along with exhaust emissions measurement to obtain a better understanding of the GDI injector's coking effects on engine performance and emissions.

Chapter 5-Investigation of Injector Coking Effects on Spray characteristics under Different Injection Pressures

This chapter provides a comprehensive understanding of gasoline direct injector coking effects on fuel injection mass flow rate and spray characteristics under different fuel injection pressures. The spray and droplet characteristics of a coked injector were compared to those of a clean injector under different injection pressures and investigated using high-speed imaging and a Phase Doppler Particle Analyzer (PDPA). X-ray 3D microtomography images were employed to shed more light on the structure of the injector nozzle deposits.

Chapter 6-Impact of Spark Plug Gap on Flame Kernel Propagation and Engine Performance

This chapter provides a comprehensive examination of the effect of the electrode spark plug gap on flame kernel development, engine performance, and emissions. High-speed Schlieren visualization was utilized to study the flame kernel growth at different equivalence ratios. Planar Laser Induced Fluorescence (PLIF) was employed to investigate the combustion zone and the flame front development on the horizontal swirl plane after spark ignition. High-speed imaging was carried out to study turbulent flame propagation. Combustion analysis, using in-cylinder pressure data and Mass Fraction Burned (MFB) was employed, along with exhaust

emissions measurement to obtain a better understanding of the spark plug gap effects on engine performance and emissions.

Chapter 7-Summary, Conclusions, and Recommendations for Future Work

This chapter summarizes the thesis, discusses its findings and contributions, and provides the key conclusions. Outlines of directions for future research are then given.

Chapter 2

LITERATURE REVIEW

The contents of this chapter are mainly focused on the presentation of a literature review and background knowledge regarding the work conducted for this thesis. The current work examines the effect of injector deposits and the spark plug gap on GDI engine performance and emissions. The measurements for this work are accomplished via an optical GDI engine, therefore; a brief general review regarding the features of modern GDI engines including the mixture formation process and the operation modes is presented. Likewise, the types of GDI injectors, the emission legislations and the major emission components are described. This is followed by the key fundamentals of injector deposit formation and its side effects on the delivered mass flow rate, spray characteristics and engine emissions. Furthermore, the methods used to reduce the deposit formation, including the use of additives and a coating are presented. Also, a literature review relevant to the influence of spark plug electrode design and structure on the GDI engine performance and emissions is discussed. Finally, the principal of laser induced fluorescence (LIF) and the common dopants selected for in-cylinder mixture concentration measurements using PLIF are considered.

2.1 Overview of Direct Injection Gasoline Engines

The environmental impact resulting from internal combustion emissions is significant. These vehicle emissions include nitrous oxides, carbon monoxide and particulates and they are significant contributors towards the global warming phenomena. These phenomena coupled with the reduction in oil reserves are the main drive for research and development (R&D) of

IC engines, to address the critical barriers towards higher efficiency, lower fuel consumption and advanced IC engines with very low emissions. Emissions legislation and tax incentives motivate engine developers to build new fuel efficient vehicles with low emissions, which must meet Euro 6 standards for exhaust emissions of NOx and other emissions including CO_2, UBHC and PM [26]. Another factor which is now becoming important is highlighted in emissions regulations for passenger vehicles traditionally being based on the New European Driving Cycle (NEDC) [27]; however, this test cycle does not represent closely enough real road driving in terms of CO_2 and other emissions levels. Consequently, an additional Real-World Driving Emissions (RDE) test was developed by the European Union (EU) for measuring vehicle emissions over a wide range of different operating conditions. Therefore, the world has moved towards gasoline direct injection (GDI) engines, which in the future will have the ability to meet these requirements of producing lower fuel consumption and higher specific power output.

In 1925, Jonas Hesselman, a Swedish engineer, was the first to propose the basic idea of injecting the gasoline fuel directly into the engine's cylinders. At that time, this idea was employed for military purposes in order to develop a new generation of strong fighter aircraft [28]. Then this idea was developed and applied for the first time in vehicles by Goliath and Gutbrod in 1952. Then in 1955, Mercedes-Benz released a first direct injection engine with a four-stroke cycle operation for production; this engine was installed in a Mercedes-Benz 300SL. The direct fuel injection system employed for these engines was manufactured by Bosch. During the 1970s, the Ford Motor Company developed a direct injection system by using a unique high-pressure pump and direct injectors, and the investigation was implemented in a V8 engine [29]. However, the project developed by Ford was soon cancelled due to the complexity of the injection systems and furthermore the extremely high cost of the fuel pump,

injector and the higher levels of NOx emissions which could not meet the Environmental Protection Agency (EPA) limit.

In 1996 Mitsubishi, succeeded in producing the first four-cylinder modern GDI engine as Galant/Legnum's 1.8 L with a straight arrangement of the cylinders [30] which was followed by new versions including six-cylinder GDI engines with a V configuration of the cylinders. Furthermore, in 1997, Toyota developed their own new GDI engine [31]. Both Mitsubishi and Toyota design helped engines to work under different operation modes: homogenous mode for high load and high-speed operation; whilst for part load and low to medium speed operation, stratification mode was employed. In 2000, Audi and Volkswagen developed fuel stratified injection (FSI) GDI engines. Furthermore, they coupled their design with different advanced technologies such as turbocharging, engine downsizing, variable valve timing and lean stratified combustion technologies, which resulted in lower fuel consumption with a percentage of 20~25 at part load, due to the lower pumping losses, the use of higher compression ratio and the use of wasted energy in the exhaust [32-34].

2.2 Operation modes and Mixture Formation in Gasoline Engine

The air/fuel mixture preparation is a key parameter for a successful GDI combustion system, especially with the limited time available for mixing process. Consequently, the technique employing metering the fuel to the engine, plays a dominant role in the mixture preparation process. For a gasoline engine, the fuel can be introduced to the engine via three methods: carburetor, port fuel injection and GDI.

Figure 2.1 demonstrates a schematic diagram of the three metered fuel devices.

(a) carburetor   (b) Port fuel injection   (c) Direct injection
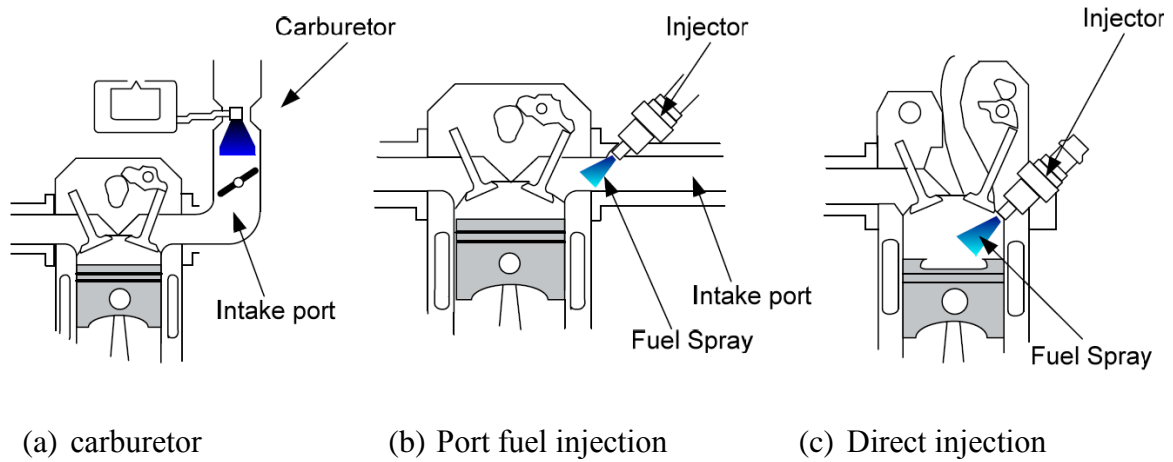
Figure 2.1.Mixture formation in gasoline engines [1]

The theory of operation of the carburetor is mainly based on Bernoulli's principle that the static pressure is inversely proportional to the air velocity. Figure 2.1.(a) displays that as the intake air passes through the throat area, the pressure drops and the air velocity increases. Consequently, the pressure difference will drive the fuel and meters it into the throttle, and then the fuel will be atomized to small droplets due to the higher velocity of the intake air. Then the fuel droplets will be vaporized and a homogenous mixture will be produced. However, the use of a carburetor becomes obsolete due to its disadvantages: 1) difficulty to control precisely the amount of fuel metered at different operating conditions; 2) higher level of emissions; 3) uneven distributions of the fuel among the cylinders; and 4) poor engine response and driveability.

In 1978, port fuel injection (PFI) was utilized instead of a carburetor, where the fuel was pressurized up to 3 bar using a pump and then injected through the induction manifold via an injector. A lot of advantages were associated with PFI in comparison to the carburetor: 1) more precise control of the air/fuel ratio and more even distribution of the fuel among the cylinders; 2) improvement in the volumetric efficiency; 3) the engine response and driveability were improved; and 4) low particulate matter (PM) emissions. By contrast, PFI encounters bad fuel

metering for cold start and transient operating conditions. Furthermore, the deposit formation around the intake valve causes a significant effect on PM emissions [35].

The limitations of PFI to meet the emissions legislation requirements are mainly addressed by the developing of the gasoline direct injection (GDI) system. In comparison to PFI, GDI has some advantages, which are summarized as follows: 1) more precise fuel metering control, better atomization of the fuel and minimum over-fueling required for cold start to ensure rapid engine start; 2) enhancement in the transient response and emissions due to faster catalyst light-off in cold start; 3) increased compression ratio, less pumping losses, higher volumetric efficiency, lower fuel economy and higher output power. However, the replacement of PFI engines with GDI engines is associated with the following areas of concern: 1) the formation of deposits with a high rate along the injector tip and inside the injector holes, besides the high possibility of spark plug fouling; 2) relatively high light-load emissions of UBHC and NOx; 3) piston and cylinder liner wetting thus more severe combustion chamber deposits; and 4) difficulty in controlling the stratified charge combustion for different operating conditions.

GDI engines experience two kinds of charge modes, homogenous and stratified charge modes, see Figure 2.2. Regarding the homogenous mode, and in order to obtain an efficient combustion process, early injection of the fuel during the intake stroke is utilized to give sufficient time for the fuel to be vaporized and to have better mixing with the air due to the higher turbulence effect. This kind of operation is utilized for slightly rich or stoichiometric conditions at high engine load. By contrast, the late injection of the fuel during the compression stroke is identified as stratified mode operation. This kind of operation is employed for partial load conditions. The load of the engine is mainly controlled by the air/fuel ratio, where the engine works under unthrottled conditions for stratified charge operation [36]. By contrast, for the

homogenous mode the load is controlled via the throttle position.

Homogeneous charge   Stratified charge
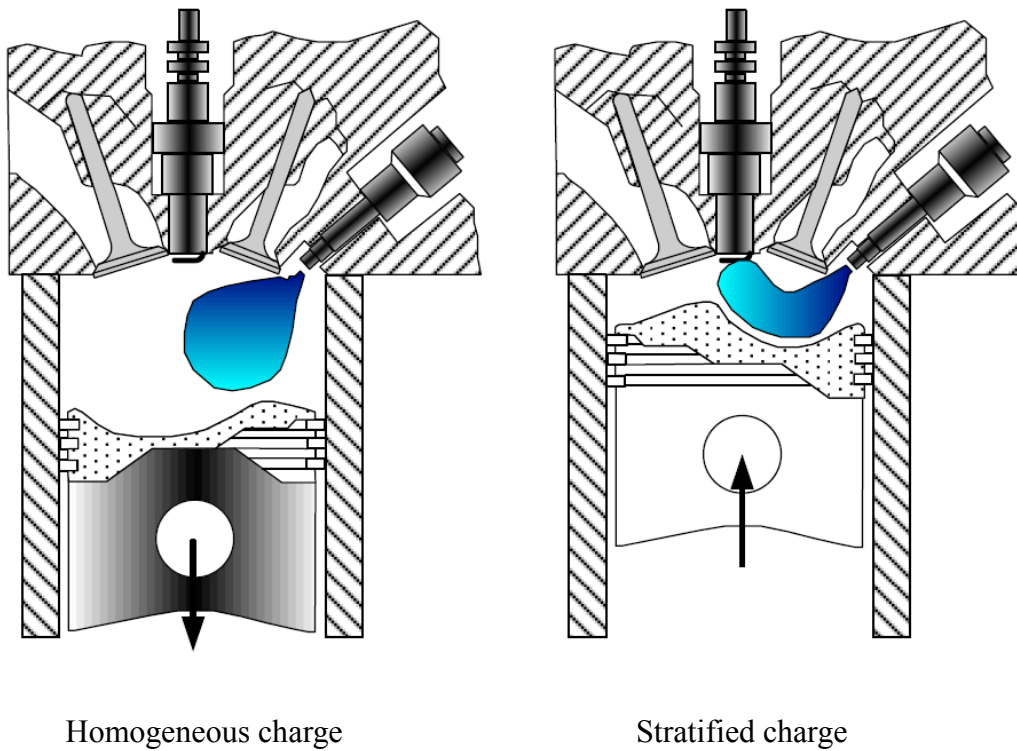
Figure 2.2. Homogenous and stratified charge mode [1]

2.3 Stratified Operation Combustion Systems

The mixture preparation process and the guidance of the spray towards the spark plug are carried out by using three different combustion concepts. These GDI combustion concepts are classified as wall-guided, air-guided and spray-guided, as shown in Figure 2.3. These concepts can be distinguished based on the way they are employed to direct the injected fuel close to the spark plug [37].

| Wall guided | Air guided | Spray guided |
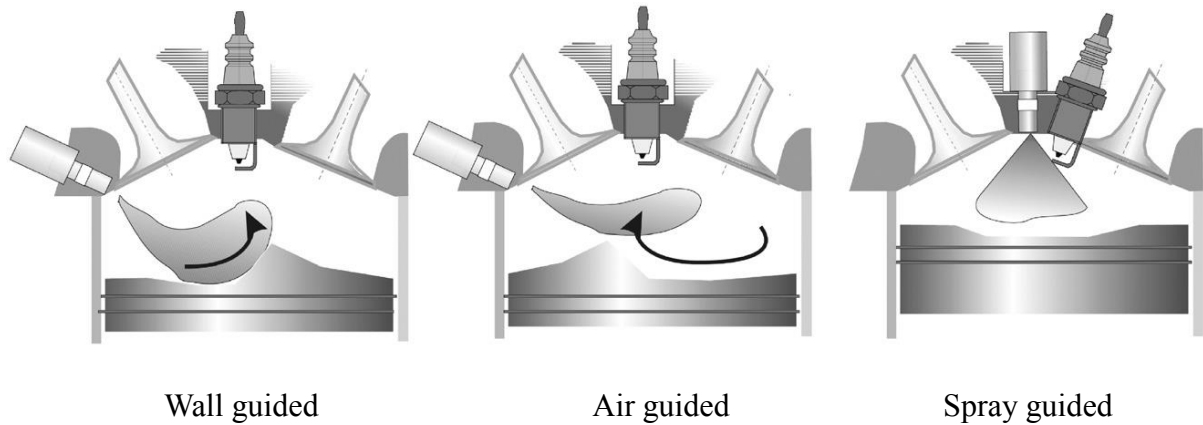
Figure 2.3. Stratified mode combustion systems [38]

In a wall-guided combustion system, the piston surface configuration is employed to direct the injected fuel towards the spark plug via the piston crown bowl. However, the wall-guided combustion operation is associated with the following areas of concern: 1) deposition of the fuel on the piston and cylinder walls; 2) higher mechanical losses due to the heavier weight of the special shape of the piston in comparison to a conventional piston; 3) severe piston wetting, which results in incomplete combustion and consequently a higher level of emissions such as HC, CO, and particulate matter; and 4) difficulty of coordinating the injection and ignition timing over a wide engine speed/load range, due to the strong dependence of the injection timing on the piston position, and consequently on the engine speed. Whilst for an air-guided combustion system, the fuel is directed towards the spark plug via the high turbulence motion of the air generated by using a special configuration of the inlet ports, as well as the special shapes of the piston surface [39]. However, the volumetric efficiency associated with an air-guided combustion system is reduced due to the swirl or tumble flow required to perform this operation [28]. For both wall and air-guided systems, intentionally the injector is positioned away from the location of the spark plug to reduce the injector tip temperature and consequently lower the rate of deposits that will be formed.

Due to the aforementioned disadvantages of both the air and wall-guided systems, the spray-guided was developed and utilized to meet the emissions legislations requirements. For the spray-guided system, the fuel is injected directly near the spark plug. This kind of system demonstrates the highest efficiency, less wall wetting, less sensitivity to the in-cylinder air flow and lower HC. However, it is noticed that some disadvantages accompany this type of system, including spark plug fouling and poor robustness (high sensitivity to variation in ignition and injection timing) [40].

2.4 High-Pressure Fuel Injection System

GDI engines mainly focus on the improvements of the fuel injection system as a key parameter affecting the combustion process. The fuel injection system must be utilized to provide the desired spray characteristics for both stratified and homogenous charge combustion modes. For homogeneous charge operation, and especially for early injection and lower in-cylinder pressure, the spray should be well atomized with even dispersion of the fuel spray. Whilst stratified charge mode requires a spray pattern with high repeatability and compactness in order to achieve a proper air/fuel mixture. These requirements can be fulfilled by using a fuel injection system which is electronically controlled. This electronic system includes a solenoid-actuated electronic high-pressure fuel injector which is employed to achieve the desired spray characteristics. Different GDI injector designs have been proposed to carry out the atomization process of the spray. These designs include: a) swirl injector, b) outward-opening injector, and c) multi-hole injector, as shown in Figure 2.4.

The first generation of modern GDI engines was mainly focused on the swirl type solenoid injectors for a wall-guided combustion system. This kind of injector consists of a single exit

orifice with an inward opening pintle [41]. The spray emerges from this single exit orifice as an annular sheet which propagates outwardly in a radial direction to form a hollow cone spray. However, these kinds of injectors experience significant changes with the injection pressure, the injector operating temperature, and the ambient pressure or density. At the designed injection pressure (between 50 to 100 bar) and elevated ambient density during the late injection of the stratified charge operation, the hollow-cone spray collapses, forming a narrow spray envelope with an increased spray penetration [28]. Therefore, for part load conditions, it is very hard to optimize the stratification mode operation due to the substantial changes occurring for the spray pattern of a swirl injector over different operating conditions of the fuel rail pressure and in-cylinder density.

(a) Swirl injector

(b) Outward-opening injector   (c) Multi hole injector
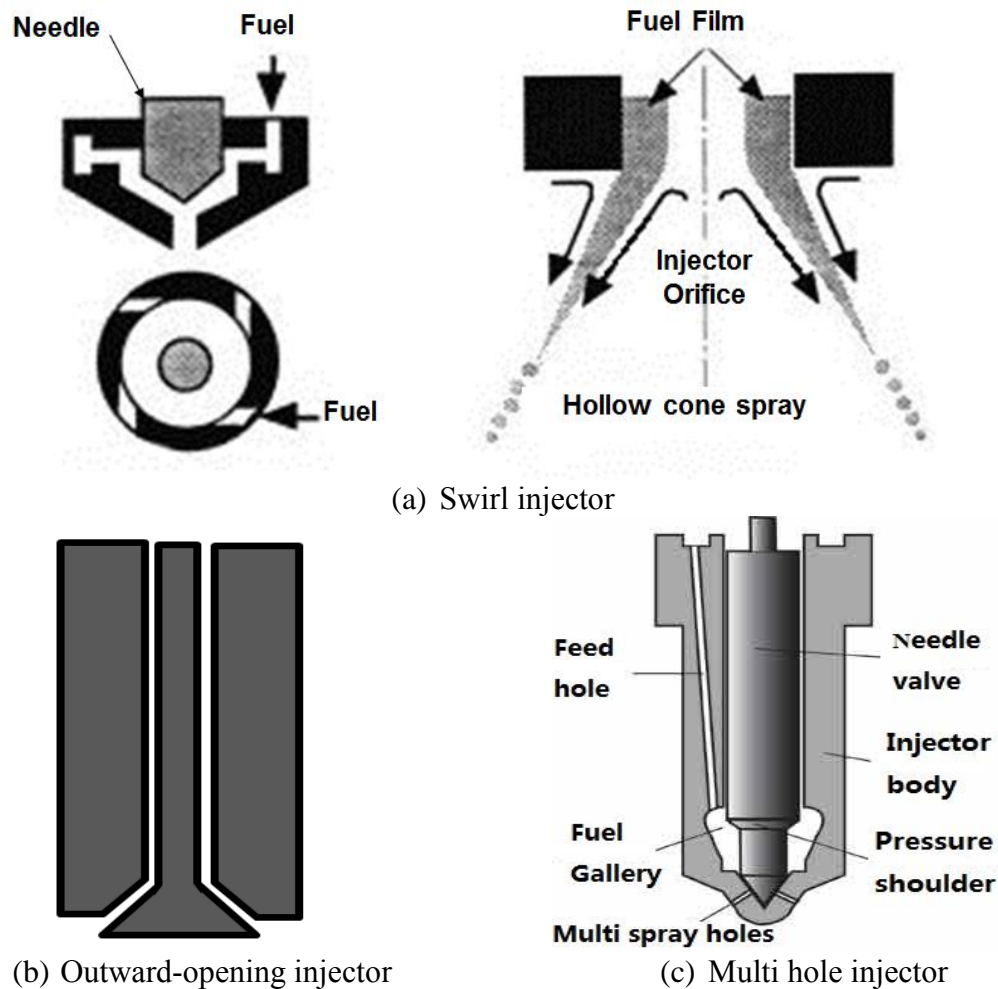
Figure 2.4. different GDI injector designs [28]

For part load conditions, spray-guided stratified combustion is carried out using either a piezo-actuated or a solenoid actuated multi-hole GDI injector to enhance the performance of GDI engines at full load [42, 43]. The main advantage of multi-hole injectors is that they can be used to produce any spatial distribution pattern of the spray based on the number of holes and the angle between the axis of the injector and the spray plumes axis. However, the main concern regarding the injector its high tendency for the injector hole to become blocked by soot deposit due to the small diameter of the nozzle holes.

An outward opening nozzle exposes the nozzle's cross section when the valve opens and generates a self-forming hollow cone spray without a pre-jet [44]. Outward opening injectors have the ability to eliminate any blocking to the injector by deposit build-up due to their outward opening pintle, in comparison with the multi-hole injector. Furthermore, the initial liquid sheet thickness, spray angle, penetration length and droplet size can be precisely controlled by the pintle stroke. Recently, the outwardly-opening piezoelectric injector is gaining popularity as a highly efficient hollow-cone spray injector due to its precise control of the spray by an accurate piezoelectric actuator [45]. In addition, it can potentially overcome the longer liquid fuel penetration problem associated with multi-hole injectors due to poor momentum exchange with the surroundings [46].

2.5 GDI Injector Spray Characteristics

Due to the limited time available for the air/fuel mixture in GDI engines to be prepared before the combustion event, the injector design and the characteristics of fuel spray have a great impact on the combustion process and the engine performance. Spray characteristics such as spray cone angle, penetration length, mean droplet diameter and fuel delivery rate are essential for fuel/air mixture preparation in GDI engines. The development and optimization of a GDI

combustion system depends mainly on the interactions between the spray characteristics, in-cylinder air flow field, piston bowl configuration and the location of the spark plug [4]. By contrast, the influences of the port fuel injector spray characteristics on the subsequent combustion event are less significant. This can be due to the longer residence time of the fuel while the intake valve is closed. Likewise, the air flow rate induction during the intake valve opening assists the secondary atomization of the fuel. In comparison to PFI engines, a GDI engines mixture preparation time is significantly less: therefore, the spray characteristics and the fuel distribution to the optimum location are the key parameters in controlling the GDI combustion process. For a PFI engine, the Sauter mean diameter (SMD) is around 200µm; whilst for a GDI engine the SMD is required to be as low as 15µm, in order to improve the combustion stability via a lower coefficient of variation (COV) of indicated mean effective pressure (IMEP) and to produce acceptable levels of UBHC emissions to meet the stringent emission legislations [4, 47]. Gasoline direct injection engines become more feasible when the vaporization process of the small fuel droplets is achieved quickly [48, 49].

The design of the GDI injector depends mainly on three key parameters: the accuracy of the fuel metering, the atomization process of the spray and robustness against deposit build-up in the harsh combustion environment. The design of the GDI multi-hole injector introduced the convenient solution to achieve the required spray plume trajectory to reach to the optimum locations, wide plume cone angle to utilize the air intervention, fine atomization of the spray, minimum spray penetration length, and improve the distribution of the volumetric flow rate from hole to hole. The aforementioned requirements are coupled with static flow of the fuel injector and the spray plume pattern to match with both the engine configuration and the charge motion during the combustion chamber, to make the injector a key component for successful GDI engines. Consequently, that makes the valve group which controls fuel quantity including

needle assembly (bail, needle shaft and armature) and valve seat complete (valve seat and spray hole plate) a vital part of the injector design; this defines the spray plume pattern, the rate of the static flow and the geometrical parameters including the diameter of the nozzle hole. Based on the hole diameter, the spray atomization level, the flow rate and the geometry of the spray plume will be determined [50].

Among all the parameters of the spray, the biggest influences on the performance and emissions of a GDI engine are due to the spray cone angle and the spray penetration length. For a longer penetration length, the HC emissions level increases and the engine efficiency decreases due to the fuel impingement on both the piston surface and cylinder wall, which generate fuel-rich zones [51]. Whilst a shorter penetration length experience uneven distribution of the fuel to the far end of the combustion chamber, and consequently this will generate an improper air/fuel mixture and eventually affect the combustion process and emissions.

2.6 GDI Injector Deposits

Engine deposits can form in the intake system, combustion chamber and injector [52]. Once formed, the deposits can often lead to changes in engine performance and emissions in both spark ignition and compression ignition engines. For GDI engines, injector deposit formation represents a significant concern for all the injector designers. This is due to the exposure of the fuel injector to the higher gas temperature inside the combustion chamber [8]. Injector coking is a common phenomenon observed in fuel injection apparatus; it occurs when chemically degraded components of the fuel and combustion products adhere to the internal surfaces of an injector [53]. The high sensitivity of the injector to the small amounts of deposits, and the subsequent partial blockage of the injector holes occurs due to the narrow passages of the fuel

nozzles where the fuel is metered and atomized. Once deposits form, both the spark ignition and compression ignition engines' performance and emissions will be affected due to the build-up of deposits. Effects of injector deposits are manifested in the degradation of spray quality and flow reduction delivered for the same injection pulse width [4]. This has an adverse effect on mixture formation and combustion, reducing efficiency and engine performance [54]. Previous investigations have shown that early stages of deposit formation for most GDI injectors, did not cause a significant reduction of the mass flow rate; however, they will have a substantial impact on the spray symmetry, and spray angle, as well as droplet size and distribution [4, 8]. Furthermore, injector plugging may occur due to the formation of carbonaceous deposits on the injector tip. Injector plugging will lead to an adverse effect on both the mixture formation and the combustion process, and consequently results in power loss, vehicle drivability problems and increased emissions [12, 55-57].

Attar et al. [58] utilized high-speed imaging to investigate the direct influence of the tip coking on the spray structures of a multi-hole injector. They reveal that the tip coking can increase plume penetration length and reduce plume angle. Moreover, the effects of the injector coking on the spray characteristics are not similar for each plume produced from each hole of the injector. Lindgren et al. [59] used a spray visualization technique to study the spray structure of a GDI pressure swirl injector which has two parts: pre-jet (transient behaviour) and main jet (steady-state behaviour). It was observed that there was a denser spray and longer penetration length associated with the fouled swirl injector pre-jet compared to the clean injector. Furthermore, Yiqiang et al. [60] used the Schlieren method to investigate the effect of GDI engine injector coking on spray characteristics. They revealed that the coked injector had poorer atomization as well as a significantly smaller spray angle and longer penetration distance, compared to that of a clean injector. Song et al. [18] investigated the spray

characteristics of a GDI injector with six-holes under the effect of deposit formation. Their coked injector had been used in a vehicle for 58,000 kilometres. They found that the flow rate of the coked injector was decreased by about 10%. Also, they demonstrated that the deposits formed changed significantly the spray behaviours through the nozzle holes of the GDI injector. They reported that the coking effect decreased the actual GDI injector nozzle aperture, resulting in smaller particle size and lower spray penetration length, while the spray cone angle increased, thus it seems that deposits affect the spray from different injectors in different ways.

The location of the injector and fuel plumes relative to the spark plug has been considered to be one of the important features of spray-guided combustion systems. The position of the fuel spray geometry with respect to the spark plug position must be optimized, in order to cover a wide map of operating conditions; and furthermore, to assist with the existence of an ignitable mixture around the spark plug at the point of ignition [4, 61]. Consequently, any shifts from the expected spray geometry will result in significant degradation of the combustion process within different operating conditions. The deposit formation has been linked to a subsequent increase in NOx and particulate emissions, some increase in CO and HC emissions, and a general decrease in a vehicle's performance in terms of its driveability, acceleration and fuel economy [9, 57]. The observed increase in NOx emissions is due to local regions of rich fuel combustion caused by poor injection characteristics of a coked injector. Also, deposits which are porous can adsorb some of the injected fuel causing an uncontrolled increase of the mixture excess air coefficient and consequently resulted in higher NOx emissions particularly at lower engine speeds [54, 62]. It is found that for a fouled injector with 8.5% fuel flow rate loss, the HC emissions increase by approximately 10% in comparison to the clean injector for 5.5–8.5 bar IMEP engine load range, as compared to a clean injector [63]. Particulate emissions from injector fouling are investigated and it is found that for an engine load of 8.5 bar IMEP, the

clean injector had PN emissions of nearly 53% and 58% of the fouled injectors, with 8.5% and 5.3% fuel flow rate loss respectively [63]. The relation between injector fouling and diffusive combustion is also investigated and it is revealed that diffusion flames result in higher particulate matter (PM) emissions [64]. Joedicke et al. [65] used fuel with a special ingredient to accelerate the deposit formation process. They observed, after 55 hours of a dirty-up test that the fuel rate losses were approximately 23.5%, accompanied by 20%, 93% and 2.45% increase of HC, CO emissions and fuel consumption respectively.

The injector tip temperature and the location of the injector in the combustion chamber are the main parameters contributing significantly to the formation of injector deposits [66, 67]. It is shown that the fuel mass flow rate losses due to the deposit accumulation increase sharply for tip temperatures exceeding 150 ˚C, peaking around 175 ˚C. Kinoshita et al. [16] observed that PM emissions are affected by the temperature at 90% volume distillation of the fuel as a key fuel property. They concluded that when the temperature at 90% volume distillation of the fuel is lower than the injector tip temperature, the pyrolysis process of the fuel occurs resulting in more formation of tip deposits. Furthermore, they delineated the relation between the injector tip temperature and T90 distillation temperature of the fuel on the formation of GDI injector deposits. They demonstrated that as long as the injector tip temperature is kept below the T90 of the fuel, the residual fuel will stay in a liquid state, which facilitates the washing process and removal of the deposit pre-cursors by the next fuel injection event. By contrast, when the temperature at 90% volume distillation of the fuel is lower than the injector tip temperature the deposit formation rate increases due to liquid fuel evaporation, which would cause the deposit precursors to agglomerate and adhere strongly to the nozzle wall [55]. Two types of injector deposits have been identified: carbonaceous sediment produced during engine operation from lubricating oil and soot, and deposits forming from the gasoline ingredients such as aromatic

or olefin components during hot soak periods [4, 30, 68]. Deposits of the latter type typically form as a thin layer of waxy residue on the injector's internal surfaces near the injector tip and at the nozzle outlet [4, 9].

Many researchers have utilized a scanning electron microscope (SEM) to investigate the internal and the external deposits of GDI injectors [9, 16, 69-71]. Song et al. [18] investigated deposit formation in coked injector orifice holes using SEM photographs. They concluded that the external surface deposits have a loosed feature and they fall off as easily as deposits from the injector tip protrusion. Meanwhile, thick deposits form along the inner surface of the holes, where the deposits are axially distributed at the internal aperture and only concentrated along one side of the hole with high density; whilst the deposits at the external aperture are radially distributed. Imoehl et al. [69] investigated the deposit formation on the seat and ball using SEM photographs and they concluded that the flow rate loss associated with deposits is mainly generated due to the restrictions over the inner holes' surface, and deposit formation in the sac volume and ball changes the entrance conditions of the hole. Furthermore, Dearn et al. [71] analysed deposits for multi-hole injectors using scanning electron microscopy with energy dispersive X-Ray spectroscopy (SEM-EDS). They showed that extensive deposits are formed in both internal and external injector holes and the external-hole deposits are radially distributed and collected in the shoulder; while the internal aperture deposits are axially distributed and tended to increase in density along one side of the hole. They concluded that C, O, S and Ca are the dominant components of the deposits based on the elemental analysis results; as the distance to the combustion chamber becomes closer, it is noticed that the C concentration increases, while S and Ca concentrations are decreased.

A high level of deposit formation is observed when the injector tip temperature is higher than

the T90 distillation temperature of the fuel [16]. Therefore, the drying of the injector tip is considered an essential parameter in the build-up of deposits, because the evaporation of the liquid fuel would cause the deposit precursors to agglomerate and adhere strongly to the nozzle wall. The variation in the deposition behaviour can be linked to the change in surface wettability (factors such as fuel composition and tip coatings) or the drying rate (factors such as fuel volatility, tip temperature, air temperature and velocity). For these reasons, Karwa et al. [72] investigated the drying rate of an isooctane thin film along the injector tip under the effect of injector tip temperature, system pressure and air flow. It is observed that at an injector tip temperature of 110˚C (superheated up to 10˚C above the boiling point of iso-octane) and back pressure of 1 bar, evaporation is the dominant mechanism and as the air velocity or injector tip temperature increases the drying rate in this regime is increased. Furthermore, they noticed that as the system back pressure reduced, the saturation temperature decreased and consequently boiling within the film will occur at a lower injector tip temperature. In addition, the drying rate increased with the reduction in the system back pressure for the same injector tip temperature; whilst the drying rate decreased with the reduction of the system back pressure at the same injector tip superheat.

2.7 Detergent and Improved Injector Design to Reduce Deposit Formation

Aradi et al. [67] investigated the control of GDI injector deposits using two types of detergents, Mannichs and polyether amines. It is demonstrated that Mannichs has a higher performance compared to the other detergent. The mass flow rate losses of a GDI injector are reduced by using Mannichs detergent and polyether amines from 11.23% to 3.14% and 8.17%, respectively. Furthermore, Miura et al. [73] examined the effect of using a commercially available detergent with different concentration labels of low, middle, and high on the injector deposit formation. They reveal that low levels of detergent are not able to keep the injector surface free of deposit,

indicating that a minimum amount of detergent is required to prevent deposit formation on the injectors. By contrast, high concentrations of detergent can accelerate the gasoline direct injector deposit (GDID) formation, even though it is generally understood that addition of detergent leads to beneficial effects.

Another way to reduce the formation of the injector deposits is to enhance the injector design in order to reduce the injector tip temperature below the proposed T90. Kinoshita et al. [16] modified the cylinder head cooling passages besides using a high thermal conductivity material in the area between the injector and engine head, and covered the tip surface exposed to the combustion gases with an insulator, to reduce the injector temperature and consequently, reduce the deposit formation. Furthermore, the injector deposit formation can be reduced using injector material coated with an amorphous hydrogenated carbon film coating to prevent the formation of carbonaceous deposit thereon [74]. The injector deposit formation was also examined using a coating with different thermal conductivity to that of the injector body [75]. They found that the coating with thermal conductivity higher than that of the injector body, the heat transfer increased and the tip temperature increased and consequently, the deposit will build-up; whilst the reverse occurred for the coating with a thermal conductivity lower than the injector body.

2.8 Spark Plug Configuration

Over the past several decades, a number of studies have been conducted to investigate the effects of spark plug design on spark-ignition (SI) engine performance. The spark plug firing end design features such as gap projection, gap size, electrode size, and tip configuration demonstrated influences on the engine performance [24, 76-78]. The evaluation of the impacts of using different spark plug designs is mainly linked to the cycle-to-cycle variations in

indicated mean effective pressure (IMEP) and engine emission levels. Improved spark plugs must be employed to ignite leaner mixtures and to endure under harsh operating conditions for the requirements of high performance [79]. Moreover, the spark plug electrode geometry design can be utilized in order to reduce the heat losses from the flame kernel to the electrode and speed up the kernel growth [80]. Likewise, the electrode material is of great practical importance for improving service life, ignitability, pre-ignition protection and fouling resistance of the electrodes [81].

Lee et al. [82] investigated the formation and evolution of the flame kernel and the engine performance under different spark plug electrode configurations. Three types of spark plugs were selected for evaluation. They were standard J-gap spark plug with 2.5 mm center electrode, J-gap spark plug with 0.6 mm center electrode, and surface gap spark plug with 0.4 mm center electrode. They concluded that the fine spark plug with a diameter of 0.6 mm has the ability to ignite a mixture with very lean conditions, besides the ability for faster mass fraction burned (MFB) times for a mixture with 0% and 20% exhaust gas recirculation (EGR). Furthermore, the results display that fine wire spark plugs enhance both the stability of the combustion process and the fuel consumption rate, and consequently improve the engine performance. However, as the equivalence ratio approaches to one, the difference between the spark plug types becomes negligible. Han et al. conducted an experimental investigation of the minimum ignition energy under different key parameters of electrode gap distance, spark duration, temperature and electrode size (cylindrical electrodes) in methane–air [83] and hydrogen–air [84] mixtures. Also, Sally et al. [85] examined the subsequent spark discharge and ignition process impacts on the fluid mechanics in a hydrogen–air mixture. They demonstrated that the cooling rate of the hot kernel is mainly affected by the geometry of the spark electrode and will affect the subsequent ignition process. Likewise, the hot gas confinement will produce higher

gas temperature which minimizes the laser energy required.

Recently, instead of using conventional spark plugs, ignition systems utilize plasma sustained ignition systems as a promising alternative approach. Mariani and Foucher [86] compared the impacts of a radio frequency sustained plasma ignition system (RFSI) with a conventional spark plug, on the performance of a spark ignition engine. They concluded that in all test conditions a reduction in the cycle-by-cycle variation is noticed, the lean limit is extended and the cycle efficiency is improved by using a RFSI, compared to that of a conventional spark plug. Furthermore, the ignition process using the RFSI reduced both the carbon monoxide and unburned hydrocarbon emissions; whilst an increase in the NOx emission is noticed due to the higher temperature associated with the combustion process.

The spark plug gap is considered as one of the key factors that must be set properly before the plug is installed inside the engine for three reasons: 1) if the gap is too wide, the electrical voltage may not be high enough to arc across, which would result in a misfire; 2) if the gap is too narrow, the spark may not ignite a "lean" air/fuel mixture, which would also result in a misfire; 3) the voltage requirement of a spark plug is directly proportional to the size of the gap. Furthermore, the electrode gap influences the early formation of a flame (kernel), which plays a dominant role in determining the subsequent behavior of that flame, and thereby influences the engine performance [22, 23]. There are two staged processes to describe the growth of the flame kernel: during the early short stage, the shock wave and the plasma expanding kernel are employed to control the mass and energy transfer process. Whilst during the next much longer stage, the mass and energy transfer are mainly controlled by the thermal conduction from the flame boundary layer and the diffusion process to keep the flame self-sustained [87]. In addition, Bhaskar [88] investigated the effect of different spark plug gaps of 0.4, 0.5, 0.6 and 0.64 mm on the coefficient of variation (COV) of the IMEP at different ignition timings and

different engine loads. He concludes that the minimum COV of IMEP is noticed for the spark gap of 0.6 mm and ignition timing of 18 CAD BTDC. Therefore, an incorrect electrode gap can lead to in-complete combustion of the air/fuel mixture and consequently will affect the engine's performance. Herweg and Ziegler [89] found that reducing the contact areas between the flame kernel and the spark plug can be achieved either by reducing the electrode diameter and/or increasing the gap leads to a faster flame kernel development. Also, the flame kernel structure is significantly affected by the flow pattern near the spark plug gap. Several parameters such as gap width spark electrode diameter and spark duration have a great impact on the flow pattern adjacent to the spark plug [90]. Furthermore, the increase of gap spacing and gap projections is beneficial in improving the brake specific fuel consumption of the engine, and the ability to ignite lean fuel/air ratios [24].

There are several ways in which a spark plug becomes inoperative, and these are outlined as follows: 1) fouling which is produced by fuel wetting of the spark plugs or by deposition of combustion products (soot and water) on the spark plug electrodes and insulator causing short circuit [91, 92]; 2) fouling with oil deposits from excessive passage of engine oil into combustion chamber due to piston ring or valve guide seal leakage causing open circuit [93]; 3) breaking of the insulator; 4) pre-ignition; 5) conduction through the insulator; and 6) electrical puncture of the insulator. In order to prevent the pre-ignition, the spark plug's firing end temperature must be kept lower, but high enough to prevent fouling and ensure adequate electrode gap life [24]. The aforementioned phenomenon is identified as "Thermal Performance", and is determined by the selected heat range.

2.9 Engine-out Emissions
2.9.1 Emission Legislations

Emission legislations specify the exhaust emissions' permissible limits emerging from commercial vehicles. Currently, the most common harmful emissions that cause concern for human health are particulate matter (PM), unburned hydrocarbons (HC), carbon monoxide (CO), and nitrogen oxides (NOx) [94]. Table 2-1 summarizes the European emission standards for both spark ignition and compression ignition passenger cars [95].

2.9.2 Regulated Engine-out Emissions
2.9.3 NOx and HC Emissions

The development of the GDI engine has a great potential impact on the reduction of UBHC emissions for cold start and warm up engine modes in comparison with PFI. This is due to the fuel injecting directly into the combustion chamber in GDI engines, which completely eliminates any formation of the liquid fuel films on the intake manifold and intake port walls. Consequently, this will enhance the stability of the fuel metering process and reduce the time-varying transport delay that is associated with the build-up of liquid pool within the port of PFI engine. During the cold start, the fuel puddling issue in PFI engines is particularly significant due to the lower level of fuel vaporization on the colder engine surfaces; this leads to significant uncertainty in fuel delivery quantity and vapor content to the cylinder, particularly taking into account variations in fuel volatility and consequently this will increase the total UBHC emissions. With GDI, fuel quantities can be controlled on a cycle-by-cycle basis, allowing more precise optimization of cold start emissions [48, 96-98].

Table 2-1. EU emission standars for passenger cars [95]

Stage	Date	CO	HC	HC+ NOₓ	NOₓ	PM	PN
		g/Km					#/Km
Spark ignition							
Euro 1†	1992.07	2.72	-	0.97	-	-	-
Euro 2	1996.01	2.2	-	0.5	-	-	-
Euro 3	2000.01	2.30	0.20	-	0.15	-	-
Euro 4	2005.01	1.0	0.10	-	0.08	-	-
Euro 5	2009.09[b]	1.0	0.10[d]	-	0.06	0.005[e,f]	-
Euro 6	2014.09	1.0	0.10[d]	-	0.06	0.005[e,f]	6.0×10^{11} [e,g]
Compression ignition							
Euro 1†	1992.07	2.72	-	0.97	-	0.14	-
Euro 2, IDI	1996.01	1.0	-	0.7	-	0.08	-
Euro 2, DI	1996.01[a]	1.0	-	0.9	-	0.10	-
Euro 3	2000.01	0.64	-	0.56	0.50	0.05	-
Euro 4	2005.01	0.50	-	0.30	0.25	0.025	-
Euro 5a	2009.09[b]	0.50	-	0.23	0.18	0.005[f]	-
Euro 5b	2011.09[c]	0.50	-	0.23	0.18	0.005[f]	6.0×10^{11}
Euro 6	2014.09	0.50	-	0.17	0.08	0.005[f]	6.0×10^{11}

† Values in brackets are conformity of production (COP) limits
a. until 1999.09.30 (after that date DI engines must meet the IDI limits)
b. 2011.01 for all models
c. 2013.01 for all models
d. and non-methane hydrocarbons (NMHC) = 0.068 g/km
e. applicable only to vehicles using DI engines
f. 0.0045 g/km using the Particle Measurement Programme (PMP) measurement procedure
g. 6.0×10^{12} 1/km within first three years from Euro 6 effective dates

GDI engines operating on stratified mode experience an increase in UBHC emissions, which can be linked to these key considerations: 1) flame quenching happened along the stratified charge outer boundary occupied by very lean mixtures. 2) The spray wall wetting will generate locally rich regions near the cylinder wall or piston crown and consequently this will lead to a poor combustion process. 3) The UBHC will be increased due to the difficulties of post-flame oxidation associated with the lower combustion temperature. 4) The catalyst system will experience lower conversion efficiency due to the reduced exhaust gas temperature; and 5) lower percentage of UBHC oxidation will occur in the exhaust port, due to the significantly lower exhaust gas temperatures. In general, for both idle and part load conditions GDI engines

yield an increase of the UBHC emissions.

NO_x emissions are highly sensitive to the distribution of in-cylinder temperature and combustion phasing, which are considered the key parameters contributing to the formation of in-cylinder NO_x [99]. The hydrogen to carbon (H/C) ratio plays a dominant role on NO_x emissions [100, 101]. This occurs due to the higher adiabatic flame temperature associated with the fuel of a higher H/C ratio and consequently this will generate higher NO_x emissions. Ronald et al. [102] demonstrated that GDI engines operating in the stratified-charge mode have higher NOx emissions despite the overall lean air–fuel ratio; this could be linked to the stratified charge core region being filled by slightly rich or stoichiometric mixtures. By contrast, PFI engines have lower levels of NOx emissions due to their operation with an air/fuel ratio leaner than 16. Furthermore, higher levels of NO_x emissions are noticed at idle conditions of GDI engines, in comparison to PFI engines. This can be linked to the higher heat release rate associated with the presence of locally stoichiometric combustion at higher charge density. By contrast, PFI engines experience lower temperature levels due to the slower homogeneous combustion process. The in-cylinder NOx formation can be reduced via several methods, including: spark timing retardation, water injection, EGR and using fuels such as ethanol or methanol, which have higher latent heat of vaporization. Likewise, three-way catalysts (TWCs) and NOx trappers are employed to reduce the generation of NOx engine exhaust emissions. Among the aforementioned methods, EGR is the most widely used method and has a significant effect on the reduction of the NOx emissions; it is primarily employed as a dilution of the air/fuel mixture during combustion [103].

2.9.4 PM Emissions

Based on the emission standards demonstrated in Table 2-1, Euro 5 specifies that the permissible limit on PM mass emissions for light duty commercial petrol vehicles must be less than 4.5 mg/km. The coming Euro 6 regulations will adopt the particle number (PN) emission limits for several categories of IC engines.

2.9.5 What is PM from Engines Made of and Where do They Form?

Whitby and Cantrell [104] are the first researchers to delineate the engine PM size distributions into three different modes; comprising of nucleation mode, accumulation mode and coarse mode, as shown in Figure 2.5. Particles with mobility diameters ranging between about 3 to 30 nm will be referred to as nucleation mode particles. The size range and boundaries of this mode are constituted mainly from volatile organic and sulfur compounds that are produced during exhaust dilution and cooling. This mode consists of 10% of the particle mass, whilst the particle number occupies more than 90% of this mode [105]. Between 30 to 500 nm in mobility diameter, particles are likely to be larger agglomerates and will be referred to as accumulation mode particles. The agglomeration of the primary carbon particles and other solid material are considered the main source of these large sized particles of the accumulation mode. On the other hand, the coarse mode contains mainly from 5-20% of the particle mass. This mode is developed due to the deposition of the accumulation mode particles on the surfaces of both the exhaust system and cylinder wall, and also to the lubricating oil droplets from the crank case [106].

2.9.6 Formation and Growth

Commonly, six identified processes participate in the transformation of the hydrocarbon (in liquid or vapor phase) to solid phase soot particles and with the possibility to return it back to gas-phase products. These processes include pyrolysis, nucleation, coalescence, surface growth, agglomeration, and oxidation. The first five processes regarding the transformation of the soot are clearly schematically demonstrated in Figure 2.6; while the sixth process which is identified as an oxidation process is employed to convert hydrocarbons and carbon monoxide to carbon dioxide and water at any point during the process.
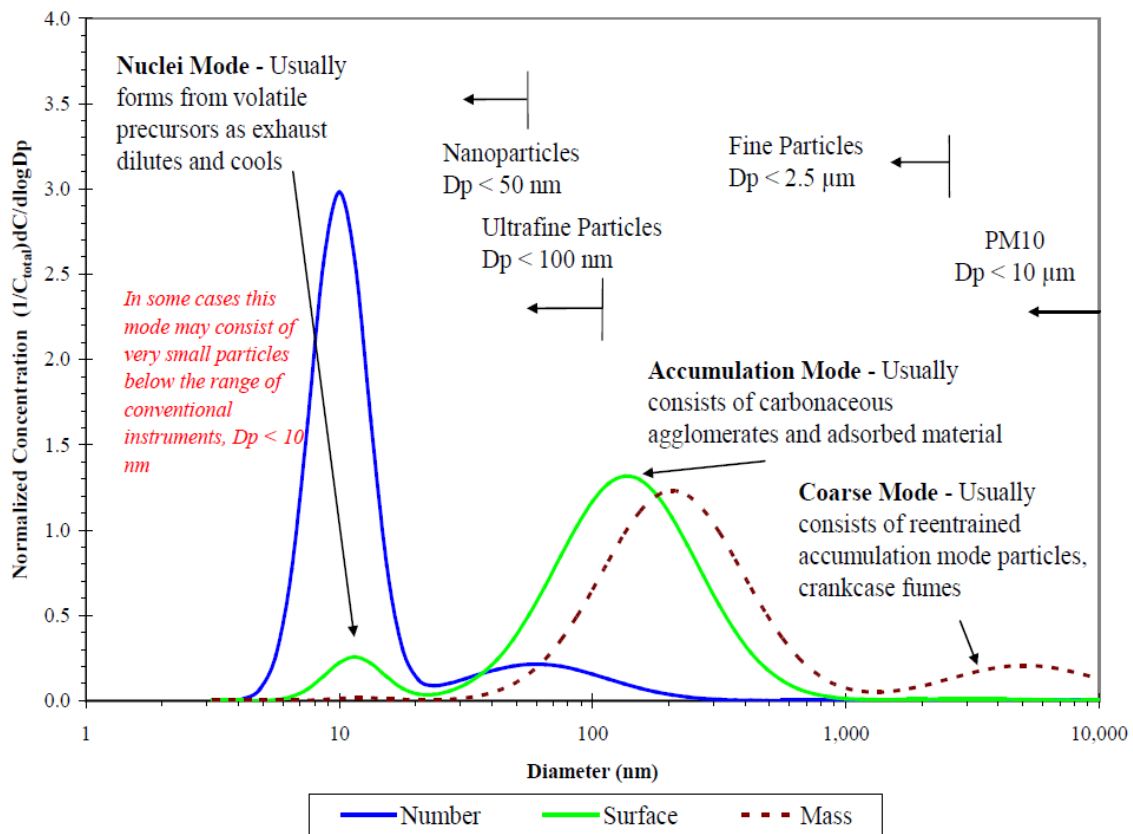
Figure 2.5.Typical engine exhaust particle size distribution by mass, number, and surface area. Dp is the aerosol particle diameter [107].

The hydrocarbon fuels disintegrate into unsaturated hydrocarbon with a short chain structure such as acetylene and then form polycyclic aromatic hydrocarbons (PAHs). The PAH molecles simply grow, and through dehydrogenation and carbonisation gradually develop and constitute

the key precursor molecule contributing to soot formation via aggregation, agglomeration and coagulation processes [108, 109].
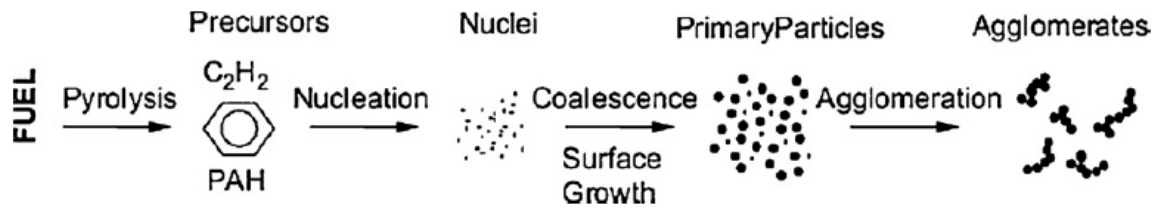
Figure 2.6. Schematic diagram of the steps in the soot formation process from gas phase to solid agglomerated particles [110].

Hydrocarbon or carbon can be converted to a combustion product species as a result of the oxidation process. This conversion of the carbon species via partial oxidation to carbon monoxide will eliminate any development of this carbon into soot particles even if it encounters locally rich fuel zones. Glassman [84] demonstrated that in order to have an oxidation process for the soot, the temperature should be exceed 1300 K. Furthermore, Smith [111] examined soot oxidation and discovered that the unusually highly resistance of soot to oxidation goes back to the graphite-like structure of some soot particles. A two stage process is carried out in order to oxidize the small particles. First, absorption which demonstrates the adheision of oxygen molecules to the particle surface; whilst the second process is the desorption which descrip the break down of the oxygen molecules attached to the fuel component from the surface to form a new product [112].

2.9.7 Dangers of PM Emissions

Both fine particles (PM2.5) and coarse particles (PM10), which include particles with a diameter less than or equal to 2.5 microns (μm) and 10 microns (μm) respectively, are commonly used as indicators to describe the PM that are relvant to health effects. In general, PM2.5 represents approximately 50–70% of PM10 [113]. The harmful effects caused by PM10 and PM2.5 lie in their extremely small particles which can be easily penetrate the respiratory

system via the thoracic region. Once inhaled, these particles can affect the heart and lungs and cause serious health effects over the short term (hours, days) and also long term (months, years); including increased daily mortality due to the aggravation of asthma, coughs and respiratory symptoms. Furthermore, it can lead to the formation of lung cancer.

Besides particulate matter's side effects to human health, particles' formation in the atmosphere influences both the solar radiation coming to the earth's surface and the infrared radiation transmitted back to space. This change in the radiation balance will contribute to increase global warming based on previous investigations [114].

2.9.8 PM Emissions in Various Engine Types (PFI, GDI, diesel)

In general, the PM emissions generated from GDI engines are more than those of PFI engines and diesel engines equipped with diesel particulate filters (DPFs) [115]. Whilst diesel engines without DPFs yield higher PM emissions of (11-40 mg/km) compared to those of GDI engines (2-13 mg/km) [116]. This increase in GDI PM emissions was linked to the short time available for preparing a homogeneous combustion mixture and the fuel impingement on the surfaces of the pistons and cylinder happening unexpectedly [4, 117, 118]. The fuel impingement leads to a favorable rich region for soot formation.

The greatest formation rate of particulate emissions is demonstrated when the GDI engine operates in stratified charge mode [4]. It is noticed that the PM emissions associated with this mode vary significantly as the engine operating point changes slightly. Two main types of rich combustion contribute to the generation of particulate matter; first, that which features areas of a local rich gaseous air/fuel mixture [119] and secondly, that which is generated due to the

association of diffusion combustion of incompletely volatilized, liquid fuel droplets. The latter type is of practical concern for PM emissions and yield for late injection. However, for homogeneous charge operation, the influence of injection timing on PM emissions is negligible; whilst for advanced injection timing the PM number concentration reduces monotonically.

2.10 Planar Laser-Induced Fluorescence (PLIF)
2.10.1 Principle of Laser Induced Fluorescence (LIF)

In order to carry out a PLIF experiment, the flow field should be illuminated using a tunable wavelength to excite a certain absorption transition of a molecular dopant. Once the molecules of the working fluid absorb the incident laser light, a fraction of the ground state molecules will be excited and moved to the upper electronic energy state. The laser light wavelength is carefully chosen in order that the wavelength associated with the exciting laser matches with an electronic absorption of the molecule. After a few nanoseconds to microseconds, some of the excited molecules due to the inelastic collisions between the electrons and neutral gas molecules will de-excite through the emission of photons. A high speed digital camera is employed to capture this light fluorescence [120]. At high combustion temperature, the electronic levels normally have a negligible population, except the lower state which occupies the ground electronic level.
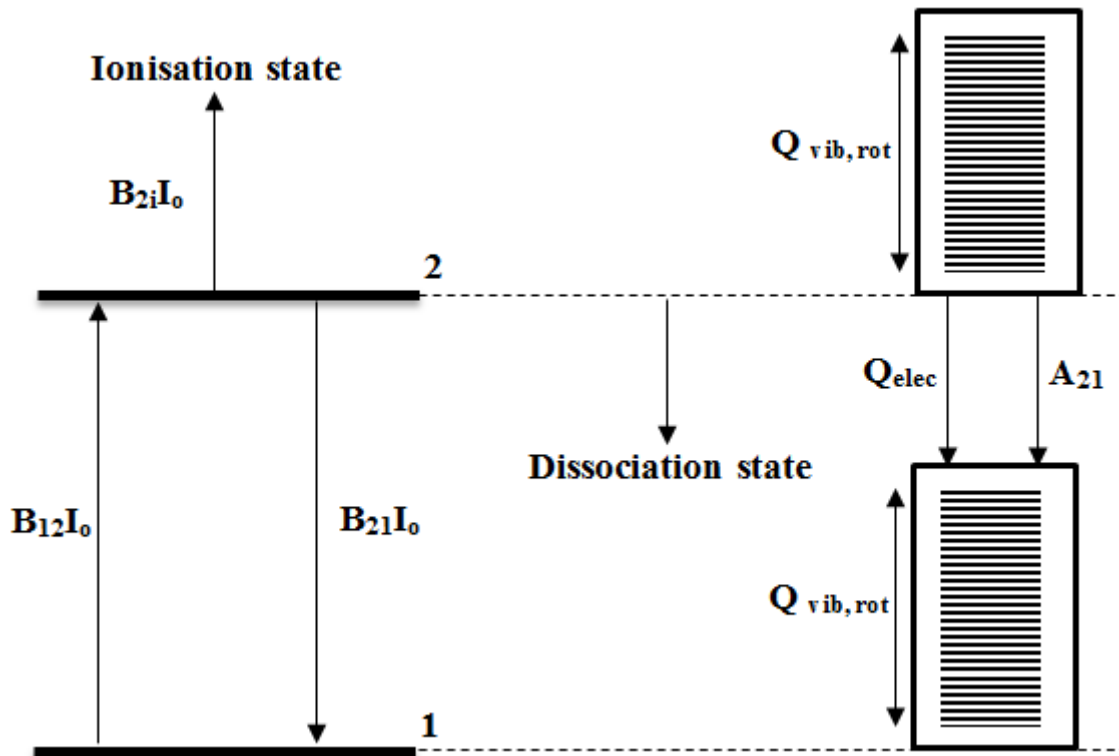
Figure 2.7. Main energy transfer process in LIF, B_{12} and B_{21} are the Einstein coefficients for simulated absorption and emission, I_o is the laser spectral intensity, A_{21} is the Einstein coefficient for spotaneous emission, Q_{elec} is the electronic energy transfer, $Q_{rot,vib}$ is the rotational and vibrational energy [120].

Once the molecule has been excited by the laser source, then this molecule will follow five important processes, as shown in Figure 2.7. First, the stimulated emission process causes this molecule to interact with other excited molecular state and consequently will drop to the original quantum state, denoted as $B_{21}I_o$. Second, this molecule can be excited to a higher state by additional photon absorption and can even reach to the ionized levels, shown as Q_{ion}. Third, the inelastic collisions which the kinetic energy does not conserve due to the action of internal friction, instead are turned into rotational and vibrational energy of the atoms, causing a heating effect and the bodies are deformed, represented by $Q_{rot, vib}$. In many cases, quenching can occur in terms of electronic energy transfer (Q_{elec}) produced from the inelastic collisions with other molecules. Fourth, the molecule dissociation process and internal energy transfer will be generated due to the interaction between the individual atoms of the molecule. This

phenomenon is determined as pre-dissociation and produced via an electronic transition from a stable to repulsive electronic (unstable) state, resulting in dissociation of the molecule at excitation energy less than the normal dissociation limit of the upper state. Finally, the laser-induced fluorescence generates as a result from the transition of the originally populated state and nearby states indirectly populated through collisions to the lower state due to the emission of light, represented by spontaneous emission, A_{21} [120].

2.10.2 Two-dimensional Fuel Distribution Measurement by PLIF

Laser-induced fluorescence (LIF) has been widely used due to the relatively high signal intensity, tremendous sensitive emission profiles and high spatial resolution. The separation between the emissions' fluorescence signal and the stray scattered light becomes easier due to the red shifted fluorescence signal from the excitation laser wavelength. The LIF technique is employed for concentration measurements due to the direct proportionality of the fluorescence intensity to the molecular density. However, applying quantitative PLIF measurements inside the combustion chamber is relatively difficult due to the high quenching possibility by the oxygen at elevated pressure and temperature and hence, the fluorescence signal intensity will be reduced.

Several considerations should be taken into account in order to perform quantitative measurements on a given species using laser-induced fluorescence. First, the absorption and emission spectrum should be well defined for that molecule. Second, the molecule absorption wavelength must be reachable to a tuned laser source. Third, because the fluorescence power is proportional to the rate of radiative decay, therefore, this rate must be identified clearly for the excited state. Fourth, all the losses regarding the excited state including pre-dissociation, photo-ionization and collisions must be taken into account.

2.10.3 Adaptation of LIF for In-cylinder Fuel Distribution Measurements.

The quantitative fuel concentration measurements in an internal combustion engine by the use of LIF can be carried out using three strategies: the natural fluorescent emission from the commercial fuel itself; the natural fluorescent emission of dopant molecules that have properties matching with the commercial fuel; and the spectrally separated fluorescence emissions of the exciplex-forming dopants. When the fuel is presented in either gaseous or liquid form, the first two strategies are employed for concentration measurements. The third approach is utilized for simultaneously obtaining quantitative measurements of droplet density and vapor concentration.

The commercial fuel itself can be used as a source for the natural fluorescence emissions which facilitate the LIF experiments. However, the interpretation of the measurements result will be complicated, due to the fuel composition variation from batch to batch; and due to the ambiguity of the photochemistry of the fluorescence component, the fluorescence signal cannot be reproducible. The components which are more likely to be fluorescence, are aromatic ones in the fuel and have a high boiling point temperature; and these components are not representative of the whole fuel.

2.10.4 Selection of Fluorescence Dopants

In order to obtain quantitative measurements of in-cylinder fuel distributions, fluorescence tracers are employed for indirect visualisation of fuel concentrations. Therefore, certain parameters must be considered regarding the selected dopant: 1) the absorption ability to the laser incident source wavelength; 2) experience of satisfactory fluorescent emission; 3) less influenced by oxygen quenching; 4) solubility characteristics, stability and non-toxic and   not

considered carcinogenic; and 5) matching with the vaporization properties of the commercial fuel. Furthermore, to facilitate the separation between the LIF signal and the scattered laser light, the fluorescence emission should be sufficiently red-shifted.

The most frequently suitable dopants utilized for quantitative measurements of fuel concentrations, are acetone, 3-pentanone, biacetyl and toluene [121]. Previous studies of the photo-physical behaviour of 3-pentanone have indicated its advantages over other common tracers for the current work [122-125]; because its boiling point temperature mimics the mid-boiling point fraction of gasoline, where 50% of gasoline components evaporate below 109 ºC and because of its insensitivity to oxygen quenching [126, 127].

2.11 Summary

This thesis mainly concerns the influence of injector deposits and the spark plug gap on the performance and emissions of a modern GDI engine. The author believes that the build-up of deposits can play an important role in increasing emissions such as NOx, UBHC and PM. Likewise, the spark plug gap has a significant effect on the stability of the combustion process as well as on the emissions.

For this study, the experimental investigations were carried out using a modern optical GDI engine; therefore, a brief description about gasoline direct-injection engines (GDI) was highlighted. Furthermore, a comparison between GDI engines and PFI engines was conducted, especially in terms of mixture on mixture formation and the operation modes. Then the emission legislations and the GDI engine technologies were presented.

This was followed by an explanation of both the injector design and types. Special focus was paid to the injector deposit formation as serious issues are associated with the GDI injectors. Consequently, the side effects of deposits on the delivered fuel flow rate, spray characteristics and emissions were presented. Furthermore, the methods used to reduce the deposit formation, including the use of additives and coatings were presented. Likewise, the impacts of the spark plug configuration on the GDI engine performance and emissions are discussed.

Finally, the principle of laser-induced fluorescence was introduced, as well as the selection of the fluorescence dopants. For the current work, two-dimensional quantitative mixture stratification measurements were conducted using 3-pentanone as a dopant for the PLIF technique.

Chapter 3

EXPERIMENTAL SET UP AND TECHNIQUES

The aim of this chapter is to discuss in more details the experimental test facilities, the data acquisition systems and the data analysis procedures utilized for this work.

3.1 Introduction

This chapter provide a detailed description of all the test equipment employed throughout the current study. This involves a description of the optical single cylinder Jaguar engine experimental setup alongside with the detailed description of the emission equipment. Furthermore, the strategy utilized to control the engine, data collection process and software analysis are described in the following subsection. Likewise, the benches of spray characteristics test are presented in details, including constant combustion vessel. Furthermore, the fuel injection system and the optical diagnostic techniques including Schlieren system, PLIF laser, LII laser, PDPA system, and high-speed Phantom camera coupled with the intensifier will be explained in more details.

Jaguar Land Rover along with the previous PhD research students at University of Birmingham has created and developed the engine test facilities. Furthermore, the development and maintenance of the single-cylinder optical engine test facility is provided by the author during the current study investigation. Likewise, PLIF technique is developed by the author to study the mixture stratification inside GDI engine, whilst LII technique is developed for qualitative study of the soot distribution inside GDI engine.

3.2 Single-Cylinder Optical Engine Test Cell

Figure 3.1 demonstrates a 4-stroke single cylinder optical engine 562 cc with extended Bowditch piston arrangement. The cylinder head was developed as a single cylinder version of the V8 Jaguar AJ133 (2010) 5.0 litre production engine. The engine utilized a pentroof combustion chamber with a centrally mounted spark plug and four valves (two inlets, two exhausts). The intake valve diameter was 36 mm, whilst the exhaust valve had a diameter of 30 mm. The engine was employed to operate on mode of spray guided DISI engine, where the spark plug positioned near the fuel injector at the center of the combustion chamber. The counterbalance assembly associated with the universal crankcase design was employed to eliminate the undesirable vibration occurring in single cylinder engines. The primary piston was mounted to the crank case of the engine block, which constitute the base for the extended Bowditch type piston arrangement. The cylinder liner and the cylinder head supports were connected to the head of the crank case. Figure 3.2 shows the piston crown included a 65 mm flat-topped quartz window, providing optical access to the combustion chamber through a 45° stationary mirror. A triangular quartz window was fitted on one side of the combustion chamber to provide additional optical access, see Figure 3.3. The fused silica optical cylinder liner is fully transparent. The thickness of the cylinder wall and diameter are 25mm and 90mm, respectively. The gaskets seal the bottom and the top of the cylinder surfaces. Engine specifications are summarised in Table 3-1. In order to raise the cylinder liner and provide the proper sealing for it against the cylinder head, a pneumatic ram was yielded and positioned under the cylinder liner. Initially air supply with a pressure of 6 bar was employed to raise the liner to the wright position, and then for motored and fired conditions of the engine a pressure of 20 bar nitrogen was applied to maintain the liner in its position and to avoid any possible leakage between the liner and the cylinder head. The main advantage of such system is the

ability to remove the cylinder liner without any effect on the cam timing. Furthermore, the

cleaning and maintenance process of both the optical components becomes easier.

(a)   (b)
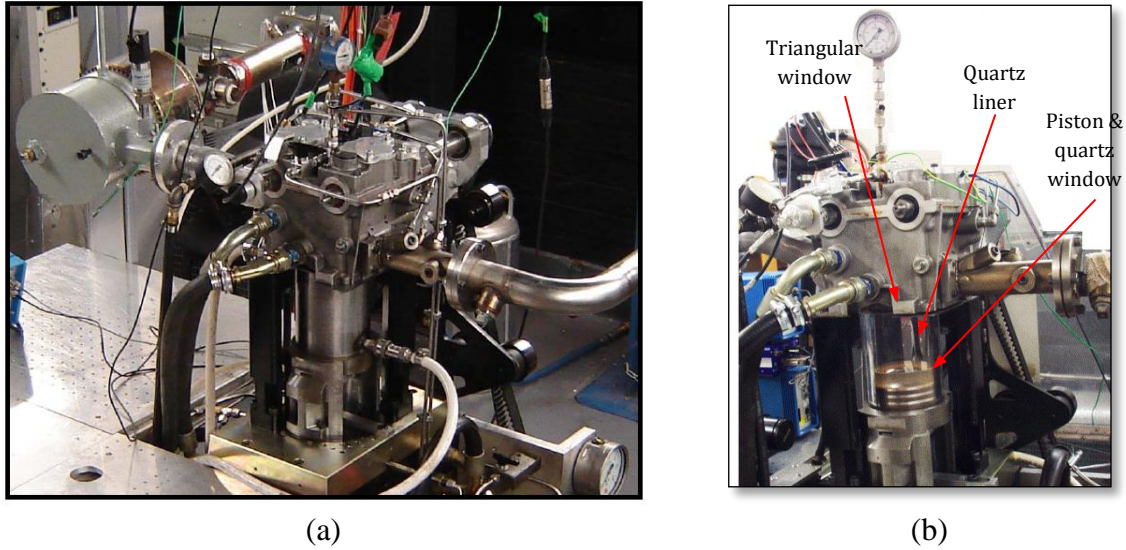
Figure 3.1. Single cylinder optical engine (a) metal liner, right: (b) optical liner

Figure 3.2. Optical flat piston with quartz piston-crown
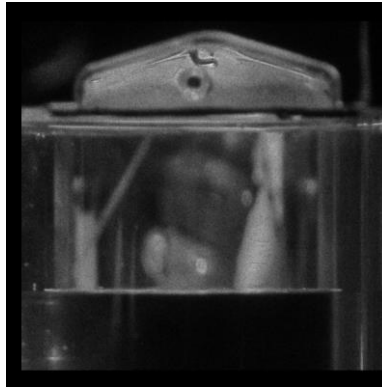
Figure 3.3. A triangular quartz window

Table 3-1 key engine specifications

Combustion chamber design	Pent-roof with centrally mounted spark plug
Displaced volume	562 cc
Bore × stroke	89 mm × 90.3 mm
Compression ratio	11:1
Maximum intake valve lift/duration	10.5 mm / 250 CAD
Maximum exhaust valve lift/duration	9.3 mm / 250 CAD
Intake Maximum Opening Position (IMOP)	109 CAD BTDC
Exhaust Maximum Opening Position (EMOP)	271 CAD ATDC
Injector type	Solenoid-actuated multi-hole (laser drilled)

3.2.1 Dynamometer and Electric Motor

An eddy dynamometer supplied by Trans-drive coupled with an electrical motor was utilized to motor the crankshaft of the optical engine. A dynamometer type three phase, 340 V electric powers was used to rotate the crank shaft at a constant speed for both motoring and firing conditions. The engine speed was controlled manually via a digital indicator on the engine control box.

3.2.2 Heating and Coolant Circuits

The dry sump system was employed to operate the engine; therefore the oil was supplied from a separated heated oil reservoir to the crankcase via in-line pump. The oil was provided separately to lubricate the overhead cams, with an open drain returning oil back to the crankcase. The heating process of the oil was implemented using a 3-kW electrical heater element within the surge tank, and preheated oil is cooled down by the coolant-oil heat exchanger to maintain a stable temperature. Regarding the cooling system, two closed water supply circuit systems were utilized for optical engine. The first circuit was responsible for warming the cylinder head to the required temperature prior the engine running, and this was carried out using an external heated water reservoir. The second circuit was employed as a cooling medium for the steel liners under fired engine operation. The water was circulated through the engine flow channels using an in-line pump for both water circuits. During the engine measurements, both the engine oil and water temperature was kept constant at $85\mp5°C$ by using a Proportional-Integral-Derivative (PID) controller.

3.2.3 Ignition System

Coil-on-plug (COP) ignition system which carries from 5,000 up to 40,000 or more volts was employed to fire the spark plugs. This ignition system was primarily coupled with a 12V 9A power supply. The main parameter regarding the ignition system includes the dwell time (which is defined as the period of time that the coil is turned on) and was kept at 6 ms with ignition energy of 35-40 mJ and spark duration of approximately 2 ms. The ignition process was carried out using J-type ground electrode (NGK-ILKAR6C10), with a thin laser welded

iridium tip central electrode for all the fired conditions. Figure 3.4 displays the orientation of the spark plug with respect to the cylinder head, taking into consideration that the earth electrode position should be perpendicular to the pent-roof triangular window.
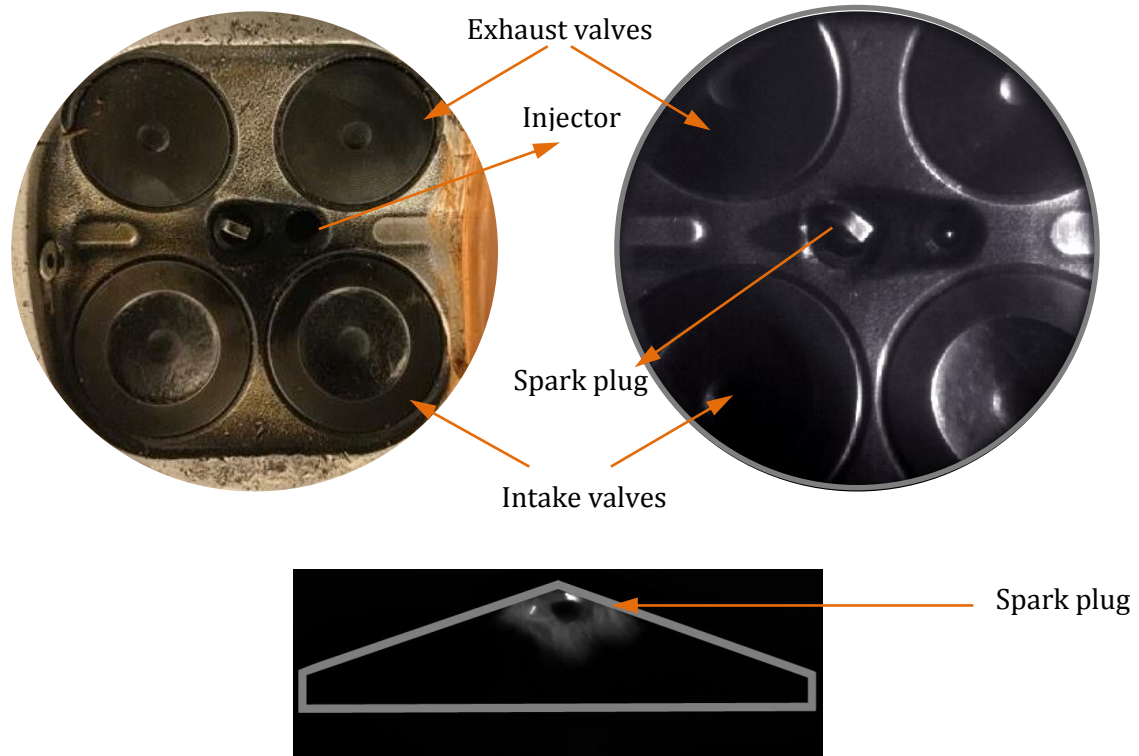
Figure 3.4. Orientation of spark plug for motoring and firing testing

3.2.4 Fuel Injection System

A 6-hole injector was utilized to provide the fuel to the combustion chamber. The injector was mounted vertically within the cylinder head. The injector oriented in close proximity to the spark-plug and located between the inlet and exhaust valves. The fuel was provided to the injector at injection pressure of 150 bar via two systems; first, through an accumulator, where the nitrogen used to pressurize the fuel without any contact, the maximum amount of fuel allowed in the fuel-accumulator and pipe network was limited to 2L for safety reasons. Second,

pressurizing the fuel can be accomplished via an air driven pump (Haskel pump DSF-60-16821-ATEX).

Each hole of the injector nozzle has a diameter of 0.2 mm, and each plume has different injection angle, enabling to generate the perfect spray pattern. Figure 3.5 shows a schematic of the injector and its spray plumes through two views. Spray was defined with the following physical parameters: 'plume penetration length' which was defined as the total distance along the plume axis from the tip of the injector to the boundary of the spray. 'Plume angle (β)' was determined as the angle formed by two straight lines that start from the injector tip and tangent to the plume outline. 'Plumes relative angle (θ)' was defined as the angle between the centre line of the injector and the centre line of the plumes. 'Spray cone angle (α)' was defined as the angle of the outer envelope of the spray. The individual fuel plume injection angle was designed in order to make sure that the spray cover over the cylinder bore, and to utilize the air-fuel mixing process before the ignition timing. The location of the injector and fuel plumes relative to the spark plug has been considered to be one of the important features of spray-guided combustion systems. In order to have an ignitable mixture at the ignition point, the spark plug position should be optimized with respect to the fuel spray geometry over a wide range of operating conditions. Furthermore, in-order to minimise the electrode wetting during fuel injection, the ignition plumes was designed to cross around the spark plug.
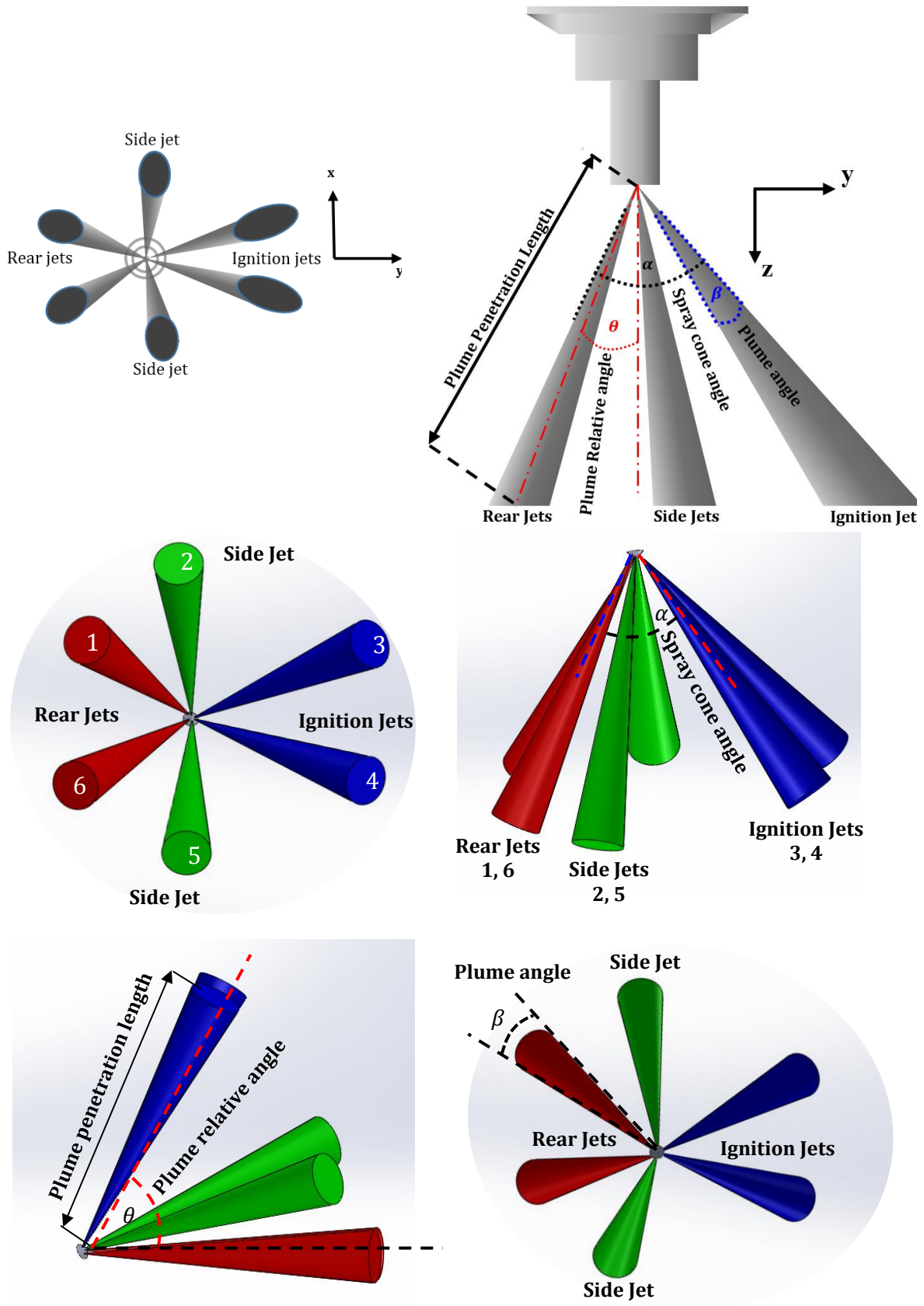
Figure 3.5. Schematic of injector and spray plumes

3.2.5 Controlling of Air Fuel Ratio (AFR)

The relative air/fuel ratio (λ) was controlled by means of a wide band lambda sensor (ETAS LA4-E). Any fuel can be determined via the lambda sensor by calculation of: C, O: C and N: C ratios. For the injection system, an electronic control unit (ECU) was employed to adjust the amount of injection using the LabVIEW program to change the air/fuel equivalence ratio. The relative air/fuel ratio (λ) can be visually displayed via the lambda sensor. The lambda values can be defined in the range of 0.4 to 10 and the value of (λ) can be precisely controlled via the data acquisition system.

3.2.6 Pressure Measurement

Kistler 6051A was employed to measure the in-cylinder pressure variation through the engine. This piezoelectric pressure transducer was mounted within the pent-roof combustion chamber. A Kistler 5011B charge amplifier was coupled with the pressure transducer in order to magnify the transducer signal. The linearity error of both the pressure transducer and the charge amplifier was $\mp$ 0.5% of the full scale. The in-cylinder pressure data for 300 consecutive cycles was recorded with a resolution of 0.1 CAD, and the data was controlled by using the LabVIEW program.

3.2.7 Data Acquisition System

The synchronization process between the engine parameter timing and the data acquisition systems was carried out via the angular position of the engine. The crank angle position was precisely controlled via a Baumer electric (CH-8501-BDT 16.05A 3600-6-4) incremental encoder, which has 3600 pulse per revolution and was directly connected to the crankshaft.

Table 3-2 summarizes the technical specifications of that encoder. This encoder has three series output of pulses (three rings of segments were included to the encoder wheel), see Figure 3.6:

a) The first set of pulses was used to define the encoder resolution and called Channel A, and supply a signal each 0.1 crank angle degree resolution.

b) The second set of pulses was utilized to determine the spin direction and offset with 90° from the first set of pulses and called channel B which has the same resolution of Channel A.

c) The third is Z-pulse Channel (zero position pulse). This generates pulses once per revolution of the encoder, and it is used to indicate when the encoder disc crosses the fixed zero position inside the encoder, and employed to determine the TDC location for each revolution of the engine.

Table 3-2. Shaft encoder specifications (Baumer)

Parameter	BDT 16.05A 3600-6-4
Sensing Method	Optical
Resolution (ppr)	3600
Pulse Tolerance	15 %
Voltage Supply	5 VDC ± 10 %
Maximum Supply Current no load	60 mA
Maximum Revolutions	12000 rpm
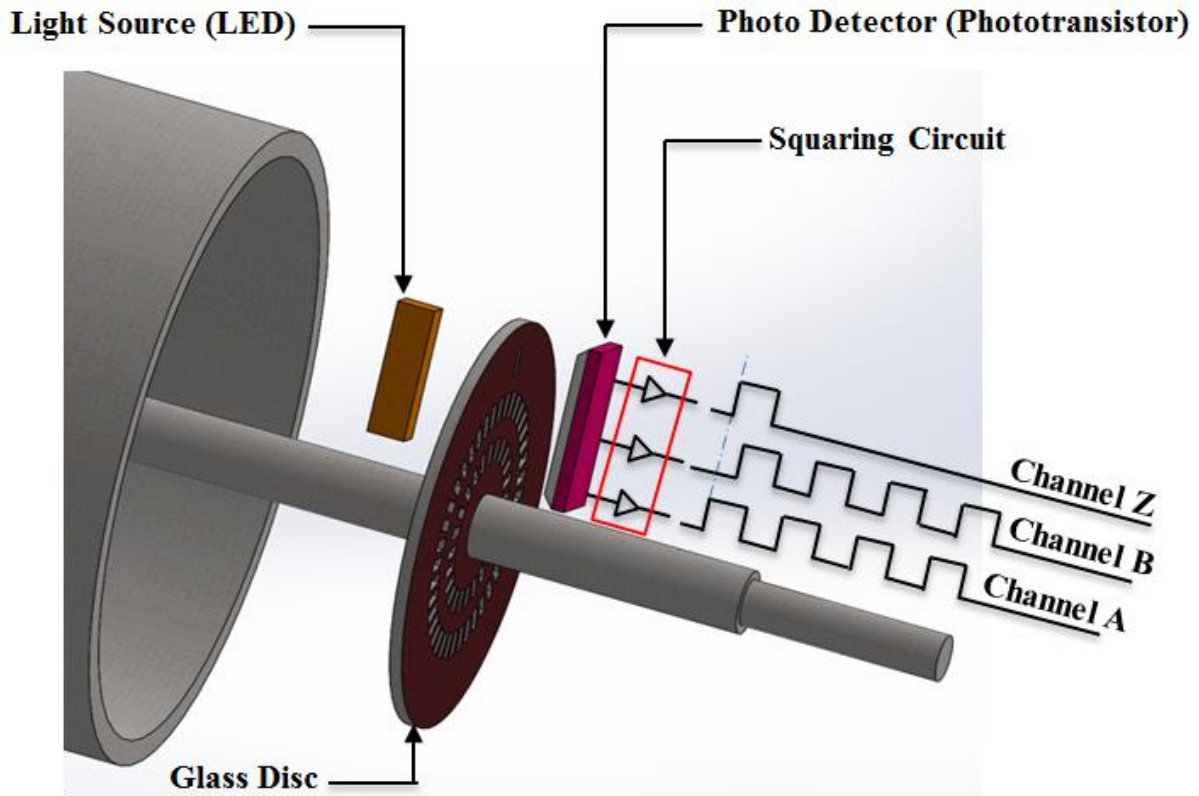
Figure 3.6. Cutaway of incremental encoder

A National Instruments acquisition card (NI PCI-6023E) was used to sample the in-cylinder data, and the sampling rate was controlled via a LABVIEW program. This acquisition card has the ability of sampling up to 16 analogue input signals at a rate of 200 KS/s (kilo samples per second) and with 12-bit resolution. The engine in-cylinder data was sampled at a resolution of 0.1 degrees crank angle via the data acquisition card. This was accomplished using the 3600 pulses per revolution signal from the crankshaft encoder as the sampling clock. The 13 independent analogue channels were employed to sample the data, in order to enable for each experiment in-cylinder pressures, lambda values and timing triggers to be logged.

Furthermore, the engine timing control system (ETCS) was utilized to precisely control the spark dwell time (refers to the period of time that the coil is turned on), spark timing, injector opining duration along with the start of injection. The engine parameters can be modified according to the test condition in real-time while the engine is running.

3.3 PDPA System

Droplet velocity and size distributions were measured using a Dantec two-dimensional Phase Doppler Particle Analyser (PDPA) system (60X41). The schematic diagram of the setup is shown in Figure 3.7. The PDPA system used a 1 W Ar-ion laser to generate two beam pairs, with wavelengths at 514.5 nm and 488 nm for the two-dimensional measurements. A Bragg cell was used to provide a frequency shift of 40 MHz between the beam pair. The focal lengths of the optical transmitter and receiver were 250 and 500 mm respectively. The angle between the transmitter and the receiver was adjusted to 70°, in order to optimize the scattering light, and it was noticed that the first order refraction of light was dominant at this angle. The fuel used was iso-octane with a refractive index of 1.391. The injection repetition rate was adjusted to 2 Hz and the measurements were taken for one minute with total number of injections of 120 injections. The validation rate for each measurement position was between 70-85%. The droplets velocities range was chosen between -36 to 244 m/s in order to make sure it covered the actual droplet velocity. For each test, validated data were acquired comprising of up to 100,000 samples. Two repeat tests were conducted to facilitate a statistical analysis. 3D traverse system was employed to control the movement of both the transmitting and the detector with an accuracy of 0.01 mm.
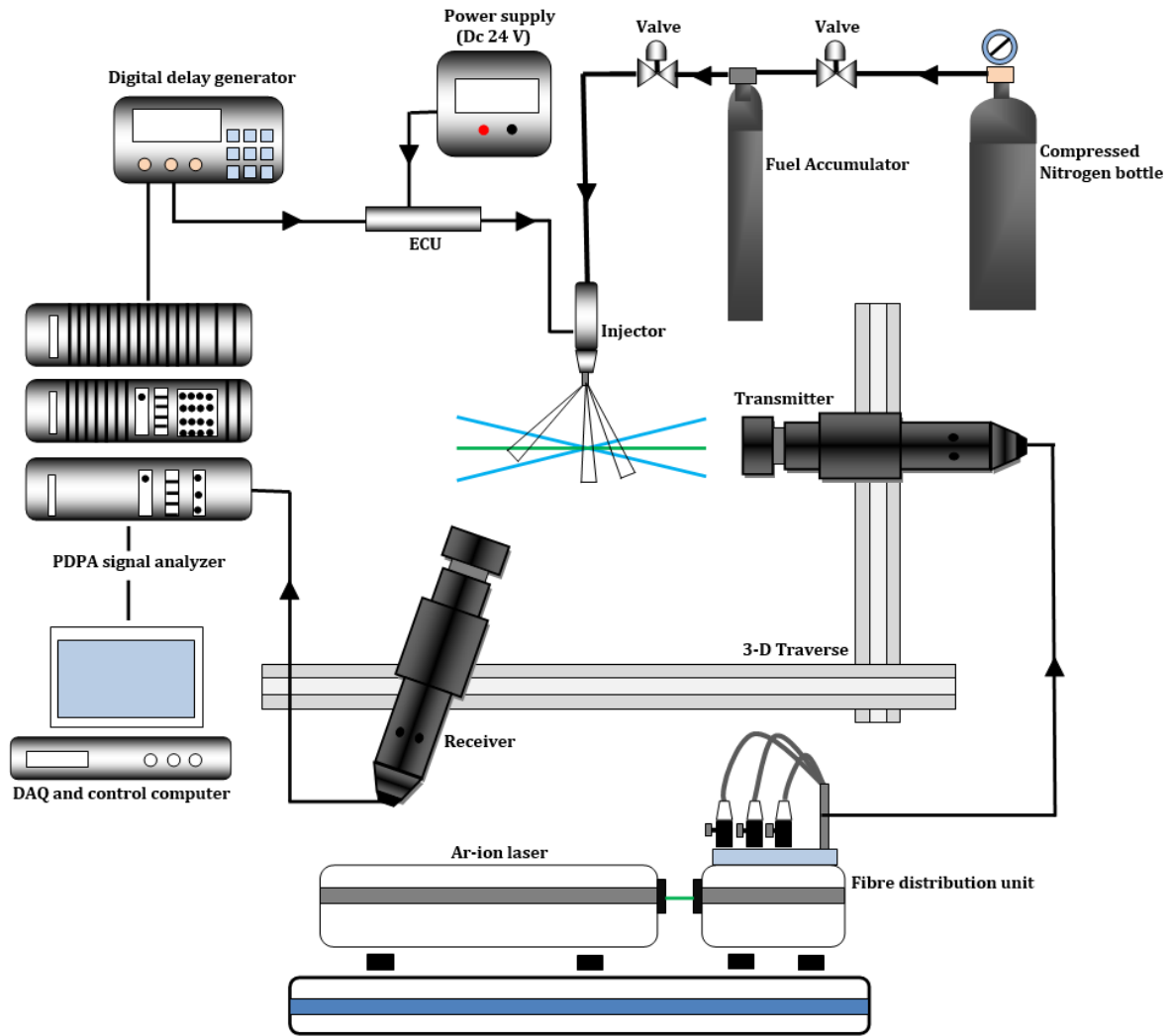
Figure 3.7. Schematic diagram of the Phase Doppler Particle Analyser (PDPA) system

The interference of the scattered light was employed to explore useful information regarding the structure and dynamics of droplets at a particular point of a spray jet. Therefore, this principle was utilized for Phase Doppler Method to examine the spray characteristics. The intersection of the two-laser beams was employed to delineate the small optical probe volume where the non-intrusive measurements were carried out. Once the liquid particle passes through this probe volume, it generates scatted light which is directed towards the detector, strategically located at an off-axis collection angle. Consequently, the spherical particle size will be determined based on the phase shift between the Doppler burst signals from different detectors.

The signal processor was used to analyse the droplets temporal and spatial information and then the computer software (BSA Flow Software v4.10) was employed to record the data.

3.3.1 The Principle of the Droplet Size and Velocity Measurement

Figure 3.8 shows the schematic of light incident on a spherical droplet. From the figure, some of the incident rays will be reflected when they come into contact with the outer surface of the spherical droplet and is defined as reflected light; whilst the other rays will be refracted and pass through the spherical droplet (first order refraction). Then these refracted rays will be reflected again along the internal surface of the spherical droplet and consequently some of the internal reflection rays will be refracted again (second order refraction).
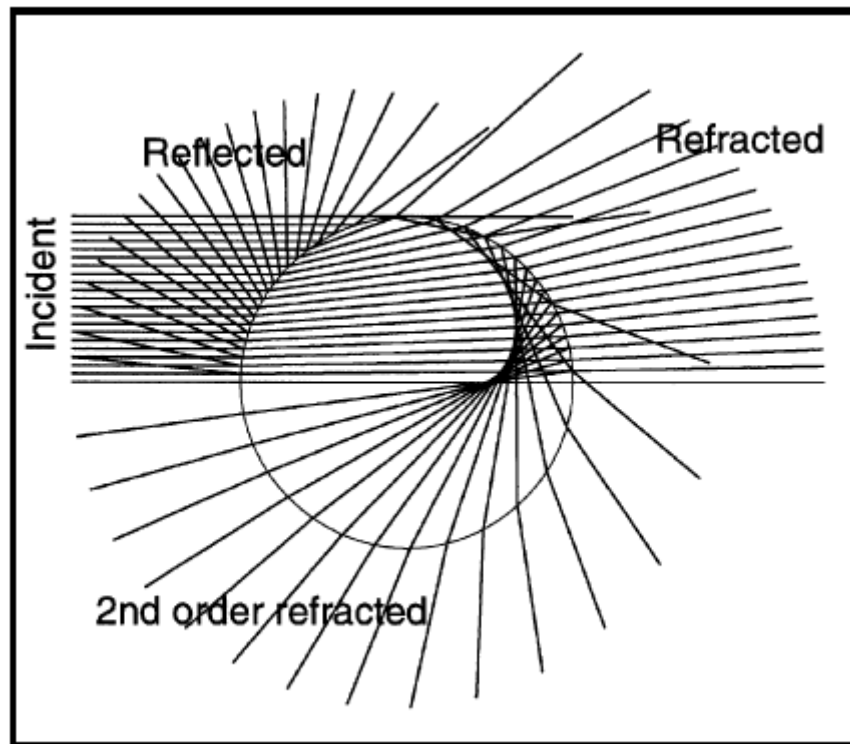
Figure 3.8. Scattering modes of a set of rays incident on a liquid droplet [128]

As the rays incident on different position of the sphere droplet a phase difference between the signals will be produced due to the light path difference and received by the signal detector.

Then the droplet size will be determined based on the linear relationship between the phase shift and droplet diameter. For the current study, the angle between the transmitter optics and the receiver was adjusted to 70°, as shown in Figure 3.7. This angle was different in comparison with previous researcher, who collected the refracted light at 30° toward the incident light. This angle was employed for several reasons. The first reason is the phase/refractive index response linearity. For the 70° scattering geometry, the phase/refractive index relationship is linear for different droplet sizes, whilst the 30° scattering geometry suffers from poor phase linearity for droplet size smaller than 10 microns. Thus it increases the ambiguity in determining droplet sizes at the 30° scattering geometry. The second reason is the sensitivity of the measurement towards the refractive index. Pitcher et al. [129] examined the sensitivity of droplet size measurement to refractive index change. Figure 3.9 shows the phase/droplet size relationships for 30° and 70° scattering geometry measured by them. It can be seen from this figure that for the 70° scattering geometry, despite the change of refractive index from 1.27 to 1.45, a single phase/droplet size factor is applicable (for their PDA system, it is 5.01° per micron). However, for the 30° scattering geometry, the phase/droplet size factor varies from 5° per micron (refractive index of 1.22) to 4° per micron (refractive index of 1.45).
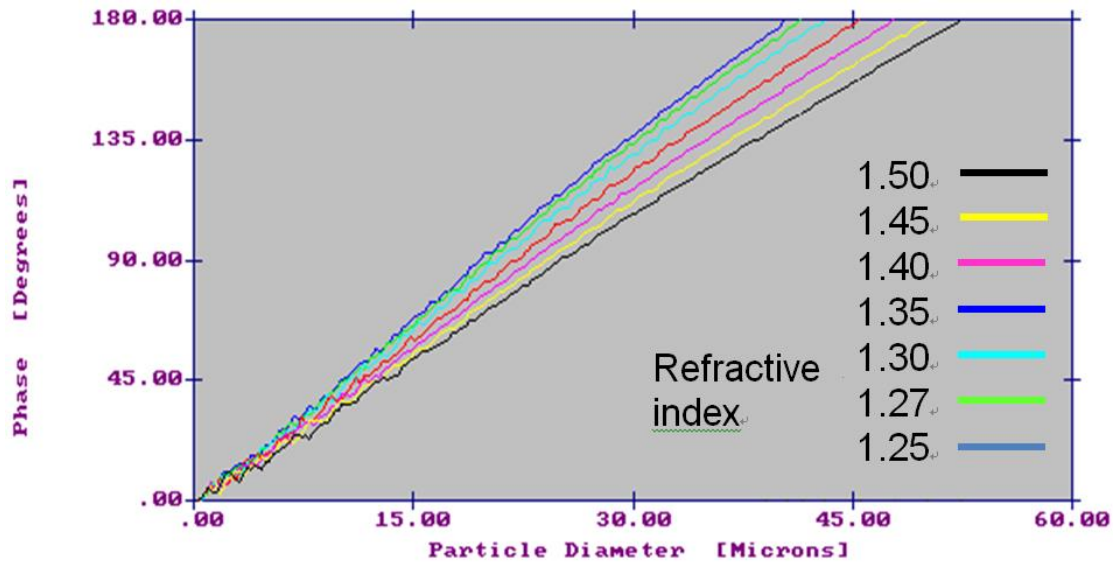
(a)
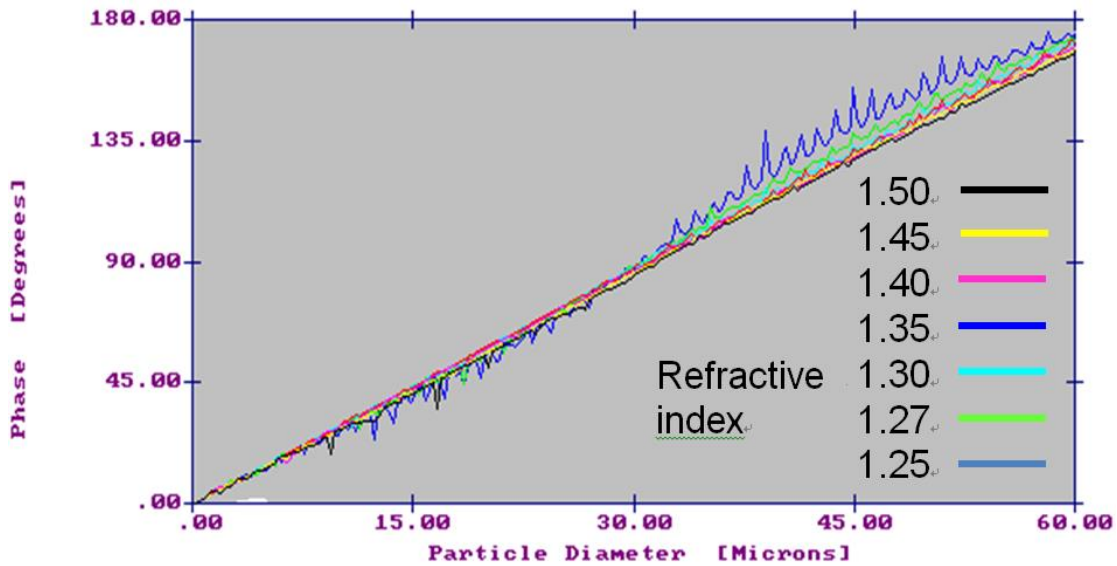
(b)

Figure 3.9. Effect of refractive index changes on PDA phase factor (a) 30° scattering geometry (b) 70° scattering geometry [129]

3.4 Planar laser induced fluorescence (PLIF) System

Figure 3.10, presents a schematic diagram of the PLIF setup. A pulsed Nd: YAG laser with an output of 87 mJ/pulse at 266 nm, was used to excite the molecules of the added tracer to the fuel to fluorescence, at a specified crank angle. For the PLIF measurements, the surrogate fuel

should have a physical and thermodynamic properties matching with the typical gasoline fuels. Therefore, isooctane was used as a surrogate fuel which is considered as a stronger representation of gasoline mid-boiling point fractions [127] and 3-pentanone was selected as a seeding tracer. The 3-pentanone was chosen as a dopant because its boiling point (375 K) and its heat of vaporisation (33.45 kJ/mole) are closely matched with the boiling point and heat of vaporization of the carrier iso-octane fuel, (372.4 K) and (30.79 kJ/mole) respectively. It experiences satisfactory fluorescent emissions, and has an absorption ability to the laser incident source wave length and insensitivity to oxygen quenching [126]. Previous investigations have concluded that among the common tracers, 3-pentanone has proven attractive photophysical behaviour for PLIF measurements [122-124]. For all the PLIF measurements, iso-octane fuel was seeded by a low 3-pentanone concentration at 3% by mass, where high fluorescence intensity was noticed and to ensure the required signal to noise ratio. This percentage of tracer was similar to the work of previous researchers who employed 3-5% by volume of 3-pentanone to iso-octane [130, 131]. However, Davy et al. [132], demonstrated the fact that 3-pentanone and isooctane form an azeotropic mixture, and the relative quantities of each component within the blend are the dominant factor controlling the evaporation characteristics not the relative volatilities of the two pure components. Furthermore, they highlighted that the evaporation rate of 3-pentanone liquid mixtures with a low initial 3-pentanone concentration higher than that of mixtures with compositions closer to the composition of the azeotrope.

A laser sheet with a thickness of approximately 1 mm and width of 49 mm was formed using wavelength matched mirrors and laser sheet optic. This beam was directed into the combustion chamber through a triangular quartz window. The fluorescence signal was imaged at a right angle to the excitation plane via a fixed mirror at 45° and was collected through a 105 mm f/4.5

UV-Nikkor lens onto a gated image intensifier (Hamamatsu C10880-03F) linked to the Phantom V710 CCD camera. The Camera gate width was 1 μs, and the intensifier was gated for a short duration of 280 ns to reduce background light and combustion luminosity. A Schott WG360 long-pass filter was placed in front of the camera to block unwanted wavelengths, passing the LIF signal and reject elastic scattering from the walls. The repetition rate of the PLIF imaging system was limited to 10 Hz due to the repetition rate of the Nd: YAG laser. Thus the- optical engine was run at 1200 rpm. A shaft encoder was used to generate the trigger pulse at a specified crank angle of the engine. The Nd: YAG Laser and imaging system (camera and intensifier) were controlled by a commercial time box and were synchronized (with one crank angle degree resolution) with the engine via a reference signal from a LabVIEW engine control unit.
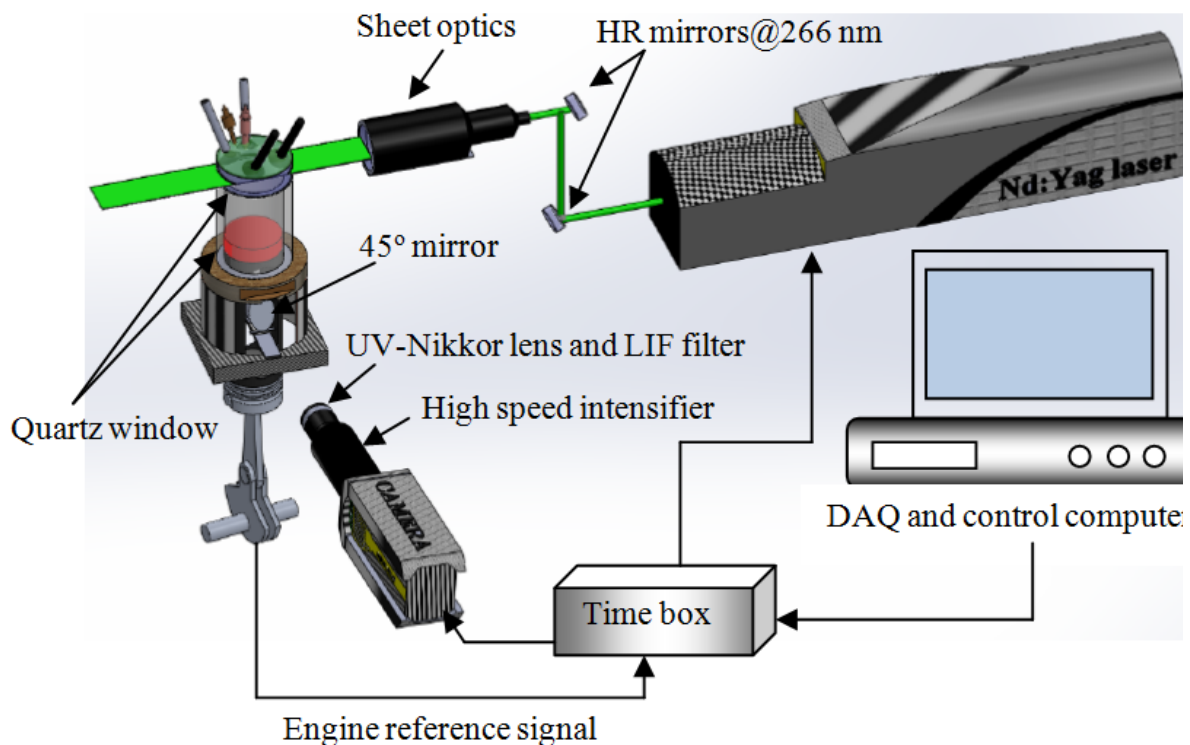
Figure 3.10. Schematic diagram of the PLIF setup

3.4.1 Beam Expander

For the current study a beam expander (sheet optics) was employed to expand the laser beam of 10 mm diameter into a laser sheet with a width of 49 mm and a thickness of 1 mm. Figure 3.11 shows the Dantec 9080X0841 beam expander, which used to precisely control the light sheet thickness and the focal length. Then this laser sheet was utilized for PLIF and PIV techniques measurements.
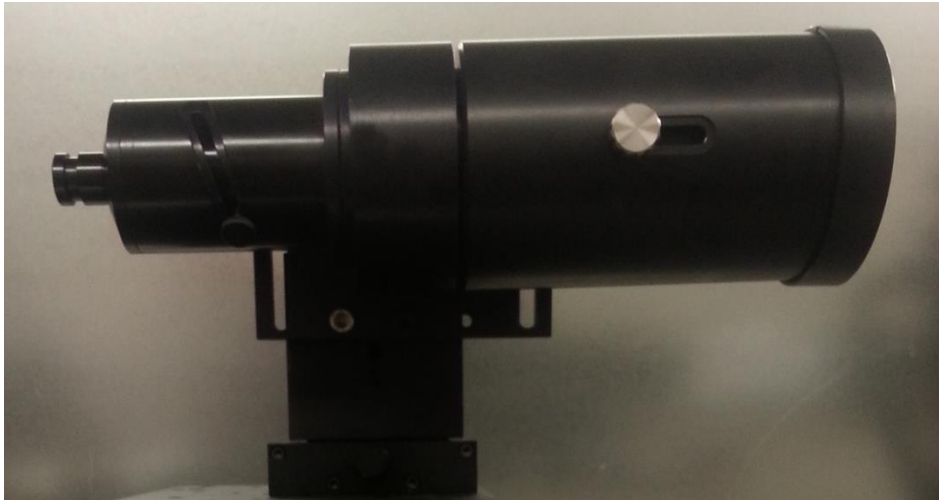
Figure 3.11.Sheet optics for PLIF laser beam

3.4.2 UV Lens and PLIF Filter

In this investigation, the Nikon 105 mm UV lens was used. The f number of the UV lens could be varied from 4.5 to 32. The UV-Nikon lens was coupled with Phantom camera for the PLIF imaging. This lens provides a high transmission (of up to 70%) on a broad spectral range of 220 nm-900 nm to travel through. A Schott WG360 long pass filter was mounted on the lens to eliminate any reflected or scattered laser light and to distinguish between the wanted emission signal and the flame chemiluminescence signal.

3.4.3 Time-box and System Synchronization

The synchronization between the camera, laser system and the optical engine was accomplished via a time-box supplied by Dantec. Dynamic Studio v4.10 Software was

employed to control precisely the timing of the camera and laser. The time box is consisted of 8 outputs BNC connection points (Bayonet Neil-Concelman) which generate TTL signal output to synchronize between the camera, intensifier and laser. The timing of this device can be precisely controlled with accuracy of up to 12.5 ns. The timing box back panel contains two inputs BNC connection channels; channel 1 and channel 2. The main role of channel one is to record one image each cycle at certain crank angle position. Whilst the role of channel two is record a number of images defined by the user, and the record of the images start from certain crank angle. Both the inputs and outputs channels were used to synchronize all the optical devices including the high-speed camera, intensifier and laser with the single cylinder engine.

3.4.4 Planar Laser Induced Fluorescence Calibration

The purpose of PLIF calibration was to establish a relationship between the air-to-fuel ratio and the measured fluorescence intensity for a given pixel. The pressure and temperature (engine crank angle dependent) affect this relationship; therefore, it must be established for all crank angles of interest. A PFI (Port Fuel Injection) injector was calibrated and used to generate homogeneous mixture with variable air-fuel ratios. Figure 3.12 presents the PFI calibration curve. The amount of air inducted for each engine cycle was measured using a calibrated gas volume meter (Romet Rotary Gas meter G40). Measurements of different equivalent ratios were compared with the lambda sensor values and similar values were obtained (uncertainty was $\pm$ 0.079 L/m). To make sure all injected fuels were vaporized for a good homogeneous mixture and to avoid build-up of liquid fuel in each cycle, the fuel was injected at 100 CAD BTDC, when the intake valves were closed to utilize the heat from the hot valves for vaporization. Figure 3.13 shows the air/fuel mixture distribution for a stoichiometric condition of φ=1, where a fairly uniform distribution of the mixture can be noticed. In addition, the normalized intensity ratio between the intensity at each pixel and the average intensity was

employed to investigate the homogeneity of this mixture. It was noticed that the normalized intensity ratio over 85% of the region of interest area varied between 0.95 and 1.05.

For this study, the engine ignition crank angle of interest was fixed at 30 CAD BTDC. This was the mapped engine ignition timing for our operating conditions. A set of 100 background images was captured with the engine, the laser and the imaging system running while there was no fuel injection. Another set of 100 PLIF images was acquired at this crank angle from 100 consecutive cycles. A MATLAB code was developed for PLIF image processing. The averaged background image was obtained and subtracted from the averaged PLIF image. Then, a Region of Interest (ROI) was defined and spatially averaged pixel intensity within this area was calculated. This area was located at centre of the combustion chamber in vicinity of spark plug. The fluorescence intensity at 30 CAD BTDC was plotted against the equivalence ratio, Figure 3.14.
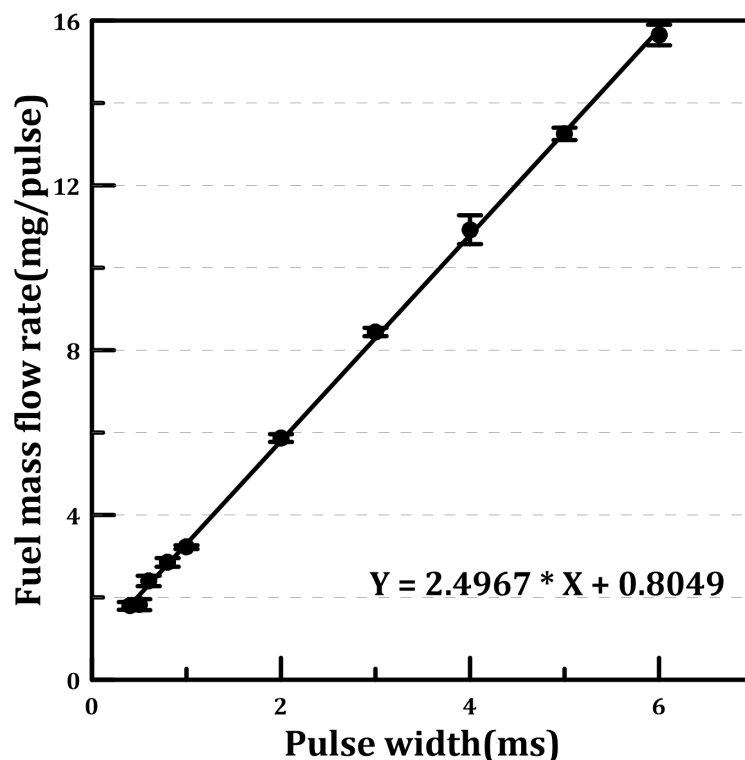
Figure 3.12. Calibration curve of the port fuel injector

(a)

(b)

(c)

(d)

0.7 0.8 0.9 1 1.1

Normalized intensity ratio

(f)
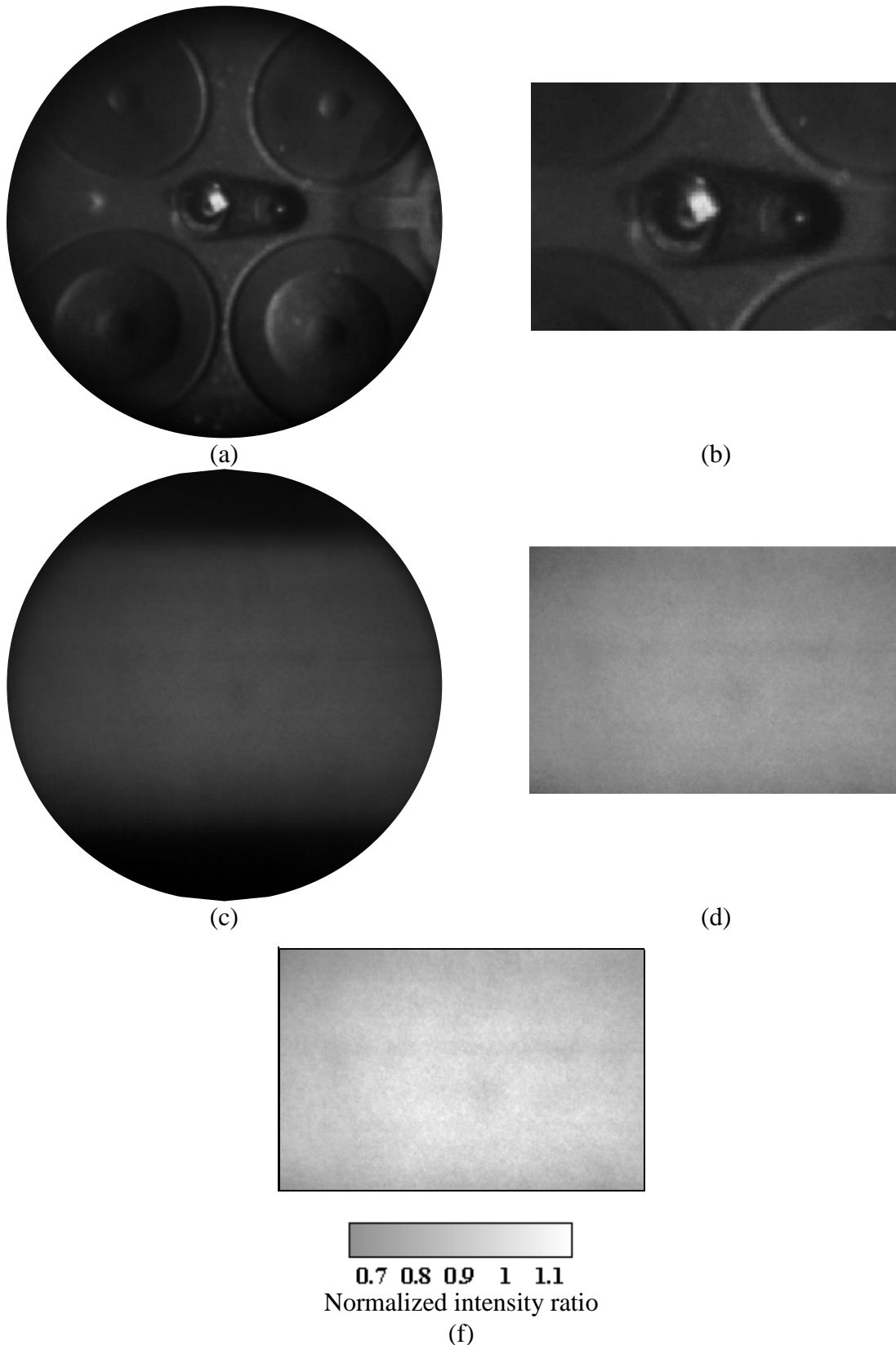
Figure 3.13. (a) Combustion chamber view at 30 CAD BTDC, (b) Selected Region of Interest (ROI), (c) In-cylinder fuel distribution at φ=1 and port fuel injection timing of 100 CAD BTDC, (d) ROI of image (c), and (f) Normalized intensity ratio between intensity at each pixel and the average intensity calculated over the ROI.
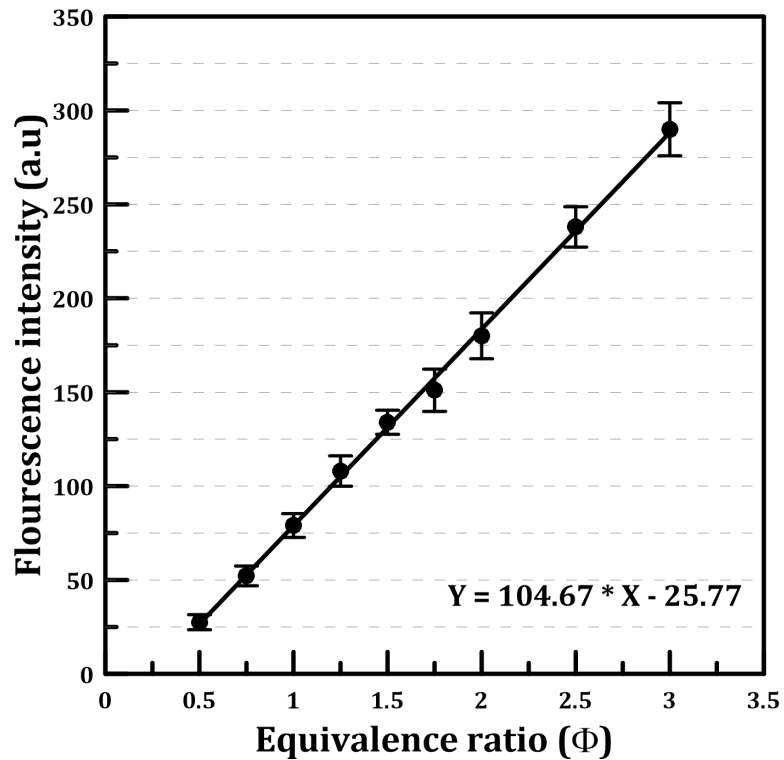
Figure 3.14. Fluorescence intensity vs. equivalence ratio for air, iso-octane and 3-pentanone mixture at 30 CAD BTDC

3.5 CCD Camera (Intensifier)

Ultra-high-speed camera Phantom V710 was used throughout this work. For the current study, the frame rate used was 10 KHz and the resolution was 800 x 800 pixels. This camera was coupled with HAMAMATSU Intensifier (C10880-03F) for high speed imaging of combustion process and PLIF system. Table 3-3 summarize both the camera and the intensifier specification.

Table 3-3. The camera and the intensifier Specification

High speed Camera Phantom V710	
Camera resolution	Up to 1280x800 @ 7500 FPS
Camera sample rate (fps)	Up to 1,400,000@ 128 x 8 pixels
Colour expression, gradations	Monochrome 8 bit and 12 bit
Storage	16GB
HAMAMATSU Intensifier (C10880-03F)	
Gate maximum repetition frequency	200 kHz
Gate time	10 ns- 9.9 ms
Spectral response	185-900 nm
Response time	10ns

3.6 Schlieren Optical Method

The laboratory setup for experimentation was a replication of the approach as detailed by Tian et al. [133] and Ma et al. [134] with Figure 3.15. Schematic diagram for Schlieren set up providing a detailed description of the arrangement. Figure 3.16 shows the whole connection of the constant volume combustion vessel including two circular quartz observation windows, each one with a diameter of 100 mm, alongside with eight heating elements, installed at each corner. Temperature modulation of the vessel was implemented via closed loop control, to monitor the heating elements described and allow continuous observation of the fuel-air mixture condition within the chamber. The fuel injection strategy was fulfilled through a gasoline direct injection (GDI) nozzle, which was mounted in the top cover of the vessel, and was driven by an ECU-computer system. Finally, to achieve the necessary spark for ignition, a pair of tungsten electrodes was positioned in the centre of the vessel, with a pressure release valve featured for safety purposes, operating at 0.7 MPa.
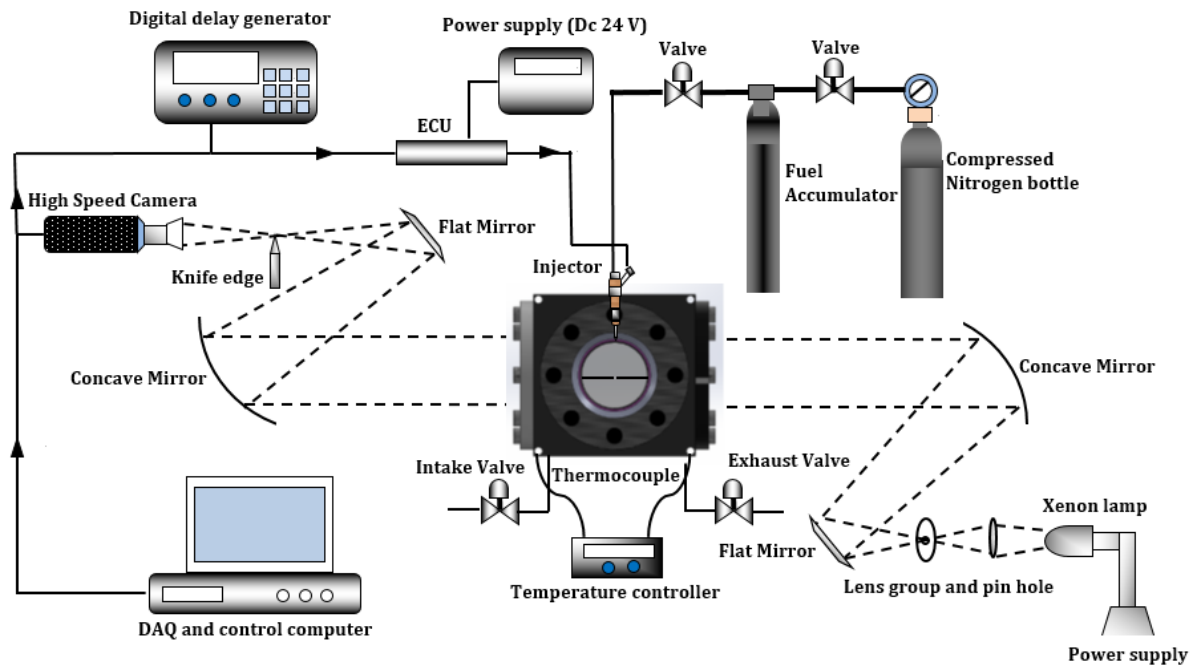
Figure 3.15. Schematic diagram for Schlieren set up
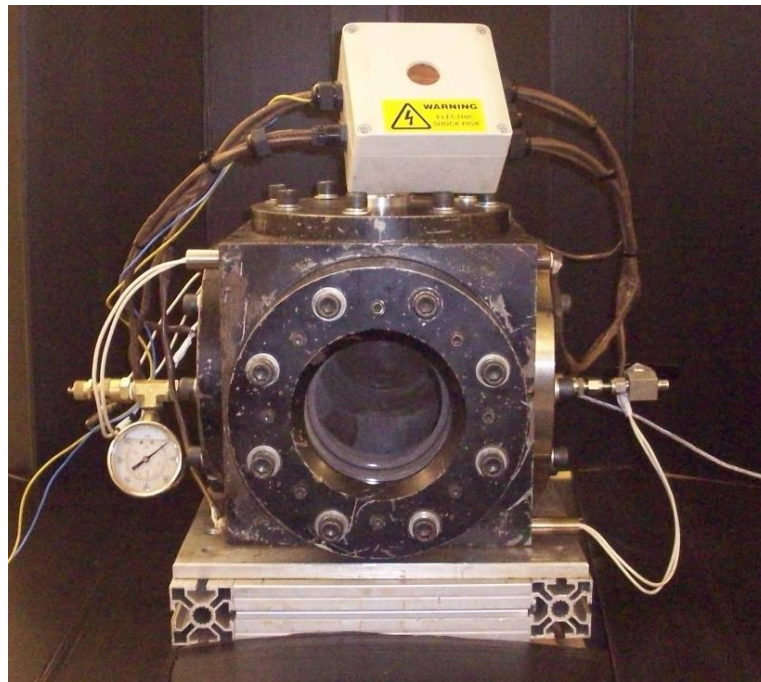
Figure 3.16. Constant volume vessel

The experiment was carried out using a 500 W xenon lamp as a point light source coupled with

a lens array, prior to an adjustable aperture. A concave mirror was employed to generate a

parallel beam from the light source and direct these beams through the vessel chamber via the

aforementioned observation windows, illuminating the test environment. Once the light passed the glass windows, a second concave mirror was employed to direct and focus this light toward the knife edge, to fulfil the required schlieren effect (2-D imaging). A high-speed camera (Phantom research V710) was utilized to record the combustion event with a frequency of 10 kHz (10,000 frames per second) and resolution of 800 x 800 pixels.

Compressed air was used to scavenge the burned gases in the exhaust. After flushing and before each test, the vessel chamber was opened to the ambient air until the air temperature inside the vessel stabilized at the test point. Once the temperature stabilized, the valves to the chamber were closed and the fuel was injected to form a homogenous fuel-air mixture, remaining undisturbed for a minimum of five minutes to guarantee homogeneity and a relative state of inactivity. Following this, the mixture was ignited via electrode spark, which simultaneously switched the camera on to record. After the combustion event, the burned products were extracted from the vessel chamber, enabling the experiment to be restarted. To ensure high confidence in procedure, each test was repeated a minimum of three times based on the calculated low variance value of 0.0000065 for the repeated tests, which indicates error minimization.

3.7 Emissions Measurement

This section discusses in more details the devices employed to measure the major emissions components including PM, NOx and HC.

3.7.1 Particulate Emissions

A differential mobility spectrometer (DMS) 500 introduced by Cambustion Ltd was employed to measure the PM emissions sample at a distance of 0.3m from the exhaust valve, downstream of the exhaust plenum. For the current study, the particles which have a size of 10-30 nm range were defined as nucleation mode particles. Whereas, the particles with size of 30-500 nm range were defined as the accumulation mode particles.

The DMS500 provides the particulate number/size spectrum in a range of 5 to 1000 nm. The DMS500 uses a classifier column Figure 3.17, operating with an external vacuum pump at 0.25 bar absolute (for the 5–1,000 nm range). A cyclone separator removes particles above the measurement range to reduce the need for cleaning. Initially, the particulates were directed and pumped into the two-stage dilution system before the sample gas passes through a corona charger and into the classifier column, see Figure 3.18. In order to eliminate any condensation of the particulates, the sample line was heated up to 150˚C. The primary dilution station was employed to dilute the particulates using metered compressed air controlled by HEPA filtered to provide a 5:1 dilution factor. This reduces the moisture content of the sample gas, and reduces particle agglomeration / nucleation. The optional 2nd diluter is of the rotating disc type. This diluter can achieve dilution factors between 12:1 and 500:1 by varying the rotation speed of the disc. Solenoid valves allow the secondary diluter to be bypassed for a 2nd dilution factor of 1:1. For this study the second dilution was fixed at 20:1. The dilution ratios was selected based on the instruction provided by the manufacturer [135], to ensure a good signal to noise ratio and to keep the device clean for long time interval. The exhaust sample was collected each 2 minutes with a rate of 1 HZ to ensure the consistency of the data collected.
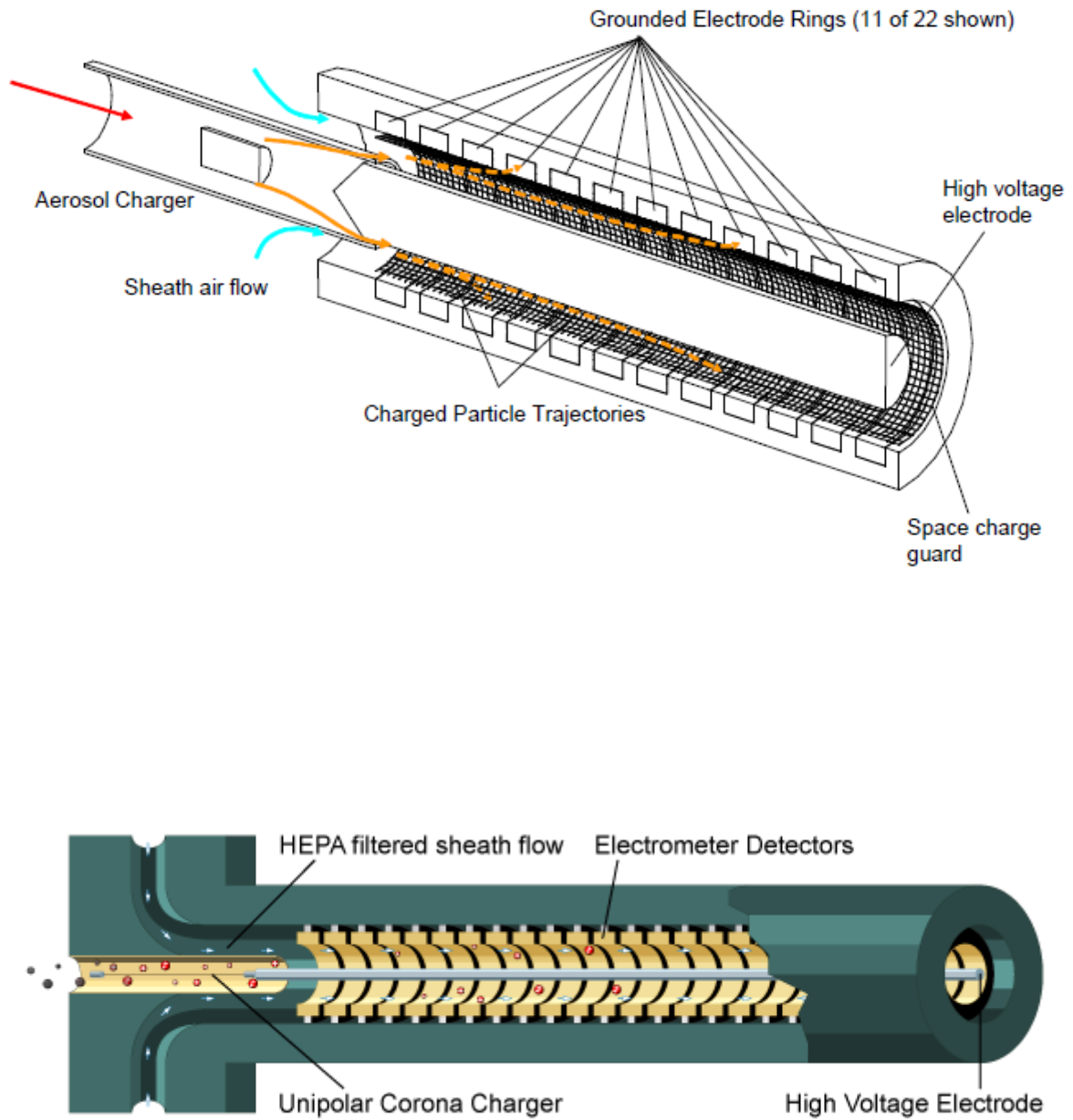
Figure 3.17. DMS500 classifiers [135]
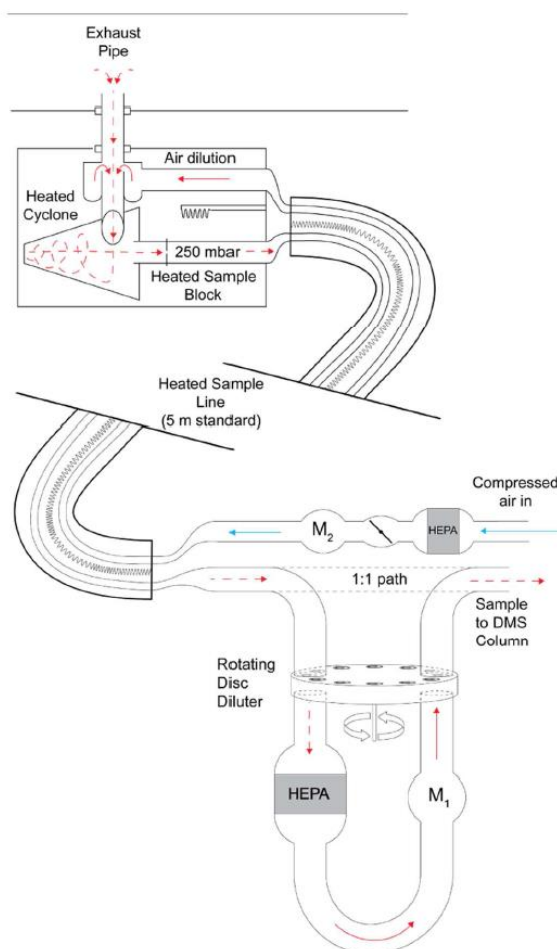
Figure 3.18. Sample path for DMS500 with heated sample line [135]

The particles then passed through a unipolar corona charger after its dilution. Consequently, these particles experienced a positive electric charge proportional to the particle size. In a predictable manner, the charged particles were carried using cylindrical laminar column of air, where the charged particles flow within a uniform particle-free sheath flow these particles, see Figure 3.17. Then the repulsion force from the central high voltage rod was employed to deflect the particles towards the grounded electrometer rings. Both the particles aerodynamic drag and charge controlled the particles landing position. Consequently, the electrometer amplifiers received the charge of the particles, and producing current which translated into particle number and size data by the user-interface. Finally, the Cambustion software interface was employed without any modification to record the particulate measurements.

3.7.2 Gaseous Emissions

Similar to particulate emissions, the gaseous sample emissions were collected at 0.3 m from the exhaust valve on an opposite direction to that of the PM collecting point, downstream of the exhaust plenum. Then the gaseous sample is passed through a pre-filter and heated line, where the temperature was kept constant at 190˚C to avoid condensation of the emissions. Consequently, Horiba MEXA-7100DEGR was employed to analyse this sample. Table 3-4 summarizes the specification of the system.

Table 3-4. Specification of Horiba MEXA-7100DEGR

Horiba MEXA-7100DEGR specification				
	CO Analyser	NO_x Analyser	CO_2 Analyser	HC Analyser
Methods	Non-Dispersive Infra-Red (NDIR) (dry)	Dry chemiluminescence detector (CLD)	Non-Dispersive Infra-Red (NDIR) (dry)	Hot-wet flame ionisation detector (FID)
Minimum. (ppm)	0-100	0-10	0-5000	0-10
Maximum. (ppm)	0-12%	0-10000	0-20%	0-50000
Zero gas	N_2	N_2	N_2	N_2/air
Span gas	CO/N_2	NO/NO_2	CO/N_2	C_3H_8
Accuracy	∓ 1%	∓ 1%	∓ 1%	∓ 1%

The majority of industries used chemiluminescence detector (CLD) technique to measure the concentrations of nitric oxide (NO_x). In the presence of O_3, this method was employed to generate NO_2 from the oxidation of NO. For each reaction of NO molecule, a quantity of light will be produced. Consequently, a photo multiplier tube (PMT) is used to detect the emitted photons. The output voltage of CLD is used to determine the sample NO concentration due to the direct proportionality between them.

The flame ionisation detector (FID) is considered the most sensitive gas chromatographic detector for hydrocarbon (HC) concentration measurements. The FID contains a hydrogen flame, where the combustion of the sample gas will be occurred. Consequently, the combustion of the hydrocarbons in the sample will lead to ion formation. Then all the positive ions are collected by a metal collector which is negatively biased with a high DC voltage, causing a current to flow, which is then electronically amplified and digitized. The direct proportionality between the ionisation rate and the collector cross current was utilized to predict the sample HC concentration.

Non-Dispersive Infra-Red (NDIR) detector is a simple spectroscopic device often used to monitor the concentration of carbon oxides (CO & CO2). When the sample gas pass through the detector, each species in the sample can absorb infrared light, causing them to bend, stretch or twist at a particular frequency. The amount of IR light absorbed at the necessary wavelength is proportional to the volumetric concentration of CO or CO_2 in the sample.

Horiba system was heated initially to its pre-set temperature and then calibrated using zero calibration gases, before each test. Compressed air was utilized to purge the system when the engine stops to avoid any build-up of condensation through the system, and consequently this will impact on the future measurements.

3.8 Heat Release Analysis

The in-cylinder pressure data was utilized to obtain the net heat release rate ($dQ/d\theta$), using Equation 3-1, and consequently to calculate MFB [136].

$$\frac{dQ}{d\theta} = \left(\frac{\gamma}{\gamma - 1} * P * \frac{dV}{d\theta} \right) + \left(\frac{1}{\gamma - 1} * V * \frac{dP}{d\theta} \right) \tag{3-1}$$

where θ is the crank angle degree; (γ) is the adiabatic index is the ratio of specific heats (C_p/C_v); Q is the released heat; ($dV/d\theta$) is the rate of change of combustion chamber volume with respect to the crank angle degree, ($dP/d\theta$) is the rate of change of combustion chamber pressure with respect to the crank angle degree. By integration of the heat release rate, the MFB at any crank angle i from the start of combustion was determined, as shown in Equation 3-2 [136].

$$MFB = \frac{\int_{\theta_s}^{\theta_i} \frac{dQ}{d\theta} \, d\theta}{\int_{\theta_s}^{\theta_e} \frac{dQ}{d\theta} \, d\theta} \qquad (3\text{-}2)$$

Where s is defined as the start of combustion, and e is defined as the end of combustion.

3.9 Summary

In this chapter an overview of the experimental test facilities used in this work has been given. The single cylinder engine and its test bed, air –fuel ratio measurements, ignition system, fuel and tracer injection and supply systems and data acquisition system were described. Furthermore, a detailed description of the PDPA system and its principle used to quantify spray droplets and velocities has been provided. Following that, the PLIF laser system and the calibration method used in this work were described in details. Finally, emissions measurements techniques were presented.

Chapter 4

INVESTIGATION OF INJECTOR COKING EFFECTS ON SPRAY, MIXTURE STRATIFICATION AND EMISSIONS

The aim of this chapter is to obtain a comprehensive understanding of gasoline direct injector coking effects on fuel injection, engine performance and emissions. Deposit build-up in the coked injectors and fouling cycle repeatability was first examined by measurements of fuel flow rate. Macroscopic spray characteristics of the clean and the coked injectors were carried out using high-speed imaging and Planar Laser Induced Fluorescence (PLIF) of spray footprint. Fuel droplet size and velocity were characterised with a two-dimensional Phase Doppler Particle Analyser (PDPA).

4.1 Introduction

Engine performance deterioration, alongside the increased emission levels associated with injector deposits cause a lot of concern for engine designers. Deposit formation through the narrow holes passages of the injector leads to a reduction in the flow capacity besides the spray quality degradation. Furthermore, injector deposits promote more particulate emissions due to the deposits ability to adsorb fuel, which burn later as a diffusion flame produced from heterogeneous combustion [64]. Therefore, it is important to shed more light on the negative impacts of injector deposits on macroscopic spray characteristics, in-cylinder mixture distributions and engine emissions.

The current study presents macroscopic imaging of the coked and the clean injectors' spray structure and quantification of spray properties, including plumes penetration length and angles (relative angle and cone angle), droplet size and droplet velocity profiles. The PLIF technique was employed to investigate effect of injector coking on in-cylinder charge stratification at the ignition timing and repeatability in mixture preparation. Combustion analysis, using in-cylinder pressure data and Mass Fraction Burned (MFB) was used, along with exhaust emissions measurement to obtain a better understanding of the GDI injector coking effects on engine performance and emissions. In order to achieve consistency in injector coking process, a fouling cycle was developed and investigated using a multi-cylinder thermal engine.

4.2 Injector Fouling Cycle and Fuel Flow Rate Measurements

The gasoline direct injectors used in this study were similar solenoid-actuated multi-hole laser-drilled injectors. Each utilized six nozzle holes with a pre-chamber arranged in a circular pattern. Figure 4.1 presents cross sections of a clean and a coked injector tip. The injectors were coked in authors' laboratory using a developed fouling cycle. Injector fouling tests were carried out on a multi-cylinder (V8) thermal engine with the same combustion chamber configuration as the single-cylinder optical engine. Injector fouling cycle consisted of engine load sweep from idle to 8 bar IMEP at 2000 rpm over 54 hours engine run. Fuel injection pressure was 150 bar. Test fuel was Unleaded Gasoline (ULG95), 3.3% Ethanol, 6.1% Ethyl Tertiary Butyl Ether (ETBE) without Deposit Control Additives (DCA) additive. By the end of the fouling cycle, as it is shown in Figure 4.1, carbon deposits were accumulated through the internal holes and pre-chambers as well as on the injector tip outer surface. The repeatability in deposit formation was investigated by measurements and comparison of fuel flow rate for the coked and the clean injectors. Flow rates of clean and coked injectors were measured at 150 bar injection pressure. Six injection pulse widths ranging from 1 to 2.5 ms were selected

and the fuel mass of 1000 injections was measured by a digital weighing scale (with a resolution of 0.1 mg).

Measurements were repeated five times and the mean averaged values were used to calculate the flow rate. The maximum uncertainty of measurements was ± 0.052 mg/pulse. Correlations of injector pulse width and fuel mass flow rate are shown in Figure 4.2. The reduction in the mass flow rate of the coked injector in comparison with the clean injector had a chaotic change for different pulse width, peaking at 1 and 2 ms pulse width with approximately 8.5%. For this study, the pulse width of 1.7 ms is the condition for the clean injector to achieve stoichiometric condition and load of 5 bar IMEP. It was observed that for a pulse width of 1.7 ms, the averaged mass flow rate of the clean injector was 23 mg/pulse, whilst for the coked injector it was 21.7 mg/pulse. This indicated that the coked injectors had ~5.6 % reduction in mass flow rate compared to the clean injectors. The pulse width for the coked injectors was thus adjusted to 1.8 ms to compensate for losses in the mass flow rate. The coked injectors were then tested with this pulse width inside the engine under the same condition, resulting in stoichiometric ratio (λ=1), which was verified using a lambda meter (ETAS LA4-E). Care was taken to maintain consistency between the injectors when taking measurements. Thus, the flow rate measurements were repeated after engine tests to check that the injectors had not developed new deposit or had their deposit washed away during the experiments.

(a)   (b)
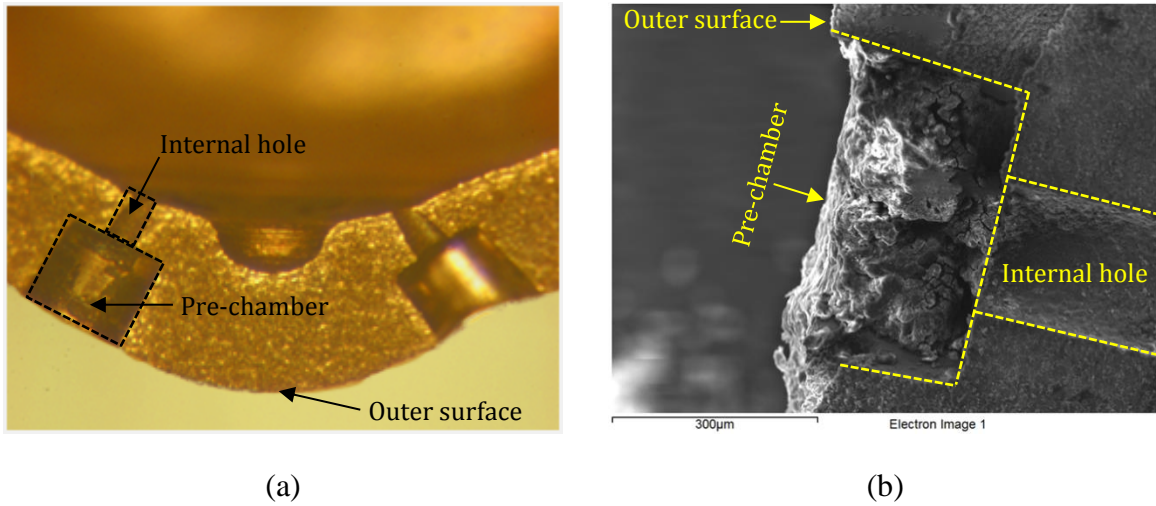
Figure 4.1. Cross section of a multi-hole injector tip, (a) clean injector [71] (b) coked injector
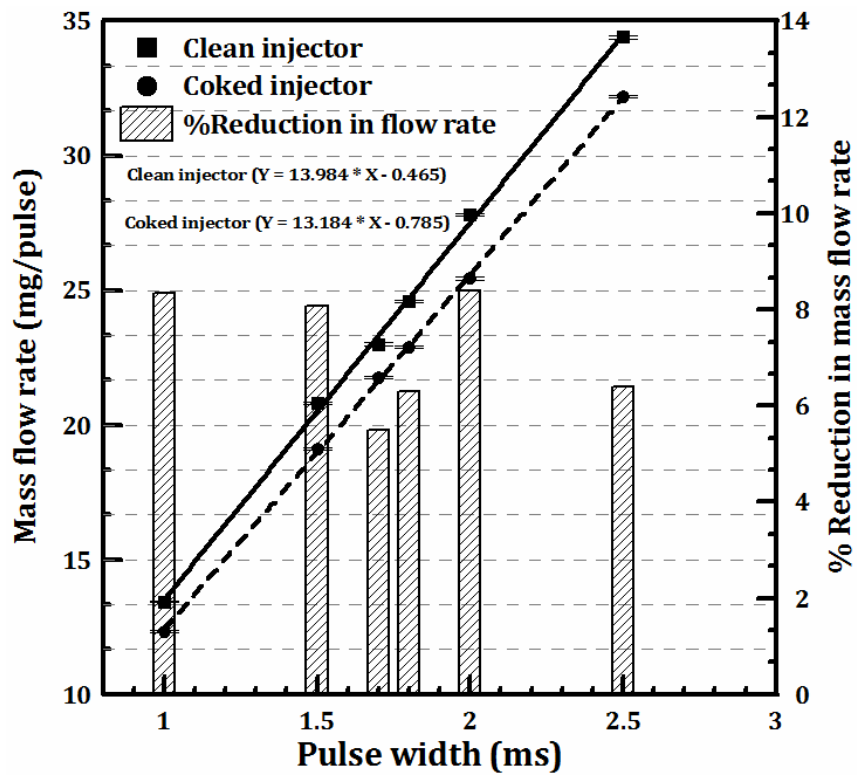
Figure 4.2. Mass flow rate versus pulse width for the clean and coked injector at injection pressure of 150 bar for iso-octane fuel

4.3 Experimental Procedure

Table 4-1 summaries experimental tests, techniques and fuels used in this work.

Table 4-1. Summary of the tests, experimental setup and fuels

Experiment	Injector fouling and flow rate measurements	Spray angle and plumes penetration length measurements	Spray foot print measurements	Droplet size and droplet velocity measurements	Combustion and emissions measurements	In-cylinder charge stratification measurements
Technique	Developed fouling engine cycle	High-speed imaging	PLIF measurements	PDPA measurements	-High-speed imaging of flame, -Combustion analysis,	PLIF measurements
Test environment	-Multi-cylinder thermal engine -Flow rate measurement rig	Constant volume chamber	Constant volume chamber	Constant volume chamber	-Single-cylinder Optical engine -Single-cylinder thermal engine	Single-cylinder Optical engine
Fuel	Gasoline (ULG95) with 3.3% ethanol, 6.1% ETBE without DCA additive	Gasoline (ULG95) with 3.3% ethanol	Iso-octane doped with 3-pentanone (3% by mass)	Gasoline (ULG95) with 3.3% ethanol	Gasoline (ULG95) with 3.3% ethanol	Iso-octane doped with 3-pentanone (3% by mass)

4.4 Effects of Injector Coking on Macroscopic Spray Behaviour

Figure 4.3 shows images of spray development as a function of time, after the start of injection for the clean and coked injectors, with injection duration of 1.7 and 1.8 ms respectively and injection pressure of 150 bar. As it shown in the images, spray has a symmetrical pattern. The two front fuel plumes (jet 3 and jet 4) are called 'ignition jets' as they were facing spark plug in the engine. The back plumes (jet 1 and jet 6) are called 'rear jets' and the two plumes on the side (jet 2 and jet 5): 'side jets'. It was observed that the six fuel plumes formed by the clean injector, had significantly shorter penetration length and higher dispersion compared with the plumes of the coked injector.

To quantify the observed differences between plumes penetration lengths and spray angles for the clean and the coked injectors, 10 injections were captured for each injector and the images

were averaged using a developed image processing MATLAB code. Initially, the illumination non-uniformity problem was reduced by subtracting the image at each time interval from the background image. Then a reference line was drawn by a MATLAB code along the plume axis and consequently the penetration length was identified based on the grayscale change along this reference line. In addition, the sensitivity analysis of the penetration length was carried out to determine the optimum threshold for image processing. Based on this sensitivity analysis a threshold (normalized intensity) of 0.027 was employed to identify the plume boundary with a maximum uncertainty of $\pm$ 2.9 mm in the calculated penetration length values. The image magnification was 6.1 pixels/mm and according to this ratio the actual penetration length was determined. The average penetration length results for all plumes are shown in Figure 4.4. The coking effect and deposit distributions were not the same for the six plumes investigated due to the different levels and shape of deposit formed in each nozzle. Maximum change in the penetration length was observed for the side jets and ignition jets, with a 25% increase at 1.8 ms after SOI, whilst the rear jets were least affected and had only a 21% increase in their penetration lengths.

Clean injector

Coked injector

(a)   (b)
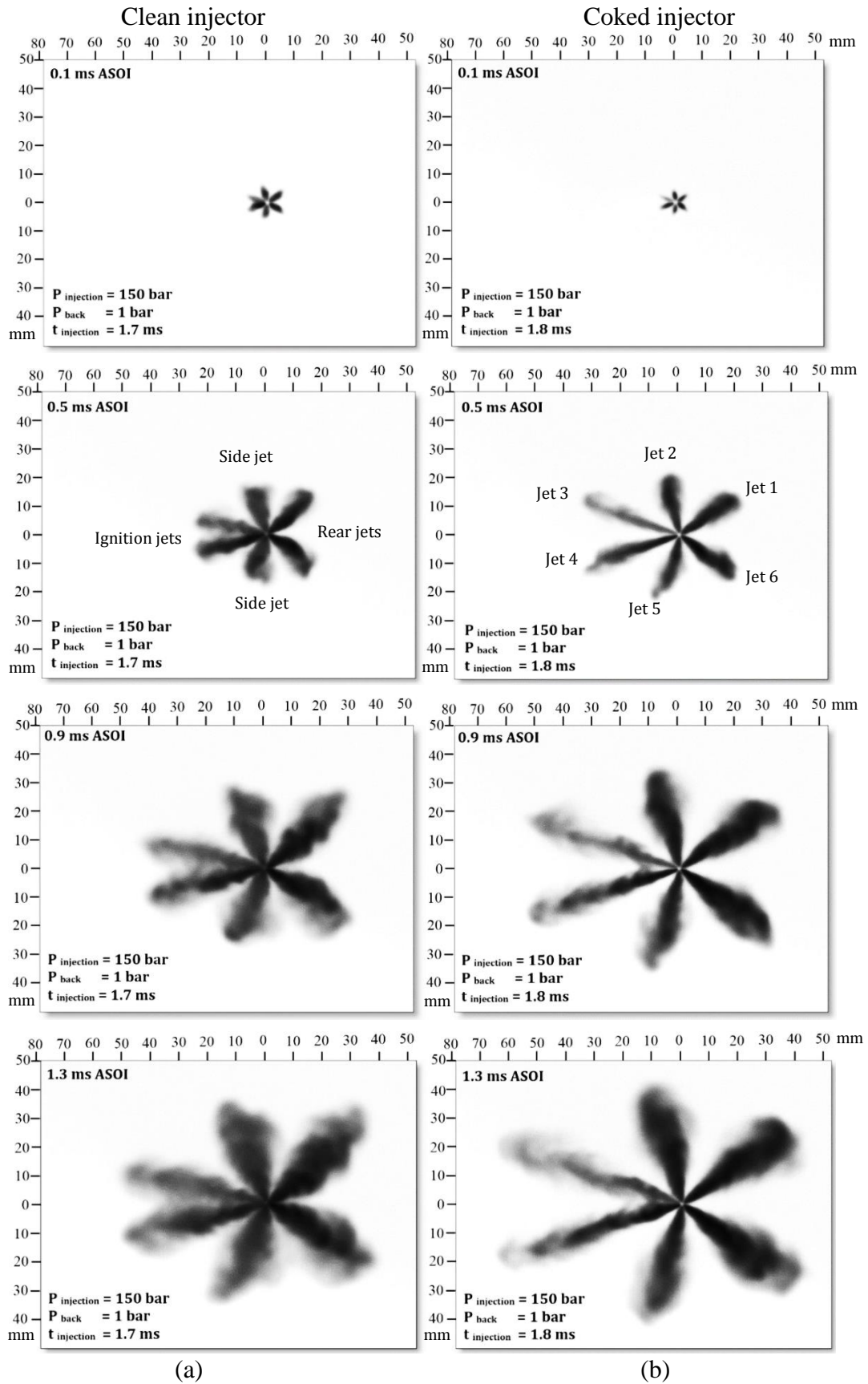
Figure 4.3. Bottom view of time resolved high-speed images of spray from (a) clean injector and (b) coked injector for iso-octane with a frame rate of 10 KHz, resolution of 800 X 800 pixels and magnification of 6.1 pixel/mm.

(a)

(b)

(c)
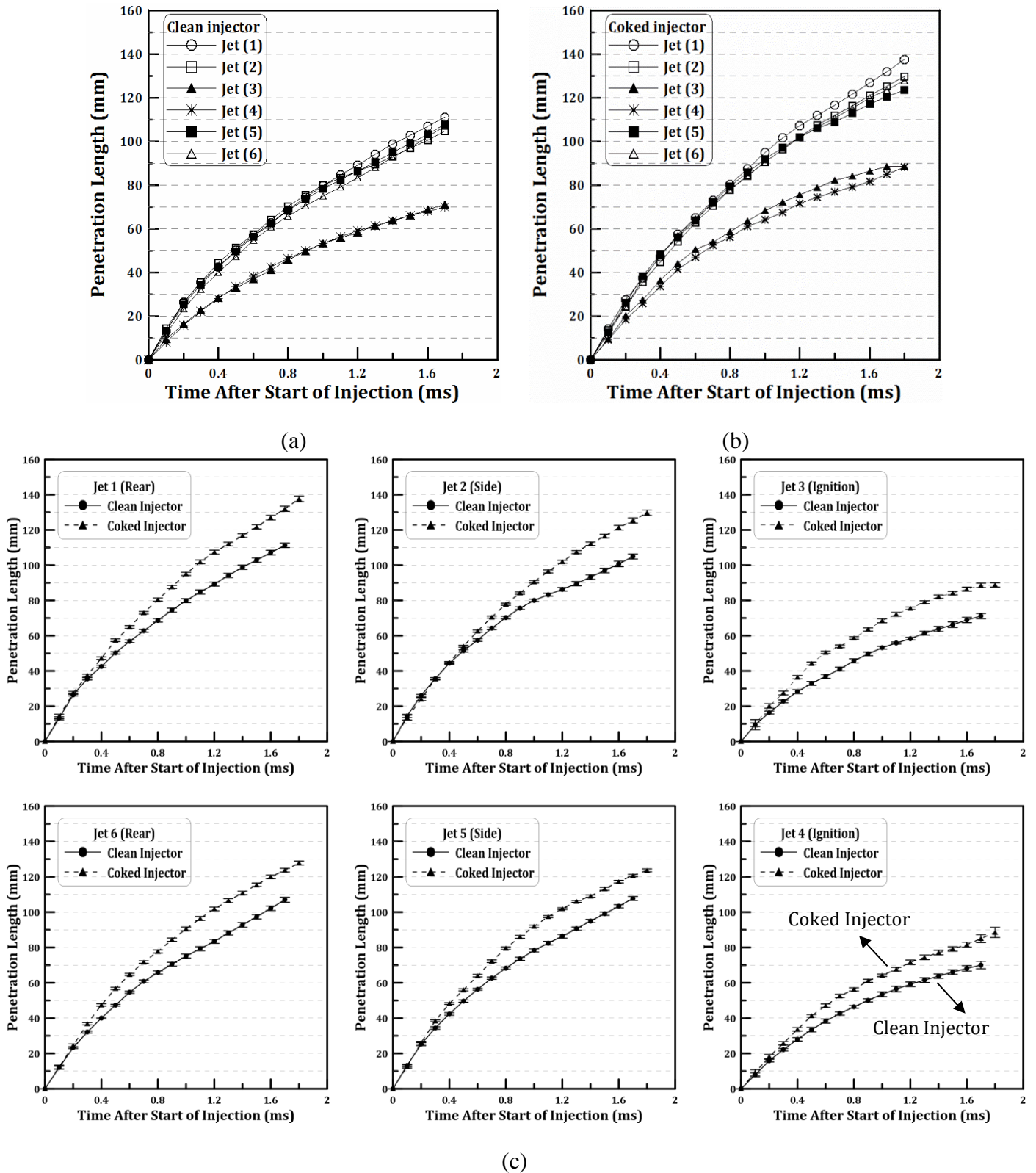
Figure 4.4. Spray penetration length for the fuel plumes of (a) Clean injector, (b) Coked injector and (c) Individual plumes for clean and coked injector for iso-octane fuel at injection pressure of 150 bar and back pressure of 1 bar.

The COV% of the penetration length measurements for the spray jets were calculated and compared for the clean and coked injectors. The COVs% followed the same trend with slightly

higher COVs% values for the coked injector. Figure 4.5 shows the COV% variations for the ignition jets (jet 3) of the clean and coked injector. Both injectors had higher COV% values (10-13%) at the start of injection and were settled to around 2% after 0.4 ms ASOI. Observed higher COV% values at the start of injection had been reported by previous researchers and this could be due to unstable hydrodynamics effects caused by the needle valve opening of the injector [137].
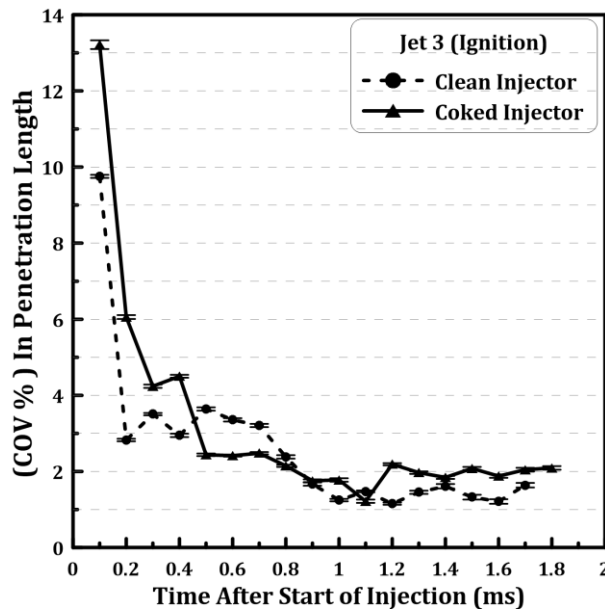
Figure 4.5. The clean and coked injector COV % for the penetration length of ignition jets for iso-octane fuel at injection pressure of 150 bar and back pressure of 1 bar.

To investigate the effect of deposit build-up on plumes' relative angle to the central axis (θ) of the injector, high speed images of spray from side view were taken as shown in Figure 4.6. The coked injectors displayed a clear increase of the plumes' relative angles, when compared to the clean injectors. This was particularly prevalent for ignition jets for which the averaged 3-D angle (θ_{cl}) was measured at 36° for the clean injectors and 45° for the coked injector (θ_{co}). This significant increase in the ignition jets relative angle could cause spark plug fouling by impingement of the spray on the electrodes and poor mixture preparation. Both phenomena increase fuel consumption and engine-out emissions and will be discussed later in this report.
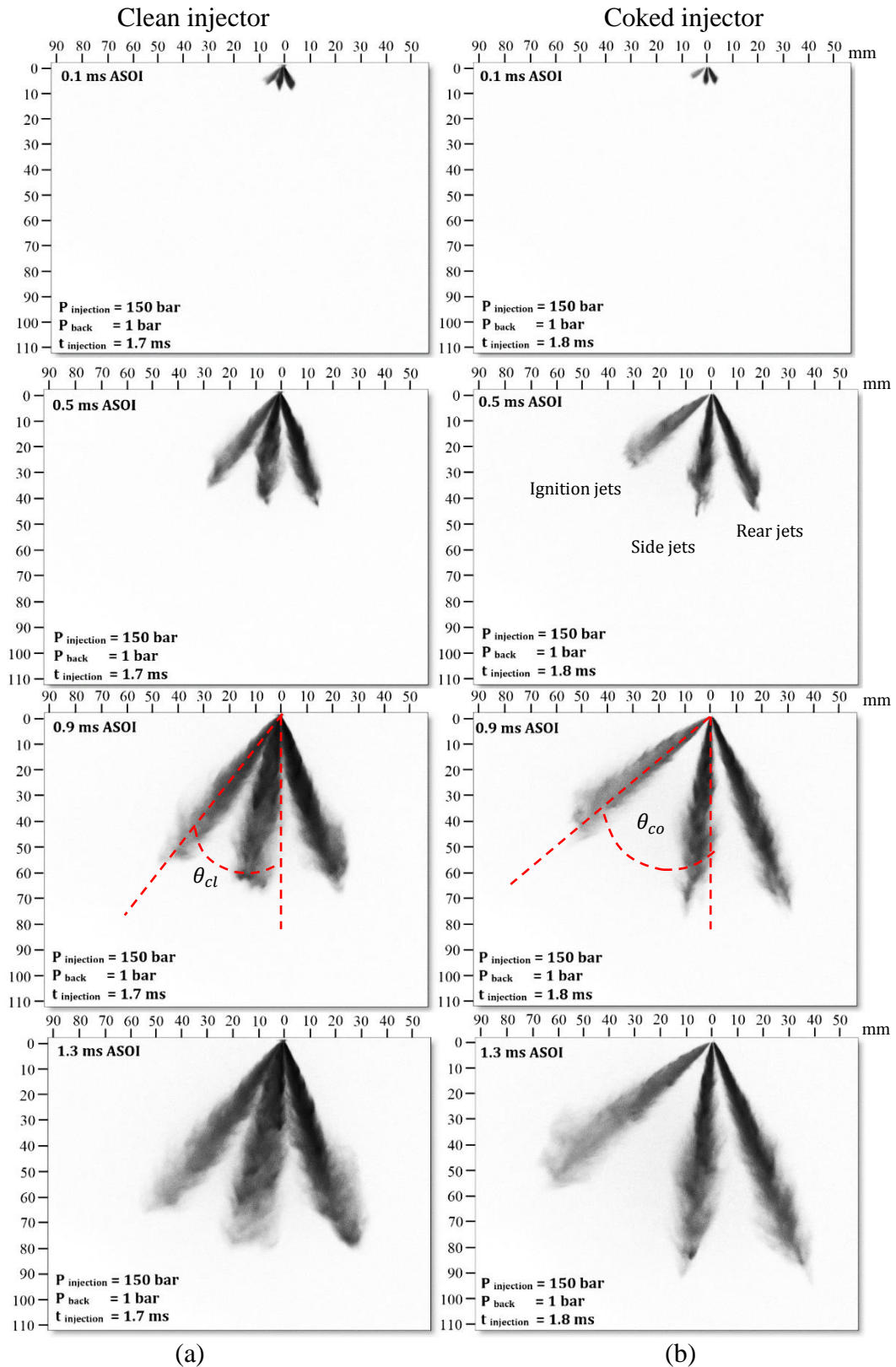
Figure 4.6. Side view of time resolved high speed images of sprays produced by the clean (a) and (b) coked injectors for iso-octane with a frame rate of 10 KHz, resolution of 800 X 800 pixels and magnification of 5.4 pixel/mm.

The calculated averaged values obtained for plumes' cone angles of the coked injectors, indicated that ignition jets had the maximum reduction of approximately 34% and side jets cone angle was reduced by approximately 31%, whilst rear jets had minimum reduction of 25%. The spray pattern was further investigated by the PLIF imaging of the spray footprint. The fuel was a mixture of iso-octane with 3% of 3-pentanone by mass. The laser sheet was first adjusted at 10 mm below the injector tip and moved to 60 mm below the injector tip with 10 mm increments. Figure 4.7 shows the bottom view PLIF footprint of the six spray jets for the clean and coked injectors. The PLIF technique was employed due to the linear proportionality between the fluorescence intensity and fuel concentration [138, 139].

The PLIF images indicated that the clean injectors exhibited larger individual spray plume cone angles with bigger footprints than the coked injectors. Furthermore, the coked injector had distorted, unsymmetrical spray envelopes, where the spray cross-sections were changed from near-circular to narrow ellipses, similar to the cross-section of a fan spray. The footprint of the ignition jets showed significant distortion for the coked injectors' case. These footprints nearly diminished past the axial position of 30 mm, consistent with the observed increase in the plumes angle $\Delta\theta$, as shown in Figure 4.6. The side and rear jets of the coked injector were less affected by coking, where the fuel concentration of spray jets remained high up to approximately 50 mm from the injector tip. The optical test indicated that even a moderate tip coking (e.g. resulting in 5.6% mass flow rate loss) could significantly alter macroscopic behaviours of the spray.

Plume penetration lengths and spray angles are primarily governed by fuel properties [140], injection pressure and temperature [140, 141], injection timing and in-cylinder charge motion [142], and injector nozzle geometry [143, 144]. In our experiments, the variable was injector nozzle geometry. As it was shown in Figure 4.1 deposit can build-up inside the nozzles and

reduce fuel passage area. This not only reduces fuel flow rate but also disturbs the balance between liquid fuel velocity and its turbulence energy. Both of which are governed by the Bernoulli's relation. The fuel penetration length from the injector nozzle to the point of spray breakup is expressed by:

$$l_b = 2a(1.03We^{0.5})ln\left(\frac{a}{\beta_0}\right) \tag{4.1}$$

$$W_e = p_l U^2 \left(\frac{a}{\sigma_t}\right) \tag{4.2}$$

Where a is the diameter of the injected fuel flow, W_e is the Weber number, β_0 is the fluctuation wave vibration amplitude caused by turbulence energy, U is fuel velocity, p_l is fuel density, σ_t is fuel surface tension [145]. The increased plume penetration lengths observed in the images were an indication of the increased fuel velocity. While the injector nozzles internal structure and their positioning are optimised to convert fuel pressure energy into kinetic energy and turbulence energy during cavitation by tracking the bubble dynamics through the injector and transferring the collapsed energy to turbulent kinetic energy, which enhances the primary break up process; the work indicates how these can be affected by deposit build-up inside these nozzles and on the injector tip.
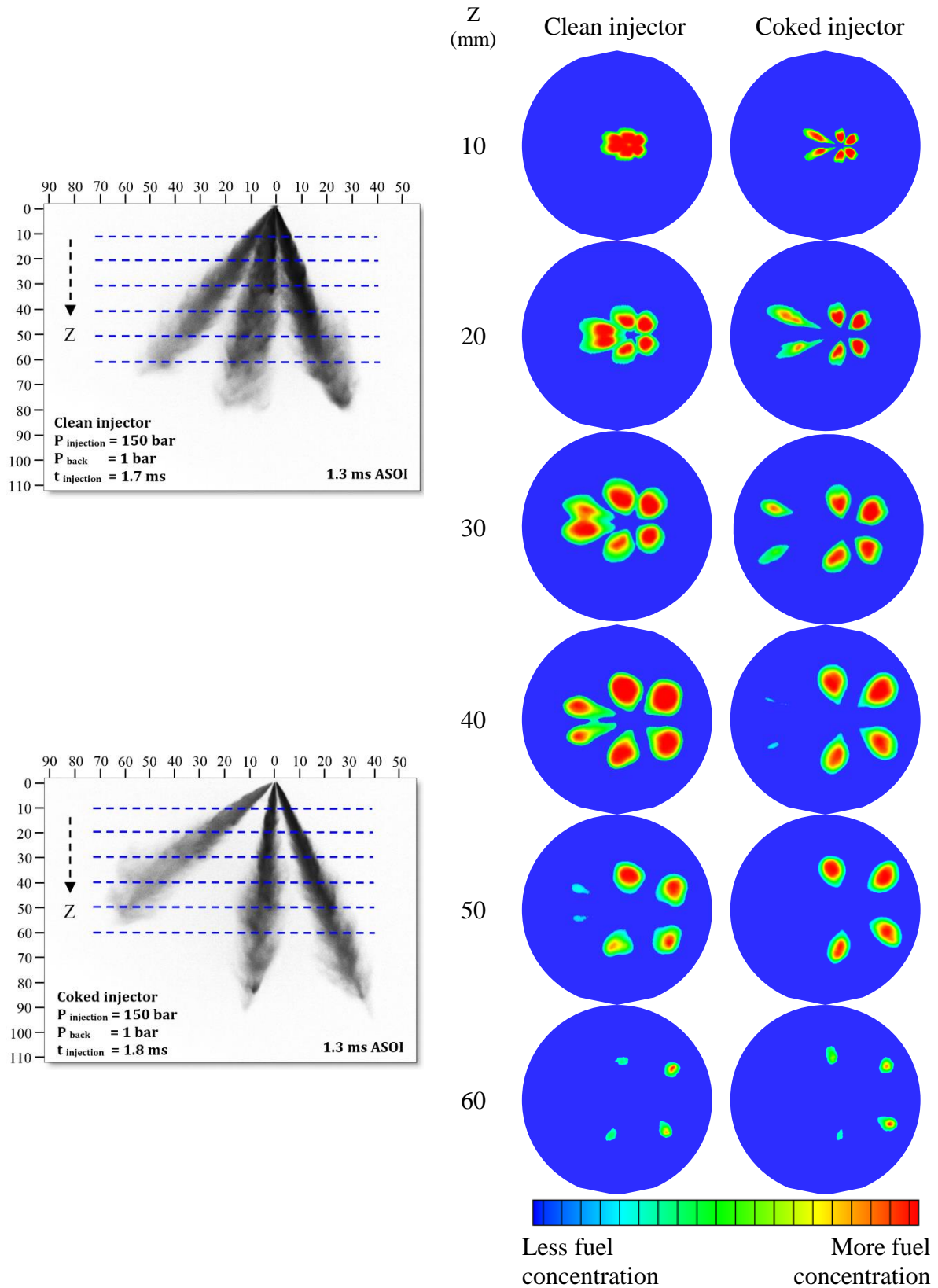
Figure 4.7. PLIF spray footprints of the clean and the coked injectors for iso-octane doped with 3-pentanone (3% by mass)

4.5 Effects of Injector Coking on Fuel Droplet Characteristics

Temporal variations of droplets mean velocities, at 35 mm from the injector tip along the spray centre line, are presented in Figure 4.8. Both individual and mean temporal droplet velocities are shown. The temporal variation of the mean droplet velocity is divided into the leading edge, head (steady) and tail stages. Approximate boundaries of the three stages are marked in Figure 4.8.a. For both the clean and coked injector the same trends of droplet velocity variations were observed at the measuring control volume, 35 mm from the nozzle exit. The leading edge exhibited high initial velocity which decreased abruptly and then increased up to the onset of the head stage. The velocity reached a relatively steady value during the head stage and towards the end of this stage a sharp decrease indicating the start of tail stage was observed. Similar to previous work [146, 147], the boundary between the head and tail stages was set at the point where droplet velocities exhibited a steep negative gradient, and this was regarded as the injector needle closing event.

Analysis of the observed velocity trend could be done by referring to droplet size measurements at the same measuring control volume which are presented in Figure 4.9. The leading edge represented the first group of droplets arriving at the measuring control volume, which had large diameters and low velocities compare to the head stage. The decrease and the consequent increase of droplet velocities can be explained by referring to the Sauter Mean Diameter (SMD) measurements and changes in droplet sizes observed at the early stages of the spray development, see Figure 4.9. The initial reduction in velocities was different from case to case for the clean and coked injectors. It is commonly known that there is residual fuel remaining from the previous injection in the inner hole of the injector, which is responsible for producing initial droplets of a spray [148]. The residual fuel is pushed out of the injector inner hole by the new injected fuel. It experiences less flow resistance as it emerges which results in larger

droplets with higher velocities. The initial SMDs were approximately twice as large as droplets of the head stage, which gives them a relatively large momentum compared to the order of magnitude of the drag force and thus they maintain their high velocity. As the spray developed during the leading edge, droplets sizes were reduced, resulting in lower momentum and drag forces, due to their smaller diameter. However, the comparative magnitude of the momentum and drag forces resulted in lower velocity at the early stage of the leading edge.

Fuel atomization process involves a breakup mechanism that takes place for the first liquid cluster out of the nozzle as it encounters the undisturbed flow field or the stagnant conditions of the surroundings. The first clusters included droplets at its leading edge following by interior droplets. The leading edge droplets transfer their momentum to the air and fast slow down [149]. Whilst, the interior droplets behind the leading edge droplets did not experience a quiescent environment any more, and consequently the leading edge droplets lost their initial velocity faster than the interior droplets by the time they arrive to the measuring control volume. This is why after the initial velocity drop of the residual fluid droplets, a velocity increase was observed up to the head stage. As the interior droplets of the cluster pass through the measuring control volume, the droplet velocity remained constant during the head stage with small stochastic fluctuations. The same initial velocity drop followed by velocity increase phenomena has previously been observed by other researchers, but no explanations were given [150].
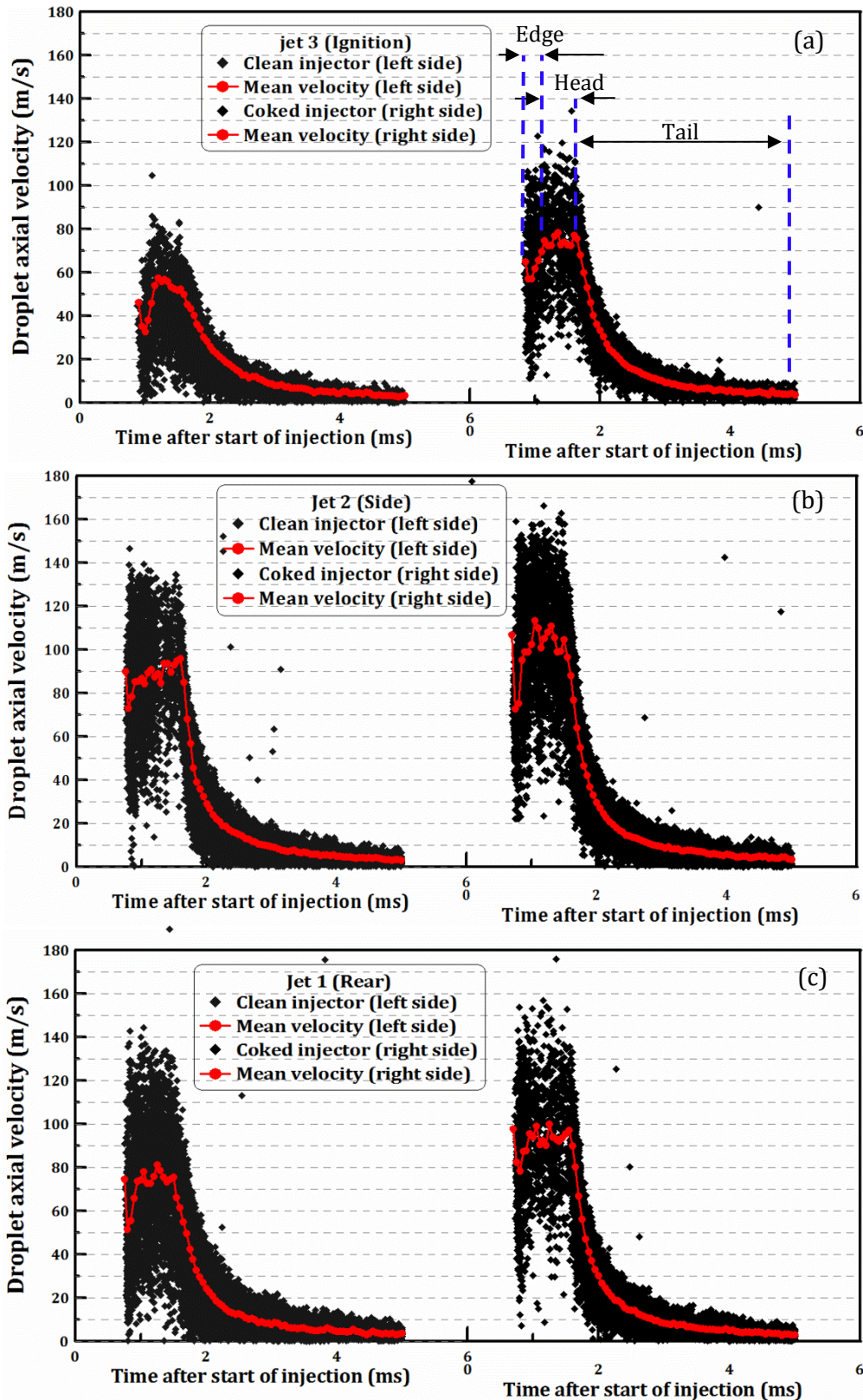
Figure 4.8. Temporal droplet axial velocity and mean droplet velocity for the clean and coked injectors at 35 mm away from the nozzle exit on the spray centre line for (a) Ignition jet, (b) Side jet, (c) Rear jet for iso-octane fuel at injection pressure of 150 bar and back pressure of 1 bar
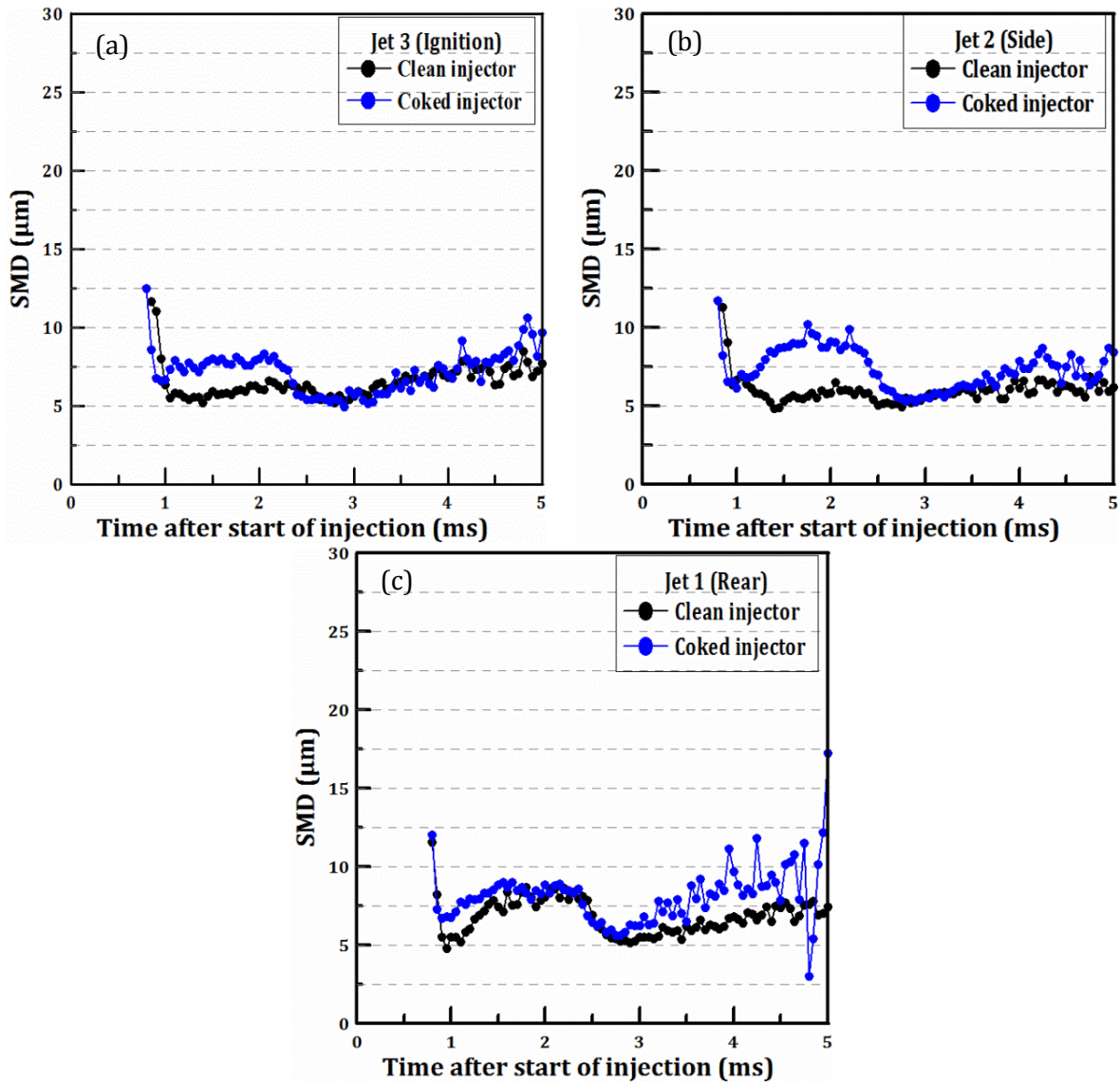
Figure 4.9. Droplet diameter distributions for the clean and the coked injectors at 35 mm away from the nozzle exit on the spray centre line for (a) Ignition jet, (b) Side jet, (c) Rear jet for iso-octane fuel at injection pressure of 150 bar and back pressure of 1 bar

The head stage was characterized by small changes in mean droplet velocities and SMDs, Figure 4.8 and Figure 4.8, respectively. The velocity span, mean velocity and average SMDs of the head stage are summarized in Table 4-2. The axial velocities of individual droplets produced by the plume jets were widely distributed during the head stage. Furthermore, deposits were seen to have a significant effect on mean droplet velocities for each jet. During the head stage, the mean velocity of the of ignition, side and rear jets were increased by 30.8%,

18% and 14% respectively, in comparison to the clean injector. Likewise, the effect of injector deposits on the average SMDs of the plume jets were obvious. It was noticed that for coked injector, the average SMDs of ignition, side and rear jets were increased by 20%, 31% and 8.5% respectively, in comparison to the clean injector. From the aforementioned results, it was clear that the side and ignition jets were more affected compared to the rear jets.

Table 4-2. Velocity span, mean velocity and average SMDs of the head stage for jet 3, jet 2 and jet 1 for the clean and coked injectors at the distance of 35 mm from the nozzle tip

	Jet 3(ignition)		Jet 2(side)		Jet 1(rear)	
Head stage	clean	coked	clean	coked	clean	coked
Velocity span (m/s)	20- 90	20-115	20-140	20-160	20-150	20-150
Mean velocity (m/s)	54	78	90	110	83	97
Average SMD (μm)	5.9	7.5	5.8	8.4	7.5	8.2

The tail stage of the spray included droplets arriving at the control volume after the injector needle started to close and up to its complete closure. It was initiated with a sharp drop in droplet velocities due to reduced injection pressure, Figure 4.8. Individual droplet velocities of the coked injector were more widely distributed compared to the clean injector. The results indicated that the coked injector had larger SMDs and droplet count (Figure 4.9 and Figure 4.10, respectively) during the tail stage. Based on the results presented in Figure 4.9, it was noticed that the SMD values after the initial drop at 1 ms after the start of injection remained almost constant through the head stage; and some increase later during the tail stage due to the reduced injection pressure. The coked injector had higher SMDs during all three stages of injection compared to the clean injector with the exception at the initiation of injection. The coked injector consistently produced larger SMD at the start of injection which indicated that more residual fuel was trapped in the coked injector. Deposit formations inside and on the injector tip provided better support for a larger mass of fuel to remain in the injector cavity,

after the end of the injection. From the aforementioned results, it was clear that the side and ignition jets were more affected in the coked injector compared to the rear jets.

Droplet histograms for the clean and the coked injectors are shown in Figure 4.10 and the cumulative number fraction (CNF) and cumulative volume fraction (CVF) are calculated and plotted against the droplet diameter. CNF is the fraction of droplets smaller than a given droplet and CVF is the volume fraction of all droplets less than the given diameter. A summary of Figure 4.10 results is presented in Table 4-3.
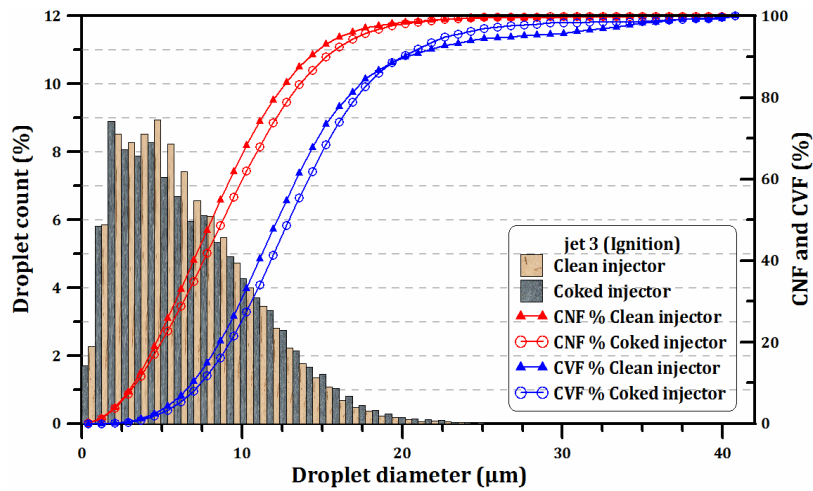
(a)
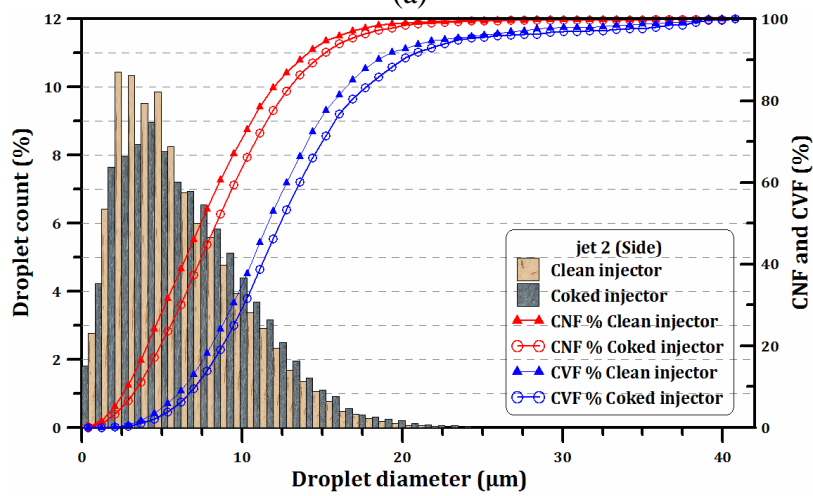
(b)
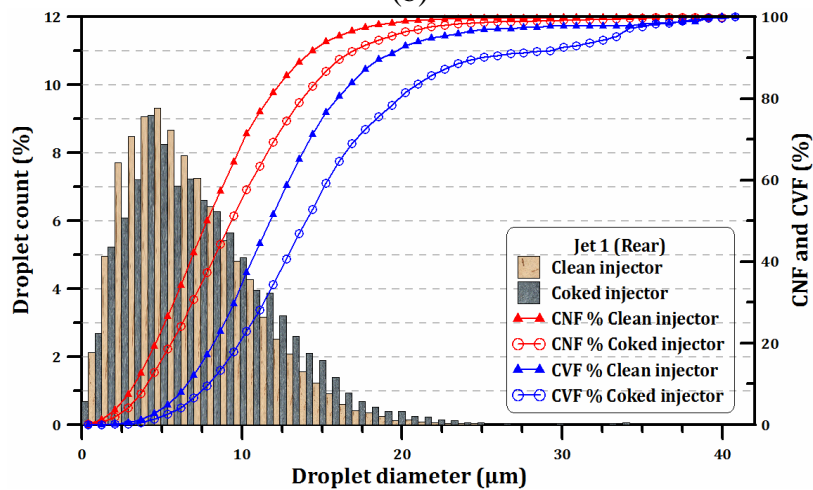
(c)

Figure 4.10. Droplet histograms, cumulative number fraction (CNF) % and cumulative volume fraction (CVF) % for the clean and coked injectors at the distance of 35 mm from the nozzle tip for (a) Ignition jet, (b) Side jet, (c) Rear jet for iso-octane fuel at injection pressure of 150 bar and back pressure of 1 bar

Table 4-3.Cumulative number fraction (CNF) % and cumulative volume fraction (CVF) % at different droplet size diameter of Jet 3, Jet 2 and Jet 1 for the clean and coked injectors at the distance of 35 mm from the nozzle tip

|		Jet 3		Jet 2		Jet 1	
		clean	coked	clean	coked	clean	coked
D< 5 μm	CNF%	25.8	22.7	31.6	23.52	26.5	18.6
	CVF%	4.3	3.3	5.8	3.82	4.9	2.5
D< 10 μm	CNF%	68.2	62	72.9	66.09	71.3	57.7
	CVF%	33.1	27.5	37.7	31.67	37.3	23
D< 15 μm	CNF%	93.1	90	94.7	91.87	93.9	89.6
	CVF%	73.5	68.4	77.7	71.44	76.6	64.7

For the number of droplets with diameters less than 5 μm, the rear jet of the coked injector showed a 29.8% decrease compared to the clean injector, whilst the side and the ignition jets showed decreases of 25.6% and 12% respectively. The difference between CNF% and CVF% for the clean and coked injectors was reduced with the droplet diameter increase. Number of droplets which had diameters less than 15 μm for the rear jet of the coked injector showed a 5% decrease, whilst the side and ignition jets showed a decrease of 3% and 3.5% respectively. At 35 mm from the injector tip, it was observed that droplets of the coked injector were larger compared to the clean injector for all spray jets investigated.

4.6 Effects of Injector Coking on Combustion

In-cylinder pressure traces of a single cylinder optical engine obtained from averaging 300 consecutive cycles for the clean and coked injectors are shown in Figure 4.11 (TDC is referred to 0 CAD). It was observed that both injectors had the same in-cylinder pressures up to TDC and afterward, the clean injector showed slightly higher pressures. The pressure difference between the clean and coked injectors had its maximum value where the in-cylinder pressure peaked. The IMEP of the clean injector was slightly higher than of the coked injector with better stability (lower coefficient of variation (COV) of Indicated Mean Effective Pressure

(IMEP)). Considering that the injection pulse width of the coked injector was adjusted to compensate for the fuel flow reduction, the lower in-cylinder pressure and lower calculated IMEP of the coked injector indicated possibility of slower combustion. The coked injector demonstrated a Brake specific consumption (BSFC) of 269.2 g/Kwh, whilst the BSFC for the clean injector was 262.7 g/Kwh, with a decrease of ≈ 2.5 % compared to the coked injector.

Figure 4.12 shows the Mass Fraction Burned (MFB) curves, calculated from the averaged in-cylinder pressure data for the clean and the coked injectors. It was observed that the burning velocity was slightly faster for the clean injector compared with the coked injector. In order to investigate the difference more clearly, the Heat Release Rate (HRR) characteristics were plotted (shown in Figure 4.13) where clean injector demonstrated slightly higher values compared with the coked injector. Furthermore, the heat release rate for clean injector started rising earlier and the peak of HRR shifted slightly towards TDC compared to that of coked injector. This suggested a better mixture preparation from the clean injector which led us to the PLIF measurements of in-cylinder charge stratification presented in next section.
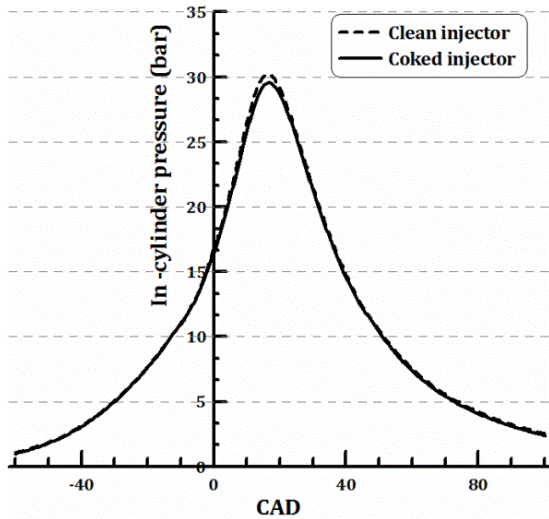
Figure 4.11.In-cylinder pressures vs. crank angle using gasoline with engine speed of 1200 rpm, ignition timing of 30 CAD BTDC, injection pressure of 150 bar, injection timing of 280 CAD BTDC and IMEP of 5 bar
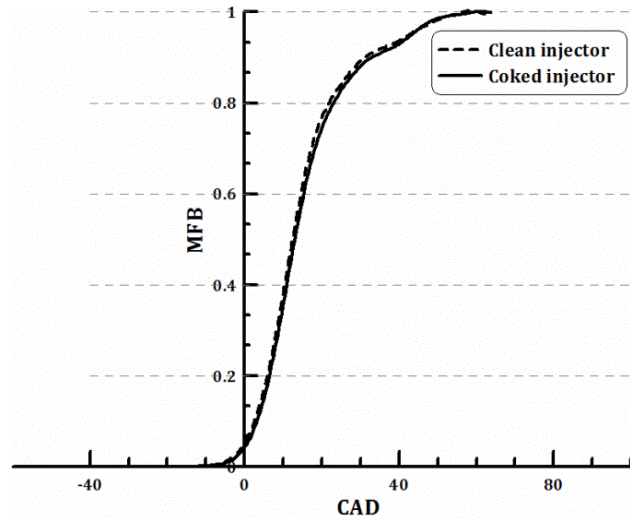
Figure 4.12.MFB vs. crank angle using gasoline with engine speed of 1200 rpm, ignition timing of 30 CAD BTDC, injection pressure of 150 bar, injection timing of 280 CAD BTDC and IMEP of 5 bar
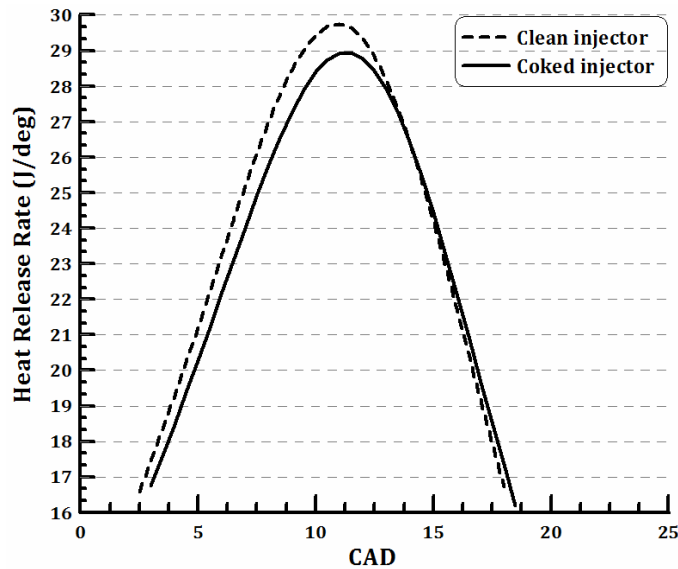
Figure 4.13. HRR vs. crank angle using gasoline with engine speed of 1200 rpm, ignition timing of 30 CAD BTDC, injection pressure of 150 bar, injection timing of 280 CAD BTDC and IMEP of 5 bar

High-speed imaging of combustion was carried for qualitative comparison of impacts of injector deposit. As in previous measurements the injection pressure was set at 150 bar, injection timing at 280 CAD BTDC and ignition timing at 30 CAD BTDC, at stoichiometric condition (λ=1). Figure 4.14 and Figure 4.15 present combustion images from 10 CAD after

ignition or Start of Combustion (SOC) to 80 CAD ASOC. In conventional PFI spark ignition engines, flame is classified as a premixed (fuel and oxidizer are uniformly mixed together prior to ignition), turbulent (due to in-cylinder charge turbulent flow through the flame) and unsteady (as flame structure and motion change with time) [151]. For the GDI engines, under certain operating conditions, we encounter partially-premixed flames and diffusion flames. Due to the presence of fuel in liquid phase instead of gas phase or the presence of a liquid fuel film of a deposited on the piston or head surface, the diffusion flame will occur [152]. The diffusion flame is distinguished with its high-luminosity and yellow colour compared to low-luminosity UV and blue radiation of the premixed flame. The small bright spots in enflamed areas of Figure 4.14 and Figure 4.15 indicate oxidation of soot particles during the main combustion. The relatively large and bright area near the injector (in Figure **4.15**) indicates diffusion flame. While the premixed flames are extinguished around 60 CAD ASOC for both the clean and coked injectors; the diffusion flame started ~40 CAD ASOC and continued until ~80 CAD ASOC for the coked injector only. It has been shown that fuel pyrolysis by thermal decomposition forms a gum type deposit inside the injector nozzles and on the injector tip [153]. As the deposit layer forms on the injector tip, it absorbs more fuel in the course of fuel injection event. This fuel is then released after the premixed flame propagation and burns as a pool fire [64, 154]. This phenomenon is considered as one of the main PM-generating path in GDI engine
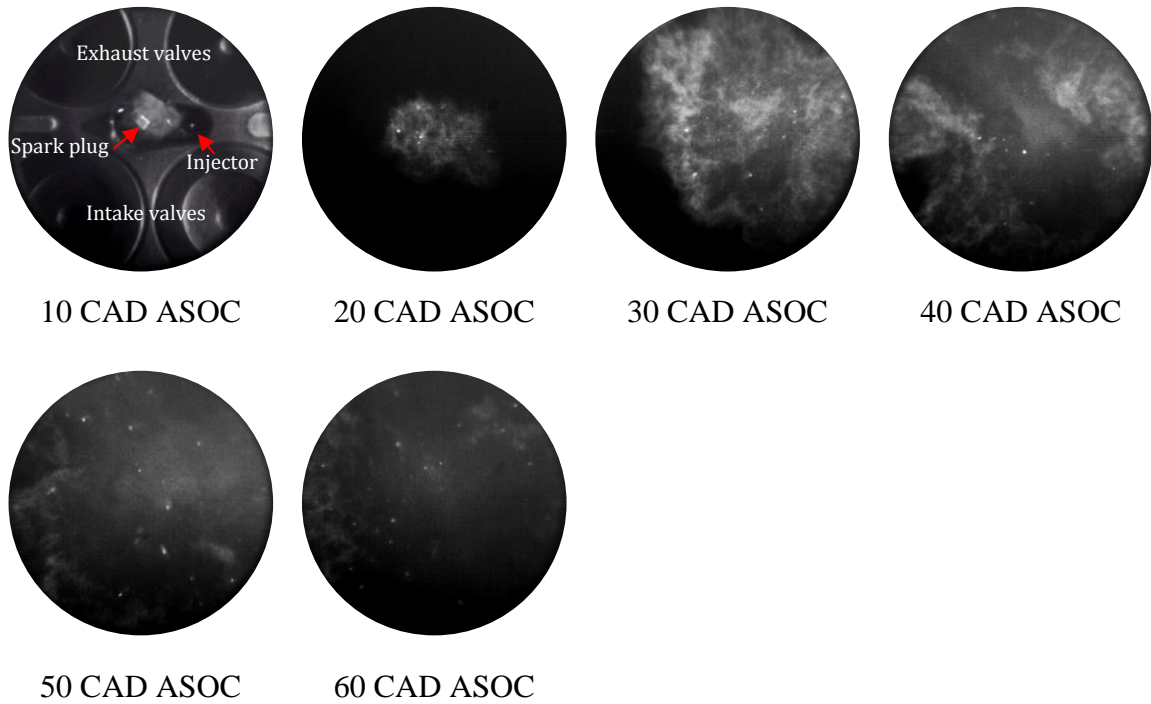
Figure 4.14. Bottom view flame images at different crank angles from the start of combustion for the clean injector at injection timing of 280 CAD BTDC and ignition timing of 30 CAD BTDC.
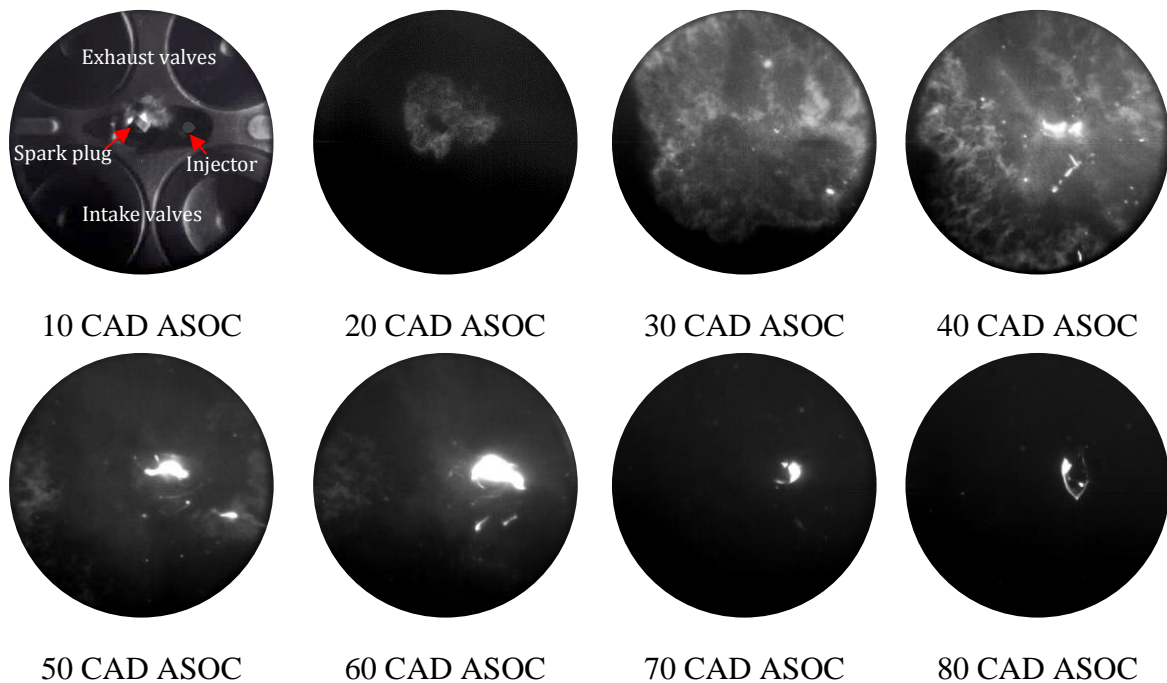
Figure 4.15. Bottom view flame images at different crank angles from the start of combustion for the coked injector at injection timing of 280 CAD BTDC and ignition timing of 30 CAD BTDC.

4.7 Effects of Injector Coking on In-cylinder Charge Stratification

In order to investigate effects of injector tip deposit build-up on mixture preparation, the fuel injection timing was swept over a wide window. Start of Injection (SOI) was changed from 320 CAD BTDC to 160 CAD BTDC. The PLIF system was synchronised with the engine crank angle to capture images at 30 CAD BTDC which was the ignition timing. PLIF tests were all performed under motoring conditions at 1200 rpm, with the engine coolant and oil temperature fixed at 90°C and injection pressure of 150 bar. Due to limited optical access for laser excitation, the laser beam was adjusted just below the spark plug ground electrode to cover the area at vicinity of the spark plug where crucial early flame developments take place. This Region of Interest (ROI) in PLIF images is shown in in Figure 4.16. The ROI consisted of 124,800 pixels (480×260) equivalent to an area of 37x20 mm^2 (with imaging resolution of ~13 pixels/ mm). PLIF image processing steps for the charge stratification study and cyclic variation are illustrated in Figure 4.17. For each test point, two sets of 100 background and 100 DI images were captured. For the background images laser was switched on but with no fuel injection. For the 'DI images' the direct injector was switched on. In addition, 100 'PFI images' with the port fuel injection (and no direct injection) at equivalence ratio of one were captured to correct laser beam profile and its attenuation across the combustion chamber. In the linear regime, the LIF signal is given by equation 4.3 [155],

$$S_f = \frac{E}{hcv} V_e \left[\frac{X_{tr}P}{k_bT} \right] \sigma \phi \frac{\Omega_c}{4\pi} \eta_c \qquad (4.3)$$

where S_f is number of photons incident per pixel at detector or photocathode of an intensified camera [photons/pixel], E is incident laser energy fluence [J/cm^2], h is the Planck's constant [Js], c is the speed of light in vacuum [cm/s], v is spatial frequency of the incident laser radiation [cm^{-1}], V_e is excited volume [cm^3], X_{tr} is tracer mole fraction, P is total pressure

[MPa], K_b is the Boltzmann constant, T is temperature [K], σ is absorption cross section [cm^2], ϕ is fluorescence quantum yield (FQY), Ω_c is collection solid angle of the optics used for imaging the fluorescence, and η_c is transmission efficiency of optics and filters used in the imaging setup [155]. As both PFI and DI images were captured during motoring run, for images taken at same crank angle, in-cylinder pressure and temperature values were the same. Assuming insignificant variation in laser pulse energy between two sets of data and a homogeneous mixture for the PFI images; by dividing the DI images by their corresponding PFI images (as it is indicated in the PLIF data processing algorithm), the LIF ratio signal represents spatial distribution of the tracer (mixed with fuel) inside the cylinder;

$$\frac{S_{f2}}{S_{f1}} \propto \frac{X_{tr\_2}}{X_{tr\_1}} \qquad (4.4)$$

(a)   (b)
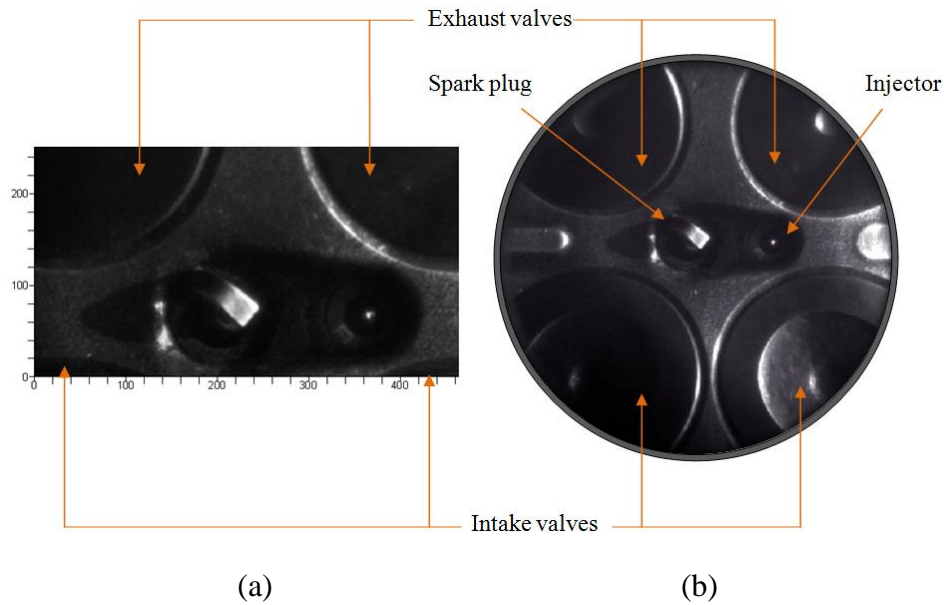
Figure 4.16. (a) Selected Region of Interest (ROI), (b) Combustion chamber view at 30 CAD BTDC
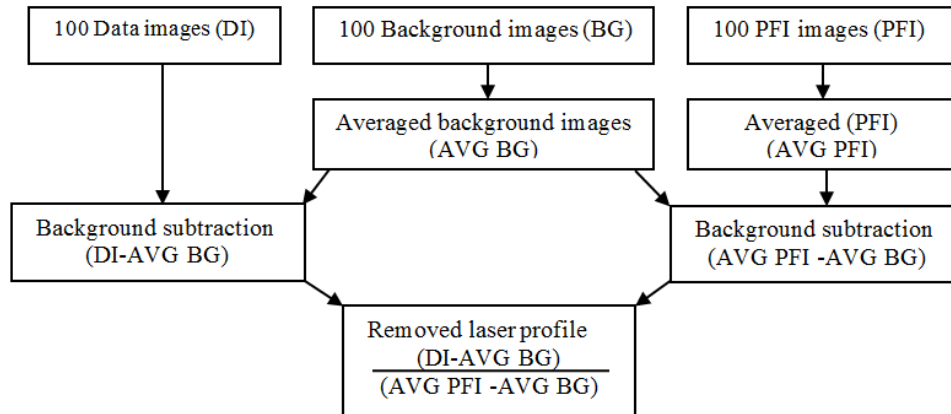
Figure 4.17. PLIF Image processing algorithm

The equivalence ratio distributions for the clean and coked injectors at 30 CAD BTDC over the SOI sweep window, are presented in

Figure 4.18. For early injections at 320 CAD and 280 CAD BTDC, a relatively homogeneous mixture with minimum variation in fuel concentration was formed. Equivalence ratios near the spark plug were in the range of 0.9 to 1.2 which were suitable for ignition. For the SOI at 240 CAD and 200 CAD BTDC a typical stratified mixture was observed. Charge stratification was more significant for the coked injector. The equivalence ratio near the spark plug for the clean injector was in a range of 0.9 to 1.3, whilst for the coked injector was in a range of 1.4 to 1.8. This can promote formation of the particulate matter precursors. For the SOI at 160 CAD and 120 CAD BTDC several rich areas covered the left side of the ROI for both the clean and coked injectors with very higher fuel concentration zone near the exhaust valves. In order to statistically evaluate the charge distribution for different injection timings, Coefficient of Variation of Spatial Light Intensity Distribution (COV of SLID) for the selected region of interest (ROI) of 100 images (one per cycle) were calculated. As the LIF signal intensity is a function of dopant concentration, the spatial distribution of light intensity on the camera sensor represents in-cylinder charge stratification. By calculating the standard deviation of pixels' intensity and normalizing them by the mean intensity value of the ROI for each individual

image, an independent value of COV of SLID was obtained which was used for comparison of different injection timings.
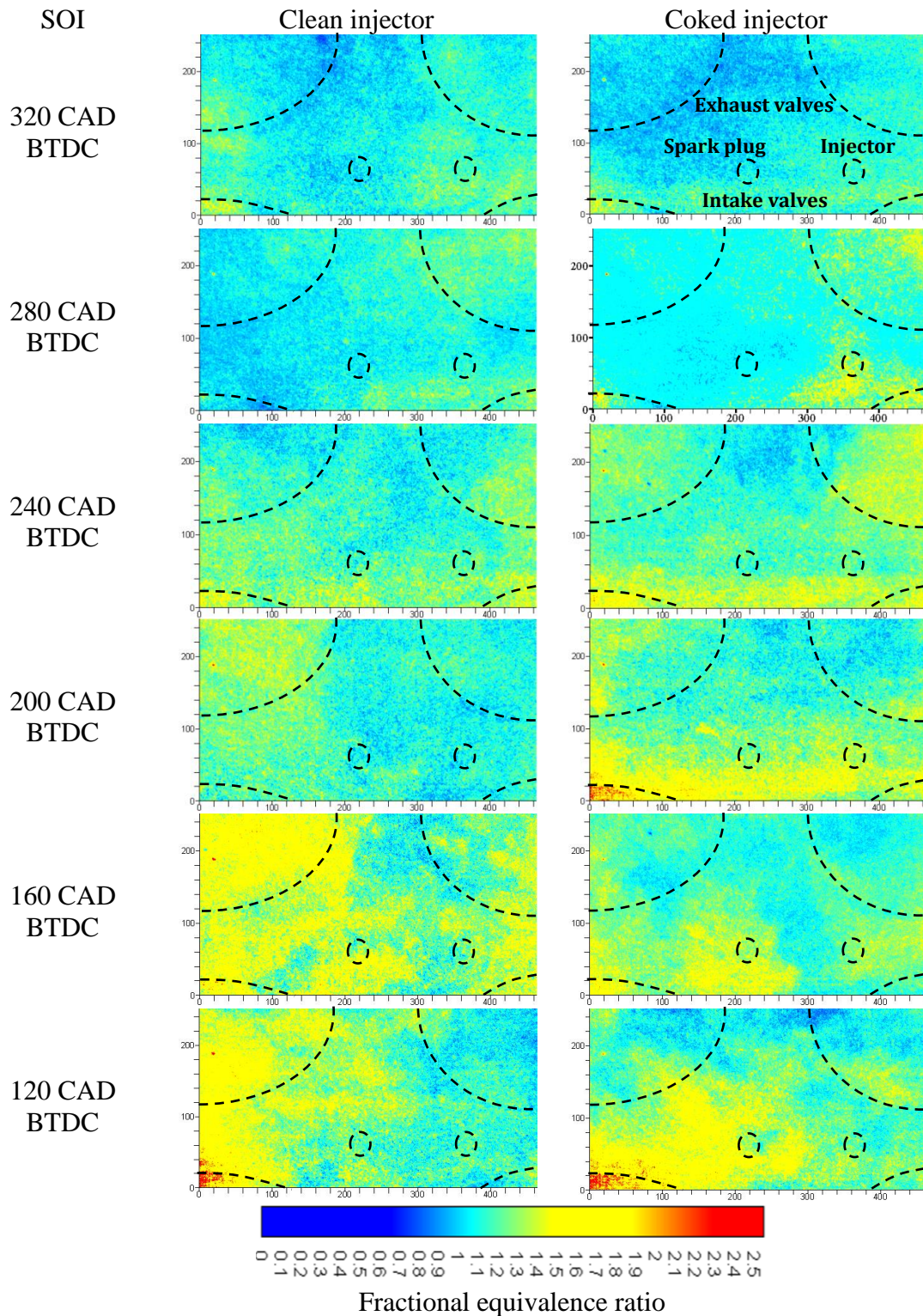
Figure 4.18. In-cylinder fuel distribution over the SOI sweep window for the clean and the coked injectors for iso-octane doped with 3-pentanone (3% by mass) and injection pressure of 150 bar.

As it is shown in Figure 4.19 the coked injector had higher variation of COV of SLID, indicating higher in-cylinder charge stratification as a result of poor mixture preparation. For the both injectors, the highest COV of SLID value was observed for the latest injection at 120 CAD BTDC. For the clean injector, the COV of SLID remained relatively low for the SOI sweep between 320 CAD to 200 CAD BTDC. Furthermore, during the PLIF image processing, the mean intensity value of the ROI of each individual image was calculated and averaged over 100 images. The mean intensity value was converged to the calculated mean intensity of the 100 images after 46 images. Then the standard deviation of the individual image mean intensity was normalized by the mean intensity value of 100 cycles captured. At each injection timing, this additional processing was employed to obtain the repeatability of stratification effect during the captured 100 cycles, instead of evaluating the stratification for individual cycle only. Set out in Figure 4.20 are corresponding results comparing the clean and the coked injectors over the range of injection timings. This statistical analysis of PLIF images indicated higher degree of cyclic variation for the coked injector which was consistent with COV of IMEP data from firing tests which is presented in Figure 4.21 and is discussed in the following paragraph.

In order to investigate these findings and correlate the PLIF work with the combustion data, additional tests were carried out in firing cycles with fixed injection pulse width, ignition timing and throttle position over the SOI sweep window. These parameters were fixed to the values required to maintain a load of 5.1 bar IMEP for SOI at 280 CAD BTDC and ignition at 30 CAD BTDC. Although this resulted in load and stability drift across the injection timings, but the fixed injection quantity and throttle position were required to eliminate influence of fuel concentration and charge motion when compared with the PLIF images. Figure 4.21 shows the effect of injection timing on the engine load and stability (COV of IMEP) for the clean and the coked injectors, where similar trends of cyclic variation as a function of injection timing was observed in both engine firing data and PLIF motoring images. Cyclic variations in the

combustion process are caused mainly by the variations in mixture motion within the cylinder at the time of spark from cycle-to-cycle. The coked injector consistently resulted in higher COV of IMEP for the entire range of equivalence ratio tested over the SOI sweep window, except at SOI of 120 CAD BTD. This could be due to the significant charge inhomogeneity associated with the coked injector
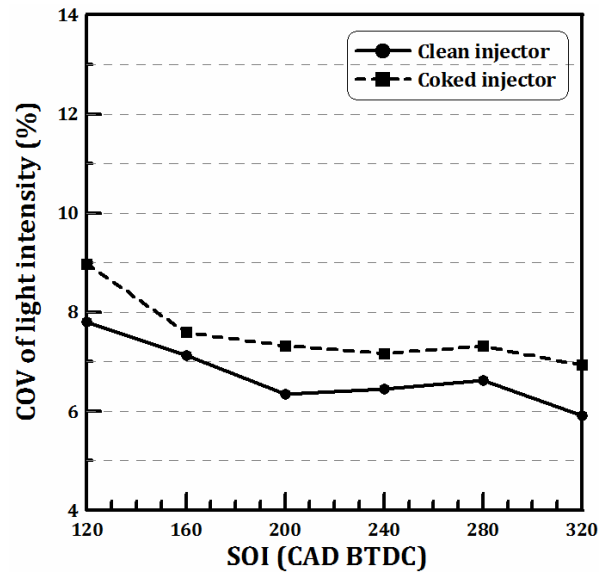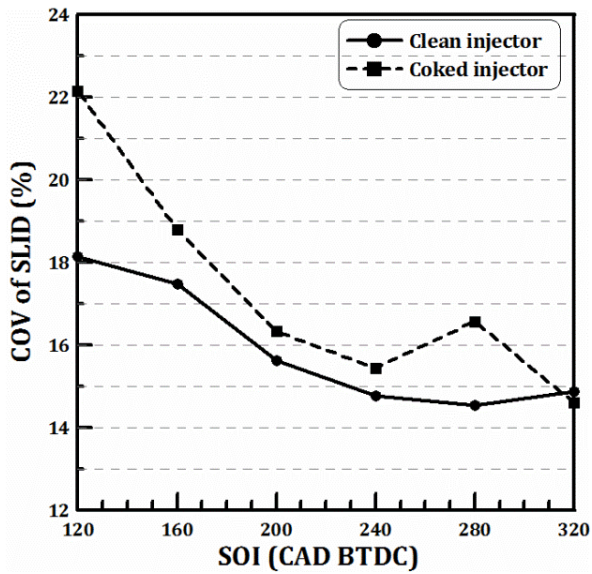
Figure 4.19. Degree of in-cylinder charge stratification calculated from PLIF images over the SOI sweep window

Figure 4.20. Degree of cyclic variation calculated from PLIF images over the SOI sweep window
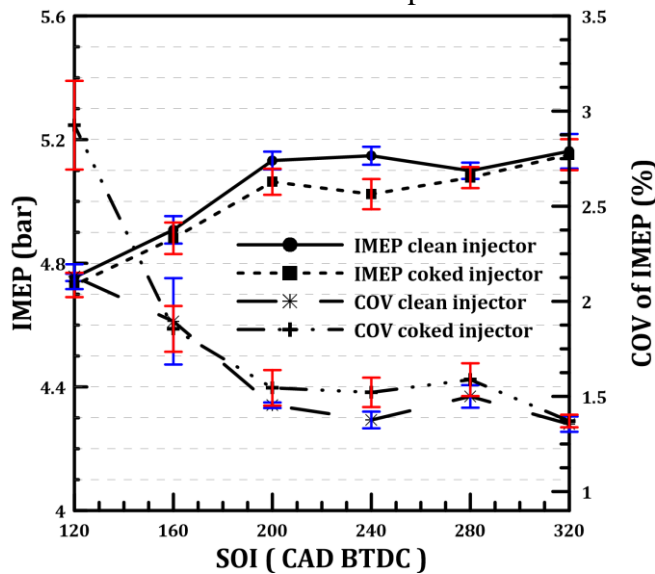
Figure 4.21. IMEP and COV of IMEP over the SOI sweep window using gasoline with engine speed of 1200 rpm, ignition timing of 30 CAD BTDC and injection pressure of 150 bar.

4.8 Effects of Injector Coking on Engine-out Emissions

Emissions of GDI engines depend strongly upon the fuel delivery system including both hardware and control strategy. In this work, the injector condition and SOI timing were examined in a single cylinder thermal engine. Figure 4.22 presents HC emissions for the (ULG95) at 150 bar injection pressure and different injection timing for the clean and coked injectors. The HC emissions were measured using a Horiba MEXA-7100DEGR gas analyser with a resolution of 1 ppmC. The coked injector had higher HC emissions for all injection timings compared with the clean injector with highest value at 120 CAD BTDC SOI. These were 7%, 5.5%, 4%, 7.3% and 8% at 320, 280, 240, 200 and 160 CAD BTDC, respectively, while at 120 CAD BTDC, there was a 15% increase in HC emissions from the coked injector. The higher HC levels of the coked injector were linked to: (a) poor fuel atomization and the increased plume penetration lengths which give high possibility for more fuel impingement on the piston surface and the liner [4], (b) poor fuel/air mixing characteristics and the higher number of locally rich areas, (c) fuel absorbed by the deposit layer formed on the injector tip that is realised after the main combustion and partially burns in diffusion flame.

The DMS500 Fast Particulate Spectrometer was employed to evaluate the real-time measurements of particle mass, number and size spectrum in a range of 5 to 1000 nm. The device charges the particle with a positive charge approximately proportional to the particle's surface area. The repulsion force between the positive charge particles and positive high voltage electrode employed to direct the particles towards the electrometer detector, which consequently used to calculate the particle size/number spectrum in real time. The Heated Sample Line was used to connect directly between the engine exhaust flow near the exhaust port and the DMS500. Two stages of dilution were used for the sampling system. The primary

dilution was carried out to dilute the particles using metered compressed air to provide a 5:1 dilution factor. The sample flow rate was 7.6 l/m and heated up to 150^0c to eliminate any condensation of the particulates. The second diluter was implemented to keep a good signal to noise ratio by using the rotating disk type. This diluter adjust the dilution factor between 1:1 and 20:1, in order keep particulate number concentration in a range of 0.5% to 5%.

The device has ~10% uncertainty in particle number measurement over the full spectrum. Figure 4.23 presents total PN concentration over the SOI sweep window for the clean and coked injectors. For all the injection timings the coked injector consistently had higher PN concentration compared to the clean injector. Higher PN levels were observed at early injection of 320 CAD BTDC. This could be attributed primarily to the high possibility of liquid fuel impingement associated with early fuel injection timing on the piston bowel [156]. This will generate more liquid fuel that is not vaporized totally resulting in improper air/fuel mixture prior to the start of combustion. As a consequence, higher PN emissions will be produced due to the local fuel-rich combustions or even pool-fires that could occur near the piston. At early injection, the coked injector had higher PN compared to the clean injector due to the long penetration length and fuel rich mixture region around the injector, shown in Figure 3.18, which led to more diffusion flame and consequently increased the soot formation and PN emissions. At 320 CAD BTDC, the coked injector had an increase in PN emissions of 4.63% compared to the clean injector. As the injection timing was retarded to 280 CAD BTDC the total PN was decreased for the clean and coked injector, the coked injector had an increase in PN emissions of 7.7% compared to the clean injector.

For injection timing of 280 CAD BTDC up to 160 CAD BTDC the total PN trend was almost constant for both injectors, especially the clean injector. At very late injection timing of 120

CAD BTDC the particulate number was started to increase again. This could happen because there was insufficient time and insufficient in-cylinder charge motions to evaporate the liquid fuel film impinged on the piston and prepare a combustible mixture. This interpretation is supported by the observed HC emissions and higher COV of IMEP at 120 CAD BTDC. The coked injector had 2.5%, 7.5%, 3.8% and 7% higher PN at 240, 200, 160 and 120 CAD BTDC respectively, compared to the clean injector.
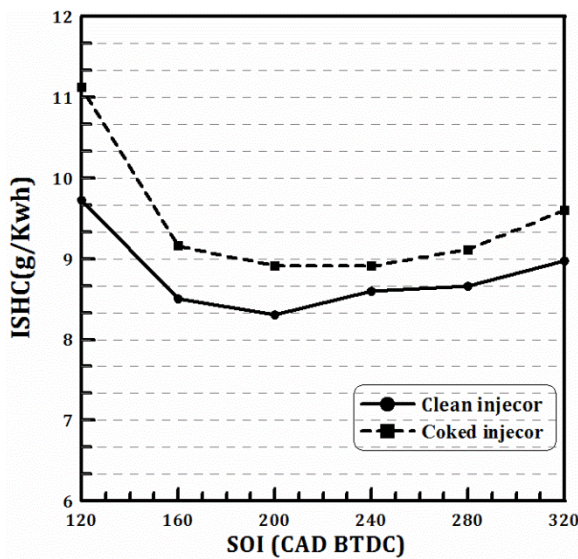
Figure 4.22. HC emissions of the clean and coked injectors over the SOI sweep window
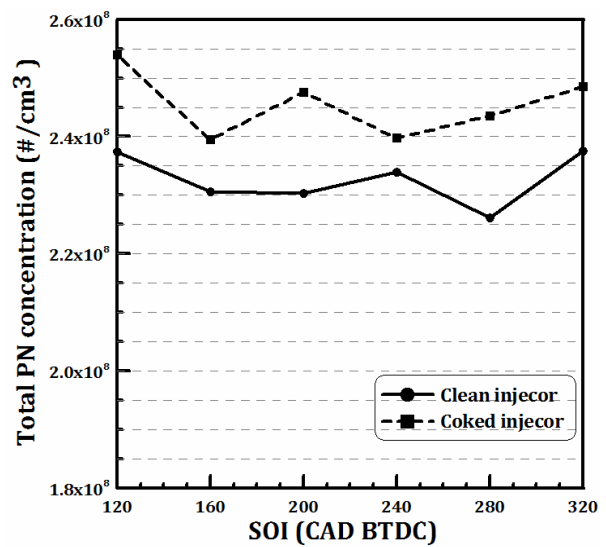
Figure 4.23. Particulate number concentration of the clean and coked injectors over the SOI sweep window

4.9 Summary

Experimental optical and thermal tests were carried out to obtain a comprehensive understanding of gasoline direct injector coking effects on fuel injection, engine performance and emissions. Macroscopic spray characteristics of clean and coked injectors were studied using high-speed imaging and Planar Laser Induced Fluorescence (PLIF) of sprays' foot print. Fuel droplets' size and velocity were characterised with a two-dimensional Phase Doppler Particle Analyser (PDPA). Impact of injector coking on in-cylinder charge stratification was

further investigated by PLIF measurements. Combustion analysis and examination of engine emissions were carried out over a wide SOI sweep window for the clean and the coked injectors. The conclusions drawn from the work are as follow:

1-Injector tip deposit can significantly alter spray structure. For the solenoid actuated multi-hole injectors that were examined in this work, the deposit accumulation effects were not similar for all six nozzles of a single injector. This indicated different levels of deposit formation in each nozzle based on their location and highlighted contribution of injector boundary conditions inside the combustion chamber.

2-In this study, ignition jets were more prone to tip coking while the rear jets were least affected. Plumes penetration length was increased by 25% and 21% for the ignition and the rear jets respectively. Plume cone angles were reduced by 34% and 25% for the ignition and the rear jets respectively. Tip coking also increased plumes relative angle. The relative angle of the ignition jet was changed from 36° for the clean injectors to 45° for the coked injector. Furthermore, the coked injector had distorted and unsymmetrical spray envelopes, where the spray cross-sections obtained by PLIF foot prints were changed from near-circular to narrow ellipses.

3-The PDPA results were in agreement with the high-speed imaging data. The ignition jets were most affected by the tip coking and the rear jets were least affected. The mean droplets' velocity was increased by 30.8%, 18% and 14% for the ignition jet, side jet and rear jet respectively. The droplets size (SMD) was also increased for the coked injectors and droplets axial velocity was more widely distributed compared to the clean injectors. The PDPA data confirmed the assumption that the injector tip coking promotes conversion of fuel pressure into liquid velocity rather than turbulence energy.

4-Combustion images revealed presence of small bright spots around the injector tip indicating injector tip diffusion flame due to deposit build-up. While injection pulse width was adjusted to compensate fuel flow reduction due to deposit build up in injector nozzles, in-cylinder pressure analysis indicated that the coked injectors provided lower in-cylinder pressure and poorer combustion stability.

5-The PLIF image analysis around the injector tip over a wide SOI sweep window was revealed similar findings. The tip deposit formation increased in-cylinder charge stratification and deteriorated repeatability in mixture preparation. Furthermore, the coked injectors consistently showed higher unburned HC emissions for all injection timings compared to the clean injectors, indicating that a portion of injected fuel escaping the combustion.

6-Particulate matter emissions measurements indicated that the tip deposit increased total particulate number concentration for almost all injection timings. The increased PN concentration levels were associated with (a) poor mixture preparations and more locally rich areas (b) altered plume penetration lengths and relative angles and (c) fuel absorption by tip deposit which partially burns in pool fire after the main combustion.

Chapter 5

INVESTIGATION OF INJECTOR COKING EFFECTS ON SPRAY CHARACTERISTICS UNDER DIFFERENT INJECTION PRESSURES

The aim of this chapter is to obtain a comprehensive understanding of gasoline direct injector coking effects on fuel injection mass flow rate and spray characteristics under different injection pressure. Spray and droplet characteristics of a coked injector were compared to those of a clean injector at the atmospheric conditions and investigated using high speed imaging and a Phase Doppler Particle Analyzer (PDPA). X-ray 3D microtomography images were analysed to understand the physical characteristics of injector nozzle deposits.

5.1 Introduction

Injector coking is a common phenomenon observed in fuel injection apparatus, and occurs when chemically degraded components of the fuel and combustion products adhere to the internal surfaces of an injector [157]. Since the fuel nozzle passages are small, injectors are highly sensitive to small amounts of deposits in the critical regions where the fuel is metered and atomized. These deposits once formed, reduce the flow rate delivered for the injection pulse width. Additionally, it also distorts the injection of the fuel spray, hence influencing its shape and penetration length [4]. This has an adverse effect on both the mixture formation and the combustion processes inside the combustion chamber. At the same time the average size of the atomized fuel droplet increases which slows down the process of mixture formation.

Furthermore, the increase in the injector needle motion resistance changes the temporal and qualitative course of opening and closing of the electromagnetic injector against the set controlling impulse [54]. As a result, all the aforementioned phenomena can lead to a reduction in engine efficiency and its performance whilst the exhaust emissions and fuel consumption tend to increase.

The current study mainly focuses on studying the effect of the injector deposits on the mass flow rate under different injection pressure. Likewise, the impacts of the injector deposits on the macroscopic characteristics of the spray, including plume penetration lengths and angles (relative angle and cone angle), droplet size and droplet velocity profiles under different pressure were further investigated. Furthermore, the coked injector was investigated using X-ray 3D microtomography to provide visual scanning of the tip.

5.2 Injector Fouling Cycle and Fuel Flow Rate Measurements

The four gasoline direct injectors used in this study were deliberately coked-up using a specially developed fouling cycle as described in section 4.2. For injector coking the test fuel employed was EN228 consisting of compliant Unleaded Gasoline (ULG95) containing 3.3% Ethanol, 6.1% Ethyl Tertiary Butyl Ether (ETBE) without Deposit Control Additives (DCA) additive. The mass flow rates of the clean and coked injectors were investigated at three different injection pressures of 50, 100 and 150 bar. For each injection pressure, five injection pulse widths ranging from 0.5 to 2.5 ms were selected and the fuel mass of 1000 injections was measured by a digital weighing scale (with a resolution of 0.1 mg).

Measurements were repeated five times and the mean average values were used to calculate the flow rate. The maximum uncertainty of measurements was $\pm$ 0.065 mg/pulse. Correlations

of injector pulse width and fuel mass flow rates are shown in Figure 5.1. For this study, the pulse width of interest was 1ms. At pulse width of 1ms, it was noticed that as the injection pressure increased the mass flow rate losses increased for the coked injector. It was observed at 50 bar injection pressure and 1 ms pulse width that the averaged mass flow rate of the clean injector was 7.7 mg/pulse, whilst for the coked injector 7.1 mg/pulse. This indicated that the coked injectors had ~7.8 % reduction in mass flow rate compared to the clean injectors. As the injection pressure increased to 100 and 150 bar, the averaged mass flow rate of the clean injector was 11 and 13.4 mg/pulse respectively, whilst for the coked injector 10 and 12.1 mg/pulse respectively. This indicated that the coked injectors had ~8.5 % and 9.5% reduction in mass flow rate compared to the clean injectors. Care was taken to maintain consistency between the injectors when taking measurements. Thus, the flow rate measurements were checked to make sure the injectors had not developed new deposits or had deposits washed away during the experiments.

(a)   (b)
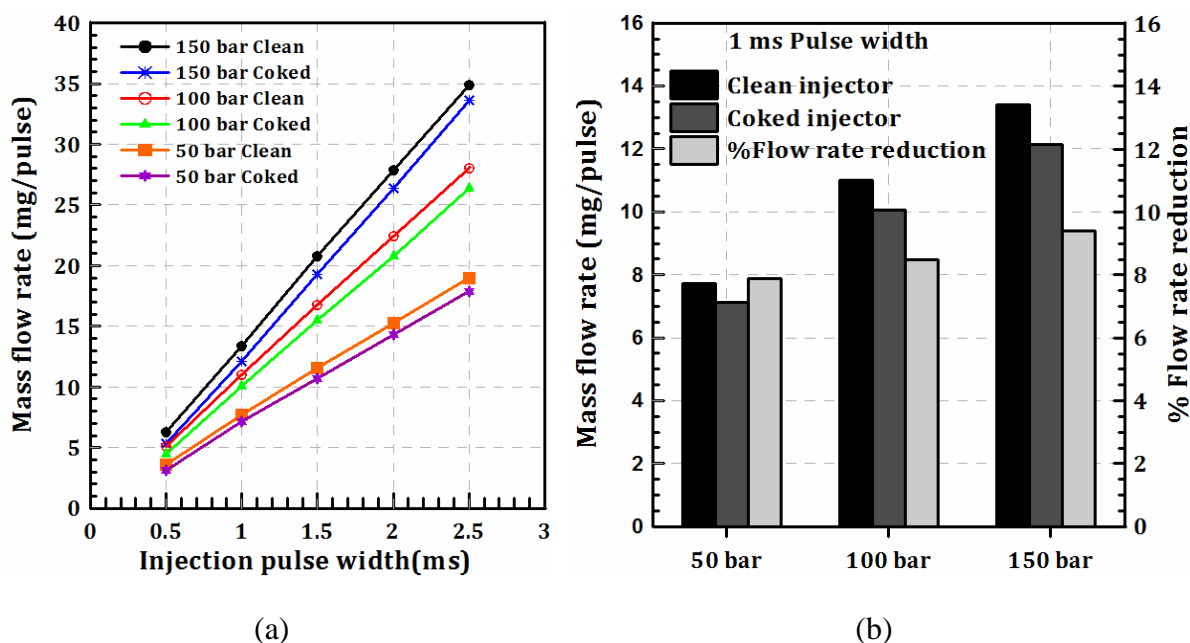
Figure 5.1. (a) Mass flow rate vs. pulse width of the clean and coked injector, (b) mass flow rate of the clean and coked injector and the reduction in mass flow rate of coked injector at 1ms pulse width for different injection pressures of 50, 100 and 150 bar, ambient temperature of 25°C and iso-octane fuel.

5.3 X-ray Analysis

The X-ray images presented in this paragraph were taken by the European Synchrotron Radiation Facility (ESRF, Grenoble, France) to shed more light on the deposits distribution inside the injector nozzles [158]. The same coked injector which had been used in the experimental measurements was sent to the ESRF to be scanned by high-resolution X-ray microtomography. These X-ray images were required to provide more information regarding the deposits formation on the counterbore and internal hole of injector nozzles. These deposits have a direct effect on the subsequent spray development and change the characteristics of the spray itself. The ESRF imaging beam line ID19 [159] was employed for high spatial resolution three-dimensional (3D) tomographic scans of deposits formation along the internal nozzle structures of the clean and coked injectors, see Figure 5.2. The pink beam configuration with an effective energy of 90 keV was utilized for the ID19 to provide the hard X-ray regime with a high photon flux density. It was noticed that deposits (red color) formed extensively through the counterbore for all the six nozzle holes. Likewise, the deposit formation through the injector ignition holes is demonstrated in Figure 5.3. Extensive deposits were observed in external injector holes and these deposits were radially distributed and collected in the shoulder while the deposit formation was reduced in the internal holes of the injector
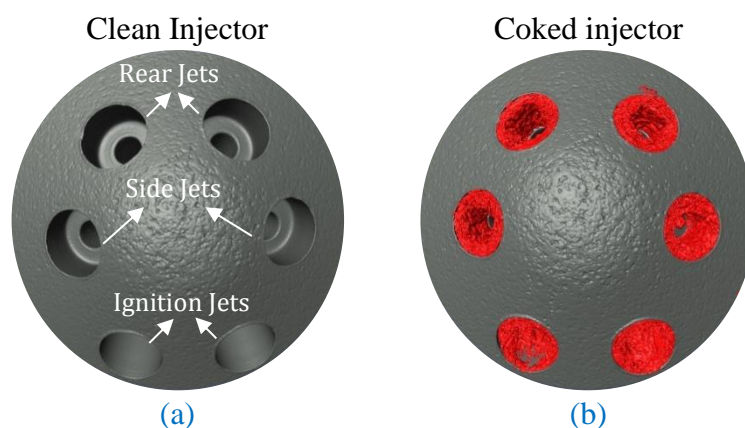
Figure 5.2. X-ray microtomography of (a) clean injector and (b) coked injector, provided by the European Synchrotron Radiation Facility [158]
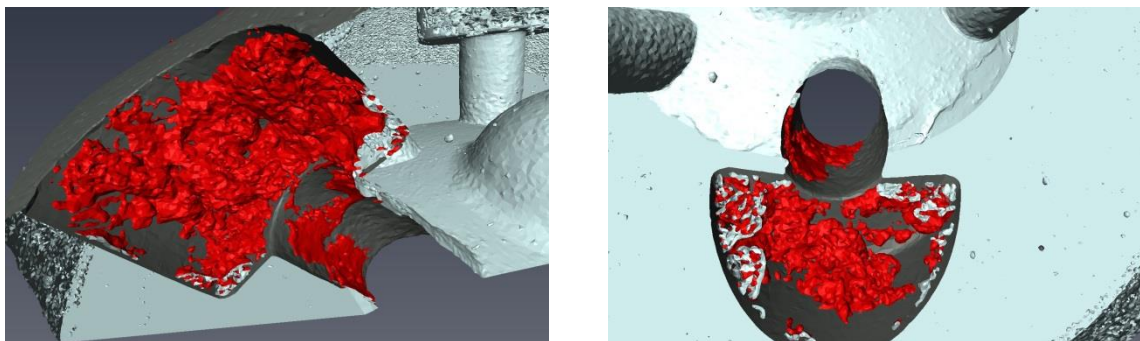
Figure 5.3. X-ray microtomography of individual holes (ignition jets) of coked injector provided by the European Synchrotron Radiation Facility

5.4 Effects of Injector Coking on Macroscopic Spray Behaviour
5.4.1 Bottom View Analysis of the Spray

Figure 5.4 shows images, taken from below, of isooctane spray development at 1ms after the start of injection (ASOI) for the clean and coked injectors. Three injection pressures of 50, 100 and 150 bar were used. As is shown in the images, the spray has a symmetrical pattern. The two front fuel plumes are called 'ignition jets' as they were facing spark plug in the engine. The back plumes are called 'rear jets', while the two plumes on the side: 'side jets'. The images revealed that each of 6 spray jets formed by the coked injector, had significantly larger penetration length and smaller spray plume angle than the clean injector, especially at higher injection pressures.
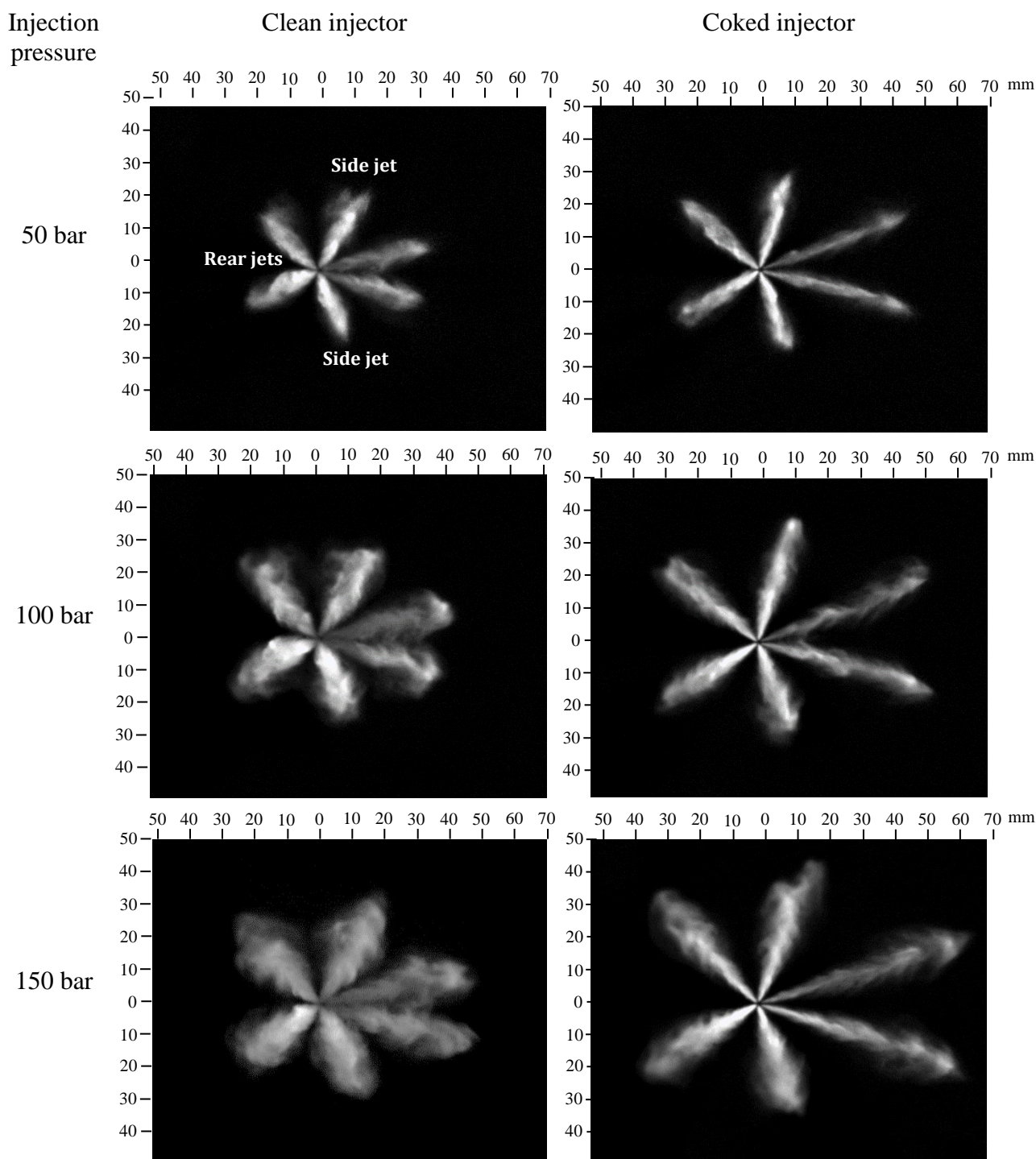
Figure 5.4. Bottom view of time resolved high-speed images of spray from (A) clean injector and (B) coked injector, at different injection pressures of 50, 100 and 150 bar at ambient temperature of 25°C after 1000 µs from SOI for iso-octane fuel with a frame rate of 10 KHz, resolution of 800 X 800 pixels and magnification of 6.8 pixel/mm.

The effect of the injection pressures on the reduction of the plume angle for the coked injector

jets had a step change as shown in Figure 5.5. The measurements were repeated ten times and

116

the averaged values were used to calculate the plume angle. At lower injection pressure of 50bar, the calculated averaged values obtained for the plume angles reduction of the coked injector indicated that rear jets and side jets had the maximum reduction of approximately 25% and 23%, respectively. By contrast the plume angle of ignition jets revealed a minimum reduction of 13%. Further increasing for the injection pressure up to 100bar led to larger magnitude of plume angle reduction of rear and ignition jets for the coked injector of 28% and 17.5% respectively. However, the side jets demonstrated no effect by increasing the injection pressure and the plume reduction remained the same with approximately 23.5%. For injection pressure of 150 bar, the reduction in the plume angle was reduced for the ignition and rear jets with 25% and 10.4% respectively compared to that of 100 bar injection pressure, whilst plume reduction for the side jets was increased up to 25.7%. Increasing the injection pressure results in a substantial increase of the plume spread angle, which utilizing more air entrainment for better mixing of air/fuel mixture [160]. Therefore, the reduction in the plume angle of the ignition and rear jets at a higher injection pressure of 150 bar compared to that of 100 bar could be linked to the increase of the spray plume angle for the clean and coked injector. For each injection pressure, the variation of the plume angle reduction from one hole to another demonstrates that each nozzle contained different levels of deposit formation based on their location and highlighted the contribution of the injector boundary conditions inside the combustion chamber.
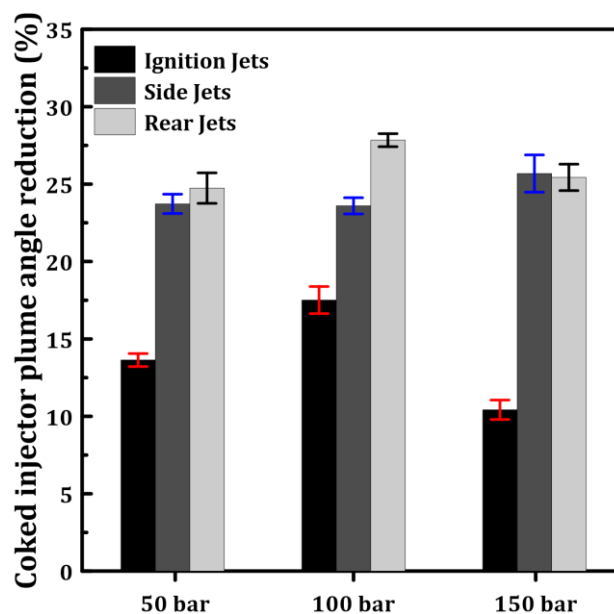
Figure 5.5. Effect of the injection pressure on the plume angle reduction for the coked injector as compared to the clean injector for iso-octane fuel at back pressure of 1 bar and ambient temperature of 25ºC after 1000 µs from SOI.

The effect of the spray plume angle on GDI engine performance was studied by Shiraishi et al. [161]. They revealed that with an increase in the spray plume angle the lean limit is extended due to the improvement in air utilization. Therefore, due to the reduction in the spray plume angle of the coked injector compared to that of the clean injector, inappropriate mixing between the air-fuel could occur and consequently the engine performance would be impaired.

5.4.2 Side View Analysis of the Spray

To investigate the effect of deposit build-up on spray cone angle and the plume relative angle between the plumes, high speed images of spray from side view were taken as shown in Figure 5.6. It was noticed that the spray cone angles of the coked injector are larger than those of the clean injectors. These results were consistent with the findings of with Song et al. [18], who concluded that deposits formed inside the GDI injector nozzle were responsible for increases in the spray cone angle. This was more likely due to the irregular structure of deposits inside the spray nozzle, which could alter the direction of the sprays, causing increased spray cone

angles. For this study, the outer envelope of the spray was used to describe the spray cone angle, which was employed to compare directly between different fuels based on the quantitative measurements of the plume convergence. In order to calculate the spray cone angle precisely, two locations were selected downstream from the nozzle tip. The first position was chosen at distance 2 mm vertically downstream the nozzle tip to eliminate the effects of very near-nozzle spray development. The second position was chosen at distance 12 mm vertically from the upper measurement location.

At a lower injection pressure of 50 bar, the calculated averaged spray cone angle of the coked injector was approximately 12% larger, compared to that of the clean injector. The difference in the spray cone angle between the coked and the clean injectors slightly increased as the injection pressure increased. At 100 and 150 bar, the coked injector demonstrated a larger spray cone angle compared to that of the clean injector with approximately 13% and 14% respectively.

Furthermore, the coked injector displayed an increase in the separation angle between adjacent spray plumes, when compared to the clean injector. This was particularly prevalent at injection pressure of 150 bar for ignition jets for which the plume relative angle θ_{cl} was measured at 37° for the clean injector and θ_{co} was 44° for the coked injector. The plume relative angle (θ) was defined as the angle between the injector centreline and the ignition plume centreline. The plume relative angle of the ignition jets defined by $\Delta\theta = (\theta_{co} - \theta_{cl})$ saw a 19 % increase for the coked injector. Reducing the injection pressure to 100 and 50 bar almost had no effect on the separation angle between adjacent spray plumes of the clean and coked injectors. The enlargement of the spray cone angle and the separation angle between the plumes either may aggravate the collision of fuel against the cylinder wall or could cause spark plug fouling by

impingement of the spray on the electrodes [4, 162], causing a poor mixture formation near the spark plug and resulted in excessive values of COV of IMEP [163]. Consequently this increases soot particles [164] and unburned hydrocarbon [165] emission. Additionally, the coked injector consistently had smaller plume angles and longer penetration length compared to that of the clean injector.
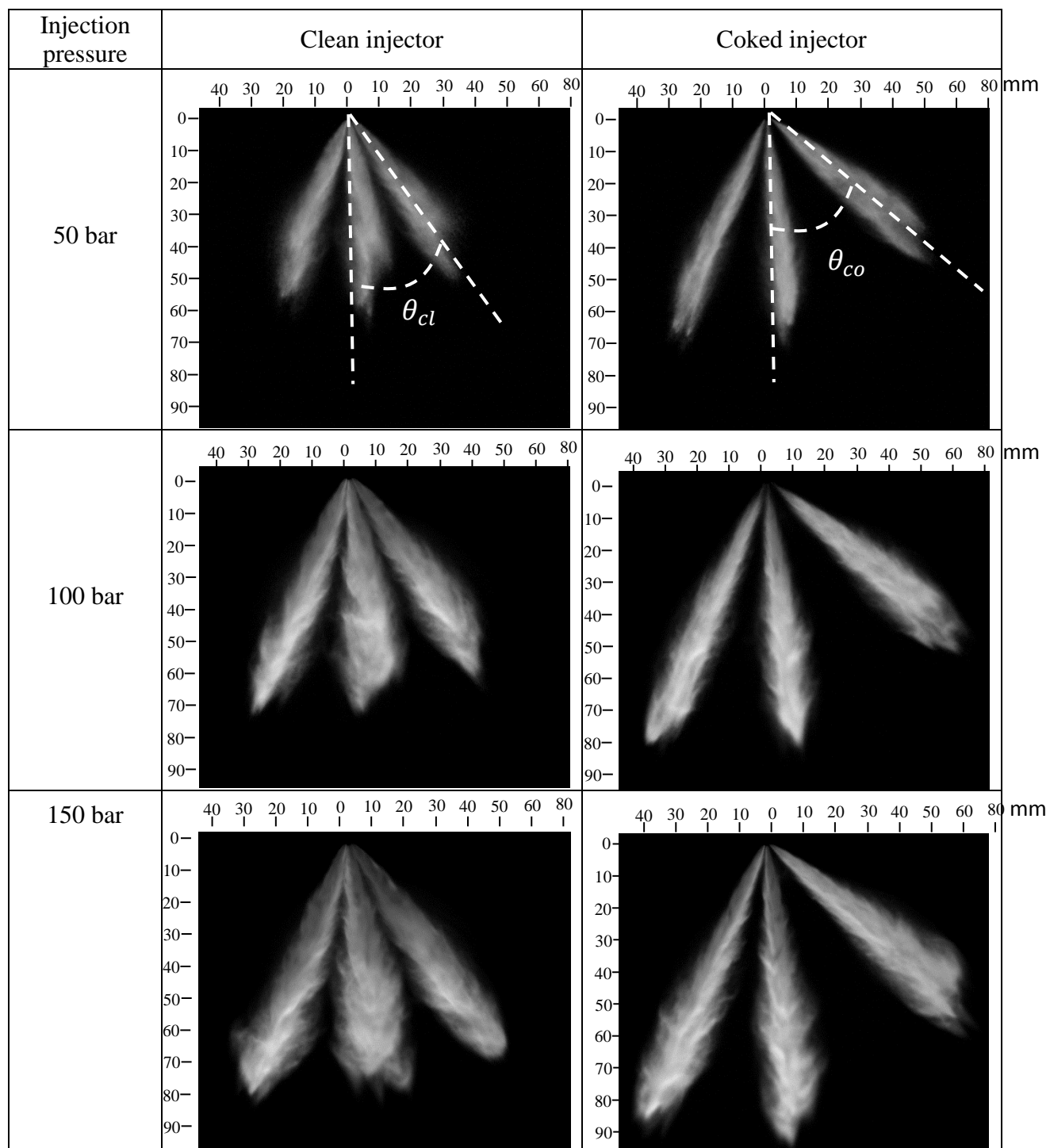
Figure 5.6. Side view of time resolved high speed images of sprays produced by the clean (A) and coked (B) injectors, at different injection pressure after 1ms for iso-octane, ambient temperature of 25°C and back pressure of 1 bar with a frame rate of 10 KHz, resolution of 800 X 800 pixels and magnification of 7.4 pixel/mm.

5.4.3 Penetration Length Quantitative Analysis of the Spray

To quantify the observed differences between plumes penetration lengths and spray angles of the clean and the coked injectors, 10 injections were captured for each injector and images averaged using a developed image processing MATLAB code as described in section 4.4 with the same threshold of 0.027 according to the sensitivity analysis. The maximum uncertainty of $\pm$ 3.1 mm was noticed in the calculated penetration length values. The average penetration length results of the ignition, side and rear plumes at different injection pressure are shown in Figure 5.7. It was noticed that the coked injector consistently had the longer penetration length for all the injection pressures compared to that of the clean injector.

At 1ms ASOI and lower injection pressure of 50 bar the penetration length for ignition and side jets of the coked injector was closely matched with that of the clean injector, although the penetration length of the coked injector jets was marginally higher. The rear jets of the coked injector demonstrated the largest difference with 64 mm compared to that of the clean injector with 56 mm, along with approximately a 14% increase. As the injection pressure was increased to 100bar, the rear jets of the coked injector experienced a longer penetration length of 77 mm compared to that of the clean injector with 67 mm, an increase of approximately 15%. Further increasing of the injection pressure up to 150bar, the coked injector rear jets yielded a longer penetration length with 94 mm compared to that of the clean injector with 74 mm, this is an approximately 27% increase. By contrast, for the side and ignition jets of the coked injector, the penetration length was 87 mm and 72 mm respectively compared to that of the clean injector with 75 mm and 64 mm respectively, with approximately 16% and 11% increase respectively. Overall, it was obvious that the effect of the injector deposit on the penetration length strongly depends on the injection pressure.
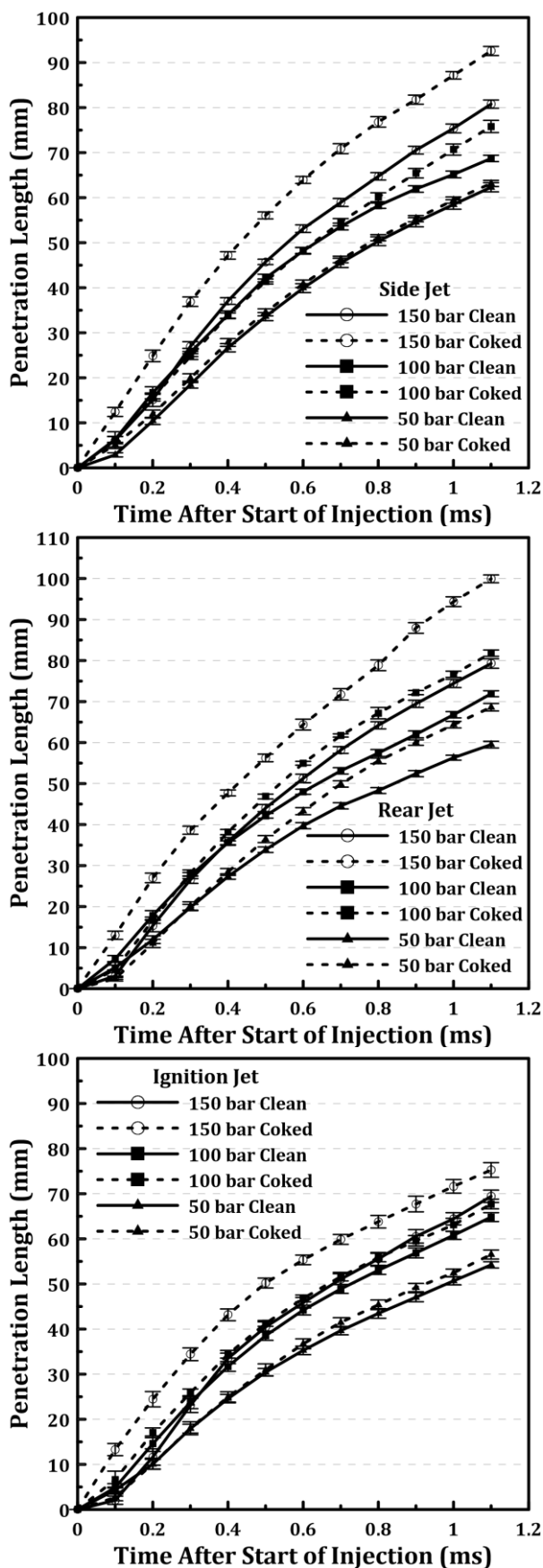
Figure 5.7. Spray penetration length for the fuel plumes of clean and coked injector at different injection pressures for iso-octane, ambient temperature of 25°C and back pressure of 1 bar.

The spray pattern was further investigated by PLIF imaging of the spray footprint. The PLIF technique was employed because it can yield a more accurate concentration field data compared to the data obtained with Mie scattering from particles. The fuel was mixture of iso-octane with 3% of 3-pentanone by mass. The laser sheet was adjusted at 20 mm below the injector tip. Figure 5.8 shows the bottom view PLIF footprint of the six spray jets for the clean and coked injectors at different injection pressures. The PLIF images indicated that at all the injection pressures the clean injectors exhibited larger individual spray plume cone angles with bigger footprints than that of the coked injectors. Furthermore, the coked injector had distorted, unsymmetrical spray envelopes, where the spray cross-sections were changed from near-circular to narrow ellipses, similar to the cross-section of a fan spray. The footprint of the spray plumes showed significant distortion for the coked injectors' case. As the injection pressure increase the plume cone angle increased and more interaction occurred between the plumes especially for the clean injector, whilst for coked injector less interaction between the plumes occurred due to the effect of the deposits, which resulted in wide separation between the adjacent plumes. The optical test indicated that even a moderate tip coking (e.g. resulting in 7.8% mass flow rate loss at injection pressure of 50 bar) can significantly alter macroscopic behaviours of the spray.
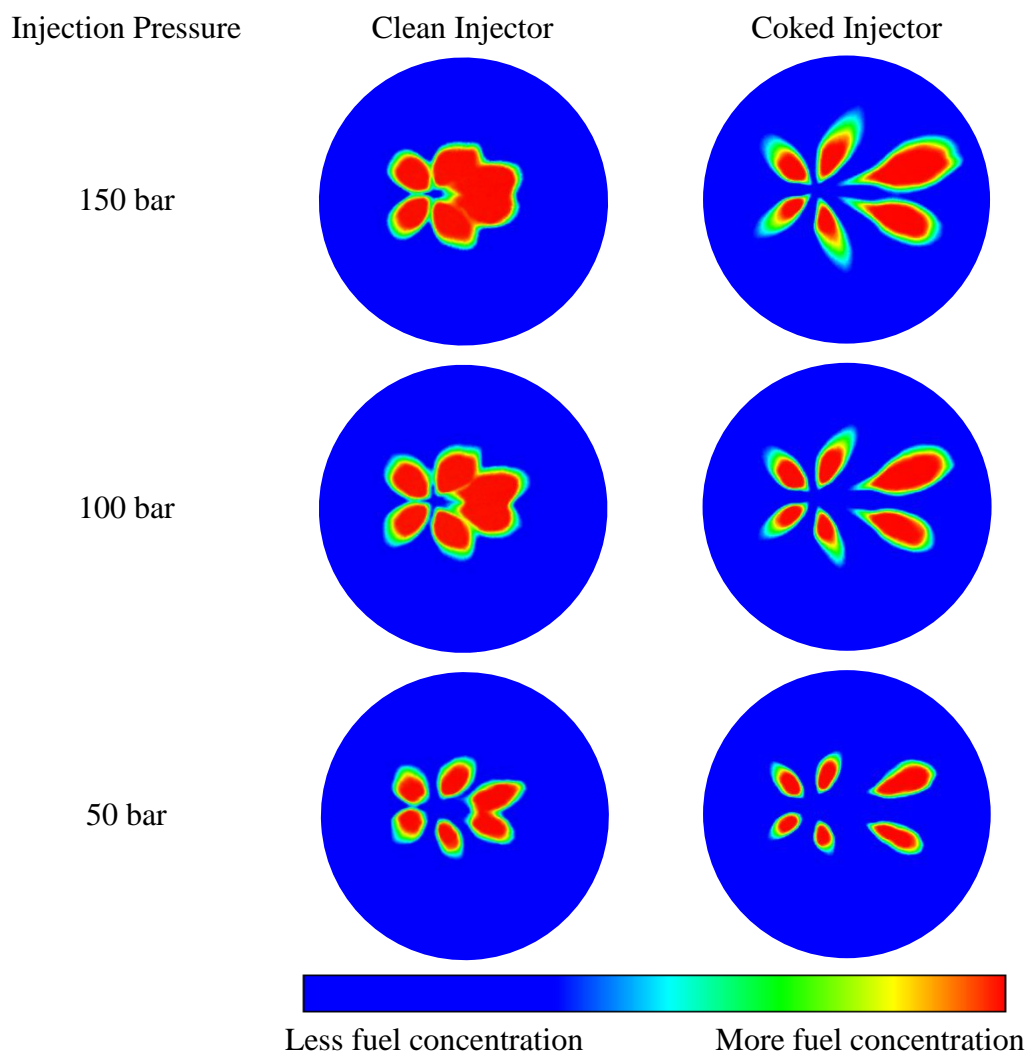
Figure 5.8. PLIF spray footprints of the clean and the coked injectors at 20 mm below the injector tip for different injection pressures for iso-octane doped with 3-pentanone (3% by mass), back pressure of 1 bar and ambient temperature of 25°C.

5.5 Microscopic Investigation of the Injector Tip Fuel Movement

In order to have a better understanding of the impact of the liquid film development along the outer surface of the injector tip on deposit formation, a long-distance microscopy (LDM) technique was utilized to investigate and visualize the fuel injection event. Furthermore, LDM was employed to examine the interactions between the plume periphery and the injector rim. Due to high fuel jet velocity, in order to receive an appropriate temporal resolution, a frame

rate of 125 kfps was selected. Figure 5.9 presents the results of the spray at four discrete times within a single injection event to highlight the pre, main, needle closing and the end of the injection. The injector was positioned so that the fuel plume pairs overlay on each other, therefore only the three front plumes could be seen effectively. The injector needle closing event could be distinguished by reduction in fuel flow rate and narrowing plumes cone angle.

The initial isooctane spray at the nominally ambient conditions (20°C Fuel temperature, 1.0 bar back pressure) displayed that the leading edge of the spray is associated with clearly discernible individual liquid ligaments and droplets. The steady state spray plume is usually used to define the spray cone angle because it has a well define boundary with clear individual features on the plume surface and boundary. Reduced break-up energy in the spray as the pintle closes at the end of the injection event results in the appearance of large fuel droplets and ligaments. These fuel droplets could significantly deteriorate the engine performance and increase unburned hydrocarbons and particulate matter emissions.

Furthermore, by investigating the LDM images, it was observed that during the main injection event when the fuel plumes cone angle increased, part of the plume hit the nozzle rim resulting in the formation of a very thin liquid fuel film that remains on the injector tip at the conclusion of the injection event as shown in Figure 5.10 and Figure 5.11. During the end of the injection event, more fuel was combined to this liquid film and propelled it in an upward direction away from the injector nozzle. Consequently, when the injector tip exposed to high combustion gas temperature, the evaporation of fuel film components and degradation processes will be increased, leading to sticky deposits.

Depending on the fuel properties and boundary conditions, part of this thin film may evaporate later and mix with air. There is also a possibility that when the premixed flame reaches the injector tip, this fuel film burns in pool fire. However, the high-speed imaging of the combustion phenomena for the clean injector demonstrated that there was not a diffusion flame noticed around the injector tip (will be discussed later in the next section). The diffusion flame was only observed for the coked injector. This exhibited that the main phenomenon was the decomposition of the liquid fuel film on the injector tip. For GDI engines when the tip temperature was above 90% vol. distillation temperature of the fuel, the fuel was pyrolysed, which created the tip deposits [16]. As the deposit layer forms, it acts as a "sponge" due to its porous structure and adsorbs more fuel in the course of fuel injection [166]. This fuel is then released after the premixed flame propagation and burns in pool fire. This tip diffusion flame was considered as one of the main PM-generating path in GDI engine [64].

In addition, drying of the injector tip was considered an essential parameter in the build-up of deposits. Karwa et al. [72] demonstrated the effect of system pressure, injector tip temperature and air flow on the drying rate of an isooctane thin film along the injector tip. It was observed that at injector tip temperature of 110°C (superheated up to 10°C above the boiling point of iso-octane) evaporation was the dominant mechanism and the drying rate in this regime was increased with injector tip temperature and air velocity. However, it displayed little dependence on the system pressure.

Overall, all the aforementioned observations regarding the appearance of liquid fuel film along the injector tip could be linked to the tip deposit formation and consequently the occurrence of diffusion flames.

| Initial spray event | Main injection event | Injector needle closing | End of main injection |
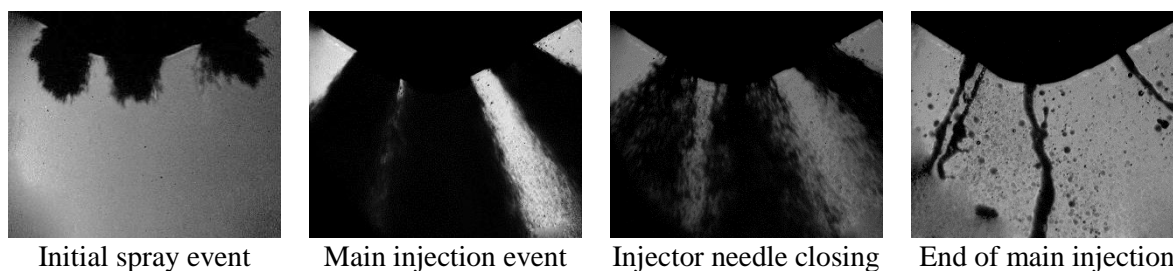
Figure 5.9. Near-nozzle long distance microscopy of the injection event (Back illumination) for iso-octane at injection pressure of 150 bar and back pressure of 1 bar.
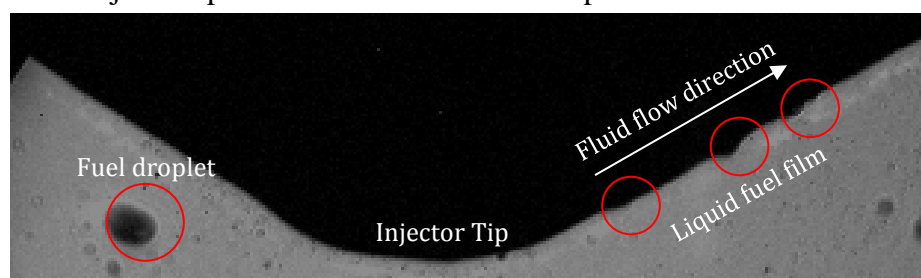
Figure 5.10. Formation of thin liquid fuel film on the clean injector tip during the end of the injection event (Back illumination) for iso-octane at injection pressure of 150 bar and back pressure of 1 bar.
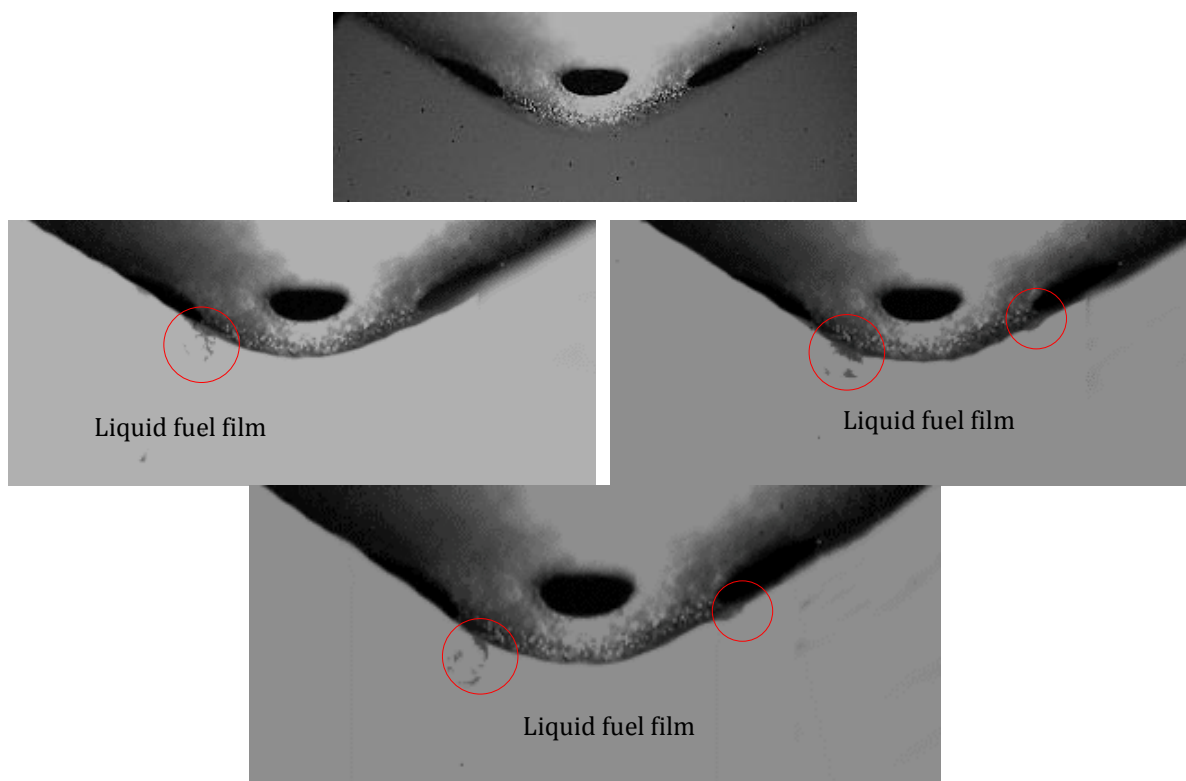
Figure 5.11. Formation of thin liquid fuel film on the clean injector tip during the end of the injection event for iso-octane at injection pressure of 150 bar and back pressure of 1 bar.

5.6 Effects of Injector Coking on Fuel Droplet Characteristics

The head stage was characterized by small variations in mean droplet velocities, Figure 5.12. At low injection pressure of 50 bar, it was noticed that effect of the deposit on the mean droplet velocities was significant for the rear jets in comparison with the ignition and side jets. For the rear jet the mean droplet velocity of the clean injector was 69 ms^{-1}, whilst the coked injector exhibited 75 ms^{-1} with droplet velocity increase of 9 % compared to that of the clean injector. For the side and ignition jets of the clean and coked injectors the mean droplet velocity profiles were more closely matched, although the mean droplet velocity of coked injector was marginally lower.
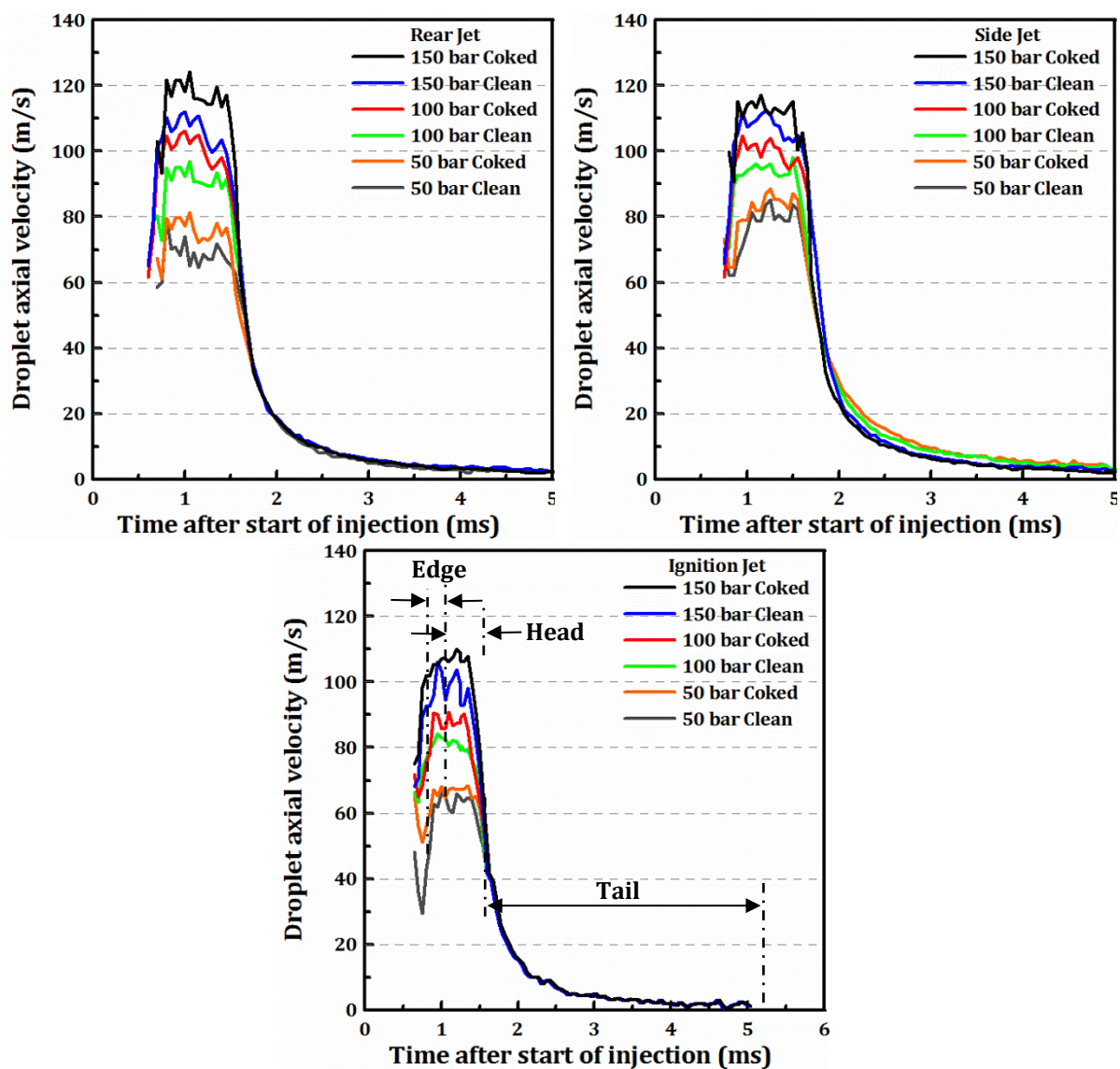
Figure 5.12. Mean droplet velocity for the clean and coked injectors at 30 mm away from the nozzle exit on the spray centre line at different injection pressures for (a) Ignition jet, (b) Side jet, (c) Rear jet for iso-octane, ambient temperature of 25°C and back pressure of 1 bar.

As the injection pressure increased up to 100 bar the mean droplet velocities increased, and the effect of injector coking becomes obvious for all the jets. For the rear jet, the coked injector demonstrated higher mean droplet velocity with 12% increase compared to that of the clean injector. Whilst the side and ignition jets displayed higher mean droplet velocity with 7% and 4.5% increase compared to that of the clean injector. A further increase of the injection pressure up to 150 bar, the rear jet of the coked injector demonstrated higher mean droplet velocity with 15% increase compared to that of the clean injector. Whilst the side and ignition jets displayed higher mean droplet velocity with 4% and 8% respectively increase compared to that of the clean injector.

Figure 5.13 presents SMD distributions along spray jets centreline verses the axial distance from the injector tip at different injection pressures. SMDs for the coked injector were consistently larger compared to the clean injector for all axial locations measured. At an axial distance of 30 mm, and injection pressure of 50 bar, the rear jet of coked injector showed an increase of 2.7% in SMD compared to the clean injector, whilst the side and ignition jets showed an increase of 18% and 2% respectively. For injection pressure of 100 bar, the rear jet of coked injector showed an increase of 6% in SMD compared to the clean injector, whilst the side and ignition jets showed an increase of 1% and 4%. At high injection pressure of 150 bar, the rear jet of coked injector showed an increase of 9% in SMD compared to the clean injector, whilst the side and ignition jets showed an increase of 2.5% and 2.3%.

It was observed that as the axial distance was increased, the SMDs were increased. This increase in SMDs with the axial distance was consistent with Shen et al [167], as they demonstrated that at fuel temperature of 20 °C, the SMDs near the nozzle are smaller than those at other positions, and they increased along the vertical direction from the injector tip to the

spray tip. This could be either due to the coalescence of smaller droplets becoming a more important than the breakup of large droplets in the downstream regions, or due to the complete evaporation and disappearance of smaller droplets whilst the larger droplets took much longer time to evaporate, according to Spalding's D^2-law [168]. This law demonstrated that the evaporation time of a droplet is proportional to the square of the initial diameter D.
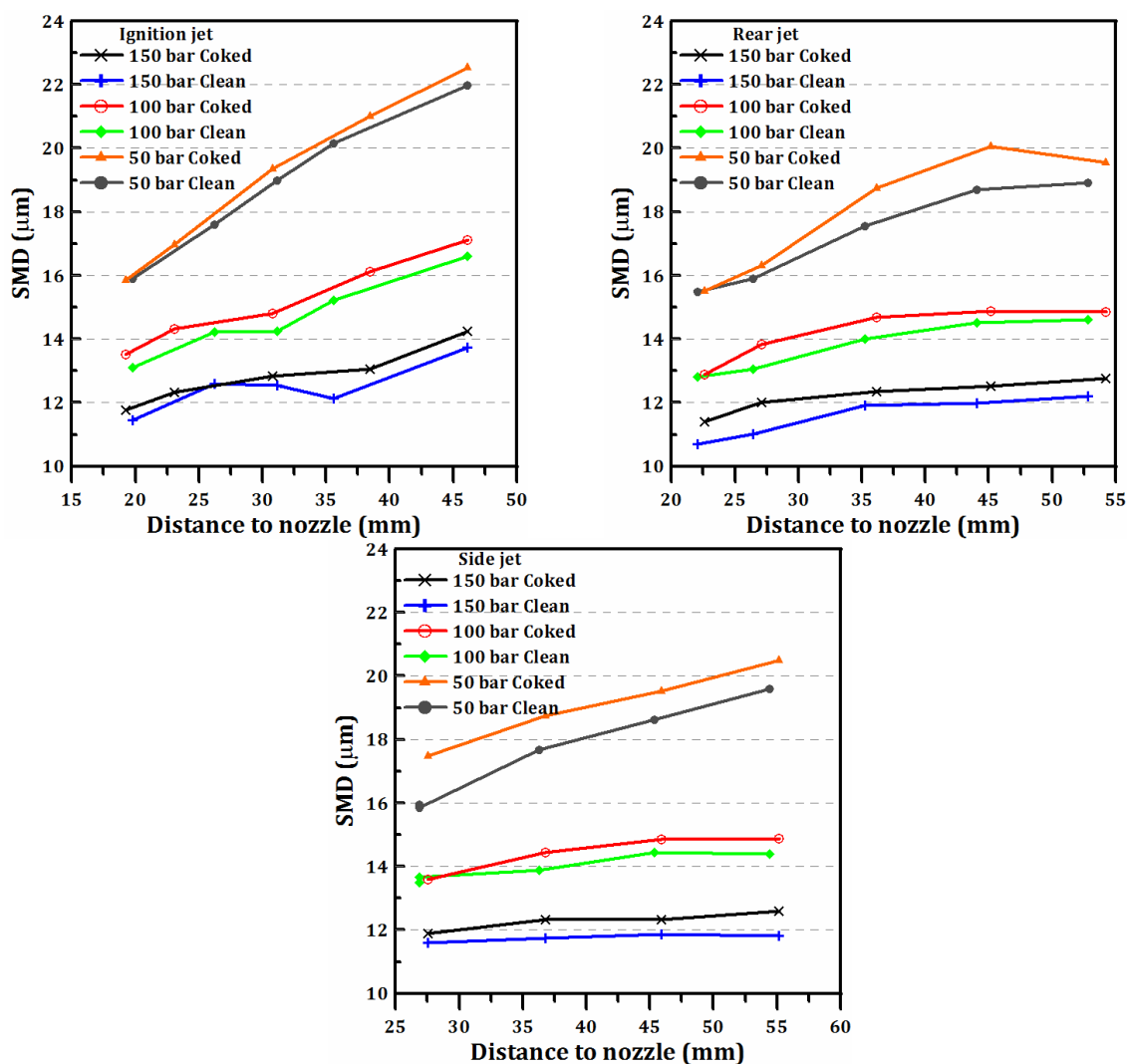
Figure 5.13. SMD distributions along the jet spray centerline axis for the clean and coked injectors for iso-octane, ambient temperature of 25°C and back pressure of 1 bar.

5.7 Effects of Injector Coking on Combustion

In-cylinder pressure traces obtained from averaging 300 consecutive cycles for the clean and coked injectors are shown in Figure 5.14 (TDC is referred to 0 CAD). The engine speed was fixed at 1200 rpm, IMEP of 5bar, stoichiometric condition and the test fuel was Unleaded Gasoline (ULG95). The presence of light in figures indicated occurrence of combustion and regions with high light intensity indicated diffusion flame phenomena. It was observed that both injectors had the same in-cylinder pressures up to 15 CAD BTDC. Afterwards, the clean injector showed slightly higher pressures. The pressure difference between the clean and coked injectors had its maximum value where the in-cylinder pressure peaked, and the peak of the clean injector slightly shifted toward TDC. The IMEP of the engine running the clean injector was slightly higher than the coked injector with better stability (lower coefficient of variation (COV) of Indicated Mean Effective Pressure (IMEP)). Figure 5.15 shows the Mass Fraction Burned (MFB) curves, calculated from the averaged in-cylinder pressure data for the clean and the coked injectors. It was observed that the burning velocity was faster for the clean injector compared with the coked injector. In order to investigate the difference more clearly, the Heat Release Rate (HRR) characteristics were plotted (shown in Figure 5.16) where the clean injector demonstrated slightly higher values compared with the coked injector. Furthermore, the heat release rate for clean injector started rising earlier and the peak of HRR shifted slightly towards TDC compared to that of coked injector. This suggested a better mixture preparation from the clean injector compared to that of the coked injector.
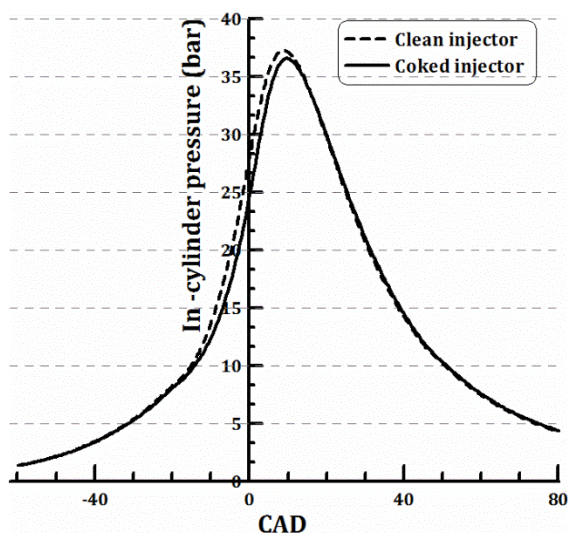
Figure 5.14. In-cylinder pressures vs. crank angle using gasoline with engine speed of 1200 rpm, ignition timing of 30 CAD BTDC, injection pressure of 150 bar, injection timing of 280 CAD BTDC and IMEP of 5 bar.
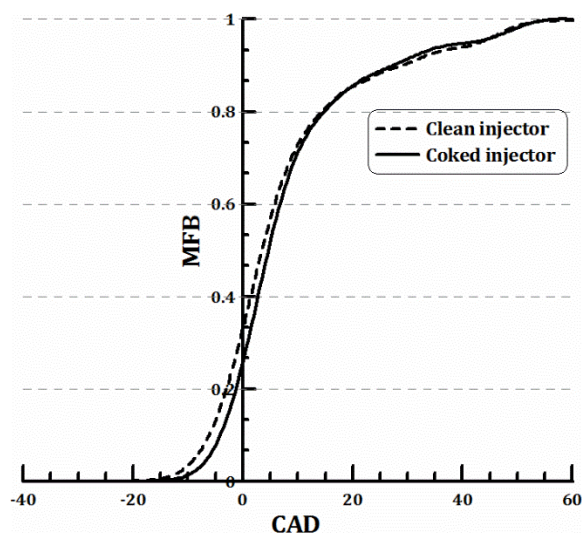
Figure 5.15. MFB vs. crank angle using gasoline with engine speed of 1200 rpm, ignition timing of 30 CAD BTDC, injection pressure of 150 bar, injection timing of 280 CAD BTDC and IMEP of 5 bar.
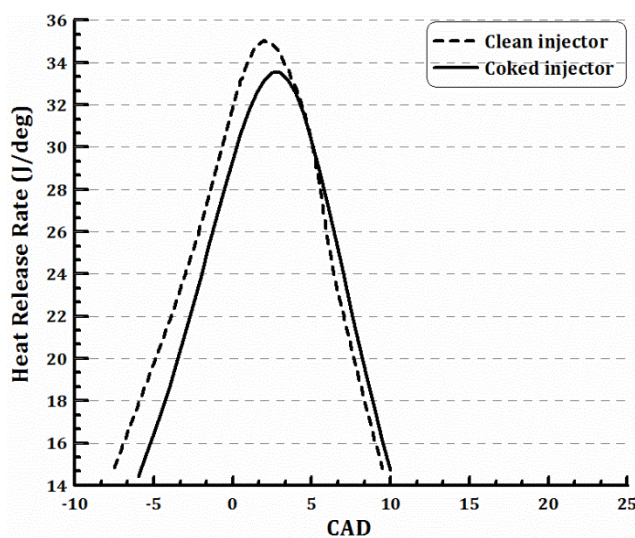
Figure 5.16. HRR vs. crank angle using gasoline with engine speed of 1200 rpm, ignition timing of 30 CAD BTDC, injection pressure of 150 bar, injection timing of 280 CAD BTDC and IMEP of 5 bar.

The bottom and side view high-speed imaging of combustion phenomena for the clean and coked injectors in GDI optical engine are shown in Figure 5.17, Figure 5.19 and Figure 5.20 at different crank angles from the start of combustion (SOC). For each crank angle, 100 images were captured with one image per cycle using a Vision Research Phantom V710 camera, with

a 105 mm f/4.5 UV-Nikkor lens (220 to 900 nm). The engine speed was fixed at 1200 rpm, stoichiometric conditions, IMEP of 5 bar, intake manifold pressure of 0.8 bar and fuel temperature at 30°C. The presence of light in figures indicated occurrence of combustion and regions with high light intensity indicated diffusion flame phenomena. It is obvious from Figure 5.18 that late in the combustion cycle, some diffusive combustion occurred in the vicinity of the coked injector tip. This phenomenon was observed for 60-70% of the 100 cycles acquired by the high speed camera. Combustion essentially started with a premixed flame kernel which expanded into the fuel- air mixture near the spark plug. Once the premixed flames, came in to contact with fuel droplets associated with the injector tip surface, it resulted in rich mixture regimes, which started to burn under diffusion (sooting) conditions. The radiation of the diffusion flames surpassed the premixed flame in both radiation intensity and duration [160, 169]. The rich mixture was mostly concentrated in specific locations; therefore, the diffusion flames are highly localized.

For the clean injector it was noticed that the premixed flames were almost completed at 70 CAD ASOC without any observation for diffusion flames. For the coked injector the premixed flames were almost completed at 70 CAD ASOC accompanied with diffusion flame which starts ≈ 30 CAD ASOC and continued until 130 CAD ASOC for the coked injector. This indicated how slow the diffusive combustions compared to the premixed flames. Furthermore, the diffusion flames were highly localized around the injector tip.
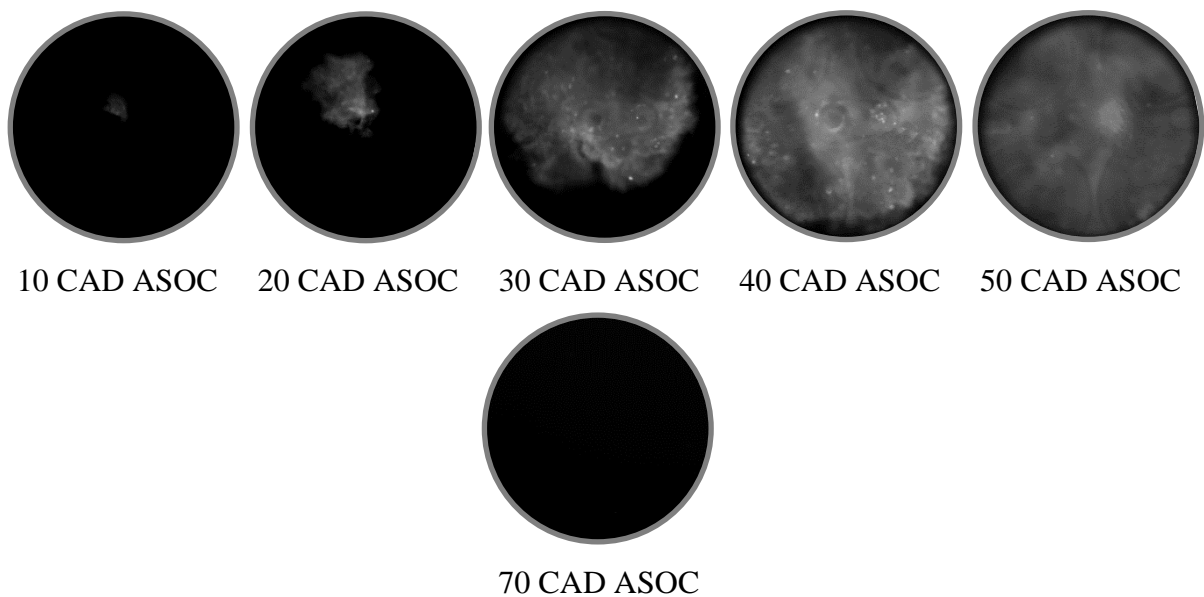
Figure 5.17. Bottom view flamed images at different crank angles for the clean injector using gasoline with engine speed of 1200 rpm, ignition timing of 30 CAD BTDC, injection pressure of 150 bar, injection timing of 280 CAD BTDC and IMEP of 5 bar.
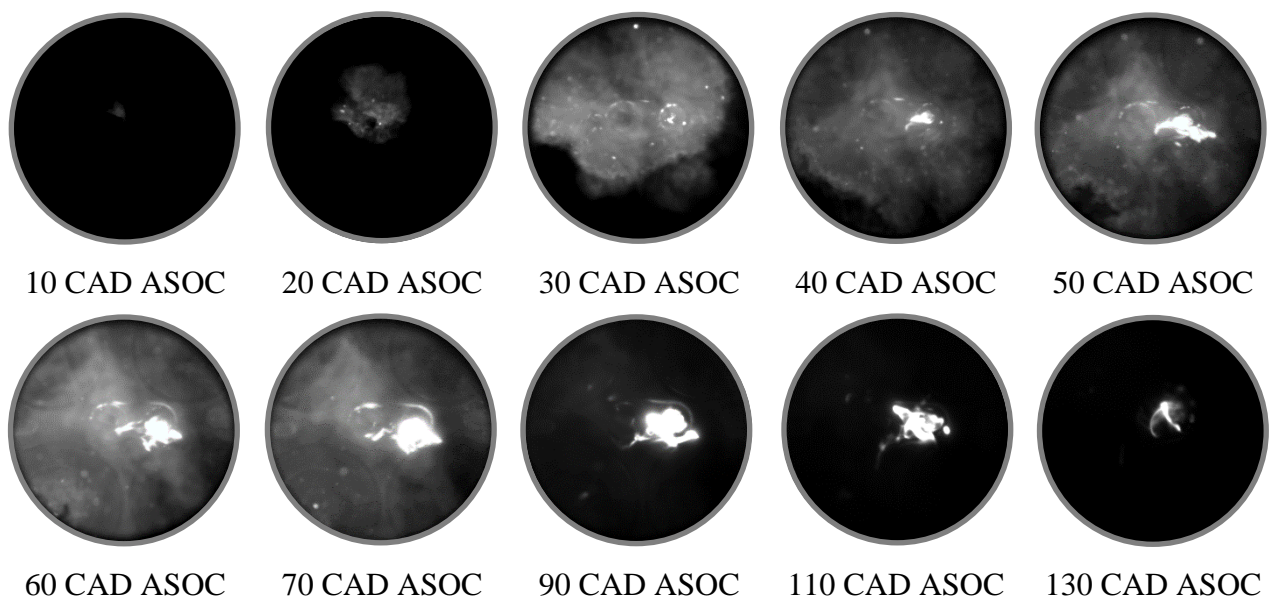
Figure 5.18. Bottom view flame images at different crank angles for the coked injector using gasoline with engine speed of 1200 rpm, ignition timing of 30 CAD BTDC, injection pressure of 150 bar, injection timing of 280 CAD BTDC and IMEP of 5 bar.
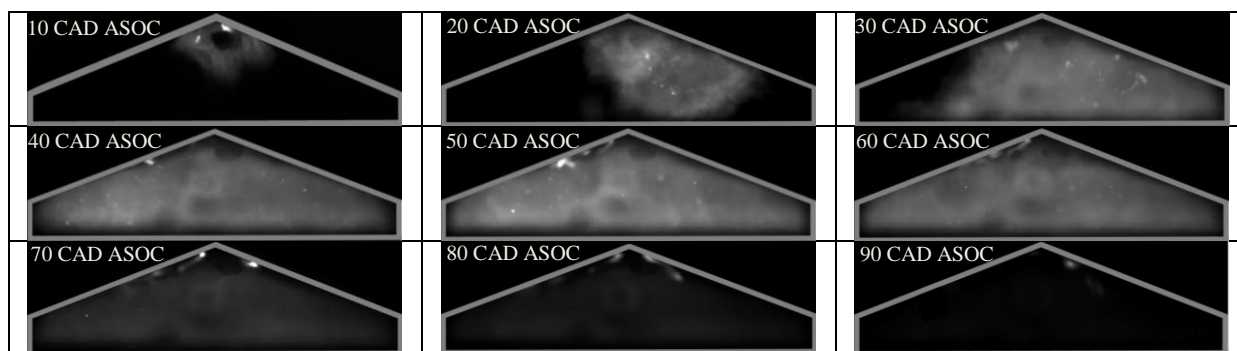
Figure 5.19.Side view for the diffusion flame images at different crank angles for the clean injector using gasoline with engine speed of 1200 rpm, ignition timing of 30 CAD BTDC, injection pressure of 150 bar, injection timing of 280 CAD BTDC and IMEP of 5 bar.
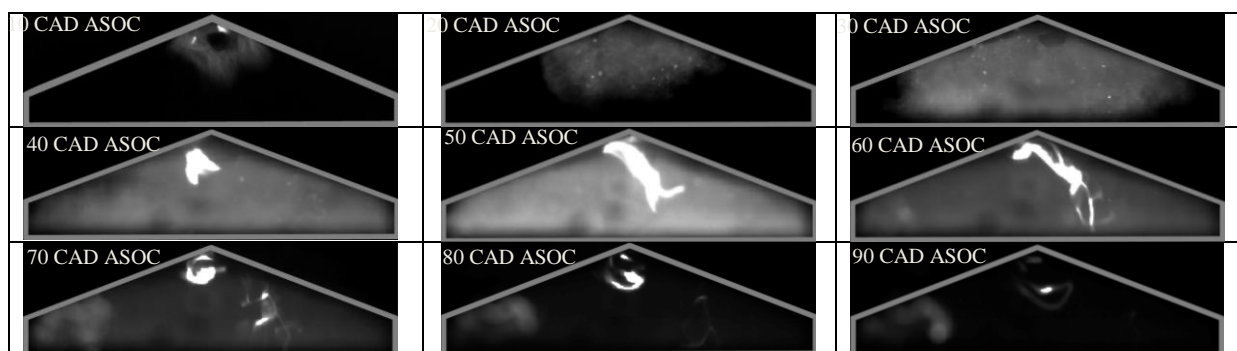
Figure 5.20. Side view for the diffusion flame images at different crank angles for the coked injector using gasoline with engine speed of 1200 rpm, ignition timing of 30 CAD BTDC, injection pressure of 150 bar, injection timing of 280 CAD BTDC and IMEP of 5 bar.

Kinoshita et al. [153] investigated injector deposit formation mechanisms and they found that injector deposits can be classified into two types: soot deposited on the nozzle and needle surface and gum type deposit inside the nozzle from fuel polymerized by thermal decomposition [4]. These deposits on the injector tip acted like a sponge and adsorbed portions of the fuel, which did not evaporate quickly enough to mix with the available air in time to be consumed by the propagating homogenous premixed flame front, leading to rich conditions in the vicinity of the injector tip. The fuel on the injector tip burned later within a slow bright diffusion flame which is visible due to the high-luminosity and yellow colour compared to the low-luminosity UV and blue radiation of the premixed flame. Furthermore, the presence of a fuel-rich mixture region around the injector tip will constitute a main source for soot particles

to be formed and consequently the PN concentrations will be increased. Berndorfer et al. [64] investigated the relation between the integral coked injector diffusion flame and the particulate emissions. It was noticed that the injector diffusion flame values showed a clear correlation to the soot mass emission; the higher the soot emission the higher the PN and the injector diffusion flame value.

Based on the combustion pressure traces Merker et al. [169] demonstrated that the diffusion flames had a negligible contribution to the heat release despite the high light intensity. However, it will be of practical importance as a source for soot production and PM from DISI engines. Furthermore, the slower combustion process associated with the diffusion flame could be due to the heterogeneous flame patterns with fuel droplet combustion. In addition, the slower combustion could be attributed to the fact that combustion was not taking place within the high frequency turbulent flow structure during the end of the compression stroke [170].

5.8 Summary

Experimental optical tests were carried out to obtain a comprehensive understanding of gasoline direct injector coking effects on spray characteristics and engine performance. SEM had been coupled with an X-ray 3D microtomography technique to study the topography and characteristics of deposits. Chemical properties have been established using an EDS (coupled with an SEM). Macroscopic spray characteristics of clean and coked injectors were studied using high-speed imaging. Fuel droplet size and velocity were characterised with a two-dimensional Phase Doppler Particle Analyser (PDPA). Combustion analysis and examination of diffusion flame phenomena were carried out for the clean and the coked injectors. The conclusions drawn from the work are as follow:

1. The X-ray testing results demonstrated that different levels of deposits were formed across the injector including the internal and external nozzle holes.

2. Extensive deposits were observed in external injector holes and the external-hole deposits were radially distributed and collected in the shoulder while the deposit formation reduced through the internal holes of the injector.

3. With the higher penetration lengths of the coked injector compared to the clean injector in general, the penetration length for ignition and side jets of the coked injector was closely matched with that of the clean injector at lower injection pressure of 50bar, whilst the rear jets penetration length of the coked injector demonstrated a 14% increase. As the injection pressure was increased to 100bar and 150bar the rear jet penetration length of the coked injector displayed a 15% and 27% increase respectively compared to the clean injector. By contrast, the side and ignition jets penetration length of the coked injector yielded 16% and 11% increase respectively.

4. The coked injector consistently had smaller plume angles compared to the clean injector. The calculated averaged values obtained for plume' angles reduction of the coked injector at lower injection pressure of 50bar, indicated that rear jets and side jets had the maximum reduction of approximately 25% and 23% respectively, whereas the plume angle of ignition jets revealed a minimum reduction of 13%. Further increasing the injection pressure up to 100 bar, caused the plume angle reduction of rear and ignition jets for the coked injector to increase to 28% and 17.5% respectively. However, the side jets demonstrated no effect of injection pressure increase and the plume reduction remained the same with approximately 23.5%. For injection pressure of 150bar, the magnitude of reduction in the plume angle was less compared to that of 100 bar injection pressure but a greater reduction was seen for the side jets.

5. Coking had a significant effect on the increase of mean droplet velocities. The ignition jet, side jet and rear jet velocities were increased by 4.5%, 7% and 12% compared to the clean injector at 100 bar injection pressure. Whilst at 150 bar injection pressure, the ignition jet, side jet and rear jet velocities were increased by 8%, 4% and 15% compared to the clean injector. Also, the injector coking caused an increase in the droplet size (SMD).

6. Combustion images revealed presence of small bright spots around the injector tip indicating injector tip diffusion flame due to deposit build-up. The in-cylinder pressure analysis indicated that the coked injectors provided lower in-cylinder pressure and poorer combustion stability. Also, the radiation of the diffusion flames surpassed the premixed flame in both radiation intensity and duration.

Chapter 6

IMPACT OF SPARK PLUG GAP ON FLAME KERNEL PROPAGATION AND ENGINE PERFORMANCE

The aim of this chapter is to obtain a comprehensive examination of the effect of the electrode spark plug gap on flame kernel development, engine performance, and emissions. High-speed Schlieren visualization was utilized to study the flame kernel growth at different equivalence ratios. Planar Laser Induced Fluorescence (PLIF) was employed to investigate the combustion zone and the flame front development on the horizontal swirl plane after spark ignition. High-speed imaging was carried out to study turbulent flame propagation. Combustion analysis, using in-cylinder pressure data and Mass Fraction Burned (MFB) was employed, along with exhaust emissions measurement to obtain a better understanding of the spark plug gap effects on engine performance and emissions.

6.1 Introduction

The spark plug gap is considered one of the key factors that must be set properly before the plug is installed inside the engine for three reasons: 1) If the gap is too wide, the electrical voltage may not be high enough to arc across, which would result in a misfire, 2) If the gap is too narrow, the spark may not ignite a "lean" air/fuel mixture, which would also result in a misfire, 3) The voltage requirement of a spark plug is directly proportional to the size of the gap. Furthermore, the electrode gap influenced the early formation of a flame (kernel), which

played a dominant role in determining the subsequent behavior of that flame, and thereby influenced the engine performance [22, 23]. There are two stage processes to describe the evolution of the flame kernel: within the early short stage, the shock wave and the plasma expanding kernel were dominated the mass and energy transfer process. Whilst during the next much longer stage, the control of energy and mass transfer were conducted by the thermal conduction from flame boundary layer and the diffusion process to keep the flame self-sustained [87]. Therefore, in order to have a complete combustion of the air-fuel mixture and consequently a better engine performance, the correct spark plug gap should be installed through the cylinder head. Herweg and Ziegler [89] found that reducing the contact areas between the flame kernel and the spark plug can be achieved either by reducing the electrode diameter and/or increasing the gap which leads to a faster flame kernel development. Also, the flame kernel structure is significantly affected by the flow pattern near the spark plug gap. Several parameters such as gap width, diameter of the electrode and spark duration have a great impact on the flow pattern adjacent to the spark plug [90]. Furthermore, increased gap spacing and gap projections are beneficial in improving the brake specific fuel consumption of the engine, and the ability to ignite lean fuel/air ratios [24].

The current study mainly focus on studying the effect of effect of the electrode spark plug gap on flame kernel development, engine performance, and emissions. Qualitative and quantitative measurements of both the flame kernel growth area and radius were carried out using High-speed Schlieren visualization and MATLAB code, respectively. Planar Laser Induced Fluorescence (PLIF) was employed to investigate the combustion zone and the flame front development on the horizontal swirl plane after spark ignition. The in-cylinder pressure measurements under different spark plug gap were employed to examine the engine combustion parameters such as COV of IMEP, MFB and HRR. The aforementioned

measurements coupled with exhaust emissions measurements were carried out to assist the spark plug gap effects on engine performance and emissions.

6.2 Spark Plug Gaps, Flame Kernel (Area & Radius) Definition and Turbulent Flame Speed Calculation

For the current study, spark plugs with three different gaps of 1mm, 1.2mm and 1.4mm were used to investigate their impacts on flame kernel growth, engine performance and emissions. Single coil-on-plug (COP) type was utilized for ignition system and charged by using a 12V 9A battery supply. The dwell time (which is defined as the period of time that the coil is turned on) was maintained at 6 ms providing ignition energy of 35-40 mJ and spark duration of approximately 2 ms. For all the fired engine testing, a spark plug (NGK-ILKAR6C10) with J-type ground electrode and thin laser welded iridium tip central electrode was employed to start the ignition even. The spark energy was fixed through the whole test and consequently the voltage was held constant for all the three gaps.

(a)   (b)
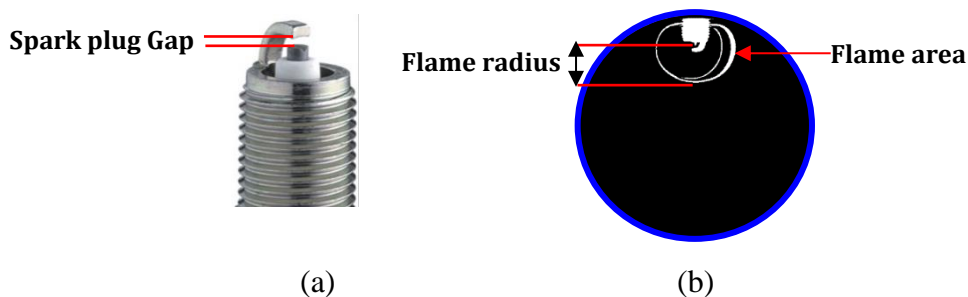
Figure 6.1. (a) Spark plug (b) Flame kernel area and radius definitions

Initially, a series of experiments were conducted to investigate the effects of different spark plug gaps on the early stages of the flame kernel formation. These experiments were performed in a constant-volume combustion chamber over a wide range of equivalence ratios in a carefully controlled environment and under laminar conditions. The flame kernel area was

defined as the outer envelope of the flame, whilst the flame kernel radius was defined as the vertical distance from the end of the center electrode to the boundary of the flame, see Figure 6.1.

An in-house developed MATLAB program was used for image processing for both the combustion vessel and engine results. To define the boundary of the flame, the raw image data were corrected by background subtraction and noise signal removal through median filtering. Consequently, the optimum threshold for image processing was identified based on the sensitivity analysis of the flame area. According to this sensitivity analysis, the threshold (normalized intensity) of 0.03 was selected and employed to identify the flame boundary. Then, the background corrected image was converted to a binary image by thresholding. The maximum uncertainty in the calculated flame area was $\mp$ 22 mm^2. Finally, the boundary of the flame shape was identified by the software as shown in Figure 6.1and Figure 6.2. For the engine raw flame images, a circular mask with a diameter slightly smaller than the piston window was laid over the original image to remove reflection from the metal housing of the optical crown. Consequently, the computer program will be able to distinguish between the location of the window area and the flame boundary.

Regarding the calculation of turbulent flame speed inside GDI engine, the average flame speed in two adjoining images was defined as:

$$V = \frac{\Delta S}{L \Delta t}$$

(6.1)

In which ΔS is the augmentation of the flame area; Δt is the time interval between the two images; and L is the length of the flame boundary. Figure 6.2 is an illustration of the calculation process.
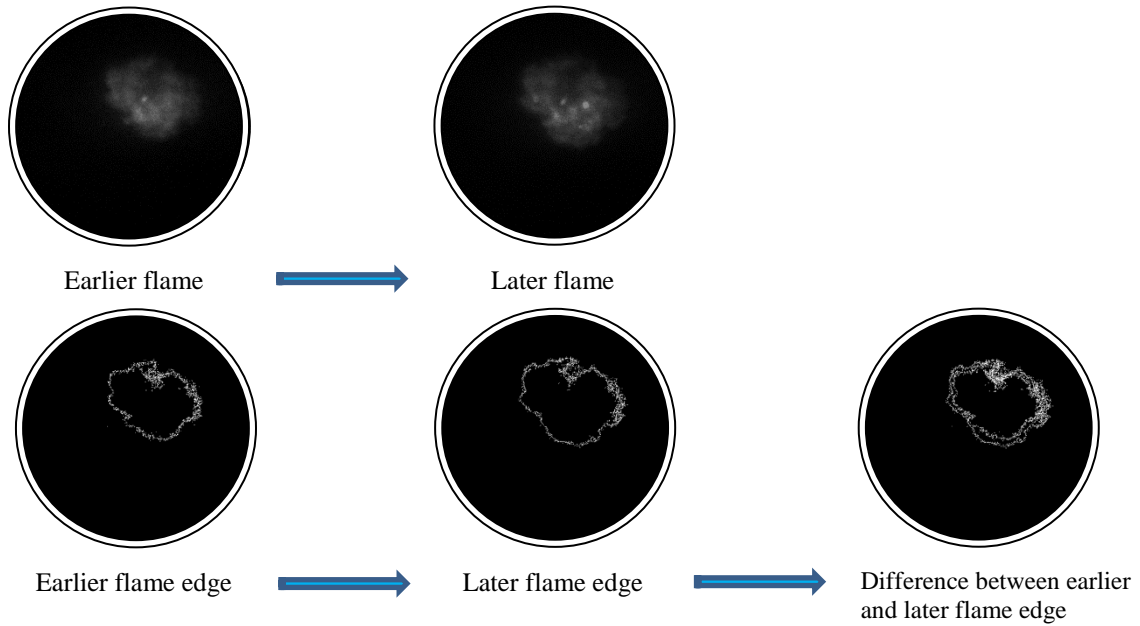
Figure 6.2. Flame speed calculation procedure

For the current study all the experimental tests, techniques and fuels are summarized in Table 6-1.

Table 6-1.Summaries experimental tests, techniques and fuels used in this work

Experiment	Flame kernel area and radius measurements	Flame front detection	Combustion flame imaging	Combustion pressure analysis and emissions measurements
Technique	Schlieren high-speed imaging of flame	PLIF measurements	High-speed imaging of flame	Horiba MEXA-7100DEGR gas analyser and DMS 500
Test environment	constant volume chamber 90°c initial temperature and 1 bar initial pressure	Single- cylinder optical engine speed:1200rpm, spark timing:25CAD BTDC, injection timing:280CAD BTDC	Single-cylinder optical engine speed:1200rpm, spark timing:25CAD BTDC, injection timing:280CAD BTDC	Single-cylinder thermal engine speed:1200rpm, spark timing:25CAD BTDC, injection timing:280CAD BTDC
Fuel	Gasoline (ULG95) with 3.3% ethanol	Iso-octane doped with 3-pentanone (3% by mass)	Gasoline (ULG95) with 3.3% ethanol	Gasoline (ULG95) with 3.3% ethanol

6.3 Results and discussion
6.3.1 Flame Kernel Propagation for Different Spark Plug Gaps

Figure 6.3 shows the flame kernel growth at equivalence ratio of φ=1 for three different spark plug gaps of 1, 1.2 and 1.4 mm. The fuel used was gasoline at initial temperature and pressure of 90°C and 1 bar, respectively. At the beginning of the flame kernel initiation and up to 1ms from the start of spark, the difference in the flame kernel size between the three gaps is relatively small especially for 1.4mm and 1.2mm compared to 1mm gap. As the time after the start of flame kernel initiation is further increased, spark plug gap of 1.4mm and 1.2mm gap generate a flame kernel area significantly larger compared to that of spark plug gap of 1mm. At 2 ms the average calculated flame kernel area of gaps 1.2 and 1.4 mm is approximately 21.3 and 35.6 mm^2 respectively compared to 8.6 mm^2 for 1mm gap. Further increasing of the time up to 8ms, the average calculated flame kernel area of gaps 1.2 and 1.4 mm is approximately 672.8 and 903 mm^2 respectively compared to 286.8 mm^2 for 1mm gap.

This big difference in the average flame kernel area can be due to the extension of the spark plug gap from 1 to1.2 and 1.4 mm, leading to higher ignition energy with a larger plasma volume and more contact with unburned gas. As a result, a faster flame kernel is developed, which accelerates the mass fraction burnt, resulting in higher heat release rate [171]. In addition, spark electrode configuration plays a dominant role in flame kernel development due to the amount of heat loss to the spark electrode. Therefore, for narrow gaps a small core flame will be produced and consequently the energy lost will be increased due to the heat transfer from the flame kernel to the electrodes. Furthermore, for narrow gaps, a portion of the spark energy in the electrical fall regions of the cathode and anode may be lost to the electrodes because of the fall regions being in close proximity to the electrode surface [172-174]. Consequently, the flame propagation rate will be limited [90]. Ishii et al. [90] revealed that as

the spark plug gap increased, the amount of heat losses reduced. By contrast, for small plug gap a large amount of hot gas was captured in the spark gap and then the recirculation flow moved the captured gas toward the spark electrode tip and contributed to the increment of heat loss. The wider the gap, the greater is the volume of air-fuel mixture exposed to the spark which assists in ignition lean mixtures [76]. As the electrode gap increases, lower quenching losses occur, and this leads to improved conditions for ignition. In contrast, larger gaps demand higher ignition voltages.

Time (ms)	1mm gap	1.2 mm gap	1.4 mm gap
0.1			
2.1			
4.1			
6.1			
8.1			
8.6			
10.1			

Figure 6.3. Comparison of typical flame growth for three different spark plug gaps of 1mm, 1.2mm and 1.4mm for gasoline at equivalence ratio of φ=1, initial temperature of 90ºC and 1 bar initial pressure.

Figure 6.4 shows the flame kernel growth for three different spark plug gaps of 1, 1.2 and 1.4mm at different equivalence ratios of φ=0.9, φ=1, φ=1.1 and φ=1.2 at 6ms after start of flame kernel initiation. For lean and stoichiometric conditions, the difference in flame kernel growth is high between the three spark plug gaps. Spark plug gap of 1.2mm and 1.4mm have

a significant larger flame kernel compared to gap 1mm. The effect of the spark plug gap reduces once it proceeds to richest conditions of φ=1.1 and φ=1.2. For rich condition of φ=1.2 the flame kernel growth is not affected by the spark plug gap especially for gaps of 1.2mm and 1.4mm. The reasons for a faster flame speed at slightly rich mixture setting with an equivalence ratio near to φ =1.2, that more fuel molecules are presented in the chamber during combustion and hence more radicals are formed ahead of the flame front, and significantly higher flame temperatures are achieved [175]. However, at very high rich conditions the flame temperature will start to decrease again due to the incomplete combustion process, and hence less thermal energy will be released. Likewise, for lean mixtures, the flame temperature decreases due to the lower fuel mass flow rate available which releases less thermal energy [99].
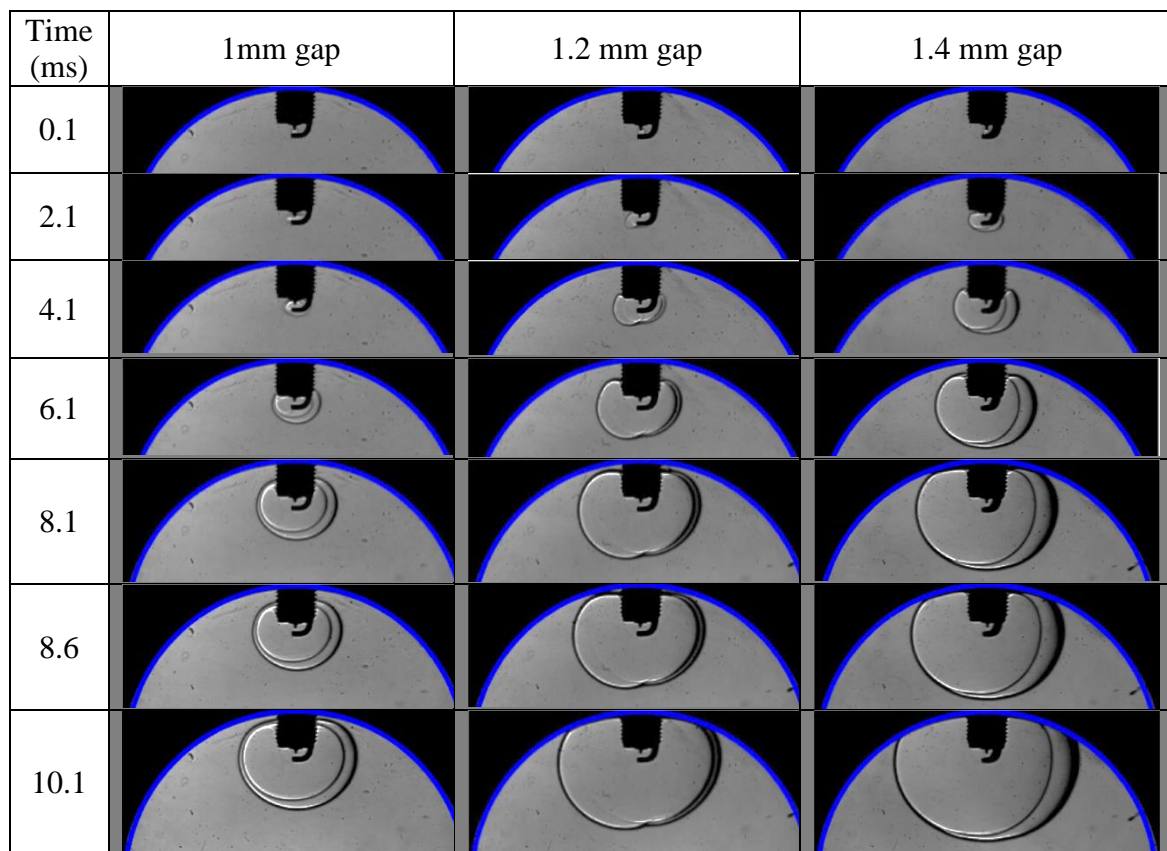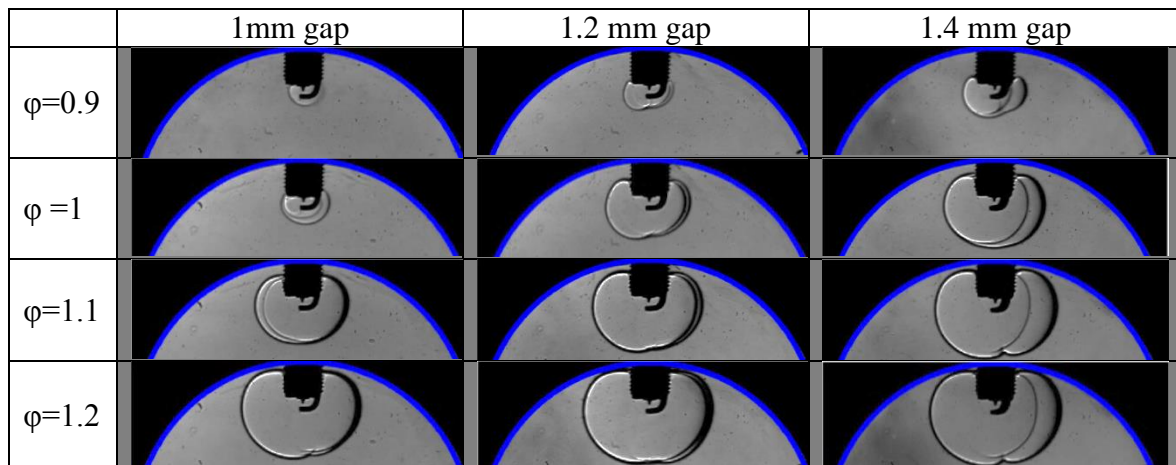

Figure 6.4. Comparison of typical flame growth for three different spark plug gaps of 1mm, 1.2mm and 1.4mm for gasoline at different equivalence ratio of φ=0.9, φ=1, φ=1.1 and φ=1.2 at 6ms after start of flame kernel initiation with initial temperature of 90°C and 1 bar initial pressure.

6.3.2 Flame Area

Figure 6.5 shows a quantitative comparison of the average flame area as a function of time after spark initiation with spark plug gaps of 1, 1.2and 1.4mm at different equivalence ratios. To ensure high confidence in data reliability, each test was repeated a minimum of three times with a maximum uncertainty of $\pm$ 22 mm^2 in flame area calculation. For all the equivalence ratios, the 1.4mm gap consistently has a larger flame area compared to the other gaps. At 1ms all the average flame area trends are closely matched for all the spark plug gaps. As the time after ignition increases, the effect of the electrode gap becomes significant especially for lean and stoichiometric conditions. As the mixture becomes richer, the effect of the electrode gap starts to diminish particularly between gaps of 1.2mm and 1.4mm. At 6ms, the average calculated areas are summarized in Table 6-2.

Table 6-2. The average flame area in mm^2 at 6ms after ignition for gasoline at different equivalence ratio of φ=0.9, φ=1, φ=1.1 and φ=1.2 with initial temperature of 90°C and 1 bar initial pressure

	1mm gap	1.2mm gap	1.4mm gap
φ=0.9	26	109	147
φ=1	88	301	456
φ=1.1	389	548	627
φ=1.2	718	795	820

The ignition energy and the heat losses are the key parameters which play a dominant role on the flame kernel propagation. When the gap is widened, the breakdown energy increases almost in proportion to the gap width [176]. These enhancements in ignition energy of the wider spark gap can be attributed to the extended surface of the plasma, which requires more energy to sustain itself, particularly in conditions where the energy density is held constant, resulting in a constant temperature gradient along the plasma surface [177, 178]. This increase in the ignition energy is derived from the larger initial kernel volume. The enlarged kernel stimulates

the flame growth which burns faster because it has a larger flame surface area making contact with the unburned gas. As a result, when the electrode gap is extended from 1mm to 1.2mm and 1.4 mm, the flame area after 6ms and φ=1 enlarges by about 3.5 and 5 times, respectively compared to that of 1mm gap.
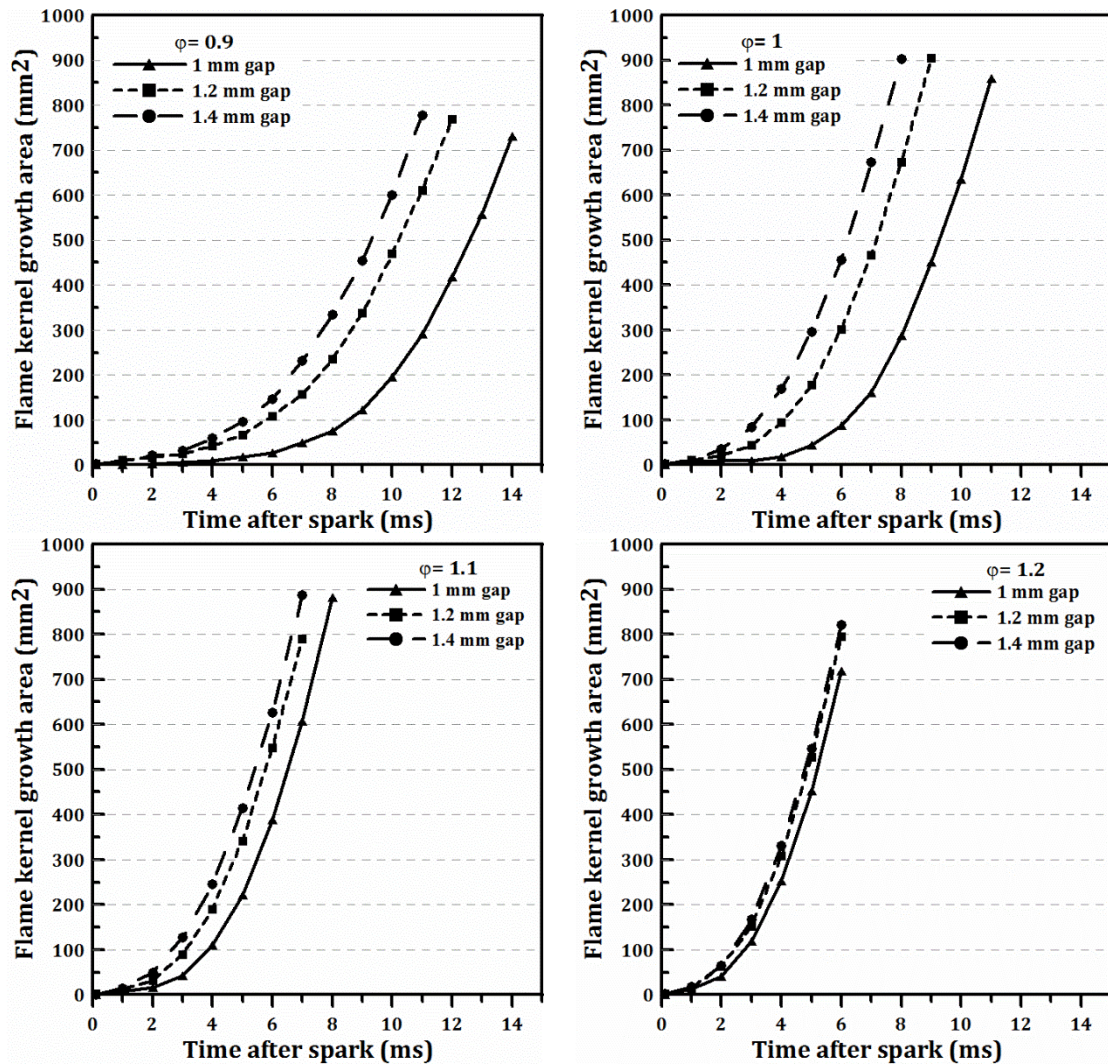
Figure 6.5. Flame kernel area development as a function of time with spark plug gap of 1, 1.2 and 1.4 mm for gasoline fuel at different equivalence ratio of φ = 0.9, φ = 1, φ = 1.1 and φ = 1.2 with initial temperature of 90ºC and initial pressure of 1 bar.

6.4 Flame Tomography Imaging using PLIF Technique

PLIF imaging of isooctane & 3-pentanone was utilized to obtain planar details of the combustion zone and the flame front development on the horizontal swirl plain after spark

ignition. PLIF was employed for accurate identification of the flame front in a certain plane just below the spark plug that could not be identified by chemiluminescence imaging due to the projected line-of-sight nature of the latter technique [179, 180]. Furthermore, PLIF system was designed to meet certain criteria, including finding all edges without any false detections and to give higher fidelity. The PLIF system was synchronised with the engine crank angle to capture images at 25 CAD BTDC which was the ignition timing. PLIF tests were all performed under stoichiometric conditions at 1200 rpm, with the engine coolant and oil temperature fixed at 90°C, injection timing at 280 CAD BTDC and injection pressure of 150 bar. Due to the limited optical access for laser excitation, the laser beam was adjusted just below the spark plug ground electrode to cover the area at vicinity of the spark plug where crucial early flame developments took place. Because of the expected regular flame propagation generated from these test conditions, the consumption of any premature tracer would happen close to the flame front. Consequently, this consumption will have no substantial effect on the flame front measurements because the practical devices spatial resolution is not high enough to resolve the flame front anyway [121]. Therefore, the flame front detection was determined based on the disappearance of the 3-pentanone concentration in the flame front. Additionally, 3-pentanone also did not induce any fluorescence through the flame zone. The fluorescence signal intensity decreased between the unburned and burn gas. After the ignition, the fluorescence images were recorded to provide a qualitative measurement of the combustion process. For each test point, two sets of 200 backgrounds without any flame and 200 flame images were captured. The background images were averaged and then subtracted from the raw flame images to eliminate any background noise. The raw flame images were then averaged. Afterwards, the instantaneous flame which closely matched the average flame image was chosen for comparison as shown in Figure 6.6.

Figure 6.6 shows that at 10 CAD after ignition timing (AIT), the flame kernel appears on the left side of the spark plug. Furthermore, the spark plug gaps of 1.2 and 1.4 mm demonstrate a larger flame area compared to that of 1mm gap. The PLIF images reveal the presence of fresh gases trapped in the burned gas area, which may be explained by the complex wrinkling of the flame front and an isotropic flame development [180, 181]. Figure 6.6 illustrates at 15 CAD AIT the flame front contours boundary between burned and unburned gases regions. The spatial location variation and the wrinkling of the flame front characterize the influence of cycle-to-cycle dispersion and turbulence motion on the flame development. The spark plug gap of 1.4mm consistently has a larger flame area compared to the other gaps. At 15 CAD AIT the flame area of the spark plug gap1.4mm is not totally covered due to the limited area of the laser sheet. At 20 CAD AIT for all the spark gaps the flame area is not totally covered by the laser sheet.
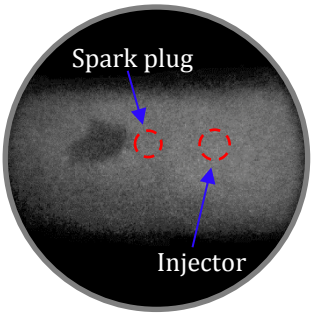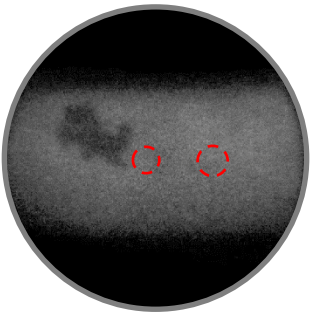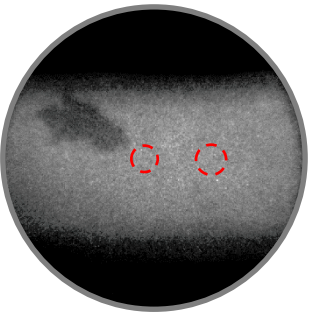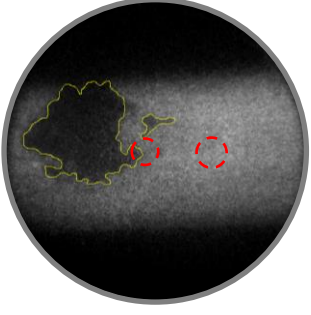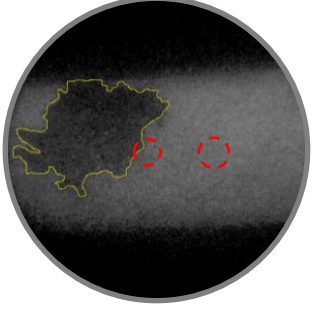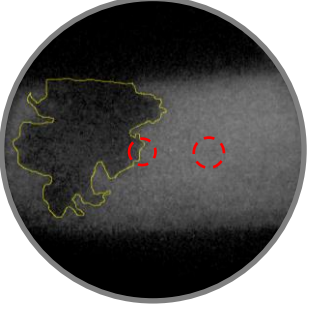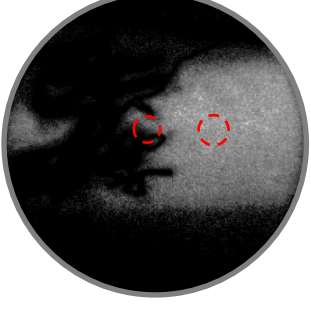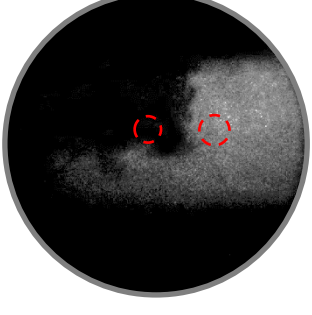
Figure 6.6.Instantaneous PLIF Images of the three spark plug gaps for gasoline at φ = 1 and different crank angle with engine speed of 1200 rpm, ignition timing of 25 CAD BTDC, injection pressure of 150 bar and injection timing of 280 CAD BTDC.

6.5 Impact of the Spark Plug Gap on the Load and COV of IMEP

Load variations versus equivalence ratios for the three different spark plug gaps investigated are presented in Figure 6.7. It can be noticed that as the equivalence ratio increases, the load increases until it reaches the maximum and then starts to decrease again for very rich conditions. The lower mean effective pressure associated with the lean and very rich conditions is fundamentally linked to the flame speed. The maximum flame speed occurs when the mixture strength for hydrocarbon fuels is about 10% rich. Therefore, for both lean and very rich

mixtures, the flame speed decreases. Lean mixtures release less thermal energy, resulting in lower flame temperatures and hence lead to lower flame speeds. Whilst, very rich mixtures experience incomplete combustion, hence also release less thermal energy resulting in lower flame speeds. The reduction of the flame speed leads to an increase in the burning time losses, and consequently reduces both the indicated mean effective pressure and engine power [182]. The smallest gap of 1 mm consistently results in lower loads for the entire range of equivalence ratios tested. For equivalence ratio smaller than 1, the larger gap of 1.4 mm results in higher load, but for the equivalence ratios higher than 1, the 1.2 and 1.4 mm gaps result in similar loads. This behaviour can be justified by the fact that lean mixtures are more susceptible to the initial kernel size, whereas there is a limit to the effect of initial kernel size on the combustion behavior of rich mixtures. These results coincide with the aforementioned observations regarding the average flame kernel area, which demonstrates that the spark plug gap has a significant effect on the flame kernel size at lean mixtures, whilst this effect nearly diminishes in rich mixtures. Figure 6.8 demonstrates the effect of the three different spark plug gaps investigated on the coefficient of variation (COV) of IMEP for different equivalence ratios. Many parameters attributed to the cyclic variations occurred for the combustion process [99, 183], such as 1) the mixture motion variation at spark timing from cycle to cycle within the cylinder, 2) the air and fuel mass flow rates feed to the engine cylinder varied from cycle to cycle, 3) the amount of residual gasses remained inside the combustion chamber varied from cycle to cycle, especially in the vicinity of the spark plug. The magnitude of cycle-by-cycle combustion variation increases as the mixture becomes leaner with excess air or more dilute with a higher burned gas fraction from residual gases.
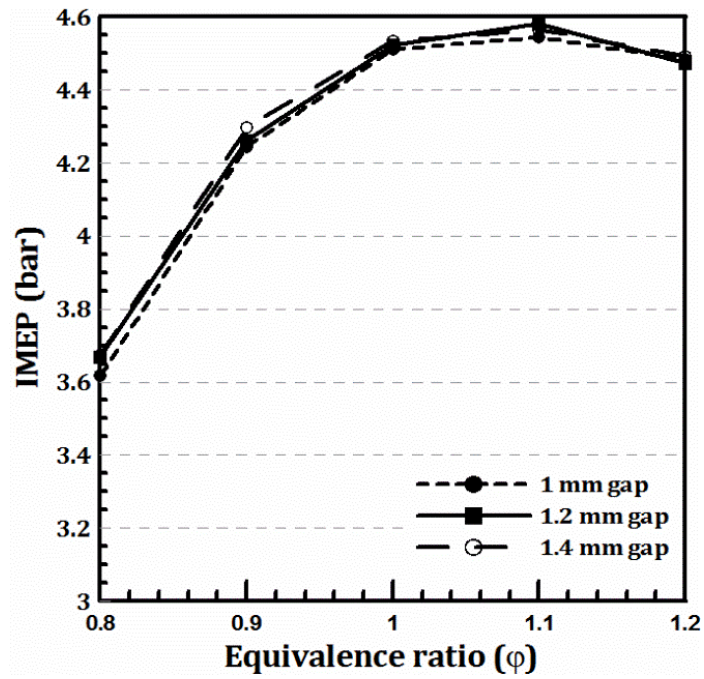
Figure 6.7. Effect of the spark plug gap on the engine load (IMEP) for gasoline at different equivalence ratio with engine speed of 1200 rpm, ignition timing of 25 CAD BTDC, injection pressure of 150 bar and injection timing of 280 CAD BTDC.
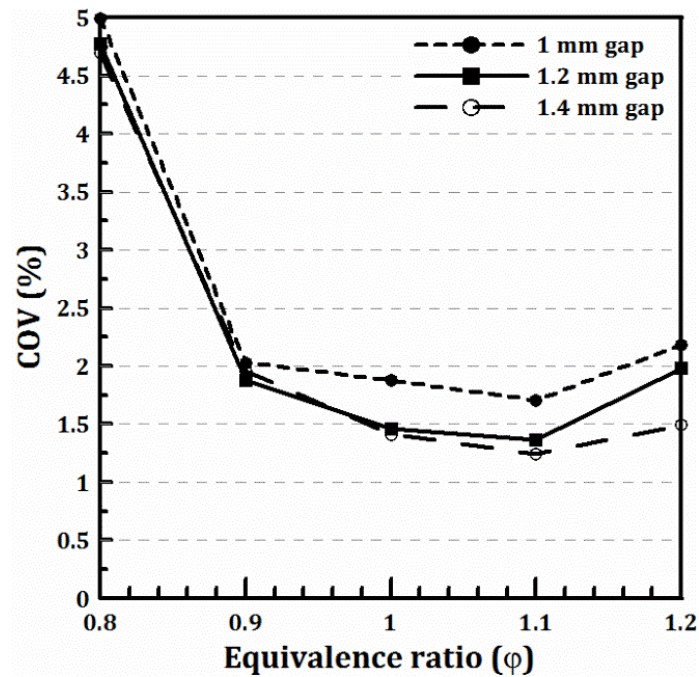
Figure 6.8. Effect of the spark plug gap on the COV of IMEP for gasoline at different equivalence ratio with engine speed of 1200 rpm, ignition timing of 25 CAD BTDC, injection pressure of 150 bar and injection timing of 280 CAD BTDC.

The smallest gap of 1 mm consistently results in higher COV of IMEP for the entire range of equivalence ratio tested. The COV of IMEP of 1.2mm and 1.4mm gaps is significantly lower compared to that of 1mm gap for stoichiometric and rich conditions. Whilst for lean conditions the difference in COV of IMEP between the gaps is reduced. Le Coz [184] demonstrated that the interactions by the flow field are categorized as the convection by the mean large-scale velocity field (low frequency velocity) and the wrinkling by the small-scale turbulence (high frequency fluctuation intensity). He revealed that the cyclic variation in flame initiation duration is predominantly affected by flame kernel convection which is determined by the large-scale fluid motion when the mixture is lean and homogeneous. Also, he stated that there would be no correlation between turbulence and early combustion if the engine is operated at air-fuel ratio leaner than φ =0.625. The small-scale turbulence affects the initiation stability mostly for the equivalence ratio higher than φ =0.8. It is generally accepted that the more homogeneous the mixture is, the lower the cyclic variability will be [185].

The higher COV of IMEP of smaller spark plug gaps can be linked to the variation in the contact area between the electrode and flame from cycle to cycle which cause cyclic variations to the amount of heat losses [90, 186]. The local flow field near the spark plug position control the contact area between flame and electrodes. Therefore, smaller contact area will be produced during the cycles in which the flame convected away from the electrode compared to that cycles in which the flame remains centred in the spark gap. The heat transfer from the hot gas kernel to the electrodes is mainly controlled by conduction and convection. The heat loss from the flame kernel to electrode affects the flame growth through two mechanisms: (1) it decreases the kernel temperature, leading to a relative contraction of the kernel, and (2) it takes heat out of the flame front, and thereby decreases the burning velocity. Consequently, the lower burning

velocity will lead to slower flame development and the cycle-by-cycle variations in the phasing of the main combustion event become larger.

Moreover, a clear difference in the COV of IMEP between the gaps is noticed especially for stoichiometric and rich conditions. This can be linked to the shrouding effect of closer gaps, which reduces the benefits of mixture turbulence within the gap, and consequently leads to large contact area between flame and electrodes, resulting in more heat losses from the flame kernel to electrode. In addition, stoichiometric and slightly rich conditions have higher flame temperature, which increases the heat losses by conduction to the electrode due to the less turbulent flow near the closer gap [186].

At stoichiometric condition φ =1, the reduction in COV of IMEP of the gap 1.2 mm and gap 1.4 mm is 22.3% and 24.7% respectively, compared to that for the gap of 1 mm. whilst for the rich condition of φ=1.1 the reduction in COV of IMEP of the gap 1.4 mm and gap 1.2 mm is 27.5 % and 20.5 % respectively, compared to gap 1 mm. For the rich condition of Φ=1.2, the reduction in COV of IMEP of the gap 1.4 mm and gap 1.2 mm is 31.96 % and 9.59 % respectively, compared to gap 1 mm.

6.6 Impact of the Spark Plug Gap on Flame Speed, ROHR, MFB and In-cylinder Pressure

The single cycle combustion images shown in Figure 6.9 represent the typical cycle for each spark plug gap at stoichiometric condition of Φ =1, 25 CAD BTDC spark timing, 280 CAD BTDC injection timing and the IMEP vary approximately around 4.5 bar due to the change of the spark plug gap. In all the images, the flames tend to propagate toward the exhaust valves due to the higher local temperature and the swirl, as shown in previous studies [187, 188].

Furthermore, this can be attributed to the spark plug's position closer to the exhaust valves and the clockwise tumble motion in the combustion chamber. In addition, the installation of the injector near to the exhaust valves along with the high possibility of spray flash boiling causes the fuel to be relatively richer around this region of the combustion chamber, resulting in higher flame propagation speed adjacent to the exhaust valve side [180]. For this condition, spark plug gaps of 1.4 and 1.2 mm demonstrate consistently higher flame speed compared to that of 1 mm gap. This may be occurred when the spark plug gap is extended from 1 mm to 1.2 mm and 1.4 mm, where the ignition energy is increased, resulting in large plasma volume which contacts more unburned gas. As a result, a faster flame kernel will be developed, which accelerates the mass fraction burnt which derives higher heat release rate.

Figure 6.9 shows the average calculated flame speed of gasoline fuel for different spark plug gaps at equivalence ratios of Φ =0.8, 1 and 1.2. The flame speed calculation is obtained from the MATLAB according to Figure 6.2. A mask has been applied individually to each image before the filtering process occurrence, in order to make sure that the program process only the flame data contained within the respective fields of view, i.e. piston crown window. Furthermore, as the flame begins to expand into the unburned charge of the combustion chamber, the flame speed is increased up to crank angles near to 30 CAD AIT. Beyond this crank angle the flame speed decreases as the flame reaches the end of the optical field of view and begins to interact with the cylinder walls. Therefore, for the current study, the flame speed is investigated mainly up to ≈ 30 CAD AIT. Figure 6.9 shows that for the all equivalence ratios the flame speed of spark plug gap of 1.4 mm and 1.2 mm is higher compared to the spark plug gap of 1 mm. At equivalence ratio Φ =1 the spark plug gap of 1.4 mm has the highest flame speed of about 6.8 m/s at 362 CAD, nearly 1.5 % faster than the peaks of the spark plug gap of 1.2 mm and 7% for gap of 1 mm. The flame speed of spark plug gap of 1.4 mm at 350 CAD is

about 3.52 m/s, 9.33% higher than that of 1.2 mm gap and 11.5 % to 1 mm gap. This means shortly after the ignition, the flame speed of 1.4 mm gap becomes significantly faster than the other two gaps. Additionally, spark plug gap of 1.4 mm has the shortest ignition delay among the three gaps. These two reasons result in the very fast flame propagation in 1.4 mm gap combustion, as shown in previous figures.
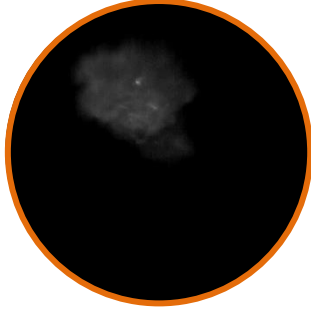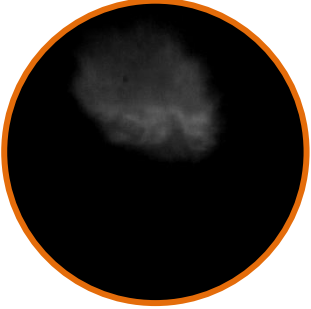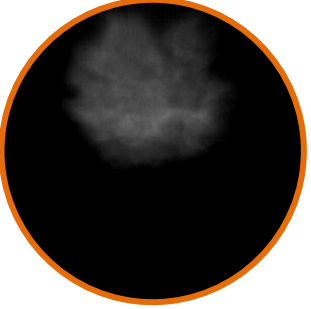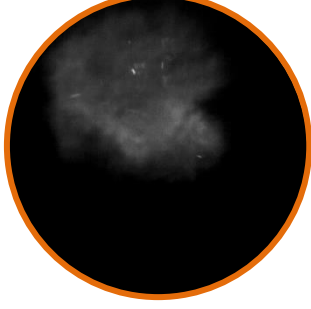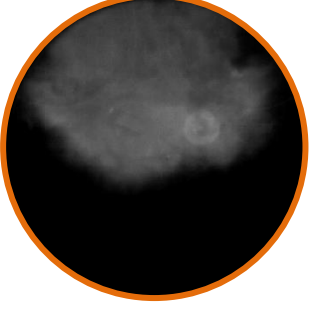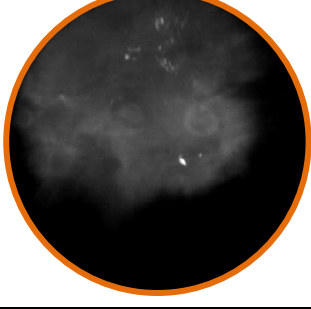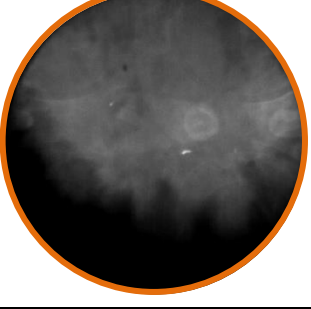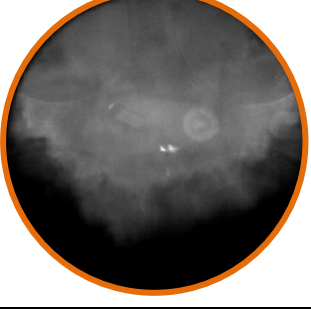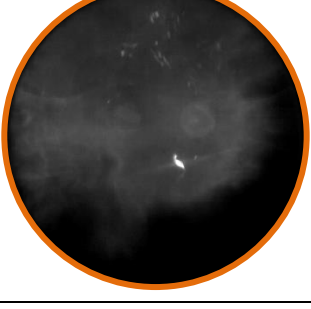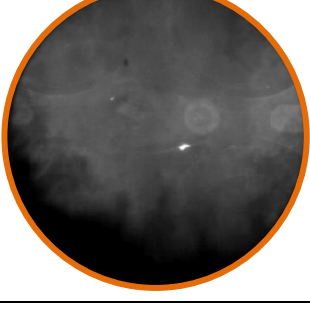
CAD AIT	Spark plug gap 1 mm	Spark plug gap 1.2 mm	Spark plug gap 1.4 mm
10			
15			
20			
25			
30			

Figure 6.9. Instantaneous flame images of gasoline at stoichiometric condition of Φ=1 under different spark plug gaps with engine speed of 1200 rpm, ignition timing of 25 CAD BTDC, injection pressure of 150 bar, injection timing of 280 CAD BTDC and IMEP of 4.5 bar.
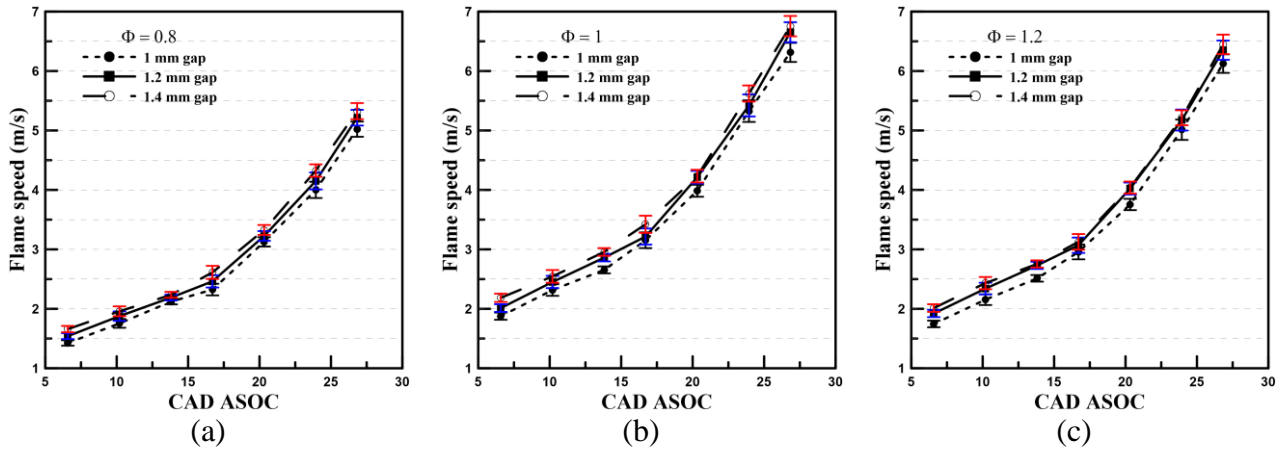
Figure 6.10. Flame speed development at various equivalence ratio (a) φ =0.8 (b) φ =1 (c) φ =1.2 under different spark plug gaps for gasoline with engine speed of 1200 rpm, ignition timing of 25 CAD BTDC, injection pressure of 150 bar and injection timing of 280 CAD BTDC.

Figure 6.11 shows the effect of variations of spark plug gaps on the in-cylinder pressure at different equivalence ratios. Kistler 6051A piezoelectric pressure transducer was used to measure the In-cylinder pressure in the engine; this transducer was incorporated with a Kistler 5011B charge amplifier to amplify the transducer signal. The linearity error for both the pressure transducer and the charge amplifier was approximately less than ∓ 0.5% of the full scale. The in-cylinder pressure data was recorded with a high resolution of 0.1 CAD for 300 consecutive cycles, and the data was precisely controlled by using the LabVIEW program. Experimental uncertainty was evaluated at 95% confidence level for the in-cylinder pressure data to ensure confidence that the difference between the gaps peak pressure was not due to the measurements error. It was found that the maximum uncertainty in the peak pressure measurements was approximately ∓0.78%.

At each testing condition, the in-cylinder pressure results were averaged from 300 consecutive cycles. The maximum in-cylinder peak pressure is demonstrated at stoichiometric condition of φ =1. For both lean and very rich conditions, the associated flame speed will be lower, and consequently the peak pressure will be reduced. For lean mixture conditions, the mass flow

rate of fuel is low which produces lower exothermic energy resulting in lower flame temperature and hence lower flame speed. Whilst for rich mixtures the in-cylinder temperatures are reduced due to the incomplete combustion, and consequently also produce less thermal energy resulting in lower flame speed. This reduces the mean effective pressure and consequently the engine power reduces. For all equivalence ratios, the maximum in-cylinder pressure occurs for spark gaps of 1.4 and 1.2mm. Furthermore, due to the faster burning of the spark plug gaps 1.4 and 1.2mm the peak pressure slightly shifts towards TDC compared to that of spark plug gap 1mm.

Figure 6.12 and Figure 6.13 show the effect of variations of spark plug gaps on the heat release rate and mass fraction burned characteristics calculated from the averaged in-cylinder pressure data. The MFB was defined as the accumulated heat released in successive crank angle ranging from the start to the end of combustion divided by the total released heat in the whole combustion process [189]. The heat release rate ($\frac{dQ}{d\theta}$) was calculated using the following equation [99];

$$\frac{dQ}{d\theta} = \left(\frac{\gamma}{\gamma - 1} * P * \frac{dV}{d\theta} \right) + \left(\frac{1}{\gamma - 1} * V * \frac{dP}{d\theta} \right) \tag{6.2}$$

where the heat capacity ratio (γ) is the ratio of specific heats (C_p/C_v); θ is the crank angle; Q is the released heat; P and V are the pressure and cylinder volume.

The highest rate of increase in the HRR curve is obtained from 1.4 mm gap, followed by 1.2 and 1 mm gap. Once more, the leanest conditions have a significantly lower peak HRR compared to that of the richest condition. The rate of combustion and heat release is mainly linked to the mixture strength. All the hydrocarbon fuels have a maximum flame speed at nearly 10% rich mixture. For both lean and very rich mixtures, the flame speed is reduced. Less heat release is associated with the lean mixture, resulting in lower flame temperature and lower

flame speed. Likewise, less heat release generated for very rich mixture due to the incomplete combustion (C and CO instead of CO_2) and consequently less flame speed will be produced.

The results demonstrate that as the spark plug gap increases, the heat release rate increases and accelerates the mass fraction burnt and this could be linked to the higher ignition energy associated with the gap extension [171]. The heat release rate is seen to have a profile similar to an isosceles triangle, with a maximum of 23 J/deg at about 13 CAD ATDC for $\varphi = 1$ for gap of 1.4 mm, corresponding to the 50% value on the mass fraction burned curve. Table 6-3 also summarize the mass burnt fraction at different equivalence ratio. For $\varphi = 0.8$, as the gap is increased from 1mm to 1.4mm, the initial flame growth becomes faster by about 1.5 CAD. These results come from the increase of ignition energy and the expansion of the plasma volume which contacts more unburned gas [171]. As a result of faster kernel development, the maximum heat release rate is increased. For stoichiometric and rich conditions, the initial flame growth becomes faster and exhibit more heat release rate.

The mass fraction burned curve has an exponential profile. In the initial phase of the combustion process, the mass burning rate will be dependent on the laminar flame speed, which is in turn a function of mixture strength. Therefore, the fastest mass burning is displayed at stoichiometric conditions compared to that of both lean and rich conditions. The spark plug gap of 1.4mm is expected to have a faster mass burning due to its large plasma volume, which contacts more unburned gas compared to that of the other gaps. Consequently, a faster flame kernel will be produced, which accelerates the mass fraction burnt, and derives higher heat release rate. For stoichiometric condition of $\varphi = 1$ the ignition delay is minimum for spark gap of 1.4mm with 27.32 CAD while for 1.2mm is 27.8 CAD and for 1 mm is 28.15 CAD. The decrease in the ignition delay for spark gap of 1.4 mm is due to the increase occurs in the

ignition energy. For 50% mass fraction burned, the spark gap of 1.4 is faster with 37.5 CAD compared with spark gap of 1.2 mm with 38 CAD and spark gap of 1 mm with 39.14 CAD. At the lower flame temperatures corresponding to leaner mixtures the rate of thermal and molecular diffusion is decreased, which restricts flame propagation [190]. Therefore, the slowest mass burned fraction is noticed for Φ=0.8.

Figure 6.11. Effect of the spark plug gap on the in-cylinder pressure for gasoline at different equivalence ratio with engine speed of 1200 rpm, ignition timing of 25 CAD BTDC, injection pressure of 150 bar and injection timing of 280 CAD BTDC.

Figure 6.12.Effect of the spark plug gap on heat release rate for gasoline at different equivalence ratio with engine speed of 1200 rpm, ignition timing of 25 CAD BTDC, injection pressure of 150 bar and injection timing of 280 CAD BTDC.
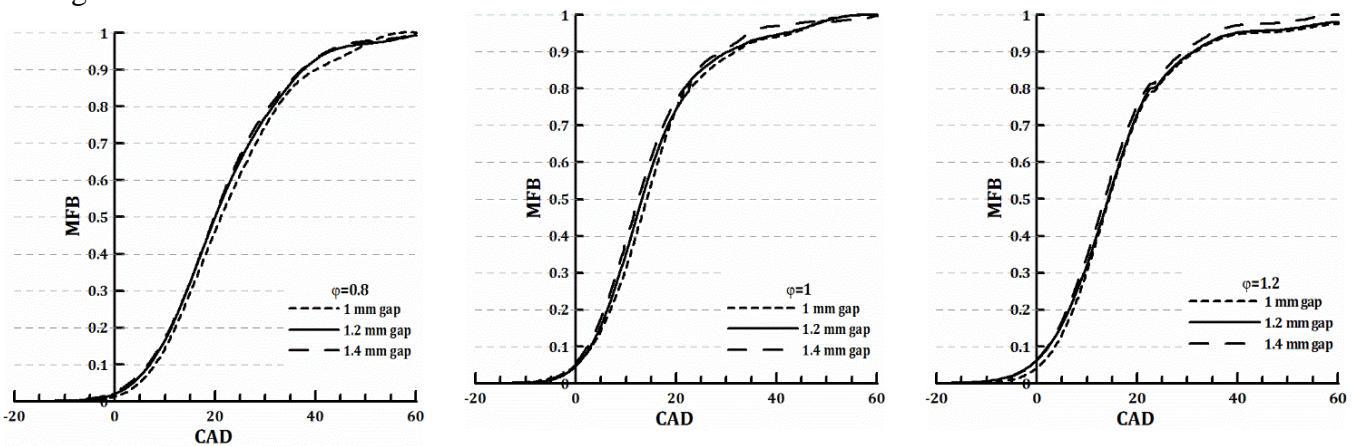
Figure 6.13. Effect of the spark plug gap on mass burned fraction for gasoline at different equivalence ratio with engine speed of 1200 rpm, ignition timing of 25 CAD BTDC, injection pressure of 150 bar and injection timing of 280 CAD BTDC.

Table 6-3. Crank angle position ASOC for different mass burned fraction

gap	φ =0.8			φ =1			φ =1.2		
	t_{0-10} (ignition delay)	t_{0-50}	t_{0-90}	t_{0-10} (ignition delay)	t_{0-50}	t_{0-90}	t_{0-10} (ignition delay)	t_{0-50}	t_{0-90}
1	33	46	65	28.15	39.14	56.5	28.5	39.5	57.5
1.2	32	45	63	27.8	38	55	27.5	39	56
1.4	31.5	44.8	62.5	27.32	37.5	54	27	38.5	54.5

6.7 Impact of the Spark Plug Gap on Emissions
6.7.1 Hydrocarbon and NOx Emissions

HC and NO_x emissions for the (ULG95) at 150 bar injection pressure were measured using a Horiba MEXA-7100DEGR gas analyser with a resolution of 1 ppm. Figure 6.14 shows the influence of the engine operating equivalence ratio on the indicated specific NOx emissions (g/kwh) for three different values of the spark plug gaps. NOx emissions are maximum at lean condition of φ = 0.9 and decrease rapidly as the equivalence ratio is increased or decreased. That is due to the interaction between the effects of increasing temperature greatly at slightly rich conditions, and Oxygen availability and gasoline high heating value on volume basis for lean conditions. In order to interpret the NOx emissions behaviour, the trend of NOx emissions should be linked to the combustion phasing and in-cylinder temperature distribution, which are considered as main parameters of in-cylinder NOx formation in the previous studies [99]. It is noticed that the spark plug gaps of 1.2 and 1.4 mm consistently are associated with higher NOx emissions for all equivalence ratios compared to that of 1mm spark plug gap. This can be demonstrated based on the in-cylinder pressure data shown in Figure 6.11. This data has clarified that the larger spark gaps consistently have higher peak pressure, and consequently higher temperature inside the cylinder resulting in higher NOx emissions [191]. The spark plug gaps of 1.4 mm and 1.2 mm show a higher NOx emission of 10.04% and 9.42%, respectively compared to 1 mm gap at lean condition of φ = 0.8. At stoichiometric conditions the spark plug gaps of 1.4 mm and 1.2 mm display an increase in NOx emission with 6.3% and 4.8%,

respectively compared to 1 mm gap. On the other hand, stoichiometric and lean mixtures exhibit higher NOx emission variability. As it is revealed in Figure 6.8, stoichiometric and lean mixtures lead to higher COV of IMEP, translated into more intense combustion variability, which leads to higher NOx emission variability [192].

Figure 6.15 shows the influence of the engine operating equivalence ratios on the indicated specific HC emissions (g/kwh) for three different values of the spark plug gaps. The hydrocarbon emissions are minimum for lean condition of φ =0.9 and increase for both very lean conditions and richest conditions. If air-fuel ratio is too lean, poorer combustion occurs and the temperature is too low for hydrocarbon to burn late in the expansion stroke, this result in large amounts of HC emissions, the extreme is total misfire at leaner air-fuel ratios. One misfire out of 1000 cycles gives exhaust emissions of 1gm/kg of fuel used [193]. Furthermore, the low flame speed at low φ means that the flame may not even reach all the mixture. With fuel rich mixture condition the level of HC increase due to incomplete combustion and crevice volume. For all equivalence ratios the spark plug gap of 1.4 mm shows the minimum hydrocarbon emissions compared to spark plug gaps of 1.2 mm and 1 mm. The maximum decrease in hydrocarbon emissions is noticed at φ = 0.8 for spark plug gap of 1.4mm at with 12.4% compared to that of 1 mm gap. followed by 1.2mm gap which displays 8.7% decrease in hydrocarbon emissions compared to 1mm gap.

Based on the aforementioned results, as the spark gap is widened, a reduction in the HC emission is achieved. These results are consistent with the findings of Burgett et al. [76], who concluded that wider gaps were responsible for decreases of HC emissions. The wider the gap, the greater is the volume of air-fuel mixture exposed to the spark which assists in the ignition of lean mixtures. Small gaps can cause the engine to misfire intermittently because the spark plug electrodes quench the flame kernel due to the possible heat transfer from the flame to

electrode. Furthermore, closer gap also provides a shrouding effect, and hence the benefits of mixture turbulence within the gap will be lost. Consequently, this will lead to improper mixing around the spark plug, resulting in less efficient combustion process and more HC emissions.
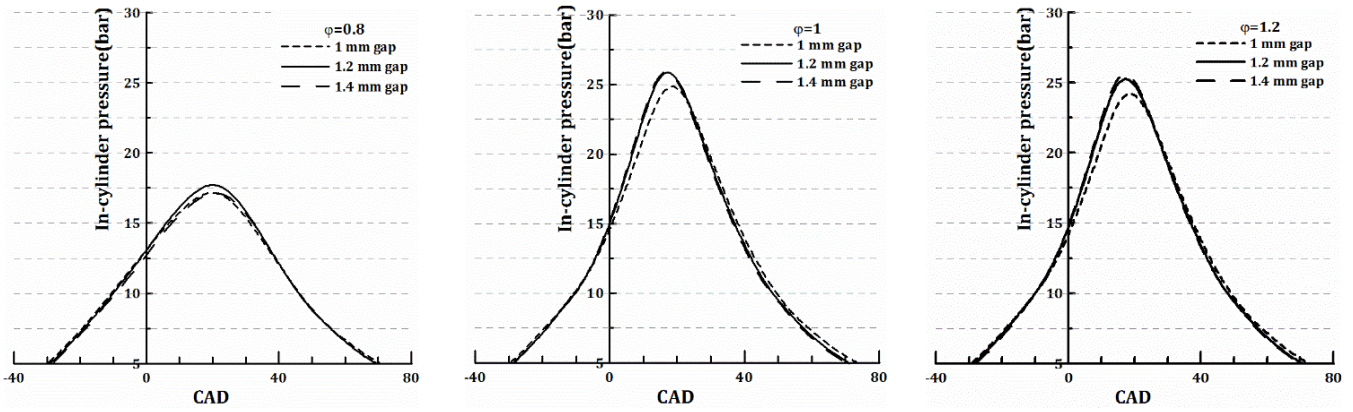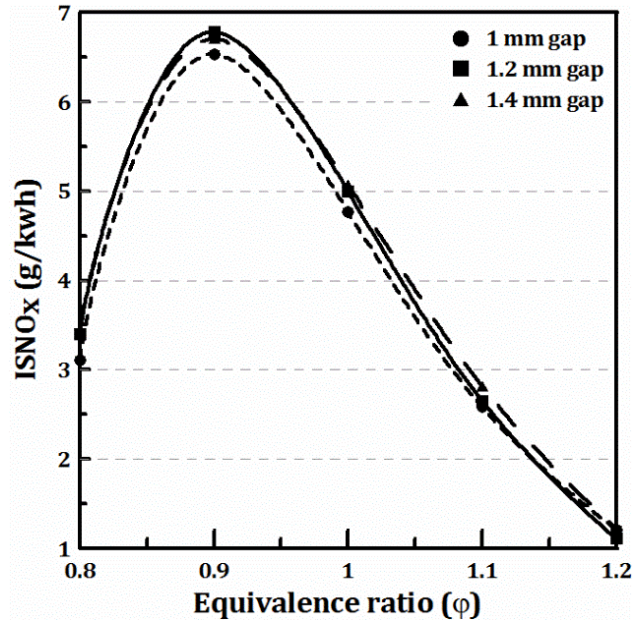

Figure 6.14. Effect of the spark plug gap on NOx emissions for gasoline at different equivalence ratio with engine speed of 1200 rpm, ignition timing of 25 CAD BTDC, injection pressure of 150 bar and injection timing of 280 CAD BTDC.
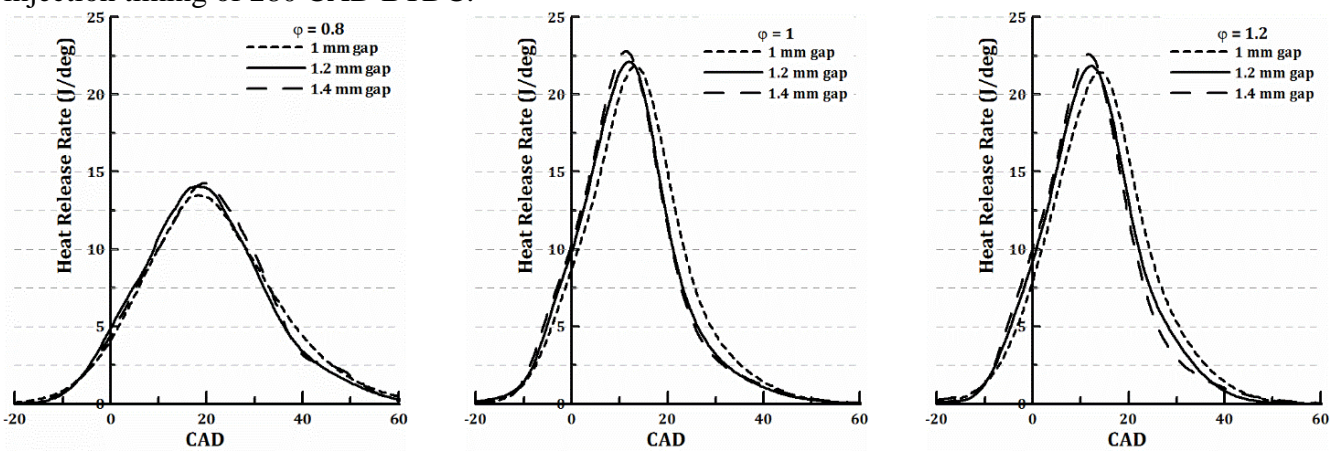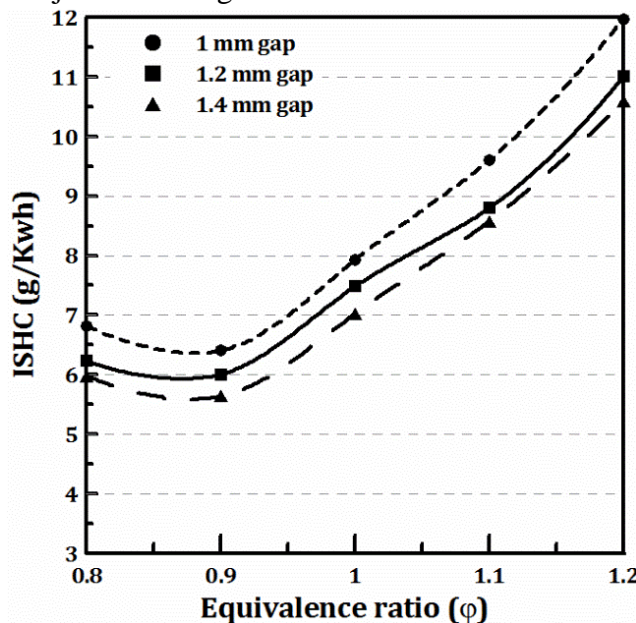

Figure 6.15. Effect of the spark plug gap on HC emissions for gasoline at different equivalence ratio with engine speed of 1200 rpm, ignition timing of 25 CAD BTDC, injection pressure of 150 bar and injection timing of 280 CAD BTDC.

6.7.2 Impact of the Spark Plug gap on the PN Emissions

Figure 6.16 presents total PN concentration over different equivalence ratio for the three spark plug gaps. The data show the sensitivity of the engine out particle size to global equivalence ratio. It was noticed that for the leanest cases, they are dominated by the smallest particle sizes, whereas the richest cases show higher concentrations of large particles. Also as φ increases, the distribution consistently shifts toward agglomeration mode particles. For injection timing of 280 CAD BTDC, as the mixture becomes richer, the amount of fuel injected increases and consequently the injection duration increases and thus could increase the likelihood of spray impingement on the in-cylinder surfaces and liquid fuel films [194]. This wetting increases the probability of locally rich mixtures, causing more soot to be formed under partially premixed or diffusive combustion conditions rather than premixed conditions [195]. This can contribute to the larger number of agglomeration mode particles seen in the study under rich equivalence ratios. Furthermore, due to the higher in-cylinder temperatures, the temperature late in the expansion stroke and during the exhaust stroke will remain higher. This higher temperature can promote greater growth of particles under rich conditions late in the expansion stroke and potentially even into the exhaust stroke. This higher temperature, combined with lower oxygen concentrations and higher hydrocarbon concentrations, can aid in soot growth.

For all the equivalence ratios tested the results of 1.2mm and 1.4mm gaps consistently have lower PN concentration compared to the 1mm gap. Small gap relatively experiences les turbulent intensity within the gap, and consequently tends to degrade the fuel-air mixing around the spark plug, which increases the HC emissions and PN concentration emissions [4]. Moreover, based on the aforementioned results, the wider gaps produce lower COV of IMEP and higher in-cylinder pressure, turbulent flame speed and heat release rate. These parameters will enhance the combustion efficiency and reduce the PN concentration emissions [196]. At

φ=0.8, as the spark plug gap increases from 1mm to 1.2mm and 1.4mm the total particulate number concentration reduces with 9.8% and 10.6%. Whilst for stoichiometric conditions φ=1, as the spark plug gap increases from 1mm to 1.2mm and 1.4mm the total particulate number concentration reduces with 20.7% and 33.2%. for rich conditions φ=1.2, as the spark plug gap increases from 1mm to 1.2mm and 1.4mm the total particulate number concentration reduce with 5.3% and 5.6%.

(a)

(b)

(c)
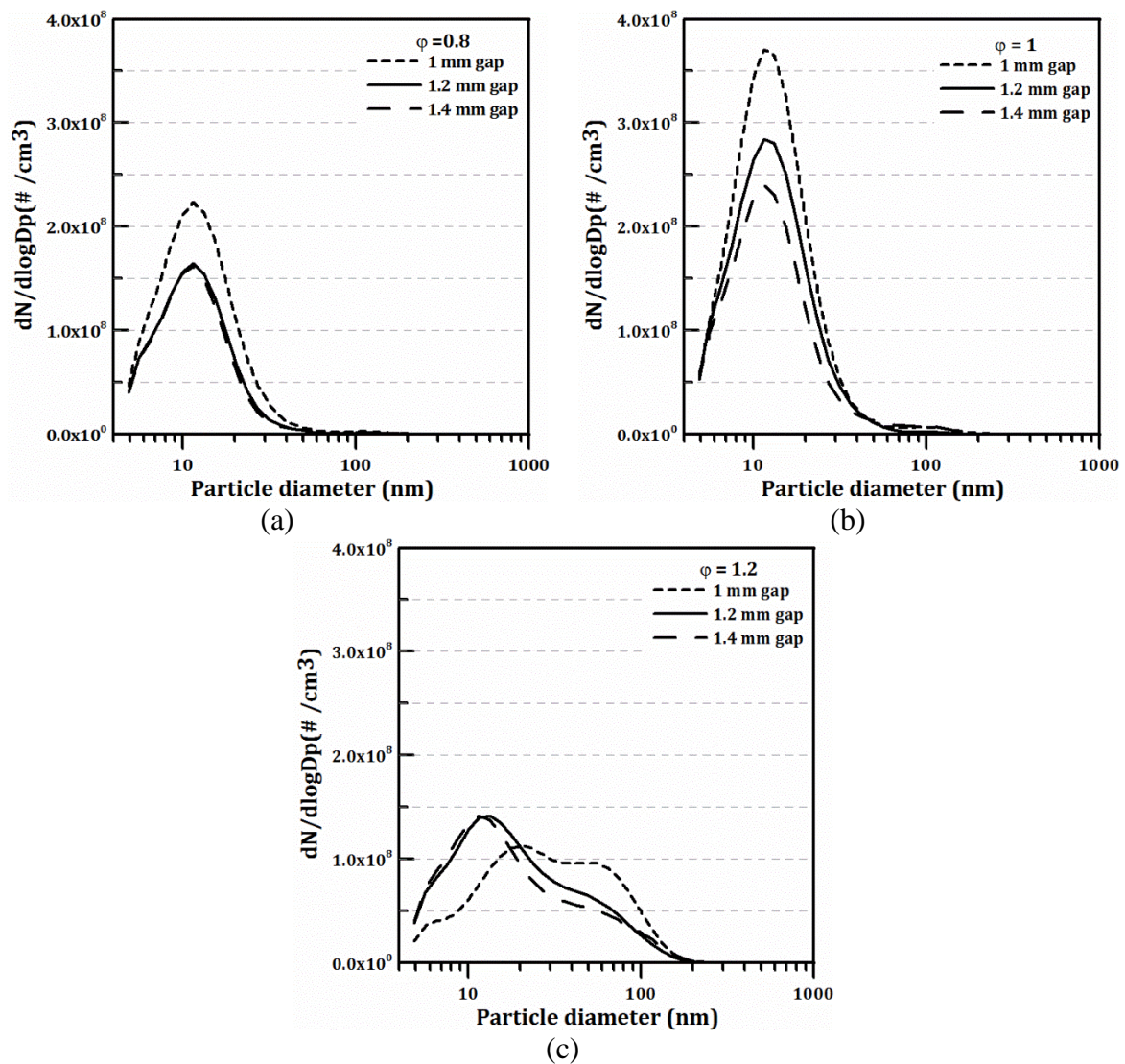
Figure 6.16. Particulate Number concentration of PN emission with NGK spark plug at equivalence ratios of (a)-Φ=0.8 (b)-Φ= 1 (c)-Φ=1 with engine speed of 1200 rpm, ignition timing of 25 CAD BTDC, injection pressure of 150 bar and injection timing of 280 CAD BTDC.

6.8. Summary and Conclusions

Experimental optical and thermal tests were carried out in a constant-volume combustion chamber and a single cylinder gasoline direct injection (GDI) engine, to obtain a comprehensive understanding of the effects of spark plug electrode gap on flame kernel development, engine performance and emissions. High-speed Schlieren visualization was utilized to study the flame kernel growth at different equivalence ratios. Planar Laser Induced Fluorescence (PLIF) was employed to investigate the combustion zone and the flame front development on the horizontal swirl plane after spark ignition. High-speed imaging technique was carried out to study turbulent flame propagation. Combustion analysis and examination of engine emissions were carried out over different spark plug gaps. The conclusions drawn from the work are as follows:

1. At the beginning of the flame kernel initiation and up to 1ms from the start of spark the difference in the flame kernel size between different spark plug gaps is relatively small especially for larger gaps such as 1.2 and 1.4 mm. As the time after ignition progresses, the larger spark plug gaps generate a significantly larger flame kernel area compared to that of the spark plug gap of 1mm.

2. The effect of the spark plug gap is dominant at lean and stoichiometric conditions and diminishes for rich conditions.

3. The smallest spark gap of 1 mm generates lower engine load output for the entire range of equivalence ratio tested. For equivalence ratio smaller than 1, the spark gap of 1.4 mm results in higher load, but for equivalence ratios higher than 1, the 1.2 and 1.4 mm gaps result in similar loads. The smallest gap of 1 mm consistently results in higher

COV of IMEP for the entire range of equivalence ratio tested. The COV of IMEP of 1.2mm and 1.4mm gaps is significantly lower compared to that of 1mm gap for stoichiometric and rich conditions. Whilst for lean conditions the difference in COV of IMEP between the gaps is reduced.

4. The in-cylinder pressure, flame speed, heat release rate and the mass fraction burned increase with the spark plug gap. The maximum spark plug gap gives minimum hydrocarbon emissions and particulate number concentration, but with higher NOx emissions due to the high temperature combustion temperature as well as the increase in flame speed and in-cylinder pressure. However, increasing the spark plug gap beyond a certain limit will demand higher voltage to arc across and create a spark; consequently, the constant voltage employed during this study will not be high enough to arc across, resulting in a misfire.

Chapter 7

SUMMARY, CONCLUSIONS, AND RECOMMENDATIONS FOR FUTURE WORK

The main aim of this thesis was to explore the impacts of injector fouling on spray characteristics, engine performance and emissions. In particular, the mixture stratification, the physical characteristics and the elemental composition of the deposits, the diffusion phenomena associated with the injector fouling, and the gaseous and particulate matter (PM) emissions were all studied and the preceding chapters demonstrate in more detail the results and discussion regarding this work. Furthermore, a comprehensive examination was carried out to study the effect of the spark plug gap on flame kernel development, engine performance and emissions. A summary, findings, and conclusions of the current investigation are summarized in this chapter, alongside suggestions for future work.

7.1 Summary and Conclusions

The optical investigation of the impacts of injector deposits and the spark plug gap on the GDI research engine performance and emissions resulted in a huge amount of useful information through the preceding three chapters. The investigation's significant findings derived from this work are summarized below.

Chapter 4-Investigation of Injector Coking Effects on Spray, Mixture Stratification and Emissions

Injector tip deposit can significantly alter spray structure. The deposit accumulation inside the holes was different from nozzle to nozzle; this could be due to their location and projection to the combustion chamber boundary conditions. Among all the jets, ignition jets were more prone to tip coking, while the rear jets were least affected. The coked injector experienced a longer penetration length and narrow plume cone angle, especially for ignition and rare jets, in comparison to the clean injector. Likewise, the coked injector increased the separation angle between the spray plumes. Furthermore, the PLIF spray foot print of the coked injector demonstrated that the plume cross section area changed from near-circular to narrow ellipses, in comparison to the circular cross section of the clean injector spray.

The PDPA results were in agreement with the high-speed imaging data. The ignition jets were most affected by the tip coking and the rear jets were least affected. The coked injector yielded a higher droplet velocity and larger droplet size (SMD) compared to that of the clean injector. The PDPA data confirmed the assumption that the injector tip coking promotes conversion of fuel pressure into liquid velocity rather than turbulence energy. Combustion images of the coked injector were associated with small bright spots around the injector tip, indicating an injector tip diffusion flame due to deposit build-up. While injection pulse width was adjusted to compensate for fuel flow reduction due to deposit build-up in the injector nozzles, in-cylinder pressure analysis indicated that the coked injectors provided lower in-cylinder pressure and poorer combustion stability.

The PLIF image analysis around the injector tip over a wide SOI sweep window revealed similar findings. The tip deposit formation increased in-cylinder charge stratification and deteriorated repeatability in the mixture preparation. Furthermore, the coked injectors consistently showed higher unburned HC emissions for all injection timings compared to the clean injectors, indicating that a portion of injected fuel escaped the combustion. Particulate matter emissions measurements indicated that the tip deposit increased total particulate number concentration for almost all injection timings. The increased PN concentration levels were associated with: (a) poor mixture preparations and more locally rich areas; (b) altered plume penetration lengths and relative angles and and (c) fuel absorption by tip deposit which partially burns in a pool fire after the main combustion.

Chapter 5-Investigation of Injector Coking Effects on Spray Characteristics under Different Injection Pressure

The X-ray testing results demonstrated that different levels of deposits were formed across the injector in the internal and external nozzle holes Extensive deposits were observed in the external injector holes and the external-hole deposits were radially distributed and collected in the shoulder; while the deposit formation reduced through the internal holes of the injector.

With the higher penetration lengths of the coked injector compared to the clean injector in general, the penetration length for the ignition and side jets of the coked injector was closely matched with that of the clean injector at a lower injection pressure of 50 bar; whilst the rear jets penetration length of the coked injector demonstrated longer penetration length. As the injection pressure was increased to 100 bar and 150 bar, the coked injector plumes demonstrated a longer penetration length compared to the clean injector. The coked injector

consistently had smaller plume angles compared to the clean injector at all the injection pressures. Coking had a significant effect on the increase of mean droplet velocities. As the injection pressure increased, the coked injector's plumes demonstrated significantly higher velocity compared to the clean injector. Also the injector coking caused an increase in the droplet size (SMD).

Chapter 6-Impact of Spark Plug Gap on Flame Kernel Propagation and Engine Performance

At the beginning of the flame kernel initiation and up to 1 ms from the start of the spark, the difference in the flame kernel size between different spark plug gaps is relatively small, especially for larger gaps such as 1.2 and 1.4 mm. As the time after ignition progresses, the larger spark plug gaps generate a significantly larger flame kernel area compared to that of the spark plug gap of 1mm. The effect of the spark plug gap is dominant at lean and stoichiometric conditions and diminishes for rich conditions.

The smallest spark gap of 1 mm generates lower engine load output for the entire range of equivalence ratio tested. For an equivalence ratio smaller than 1, the spark gap of 1.4 mm results in higher load, but for equivalence ratios higher than 1, the 1.2 and 1.4 mm gaps result in similar loads. The smallest gap of 1 mm consistently results in a higher COV of IMEP for the entire range of equivalence ratios tested. The COV of IMEP of 1.2 mm and 1.4 mm gaps is significantly lower compared to that of the 1 mm gap for stoichiometric and rich conditions. Whilst for lean conditions, the difference in the COV of IMEP between the gaps is reduced. The in-cylinder pressure, flame speed, heat release rate and the mass fraction burned increase with the spark plug gap. The maximum spark plug gap gives minimum hydrocarbon emissions

and particulate number concentration, but gives higher NOx emissions due to the high combustion temperature as well as the increase in flame speed and in-cylinder pressure.

7.2 Suggestions for Future Work

The following are some suggestions for future work.

Spray characteristics

The spray characteristics of the injector coking effect including the penetration length, plume angle, mean droplet diameter and droplet velocity can be investigated under flash boiling conditions using the optical engine. Furthermore, particle image velocimetry (PIV) can be employed to examine the effect of the spray produced by the injector deposit on the flow field in a GDI engine.

Soot distribution

Quantitative and qualitative investigation of the soot distribution inside a GDI engine using laser-induced incandescent (LII) of both clean and coked injectors would be of interest.

Numerical investigation of the spray characteristics of a coked injector

The main difficulties associated with the injector coking modelling is the real area occupied by the deposit on the inner surface of the nozzle holes. An X-ray image represnts a convinient

solution to overcome this problem and consequently, this image is employed to discover the real area and obtain comparative results with the expermental measurements.

Different fuel and additives to reduce the formation of injector deposits

The GDI injector fouling is reduced by using ethanol or additives to minmize the formation of the injector deposits as demonstrated by previous studies. Therefore, a detailed study of different fuel and additives' effects on the reducton of the deposit formation may be of interest.

Spark plug gap, material and configuration

This study demonstrated how the spark plug gap can lead to more combustion stability and lower emissions. However, the investigation of the spark plug gap on emissions is limited and narrow, therefore wide investigation for that parameter on PM emissions will be valuable. Likewise, the wide investigation of the spark plug parameter including material and configuration impacts on emissions will be interesting.

REFERENCES

[1] M. B. Çelik and B. Ozdalyan, Gasoline direct injection,: Fuel injection, InTech, 2010.

[2] E. Parliament, "Setting emission performance standards for new passenger cars as part of the Community's integrated approach to reduce CO_2 emissions from light-duty vehicles," Regulation (EC) No, vol. 443, p. 23, 2009.

[3] C. Thiel, W. Nijs, S. Simoes, J. Schmidt, A. van Zyl, and E. Schmid, "The impact of the EU car CO_2 regulation on the energy system and the role of electro-mobility to achieve transport decarbonisation," Energy Policy, vol. 96, pp. 153-166, 2016.

[4] F. Zhao, M.-C. Lai, and D. L. Harrington, "Automotive spark-ignited direct-injection gasoline engines," Progress in energy and combustion science, vol. 25, pp. 437-562, 1999.

[5] T. V. Johnson, "Review of CO_2 emissions and technologies in the road transportation sector," SAE International Journal of Engines, vol. 3, SAE Paper 2010-01-1276, 2010.

[6] C. Patil, S. Varade, and S. Wadkar, "A Review of Engine Downsizing and its Effects," International Journal of Current Engineering and Technology, vol. 7, pp. 319-324, 2017.

[7] S. Shahed and K.-H. Bauer, "Parametric studies of the impact of turbocharging on gasoline engine downsizing," SAE International Journal of Engines, vol. 2, SAE Paper 2009-01-1472, 2009.

[8] P. S. Von Bacho, J. K. Sofianek, J. M. Galante-Fox, and C. J. McMahon, "Engine test for accelerated fuel deposit formation on injectors used in gasoline direct injection engines," SAE Technical Paper 2009-01-1495, 2009.

[9] D. C. Arters, E. A. Bardasz, E. A. Schiferl, and D. W. Fisher, "A Comparison of Gasoline Direct Injection Part I-Fuel System Deposits and Vehicle Performance," SAE Technical Paper 1999-01-1498, 1999.

[10] E. A. Bardasz, D. C. Arters, E. A. Schiferl, and D. W. Righi, "A Comparison of Gasoline Direct Injection and Port Fuel Injection Vehicles: Part II-Lubricant Oil Performance and Engine Wear," SAE Technical Paper 1999-01-1499, 1999.

[11] A. D. Zand, A. Mikaeili, and H. Pezeshk, "The influence of deposit control additives on exhaust CO and HC emissions from gasoline engines (case study: Tehran)," Transportation Research Part D: Transport and Environment, vol. 12, pp. 189-194, 2007.

[12] A. A. Aradi, J. Evans, K. Miller, and A. Hotchkiss, "Direct Injection Gasoline (DIG) Injector Deposit Control with Additives," SAE Technical Paper 2003-01-2024, 2003.

[13] G. T. Kalghatgi, "Deposits in gasoline engines-a literature review," SAE Technical Paper 902105, 1990.

[14] F. Owrang, H. Mattsson, A. Nordlund, J. Olsson, and J. Pedersen, "Characterization of combustion chamber deposits from a gasoline direct injection SI engine," SAE Technical Paper 2003-01-0546, 2003.

[15] O. Güralp, M. Hoffman, D. N. Assanis, Z. Filipi, T.-W. Kuo, P. Najt, et al., "Characterizing the effect of combustion chamber deposits on a gasoline HCCI engine," SAE Technical Paper 2006-01-3277, 2006.

[16] M. Kinoshita, A. Saito, S. Matsushita, H. Shibata, and Y. Niwa, "A method for suppressing formation of deposits on fuel injector for direct injection gasoline engine," SAE Technical Paper 1999-01-3656, 1999.

[17] C. Jiang, H. Xu, D. Srivastava, X. Ma, K. Dearn, R. Cracknell, et al., "Effect of fuel injector deposit on spray characteristics, gaseous emissions and particulate matter in a gasoline direct injection engine," Applied Energy, vol. 203, pp. 390-402, 2017.

[18] H. Song, J. Xiao, Y. Chen, and Z. Huang, "The effects of deposits on spray behaviors of a gasoline direct injector," Fuel, vol. 180, pp. 506-513, 2016.

[19]   B. Wang, T. Badawy, Y. Jiang, H. Xu, A. Ghafourian, and X. Zhang, "Investigation of deposit effect on multi-hole injector spray characteristics and air/fuel mixing process," Fuel, vol. 191, pp. 10-24, 2017.

[20]   S. Henkel, Y. Hardalupas, A. Taylor, C. Conifer, R. Cracknell, T. K. Goh, et al., "Injector Fouling and Its Impact on Engine Emissions and Spray Characteristics in Gasoline Direct Injection Engines," SAE International Journal of Fuels and Lubricants, vol. 10, SAE Technical Paper 2017-01-0808, 2017.

[21]   P. H. Shu-Yi, A. Khalid, A. Mohamad, B. Manshoor, A. Sapit, I. Zaman, et al., "Analysis of Spark Plug Gap on Flame Development using Schlieren Technique and Image Processing," in IOP Conference Series: Materials Science and Engineering, 2016, p. 012044.

[22]   P. Hill and A. Kapil, "The relationship between cyclic variations in spark-ignition engines and the small structure of turbulence," Combustion and Flame, vol. 78, pp. 237-247, 1989.

[23]   D. Bradley and F.-K. Lung, "Spark ignition and the early stages of turbulent flame propagation," Combustion and Flame, vol. 69, pp. 71-93, 1987.

[24]   R. J. Craver, R. S. Podiak, and R. D. Miller, "Spark plug design factors and their effect on engine performance," SAE Technical Paper 700081, 1970.

[25]   H. Bhaskar, "Effect of Spark Plug Gap on Cycle-by-Cycle Fluctuations in Four Stroke Spark Ignition Engine," International Journal of Innovative Research and Development, vol. 5, 2016.

[26]   A. Singh, A. Lanjewar, and A. Rehman, "Direct Fuel Injection System in Gasoline Engine-A," International Journal of Innovative Technology and Exploring Engineering, pp. 21-28, 2014.

*R*eferences

[27] J. Demuynck, C. Favre, D. Bosteels, H. Hamje, and J. Andersson, "Real-World Emissions Measurements of a Gasoline Direct Injection Vehicle without and with a Gasoline Particulate Filter," SAE Technical Paper 2017-01-0985, 2017.

[28] H. Zhao, Advanced Direct Injection Combustion Engine Technologies and Development: Diesel Engines vol. 2: Elsevier, 2009.

[29] A. Scussel, A. Simko, and W. Wade, "The Ford PROCO engine update," SAE Technical Paper 780699,1978.

[30] Y. Iwamoto, K. Noma, O. Nakayama, T. Yamauchi, and H. Ando, "Development of gasoline direct injection engine," SAE technical paper 970541, 1997.

[31] J. Harada, T. Tomita, H. Mizuno, Z. Mashiki, and Y. Ito, "Development of direct injection gasoline engine," SAE Technical Paper 970540, 1997.

[32] N. Jackson, J. Stokes, P. Whitaker, and T. Lake, "Stratified and homogeneous charge operation for the direct injection gasoline engine-high power with low fuel consumption and emissions," SAE Technical Paper 970543, 1997.

[33] S. Kono, "Study of the stratified charge and stable combustion in DI gasoline engines," JSAE review, vol. 16, pp. 363-368, 1995.

[34] T. Tomoda, S. Sasaki, D. Sawada, A. Saito, and H. Sami, "Development of direct injection gasoline engine-study of stratified mixture formation," SAE Technical Paper 970539, 1997.

[35] B. Bitting, F. Gschwendtner, W. Kohlhepp, M. Kothe, C. Testroet, and K. Ziwica, "Intake Valve Deposits—Fuel Detergency Requirements Revisited," SAE Technical Paper 872117, 1987.

[36] U. Spicher, A. Kölmel, H. Kubach, and G. Töpfer, "Combustion in Spark Ignition Engines with Direct Injection," SAE Technical Paper 2000-01-0649, 2000.

References

[37] R. Ortmann, S. Arndt, J. Raimann, R. Grzeszik, and G. Wuerfel, "Methods and analysis of fuel injection, mixture preparation and charge stratification in different direct injected SI engines," SAE Technical Paper 2001-01-0970, 2001.

[38] J. Fischer, Einfluss variabler Einlassströmung auf zyklische Schwankungen bei Benzin-Direkteinspritzung. Dissertation, Universität Karlsruhe (TH), Germany, 2004.

[39] C. Baumgarten, Mixture formation in internal combustion engines: Springer -Verlag, Berlin, 2006.

[40] G. Cathcart and D. Railton, "Improving robustness of spray guided DI combustion systems: the air-assisted approach," in JSAE Spring Convention, SAE Technical Paper 2001-08-0049, , 2001.

[41] W. Hentschel, A. Homburg, G. Ohmstede, T. Mueller, and G. Grünefeld, "Investigation of spray formation of DI gasoline hollow-cone injectors inside a pressure chamber and a glass ring engine by multiple optical techniques," SAE Technical Paper 1999-01-3660, 1999.

[42] T. Stach, J. Schlerfer, and M. Vorbach, "New generation multi-hole fuel injector for direct-injection SI engines-optimization of spray characteristics by means of adapted injector layout and multiple injection," SAE Technical Paper 2007-01-1404, 2007.

[43] E. Achleitner, H. Bäcker, and A. Funaioli, "Direct injection systems for otto engines," SAE Technical Paper 2007-01-1416, 2007.

[44] M. Skogsberg, P. Dahlander, and I. Denbratt, "Spray shape and atomization quality of an outward-opening piezo gasoline DI injector," SAE Technical Paper 2007-01-1409, 2007.

[45] C. Schwarz, E. Schünemann, B. Durst, J. Fischer, and A. Witt, "Potentials of the spray-guided BMW DI combustion system," SAE Technical Paper 2006-01-1265, 2006.

*R*eferences

[46] M. Skogsberg, P. Dahlander, R. Lindgren, and I. Denbratt, "Effects of injector parameters on mixture formation for multi-hole nozzles in a spray-guided gasoline DI engine," SAE Technical Paper 2005-01-0097, 2005.

[47] S. Moon, T. Li, K. Sato, and H. Yokohata, "Governing parameters and dynamics of turbulent spray atomization from modern GDI injectors," Energy, vol. 127, pp. 89-100, 2017.

[48] R. Anderson, D. Brehob, J. Yang, J. Vallance, and R. Whiteaker, "A new direct injection spark ignition (DISI) combustion system for low emissions," FISITA-96, No. P0201, 1996.

[49] W. Anderson, J. Yang, D. Brehob, J. Vallance, and R. Whiteaker, "Understanding the thermodynamics of direct injection spark ignition (DISI) combustion systems: an analytical and experimental investigation," SAE Technical Paper 962018, 1996.

[50] B. Befrui, G. Corbinelli, M. D'Onofrio, and D. Varble, "GDI multi-hole injector internal flow and spray analysis," SAE Technical Paper 2011-01-1211, 2011.

[51] R. Kiplimo, E. Tomita, N. Kawahara, and S. Yokobe, "Effects of spray impingement, injection parameters, and EGR on the combustion and emission characteristics of a PCCI diesel engine," Applied Thermal Engineering, vol. 37, pp. 165-175, 2012.

[52] G. Kalghatgi, "Fuel/engine interactions," SAE International, Warrendale, Pennsylvania, USA, 2014.

[53] O. Altin and S. Eser, "Carbon deposit formation from thermal stressing of petroleum fuels," Prepr. Pap.-Am. Chem. Soc., Div. Fuel Chem, vol. 49, p. 764, 2004.

[54] Z. Stępień, "Deposits in spark ignition engines–formation and threats," Combustion Engines, vol. 160, pp. 36-48, 2015.

*R*eferences

[55]   H. Xu, C. Wang, X. Ma, A. K. Sarangi, A. Weall, and J. Krueger-Venus, "Fuel injector deposits in direct-injection spark-ignition engines," Progress in Energy and Combustion Science, vol. 50, pp. 63-80, 2015.

[56]   W. J. Imoehl, "Method of optimizing direct injector tip position in a homogeneous charge engine for minimum injector deposits," ed. US Patent 6832593 B2, 2004.

[57]   D. C. Arters and M. J. Macduff, "The effect on vehicle performance of injector deposits in a direct injection gasoline engine," SAE Technical Paper 2000-01-2021, 2000.

[58]   M. Anbari Attar, T. Badawy, and H. Xu, "Optical investigation of influence of injector nozzle deposit on particulate matter emissions drift," Internal Combustion Engines, IMechE, London, 2015.

[59]   R. Lindgren, M. Skogsberg, H. Sandquist, and I. Denbratt, "The influence of injector deposits on mixture formation in a DISC SI engine," SAE Technical Paper 2003-01-1771, 2003.

[60]   H. C. Yiqiang P, Jing Q, Jianwei Z, Xiang L, Bin L, Tiegang H, Xuesong W, "Effect of GDI Engine Injector Coking on Spray," Journal of Tianjin University, vol. 48, 2015.

[61]   T. D. Fansler, D. L. Reuss, V. Sick, and R. N. Dahms, "Invited Review: Combustion instability in spray-guided stratified-charge engines: A review," International Journal of Engine Research, vol. 16, pp. 260-305, 2015.

[62]   Z. Stępień and S. Oleksiak, "Deposit forming tendency in sparkignition engines and evaluation of gasoline detergent additives effectiveness," Journal of KONES, vol. 16, pp. 421-431, 2009.

[63]   C. Wang, H. Xu, J. M. Herreros, J. Wang, and R. Cracknell, "Impact of fuel and injection system on particle emissions from a GDI engine," Applied Energy, vol. 132, pp. 178-191, 2014.

References

[64] A. Berndorfer, S. Breuer, W. Piock, and P. Von Bacho, "Diffusion combustion phenomena in GDi engines caused by injection process," SAE Technical Paper 2013-01-0261, 2013.

[65] A. Joedicke, J. Krueger-Venus, P. Bohr, R. Cracknell, and D. Doyle, "Understanding the effect of DISI injector deposits on vehicle performance," SAE Technical Paper 2012-01-0391, 2012.

[66] H. Sandquist, I. Denbratt, F. Owrang, and J. Olsson, "Influence of fuel parameters on deposit formation and emissions in a direct injection stratified charge SI engine," SAE Technical Paper 2001-01-2028, 2001.

[67] A. A. Aradi, W. J. Colucci, H. M. Scull, and M. J. Openshaw, "A study of fuel additives for direct injection gasoline (DIG) injector deposit control," SAE Technical Paper 2000-01-2020, 2000.

[68] A. A. Aradi, B. Imoehl, N. L. Avery, P. P. Wells, and R. W. Grosser, "The Effect of Fuel Composition and Engine Operating Parameters on Injector Deposits in a High-Pressure Direct Injection Gasoline (DIG) Research Engine," SAE Technical Paper 1999-01-3690, 1999.

[69] W. Imoehl, L. Gestri, M. Maragliulo, L. Del-Frate, M. Klepatsch, and R. Wildeson, "A DOE approach to engine deposit testing used to optimize the design of a gasoline direct injector seat and orifice," SAE International Journal of Fuels and Lubricants, vol. 5, pp. 1078-1095, 2012.

[70] T. Ashida, Y. Takei, and H. Hosi, "Effects of fuel properties on SIDI fuel injector deposit," SAE Technical Paper 2001-01-3694, 2001.

[71] K. Dearn, J. Xu, H. Ding, H. Xu, A. Weall, P. Kirkby, et al., "An investigation into the characteristics of DISI injector deposits using advanced analytical methods," SAE International Journal of Fuels and Lubricants, vol. 7, pp. 771-782, 2014.

*R*eferences

[72] N. Karwa, P. Stephan, W. Wiese, and D. Lejsek, "Gasoline direct injection engine injector tip drying," in 19th Australasian Fluid Mechanics Conference, 2014, pp. 1-4.

[73] Y. Miura, K. Miyahara, S. Sasaki, T. Kashio, and K. Yoshida, "Development of a Gasoline Direct Injector Fouling Test and Its Application to Study of Keep-Clean Performance at Different Additive Treat Rates," SAE Technical Paper 2016-01-2248, 2016.

[74] T. J. Potter, X. Zhang, W. Vassell, M. R. Rigley, and R. E. Hetrick, "Carbonaceous deposit-resistant coating for engine components," ed: US Patent5771873, 1998.

[75] A. C. Green, M. D. D. Lambert, and M. Nandy, "Injection nozzle. Delphi Technologies Inc.," ed: Patent EP1081374 A2 patent application, 2001.

[76] R. R. Burgett, J. M. Leptich, and K. V. Sangwan, "Measuring the effect of spark plug and ignition system design on engine performance," SAE Technical Paper 720007, 1972.

[77] K. Nishio, T. Oshima, and H. Ogura, "A study on spark plug electrode shape," International Journal of Vehicle Design, vol. 15, pp. 119-130, 1994.

[78] T. Yamaguchi, S. Nakamura, and T. Oshima, "Spark plug and its electrode configuration," ed: US Patent 4,700,103, 1987.

[79] Y. Shimanokami, Y. Matsubara, T. Suzuki, and W. Matsutani, "Development of high ignitability with small size spark plug," SAE Technical Paper 2004-01-0987, 2004.

[80] S. Hood, "The V-grooved electrode spark plug," SAE Technical Paper 901535, 1990.

[81] M. Lenk and R. S. Podiak, "Copper cored ground electrode spark plug design," SAE Technical Paper 881777, 1988.

[82] Y. Lee and J. Boehler, "Flame kernel development and its effects on engine performance with various spark plug electrode configurations," SAE Technical Paper 2005-01-1133, 2005.

[83]   J. Han, H. Yamashita, and N. Hayashi, "Numerical study on the spark ignition characteristics of a methane–air mixture using detailed chemical kinetics: Effect of equivalence ratio, electrode gap distance, and electrode radius on MIE, quenching distance, and ignition delay," Combustion and Flame, vol. 157, pp. 1414-1421, 2010.

[84]   J. Han, H. Yamashita, and N. Hayashi, "Numerical study on the spark ignition characteristics of hydrogen–air mixture using detailed chemical kinetics," International Journal of Hydrogen Energy, vol. 36, pp. 9286-9297, 2011.

[85]   S. P. Bane, J. L. Ziegler, and J. E. Shepherd, "Investigation of the effect of electrode geometry on spark ignition," Combustion and Flame, vol. 162, pp. 462-469, 2015.

[86]   A. Mariani and F. Foucher, "Radio frequency spark plug: An ignition system for modern internal combustion engines," Applied Energy, vol. 122, pp. 151-161, 2014.

[87]   T. Kravchik and E. Sher, "Numerical modeling of spark ignition and flame initiation in a quiescent methane-air mixture," Combustion and flame, vol. 99, pp. 635-643, 1994.

[88]   H. Bhaskar, "Effect of Spark Plug Gap on Cycle-by-Cycle Fluctuations in Four Stroke Spark Ignition Engine," International Journal of Innovative Research and Development|| ISSN 2278–0211, vol. 5, 2016.

[89]   R. Herweg and G. Ziegler, "Flame kernel formation in a spark-ignition engine," in International symposium COMODIA, 1990, pp. 173-178.

[90]   K. Ishii, T. Tsukamoto, Y. Ujiie, and M. Kono, "Analysis of ignition mechanism of combustible mixtures by composite sparks," Combustion and Flame, vol. 91, pp. 153-164, 1992.

[91]   A. A. Quader and C. J. Dasch, "Spark plug fouling: A quick engine test," SAE Technical Paper 920006, 1992.

R*eferences*

[92]   N. Collings, S. Dinsdale, and T. Hands, "Plug fouling investigations on a running engine-an application of a novel multi-purpose diagnostic system based on the spark plug," SAE Technical Paper 912318, 1991.

[93]   C. Hall, R. Beaubier, E. Marckwardt, and R. Courtney, "Spark plug fouling-a survey-test procedures-fuel factors," SAE Technical Paper 570254, 1957.

[94]   V. Manente, C.-G. Zander, B. Johansson, P. Tunestal, and W. Cannella, "An advanced internal combustion engine concept for low emissions and high efficiency from idle to max load using gasoline partially premixed combustion," SAE Technical Paper 2010-01-2198, 2010.

[95]   M. Williams and R. Minjares, "A technical summary of Euro 6/VI vehicle emissions standards," ICCT International council on clean transportation, 2016.

[96]   M. S. Peckham, A. Finch, and B. Campbell, "Analysis of transient HC, CO, NOx and CO_2 emissions from a GDI engine using fast response gas analyzers," SAE International Journal of Engines, vol. 4, pp. 1513-1522, 2011.

[97]   K. Shimotani, K. Oikawa, Y. Tashiro, and O. Horada, "Characteristics of exhaust emission on gasoline in-cylinder direct injection engine," in Proceedings of the Internal Combustion Engine Symposium—Japan (in Japanese), 1996, pp. 115-20.

[98]   M. C. Drake, T. D. Fansler, A. S. Solomon, and G. Szekely, "Piston fuel films as a source of smoke and hydrocarbon emissions from a wall-controlled spark-ignited direct-injection engine," SAE Technical Paper 2003-01-0547, 2003.

[99]   J. Heywood, Internal combustion engine fundamentals: McGraw-Hill Education, 1988.

[100]   J. Harrington and R. Shishu, "A Single-Cylinder Engine Study of the Effects of Fuel Type, Fuel Stoichiometry, and Hydrogen-to-Carbon Ratio on CO, NO, and HC Exhaust Emissions," SAE Technical Paper 730476, 1973.

*R*eferences

[101] R. Daniel, G. Tian, H. Xu, M. L. Wyszynski, X. Wu, and Z. Huang, "Effect of spark timing and load on a DISI engine fuelled with 2, 5-dimethylfuran," Fuel, vol. 90, pp. 449-458, 2011.

[102] B. Ronald, T. Helmut, and K. Hans, "Direct fuel injection—a necessary step of development of the SI engine," FISITA Technical Paper, No. P1613, 1996.

[103] H. Heisler, "Advanced engine technology," SAE International, 1995.

[104] K. Whitby and B. Cantrell, "Atmospheric aerosols- Characteristics and measurement," in International Conference on Environmental Sensing and Assessment, Las Vegas, Nev, 1976, p. 1.

[105] M. M. Maricq, S. J. Harris, and J. J. Szente, "Soot size distributions in rich premixed ethylene flames," Combustion and Flame, vol. 132, pp. 328-342, 2003.

[106] D. Kittelson and M. Kraft, "Particle formation and models in internal combustion engines," preprint series of the cambridge centre of computational chemical engineering ISSN 1473-4273. Technical Report 142, c4e-Preprint Series, Cambridge, 2014.

[107] D. B. Kittelson, "Engines and nanoparticles: a review," Journal of aerosol science, vol. 29, pp. 575-588, 1998.

[108] K. Homann, "Formation of large molecules, particulates and ions in premixed hydrocarbon flames; progress and unresolved questions," in Symposium (International) on Combustion, 1985, pp. 857-870.

[109] Z. Mansurov, "Soot formation in combustion processes (review)," Combustion, Explosion and Shock Waves, vol. 41, p. 727, 2005.

[110] D. R. Tree and K. I. Svensson, "Soot processes in compression ignition engines," Progress in Energy and Combustion Science, vol. 33, pp. 272-309, 2007.

References

[111] O. I. Smith, "Fundamentals of soot formation in flames with application to diesel engine particulate emissions," Progress in Energy and Combustion Science, vol. 7, pp. 275-291, 1981.

[112] I. Glassman, "Combustion. 3rd," ed: Academic Press, San Diego, California, 1996.

[113] K. L. Jansen, T. V. Larson, J. Q. Koenig, T. F. Mar, C. Fields, J. Stewart, et al., "Associations between health effects and particulate matter and black carbon in subjects with respiratory disease," Environmental health perspectives, pp. 1741-1746, 2005.

[114] V. Ramanathan and G. Carmichael, "Global and regional climate changes due to black carbon," Nature geoscience, vol. 1, pp. 221-227, 2008.

[115] U. Mathis, M. Mohr, and A.-M. Forss, "Comprehensive particle characterization of modern gasoline and diesel passenger cars at low ambient temperatures," Atmospheric Environment, vol. 39, pp. 107-117, 2005.

[116] C. Parkin, "Update on the UN-ECE Particle Measurement Programme (PMP)," Cambridge Particle Meeting, Department of Engineering, University of Cambridge (UK), 2008.

[117] M. M. Maricq, J. J. Szente, and K. Jahr, "The impact of ethanol fuel blends on PM emissions from a light-duty GDI vehicle," Aerosol Science and Technology, vol. 46, pp. 576-583, 2012.

[118] C.-L. Myung, J. Kim, K. Choi, I. G. Hwang, and S. Park, "Comparative study of engine control strategies for particulate emissions from direct injection light-duty vehicle fueled with gasoline and liquid phase liquefied petroleum gas (LPG)," Fuel, vol. 94, pp. 348-355, 2012.

[119] W. Piock, G. Hoffmann, A. Berndorfer, P. Salemi, and B. Fusshoeller, "Strategies towards meeting future particulate matter emission requirements in homogeneous

gasoline direct injection engines," SAE International Journal of Engines, vol. 4, pp. 1455-1468, 2011.

[120] H. Zhao, Laser diagnostics and optical measurement techniques in internal combustion engines: SAE International, 2012.

[121] C. Schulz and V. Sick, "Tracer-LIF diagnostics: quantitative measurement of fuel concentration, temperature and fuel/air ratio in practical combustion systems," Progress in Energy and Combustion Science, vol. 31, pp. 75-121, 2005.

[122] J. Ghandhi and P. Felton, "On the fluorescent behavior of ketones at high temperatures," Experiments in Fluids, vol. 21, pp. 143-144, 1996.

[123] F. Grossmann, P. Monkhouse, M. Ridder, V. Sick, and J. Wolfrum, "Temperature and pressure dependences of the laser-induced fluorescence of gas-phase acetone and 3-pentanone," Applied Physics B: Lasers and Optics, vol. 62, pp. 249-253, 1996.

[124] A. Braeuer, F. Beyrau, and A. Leipertz, "Laser-induced fluorescence of ketones at elevated temperatures for pressures up to 20 bars by using a 248 nm excitation laser wavelength: experiments and model improvements," Applied optics, vol. 45, pp. 4982-4989, 2006.

[125] M. C. Thurber, F. Grisch, and R. K. Hanson, "Temperature imaging with single-and dual-wavelength acetone planar laser-induced fluorescence," Optics letters, vol. 22, pp. 251-253, 1997.

[126] T. Baritaud and T. Heinze, "Gasoline distribution measurements with PLIF in a SI engine," SAE Technical Paper 922355, 1992.

[127] C. Weaver, S. Wooldridge, S. Johnson, V. Sick, and G. Lavoie, "PLIF measurements of fuel distribution in a PFI engine under cold start conditions," SAE Technical Paper 2003-01-3236, 2003.

[128] Dantec-Dynamics, " BSA Flow Software Version 4.10 Installation & User's Guide. 10th ed.," 2006.

[129] G. Pitcher, G. Wigley, and M. Saffman, "Sensitivity of dropsize measurements by phase Doppler anemometry to refractive index changes in combusting fuel sprays," in Applications of Laser Techniques to Fluid Mechanics, ed: Springer, 1991, pp. 227-247.

[130] M. Richter, B. Axelsson, K. Nyholm, and M. Aldén, "Real-time calibration of planar laser-induced fluorescence air-fuel ratio measurements in combustion environments using in situ Raman scattering," in Symposium (International) on Combustion, 1998, pp. 51-57.

[131] X. Ma, X. He, J.-x. Wang, and S. Shuai, "Co-evaporative multi-component fuel design for in-cylinder PLIF measurement and application in gasoline direct injection research," Applied energy, vol. 88, pp. 2617-2627, 2011.

[132] M. Davy, P. Williams, D. Han, and R. Steeper, "Evaporation characteristics of the 3-pentanone–isooctane binary system," Experiments in fluids, vol. 35, pp. 92-99, 2003.

[133] G. Tian, R. Daniel, H. Li, H. Xu, S. Shuai, and P. Richards, "Laminar burning velocities of 2, 5-dimethylfuran compared with ethanol and gasoline," Energy & Fuels, vol. 24, pp. 3898-3905, 2010.

[134] X. Ma, C. Jiang, H. Xu, S. Shuai, and H. Ding, "Laminar burning characteristics of 2-methylfuran compared with 2, 5-dimethylfuran and isooctane," Energy & Fuels, vol. 27, pp. 6212-6221, 2013.

[135] Cambustion LTD, "DMS 500 User Manual, Version 3.5 Software Version UI v4.11," 2011.

[136] R. Stone, Introduction to internal combustion engines: Macmillan, London, 1999.

[137] J. Stegemann, J. Seebode, J. Baltes, C. Baumgarten, and G. Merker, "Influence of throttle effects at the needle seat on the spray characteristics of a multihole injection

nozzle," Proceedings of the 18th Annual Conference on Liquid Atomization and Spray Systems, ILASS Europe, vol. 9, p. 11, 2002.

[138] R. Stevens, H. Ma, C. Stone, H. Walmsley, and R. Cracknell, "On planar laser-induced fluorescence with multi-component fuel and tracer design for quantitative determination of fuel concentration in internal combustion engines," Proceedings of the Institution of Mechanical Engineers, Part D: Journal of Automobile Engineering, vol. 221, pp. 713-724, 2007.

[139] B. Williams, P. Ewart, X. Wang, R. Stone, H. Ma, H. Walmsley, et al., "Quantitative planar laser-induced fluorescence imaging of multi-component fuel/air mixing in a firing gasoline-direct-injection engine: effects of residual exhaust gas on quantitative PLIF," Combustion and Flame, vol. 157, pp. 1866-1878, 2010.

[140] P. Aleiferis and Z. Van Romunde, "An analysis of spray development with iso-octane, n-pentane, gasoline, ethanol and n-butanol from a multi-hole injector under hot fuel conditions," Fuel, vol. 105, pp. 143-168, 2013.

[141] G. Hoffmann, B. Befrui, A. Berndorfer, W. F. Piock, and D. L. Varble, "Fuel system pressure increase for enhanced performance of GDi multi-hole injection systems," SAE International Journal of Engines, vol. 7, pp. 519-527, 2014.

[142] P. Aleiferis, J. Serras-Pereira, Z. Van Romunde, J. Caine, and M. Wirth, "Mechanisms of spray formation and combustion from a multi-hole injector with E85 and gasoline," Combustion and Flame, vol. 157, pp. 735-756, 2010.

[143] J. Kazour, B. Befrui, H. Husted, M. Raney, and D. Varble, "Innovative Sprays and Particulate Reduction with GDi Injectors," SAE Technical Paper 2014-01-1441, 2014.

[144] H. Shibata, Kito, T., Saitoh, S., Walford, M., Williams, I., Kaneta, H, "Gasoline direct injection spray improvements for future emission legislation," Fuel Systems for IC Engines, IMechE, London, 2015.

[145] M. Pilch and C. Erdman, "Use of breakup time data and velocity history data to predict the maximum size of stable fragments for acceleration-induced breakup of a liquid drop," International journal of multiphase flow, vol. 13, pp. 741-757, 1987.

[146] I. Roisman, L. Araneo, and C. Tropea, "Effect of ambient pressure on penetration of a diesel spray," International journal of multiphase flow, vol. 33, pp. 904-920, 2007.

[147] J. Lacoste, C. Crua, M. Heikal, D. Kennaird, and M. Gold, "PDA characterisation of dense diesel sprays using a common-rail injection system," SAE Technical Paper 2003-01-3085, 2003.

[148] G. Tian, H. Li, H. Xu, Y. Li, and S. M. Raj, "Spray characteristics study of DMF using phase doppler particle analyzer," SAE International Journal of Passenger Cars-Mechanical Systems, vol. 3, pp. 948-958, 2010.

[149] L. Allocca, S. Alfuso, L. Marchitto, and G. Valentino, "GDI multi-hole injector: particle size and velocity distribution for single and jet-to-jet evolution analysis," in The 11th Triennial Intl. Annual Conf. on Liquid Atomization and Spray Systems, 2009.

[150] S. Lee, Y. Oh, and S. Park, "Characterization of the spray atomization process of a multi-hole gasoline direct injector based on measurements using a phase Doppler particle analyser," Proceedings of the Institution of Mechanical Engineers, Part D: Journal of Automobile Engineering, vol. 227, pp. 951-965, 2013.

[151] I. Glassman, R.A. Yetter, "Combustion," ed. (4th ed.), Academic Press, Amsterdam, Boston, 2008.

[152] I. Namyatov, S. Minaev, V. Babkin, V. Bunev, and A. Korzhavin, "Diffusion combustion of a liquid fuel film on a metal substrate," Combustion, Explosion and Shock Waves, vol. 36, pp. 562-570, 2000.

[153] M. Kinoshita, "Study of nozzle deposit formation mechanism for direct injection gasoline engines," in Proceedings of JSAE Fall Convention (in Japanese), No. 976, 1997, pp. 21-4.

[154] M. Anbari Attar, Badawy, T., Xu, H, "Optical investigation of influence of injector nozzle deposit on particulate matter emissions drift," presented at the Internal Combustion Engines, IMechE, London, 2015.

[155] B. H.-y. Cheung, Tracer-based planar laser-induced fluorescence diagnostics: quantitative photophysics and time-resolved imaging: Ph.D. thesis, Stanford University, 2011.

[156] X. He, M. A. Ratcliff, and B. T. Zigler, "Effects of gasoline direct injection engine operating parameters on particle number emissions," Energy & Fuels, vol. 26, pp. 2014-2027, 2012.

[157] O. Altin and S. Eser, "Carbon deposit formation from thermal stressing of petroleum fuels," Am. Chem. Soc. Div. Fuel Chem, vol. 49, pp. 764-766, 2004.

[158] B. Wang, Y. Jiang, P. Hutchins, T. Badawy, H. Xu, X. Zhang, et al., "Numerical analysis of deposit effect on nozzle flow and spray characteristics of GDI injectors," Applied Energy, vol. 204, pp. 1215-1224, 2017.

[159] D. Paganin, S. Mayo, T. E. Gureyev, P. R. Miller, and S. W. Wilkins, "Simultaneous phase and amplitude extraction from a single defocused image of a homogeneous object," Journal of microscopy, vol. 206, pp. 33-40, 2002.

[160] W. F. Piock, B. Befrui, A. Berndorfer, and G. Hoffmann, "Fuel Pressure and Charge Motion Effects on GDi Engine Particulate Emissions," SAE International Journal of Engines, vol. 8, pp. 464-473, 2015.

[161] T. Shiraishi, M. Fujieda, and M. Oosuga, "Influence of the spray pattern on combustion characteristics in a direct injection engine," JSAE review, vol. 18, pp. 401-403, 1997.

[162] J. Serras-Pereira, P. Aleiferis, D. Richardson, and S. Wallace, "Spray development, flow interactions and wall impingement in a direct-injection spark-ignition engine," SAE Technical Paper 2007-01-2712, 2007.

[163] E. Galloni, "Analyses about parameters that affect cyclic variation in a spark ignition engine," Applied Thermal Engineering, vol. 29, pp. 1131-1137, 2009.

[164] F. Schulz, J. Schmidt, A. Kufferath, and W. Samenfink, "Gasoline wall films and spray/wall interaction analyzed by infrared thermography," SAE International Journal of Engines, vol. 7, pp. 1165-1177, 2014.

[165] H. Sandquist, R. Lindgren, and I. Denbratt, "Sources of hydrocarbon emissions from a direct injection stratified charge spark ignition engine," SAE Technical Paper 2000-01-1906, 2000.

[166] A. Harrison, R. Cracknell, J. Krueger-Venus, and L. Sarkisov, "Computer Simulation Studies of Adsorption of Binary and Ternary Mixtures of Gasoline Components in Engine Deposits," SAE International Journal of Fuels and Lubricants, vol. 7, pp. 756-761, 2014.

[167] S. Shen, M. Jia, T. Wang, Q. Lü, and K. Sun, "Measurement of the droplets sizes of a flash boiling spray using an improved extended glare point velocimetry and sizing," Experiments in Fluids, vol. 57, pp. 1-16, 2016.

[168] D. B. Spalding, Combustion and mass transfer: a textbook with multiple-choice exercises for engineering students: Elsevier, 2013.

[169] G. P. Merker, C. Schwarz, and R. Teichmann, Combustion engines development: mixture formation, combustion, emissions and simulation: Springer, Heidelberg, Dordrecht, London, New York, 1998.

[170] P. Efthymiou, C. P. Garner, G. K. Hargrave, and D. Richardson, "An Optical Analysis of a DISI Engine Cold Start-Up Strategy," SAE Technical Paper 2015-01-1877, 2015.

References

[171]   J. Song, Y. Seo, and M. Sunwoo, "Effects of Ignition Energy and System on Combustion Characteristics in a Constant Volume Combustion Chamber," SAE Technical Paper 2000-05-0016, 2000.

[172]   C. C. Swett Jr, "Spark ignition of flowing gases," NACA Report no. 1287 1956.

[173]   Y. Ko and R. W. Anderson, "Electrode heat transfer during spark ignition," SAE Technical Paper 892083, 1989.

[174]   G. F. Ziegler, E. P. Wagner, and R. R. Maly, "Ignition of lean methane-air mixtures by high pressure glow and arc discharges," in Symposium (International) on Combustion, 1985, pp. 1817-1824.

[175]   A. G. Brown, "Measurement and modelling of combustion in a spark ignition engine," Brunel University School of Engineering and Design PhD Theses, 1991.

[176]   J. Song and M. Sunwoo, "Analysis of flame kernel development with Schlieren and laser deflection in a constant volume combustion chamber," Proceedings of the Institution of Mechanical Engineers, Part D: Journal of Automobile Engineering, vol. 216, pp. 581-590, 2002.

[177]   C. Arcoumanis and C. Bae, "Correlation between spark ignition characteristics and flame development in a constant-volume combustion chamber," SAE Technical Paper 920413, 1992.

[178]   C. Arcoumanis and C. Bae, "Visualization of flow/flame interaction in a constant-volume combustion chamber," SAE Technical Paper 930868, 1993.

[179]   R. Schießl, A. Dreizler, and U. Maas, "Comparison of different ways for image post-processing: detection of flame fronts," SAE Technical Paper 1999-01-3651, 1999.

[180]   P. G. Aleiferis and M. K. Behringer, "Flame front analysis of ethanol, butanol, iso-octane and gasoline in a spark-ignition engine using laser tomography and integral length scale measurements," Combustion and Flame, vol. 162, pp. 4533-4552, 2015.

References

[181] J. C. Sacadura, L. Robin, F. Dionnet, D. Gervais, P. Gastaldi, and A. Ahmed, "Experimental investigation of an optical direct injection SI engine using fuel-air ratio laser induced fluorescence," SAE Technical Paper 2000-01-1794, 2000.

[182] H. N. Gupta, Fundamentals of internal combustion engines: PHI Learning Private Limited, Delhi, 2013.

[183] J. Whitelaw and H. Xu, "Cyclic variations in a lean-burn spark ignition engine without and with swirl," SAE Technical Paper 950683, 1995.

[184] J. Le Coz, "Cycle-to-cycle correlations between flow field and combustion initiation in an SI engine," SAE Technical Paper 920517, 1992.

[185] B. Pundir, V. Zvonow, and C. Gupta, "Effect of charge non-homogeneity on cycle-by-cycle variations in combustion in SI engines," SAE Technical Paper 810774, 1981.

[186] S. Pischinger and J. B. Heywood, "How heat losses to the spark plug electrodes affect flame kernel development in an SI-engine," SAE Technical Paper 900021, 1990.

[187] X. Ma, C. Jiang, H. Xu, and S. Richardson, "In-cylinder optical study on combustion of DMF and DMF fuel blends," SAE Technical Paper 2012-01-1235, 2012.

[188] X. Ma, H. Xu, C. Jiang, and S. Shuai, "Ultra-high speed imaging and OH-LIF study of DMF and MF combustion in a DISI optical engine," Applied Energy, vol. 122, pp. 247-260, 2014.

[189] J. Andersson, A. Collier, and B. Wedekind, "Particle and Sulphur Species as Key Issue in Gasoline Direct Injection Diesel Exhaust," JSAE Technical paper; Society of Automotive Engineers: Tokyo, Japan,, 1999.

[190] S. Sakai, M. Hageman, and D. Rothamer, "Effect of equivalence ratio on the particulate emissions from a spark-ignited, direct-injected gasoline engine," SAE Technical Paper 2013-01-1560, 2013.

*R*eferences

[191] F. Alasfour, "NO x emission from a spark ignition engine using 30% iso-butanol–gasoline blend: Part 2—ignition timing," Applied thermal engineering, vol. 18, pp. 609-618, 1998.

[192] A. Karvountzis-Kontakiotis, L. Ntziachristos, Z. Samaras, A. Dimaratos, and M. Peckham, "Experimental investigation of cyclic variability on combustion and emissions of a high-speed SI engine," SAE Technical Paper 2015-01-0742, 2015.

[193] V. Ganesan, Internal combustion engines: Tata McGraw-Hill Publishing Company Limited, New Delhi, 2003.

[194] J. Seo, H. Y. Kim, S. Park, S. C. James, and S. S. Yoon, "Experimental and Numerical Simulations of Spray Impingement and Combustion Characteristics in Gasoline Direct Injection Engines under Variable Driving Conditions," Flow, Turbulence and Combustion, vol. 96, pp. 391-415, 2016.

[195] M. M. Maricq, "Soot formation in ethanol/gasoline fuel blend diffusion flames," Combustion and Flame, vol. 159, pp. 170-180, 2012.

[196] P. Eastwood, Particulate emissions from vehicles vol. 20: Wiley–PEPublishing Series, John Wiley & Sons, 2008.